Studi e Ricerche

Soil-structure interaction for the seismic design of integral abutment bridges

From advanced numerical modelling to simplified procedures

Domenico Gallese

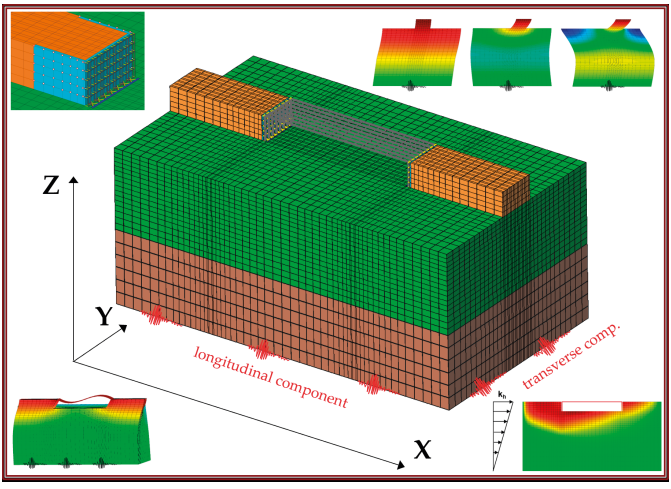

University Press

SAPIENZA
UNIVERSITÀ EDITRICE

Collana Studi e Ricerche 159

Soil-structure interaction for the seismic design of integral abutment bridges

From advanced numerical modelling to simplified procedures

Domenico Gallese

SAPIENZA
UNIVERSITÀ EDITRICE

2025

Sapienza Università Editrice
Piazzale Aldo Moro 5 – 00185 Roma

www.editricesapienza.it
editrice.sapienza@uniroma1.it

Iscrizione Registro Operatori Comunicazione n. 11420
Registry of Communication Workers registration n. 11420

ISBN 978-88-9377-362-1

DOI 10.13133/9788893773621

Pubblicato nel mese di marzo 2025 | *Published in March 2025*

Impaginazione a cura di | *Layout by*: Domenico Gallese

In copertina | *Cover image*: Domenico Gallese, *Representation of the 3D soil-bridge model used for the advanced numerical analyses* (2024).

a Sara, Italo,Silvia,
Giancarlo ed Emanuele

Contents

Preface

This thesis represents the final dissertation submitted in fulfillment of the requirements for the degree of Doctor of Philosophy at the Department of Structural and Geotechnical Engineering at Sapienza University of Rome in May 2022 (XXXIV cycle). The current version presented here was edited to align with the award of the "Prize for PhD Thesis 2023" organised by Sapienza University Press. This edition includes minor revisions primarily to correct typographical errors. No substantial modifications or additions have been made in this revision.

I would like to take this opportunity to thank my supervisor, Prof. Luigi Callisto, and my tutor, Dr. Davide Noè Gorini, who supported me from the conceptualization through the final development of this work. Additionally, I would like to express my gratitude to Prof. Pedro Arduino for his valuable contribution and for hosting me as a visiting researcher at the University of Washington (Seattle, US).

A special thought goes to my grandfather, who passed away shortly after my PhD defense.

To conclude, I wish to share a quote from the renowned athlete Pietro Paolo Mennea who set the world record for the 200 meters in 1979. His record lasted for nearly 17 years, making it one of the longest in athletics history, and it continues to be the European record. His passion, determination, humility, and selflessness have always been a source of inspiration and motivation for me.

La fatica non è mai sprecata, soffri ma sogni.
Effort is never wasted, you suffer but you dream.

Some papers extracted from this thesis are listed below:

- Gallese D., Gorini D.N., Callisto L. (2023). A nonlinear static analysis for the seismic design of single-span integral abutment bridges. Géotechnique. https://doi.org/10.1680/jgeot.22.00229.
- Marchi A., Gallese D., Gorini D.N., Franchin P., Callisto L. (2023). On the seismic performance of straight integral abutment bridges: From advanced numerical modelling to a practice-oriented analysis method. Earthquake Engng Struct Dyn. 2023; 52: 164-182. https://doi.org/10.1002/eqe.3755.
- Gallese, D., Gorini, D.N., Callisto, L. (2023). Modelling Nonlinear Static Analysis for Soil-Structure Interaction Problems. EOS 2022. https://doi.org/10.1007/978-3-031-30125-4_34.
- Gallese, D., Gorini, D.N., Callisto, L. (2022). On a Novel Seismic Design Approach for Integral Abutment Bridges Based on Nonlinear Static Analysis. PBD-IV 2022. https://doi.org/10.1007/978-3-031-11898-2_46.

First edition: May 2022
Second edition: October 2024

Abstract

Integral abutment bridges are bridges characterised by a monolithic connection between the deck and the abutments. Because of this connection, their behaviour during a seismic event is controlled by the interaction of the entire structure with the surrounding soil, and markedly with the approach embankment. Although this is becoming a popular design solution due its low maintenance requirements, procedures for the seismic design are still characterised by substantial uncertainties, mostly because of a lack of comprehension of the dynamic response of the soil-structure system. This study provides a contribution to the interpretation of the seismic behaviour of integral abutment bridges, focusing on a single-span structural scheme type that has received significant attention in recent years. The dynamic interaction between the bridge and the soil is studied with global numerical models of the soil-bridge systems developed in OpenSees and subjected to a variety of ground motions. The results of these dynamic calculations, interpreted also with the aid of a modal analysis of the system, are used to develop simplified design procedures aimed at evaluating the deformation and the internal forces in the structure. In details, a novel seismic design approach based on a nonlinear static analysis is provided for the longitudinal component of the seismic motion, that typically dominates the design of this type of bridges. In addition, a second simplified procedure is developed to take into account the influence of the transverse component of the seismic motion as well as of the wing walls. Two-directional time-domain analyses carried out on the full soil-structure model show that these complementary procedures lead to a seismic design of these bridges without any considerable underestimation. Finally, the possibility to use

an average response spectrum prescribed by technical provisions makes this approach immediately applicable to the ordinary design.

The thesis is organised into the following chapters.

Chapter 1 presents a literature review on bridges with integral abutments, discussing their main advantages and disadvantages. It analyses various modern bridge analysis procedures, highlighting gaps especially regarding the seismic design.

Chapter 2 explores the potential of the open-source analysis framework OpenSees and the significant computing power offered by the TACC for high-performance computing (HPC).

Chapter 3 focuses on a case study of a single-span integral bridge, detailing the calibration of the constitutive model, the definition of seismic actions, the modeling details and construction stages.

Chapter 4 demonstrates the potential of modal analysis as a powerful and versatile tool for analysing geotechnical systems. Although in this work the modal analysis was not directly used for the seismic design of the bridge, it has provided valuable insights for the the development of the simplified design procedure discussed in Chapter 5.

Chapter 5 discusses the response of the bridge in the longitudinal direction, which is of greater engineering interest. A simplified procedure combining nonlinear static analysis (NLSA) of geotechnical systems and the well-established capacity spectrum method (CSM) is calibrated and successfully validated.

Chapter 6 presents the results of bidirectional analyses on a complete 3D bridge-soil model. It is shown that in the case study at hand, the response in the transverse and longitudinal directions can be considered decoupled. Therefore, a complementary and more simplified procedure has been developed and validated for the design of the bridge in the transverse direction.

Chapter 7 examines the influence of wing walls on the overall seismic response of the system. While the presence of the wing walls is significant in the transverse direction, the response of the system can still be considered decoupled. Consequently, no substantial modifications were necessary for the design in the longitudinal direction, but a slight extension of the simplified procedure was required for the transverse direction. Some considerations that emerge from the interpretation of the results suggest that, although the case study pertains to a simple,

geometrically regular model with a single span, the inclusion of wing walls in asymmetric geometries, along with various abutment typologies, may result in a potential coupling of the longitudinal and transverse responses. Thus, for these specific cases, decomposing the response into two main directions may no longer be applicable and appropriate numerical 3D models necessarily need to be developed.

Finally, the main conclusions are summarised in the last section. The two complementary procedures developed in this work can be combined to achieve a comprehensive seismic design for such systems. In detail, although the more notable procedure developed for the longitudinal seismic design (NLSA) has been validated on a single case study, it has general applicability and can be extended, if appropriately calibrated, to other geotechnical systems, such as tunnels, underground frame structures and slopes. This approach, conceived and developed through a careful interpretation of modal analysis, has extended the nonlinear static analysis of geotechnical systems toward new horizons, highlighting the role of the capacity curve as an intrinsic representation of their highly nonlinear behavior. On the other hand, the procedure developed for the transverse direction, while simple and streamlined, allows for considering the potential presence of wing walls that, as can be inferred, increase the volume of surrounding soil involved in the transverse response. Finally, it is important to note that since both procedures use a decoupled approach for defining seismic demand, the adoption of an appropriate spectrum prescribed by technical provisions makes this tool readily applicable for routine seismic design.

1. Integral abutment bridges

Today's bridge designers are essentially striving to achieve the same goals as their counterparts were 70 years ago: long-term service ability, low maintenance characteristics, and economy of construction (Wasserman and Walker 1996). One of the most important aspect of design is the reduction or elimination of roadway expansion devices and associated bearings common in conventional bridges that are expensive in their materials and installation.

Bridges are traditionally built with expansion joints at the ends to allow for longitudinal displacements of the superstructure due to temperature variations. Expansion joints may allow water, accumulation of dirt and especially in geographical regions that experience low seasonal temperatures and an abundance of snow and freezing rain, the use of the de-icing chemicals also have a significantly adverse effect on the durability and integrity of these bridges (Burke 2009). The expansion joints have allowed roadway drainage, contaminated with these agents, to penetrate below roadway surfaces and wash over supported beam, bearings and other main structural members. The resulting corrosion and deterioration have been so serious that some bridges have collapsed while others have had to be closed to traffic to prevent their collapse. So, many jointed bridges have required extensive repairs while most of them that have remained in service, have required almost continuous maintenance to counteract the adverse effects of contaminated deck drainage. Consequently joints and bearings have caused considerable maintenance problems for transportation agencies not just for the cost of maintaining and repairing all these elements, but also for the disruption to traffic with road closures.

Therefore, considering all the problems associated with expansion joints and supports in traditional bridges, the idea of physically connecting superstructure and substructure to create what is commonly called *integral abutment bridge* (IAB) is becoming increasingly popular (Fig. 1.1). This concept avoids all the problems associated with connecting and supporting devices because it considers a structure with one or more spans without expansion joints and supports: piers, deck and abutments are connected monolithically to create a complex structural and geotechnical interaction.

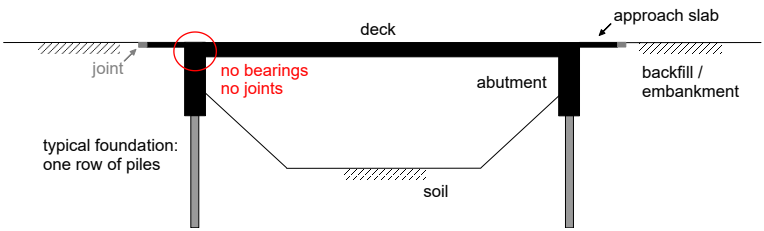

Fig. 1.1. Typical single-span integral abutment bridge.

1.1. Historical background

The use of integral bridges began thousands of years ago since masonry arches were first introduced; today there are many examples of masonry arch viaducts and aqueducts, hundreds of meters in length, which have survived for a very long time (Hambly 1997). According to Martin P.Burke, Jr. (1990), the Ohio Department of Transportation (US) was one of the first agencies to initiate the routine use of continuous construction in the 1930s; the first integral bridge was the *Teens Run Bridges*, built in 1938 near Eureka in Gallia County, Ohio (Fig. 1.2). It consists of five continuous reinforced concrete slab spans supported by capped pile piers and abutments. The design of these bridges was facilitated by a simple and straightforward method that Professor Hardy Cross in 1930 published in a paper in the *Proceeding of the American Society of Civil Engineers* that allows for the analysis of continuous beams and frames by means of moment distribution. This created a minor revolution in the design and construction of short- and medium-span bridges (Burke 1990). Before Cross's "moment distribution", multiple-span bridges were generally constructed as a series of simple spans. Following the introduction of the "moment distribution" approach, bridge engineers began

eliminating troublesome deck joints at piers by providing continuous superstructure. Although the Hardy Cross Method was a significant advancement, it still required time consuming and tedious hand calculations. In fact, the real boom in the design and construction of continuous bridges began with the widespread use of the computer.

Fig. 1.2. Teens Run Bridge, near Eureka, Ohio, 1938. It is thought to be the first integral bridge constructed in the United States and possibly in the world. (Burke 2009)

Nowadays in USA, there are more than 9000 integral abutment bridges (White et al. 2010); in Europe the experience with IABs is significantly less, apart some exceptions already built in Sweden and Germany, but the experience gained so far has been positive. As a result, the trend is toward making IAB a larger percentage of all newly constructed bridges across Europe. The U.K. and Ireland (BA 42/96) requires that all bridges less than 60 m and with a skew less than 30° be constructed as an IAB unless there are overriding reasons. Other authors as Connal (2004) reported more attention and interest to these bridges in Australia, Nakamura et al. (2002) mentioned IABs as a new technology of constructing composite bridges in Japan while Waldin et al. (2012) and Wood (2015) focus on the seismic performance assessments of these bridge in New Zealand. Presumably, with continued care and consideration, it appears that the use of integral bridges will continue to see a gradual increase in the numbers of transportation departments adopting the integral bridge

concept for routine bridge applications. Last but not least, following these trend, transportation departments are also beginning to convert existing bridges into IABs (integral retrofitting). A whole new industry is so born.

1.2. Typology of bridges

What makes these bridges really special from a design standpoint is that IABs do not have a well established typology worldwide. The 6694-1 has described at least three types of frame abutments, shown in Fig. 1.3 a-c, also known as full-height abutments as they have relatively great height in the range of 5 to 8 m, one embedded wall (Fig. 1.3 d), three different bank pad abutments (Fig. 1.3 e-g) including an abutment on discrete piles, similar to the type met in the USA; three different flexible support abutments (Fig. 1.3 h-j) with piles or columns in sleeves or reinforced earth wall or with reinforced earth wall being independent of the abutment and another three semi-integral abutments (Fig. 1.3 k-m), where the *semi-integral abutment bridges* are bridges with continuous superstructure and without expansion joints where supports are installed at the ends of the bridge. Furthermore, heights, materials, boundary conditions and connections are also varying drastically among IAB designs and no studies exist that systematically compare the behaviour of IABs having different types of integral abutments. White et al. (2010) looking at the results of the European Surveys responses and past surveys of USA transportation agencies, observed that there are at the same time similarities and significant differences in design assumptions and construction practices such as type of the backfill soil, foundations, drainage system, reinforcement, influence and disposition of wing walls and use of the approach slab.

Despite the large number of realizations all over the world, the design of IAB remains a problem that calls into play soil-structure interaction considerations. Additionally, since the typology is very different, as shown in the Fig. 1.3, indications are missing even in modern construction codes. This is particularly evident for the specific aspect of seismic design. Recognising the importance of IABs due to their benefits over conventional construction types, this type of bridges was explicitly included in the mandate of the Eurocode Committee for the evolution of Eurocodes by 2020.

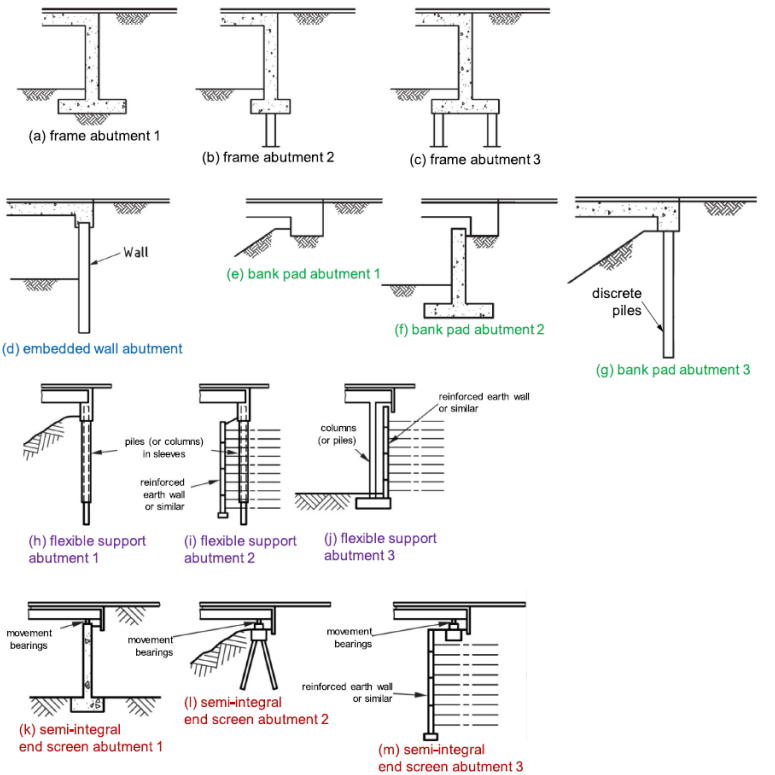

Fig. 1.3. Types of abutments in integral bridge construction (from PD6694-1).

1.3. Static considerations

1.3.1. Thermal effects: a review

Without the freedom offered by bearings, which naturally accommodate the daily and seasonal thermal expansions of the bridge deck as movement relative to the abutments, these thermal expansions must instead be accommodated through interaction of the abutments themselves with the fill that is placed behind them (Fig. 1.4). *Thus, from a structural point of view, the design question is: what are the magnitudes of the earth pressures that are generated on the abutments and what are the magnitudes of the resulting bending moment?* (Muir Wood 2004)

It appears that this is a simple problem of calculation of earth pressures and, since thermal expansion causes the abutment wall to move towards the fill, it must be passive pressure that will dominate the loading. However, it is known that passive pressure is mobilised rather

slowly with increasing wall displacement so it must be appropriate to make some allowance for actual wall movement in estimating the passive pressure coefficient to be used. On the other hand, the process of construction of the abutment will involve compaction of the fill and this will itself lock in certain initial stress into the wall. This is a classic example of soil-structure interaction where the structural consequences of the thermal movements are dependent on the relative stiffness of the fill and the structure.

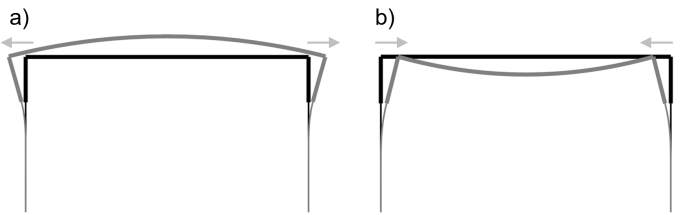

Fig. 1.4. Temperature-induced displacement patterns in IABs: (a) expansion; (b) contraction.

In these type of bridge, the abutment has a dual role. It is primarily requested to resist the vertical load from the bridge deck so that the main requirement is that it should be stiff vertically; in addition, it must be sufficiently strong laterally to contain the backfill soil and possibly resist loads generated by the traffic on the approach embankment. An extremely flexible abutment will withstand deck expansion by flexure near its top and may not move towards the fill sufficiently to generate any significant passive pressure: indeed it may retain an outward deflection from the initial construction placement and compaction of the backfill (Fig. 1.5). On the contrary, a much stiffer or rigid abutment would tend to move into the backfill more monolithically and would be expected to generate the passive pressure over much of its height. In order to control the magnitude of the bending moments that arise in the abutment there is some advantage in aiming for a flexible structural element which tries to reduce the mobilitasion of high earth pressures. Obviously the structural consequences of the thermal movements are dependent on the relative stiffness of the fill and the structure. This is the main reason for which these bridges have a flexible abutment; this is in fact conceived to mitigate the internal stresses produced by thermal changes.

Following the growing and renewed interest in the behavior of these bridges, many authors have begun to study their static behavior since

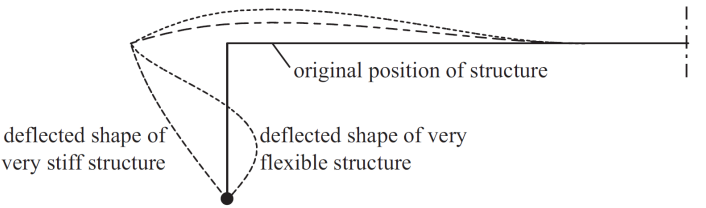

Fig. 1.5. Schematic influence of abutment flexibility on abutment deflections (abutment assumed pinned at base) (Muir Wood 2004).

the second half of the 90s. Springman et al. (1996) investigated two special case of IABs, frame abutment (Fig. 1.3-a) and embedded wall abutment (Fig. 1.3-d), examining the relationship between the abutment movements with both the magnitude and distribution of lateral earth pressures on the walls, as well as the volume loss/settlement behind the wall. This investigation in coarse-grained soil was carried out using a comparison between centrifuge test and numerical analysis. The authors suggested that the backfill soil should be specified to achieve medium dense fill with relative density $D_R \sim 80\%$. Using uncompacted fill with low D_R to try to limit lateral earth pressures is not an advantage since this loose packing is destroyed by cyclic straining, lateral earth pressures rise accordingly and large shear and volumetric deformations cause significant settlements. The continuous two-way cycling of the backfill due to daily and seasonal temperature fluctuations leads to strain hardening and soil densification. This phenomenon called *soil ratcheting* produces an increase in stiffness of the soil response and therefore an increase of the lateral earth pressure with the number of cycles. Finally, for the two prototypes examined, the authors provided two different lateral earth pressure distributions for the static design as well as some recommendations for placing the run-on slab to transfer the effect of differential movements.

England et al. (2000) continued the previous study with further numerical analyses and employed well-designed laboratory experiments of the frame abutment typology (Fig. 1.3-a). Investigating the escalation of the mobilised lateral earth pressure over time, they observed that there is a quickly increment during the early temperature cycles until a steady-state value, representative of long-term conditions, is reached. The extent of stress escalation and the time required to reach this steady

state are determined primarily by the bridge dimension and the nature of thermal fluctuations, both seasonally and daily. Furthermore the long term condition does not appear to be significantly influenced either by the the initial density of the backfill or the completation date of the construction (first cycles in summer or winter). However, unlike the steady state for soil stresses, settlement is continuous throughout the life of the bridge.

Muir Wood and Nash (2000) through numerical 2D plane strain analyses on frame abutment prototype (Fig. 1.6) with abutments pinned at their bases and using a Mohr-Coulomb model, showed that the backfill strength has a negligible effect on the horizontal stresses in the abutment (Fig. 1.7 a) while on the other hand, relative stiffness between backfill and abutment has a dramatic effect (Fig. 1.7 b-c). This apparent and counter intuitive independence of the results from the angle of friction of the backfill over large range (from 35° to 55°) can be understood when the stress path for a typical element of soil at middle height just behind the wall is considered. There is of course some rotation of principal axes (Fig. 1.8 b) resulting from the generation of shear stresses on vertical planes in the backfill from the shear resistance on the back of the wall so that principal stresses are not actually sufficient to describe the stress state completely. However, in terms of principal stress quantities, the major and the minor principal stresses σ_1 and σ_3, a plane strain mean stress $s = (\sigma_1 + \sigma_3)/2$ and shear stress $t = (\sigma_1 - \sigma_3)/2$ can be defined. Except for a small row of elements close to the top of the wall where the stress level is so low that the available shearing resistance is mobilised, around the mid-height of the wall, where the most significant stress changes occur, the movement of the wall towards the backfill tends to increase the horizontal stress producing a major change in the mean stress s but a rather small change in the shear stress t. Thus, the stress state is moving towards a more isotropic condition with a *lower* mobilised strength (Fig. 1.8). The wall friction is also helping to generate some additional vertical stress and hence provides some additional confinement to the fill. The majority of the backfill is therefore being loaded entirely elastically and its frictional strength plays no important role, except just towards the top of the abutment, but the stresses here have negligible effects on the generation of moments in the abutment.

All the results seen until now, provided the basis of the recommendations summarised by the UK Highways Agency in the BA 42/96 amendment No.1 (2003). Over the years, other studies were aimed at improving

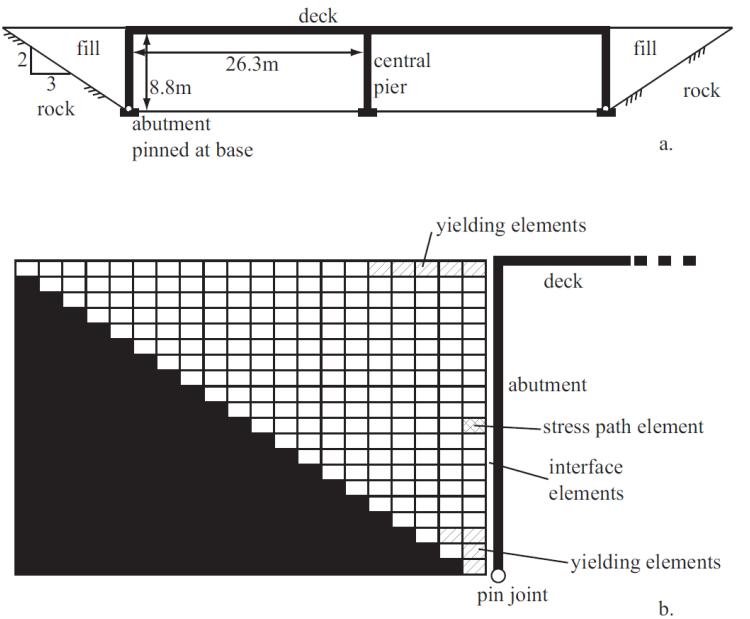

Fig. 1.6. Integral abutment bridge: (a) prototype dimension; (b) FLAC plane strain model (Muir Wood and Nash 2000).

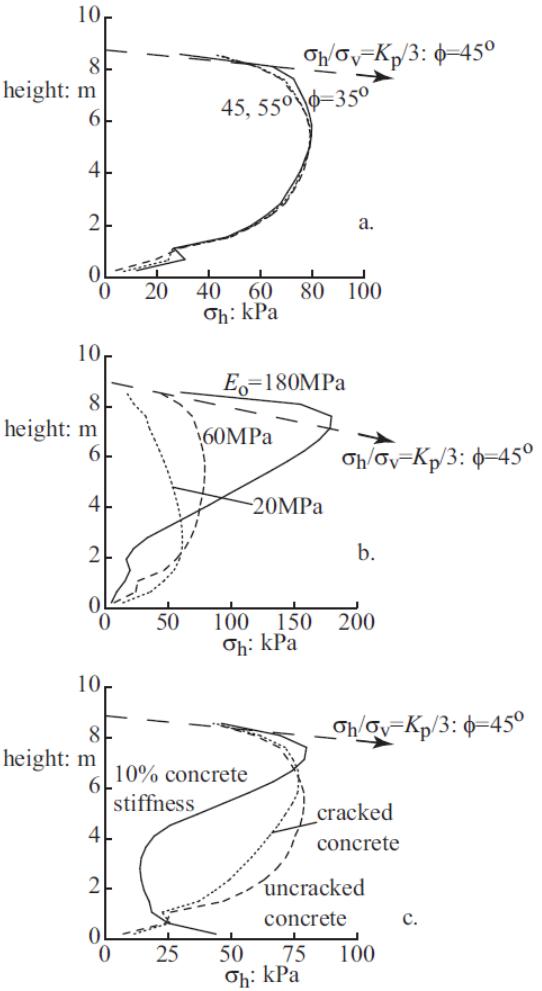

Fig. 1.7. Horizontal stresses on abutment: (a) effect of angle shearing resistance of fill; (b) effect of fill stiffness; (c) effect of abutment stiffness (Muir Wood 2004).

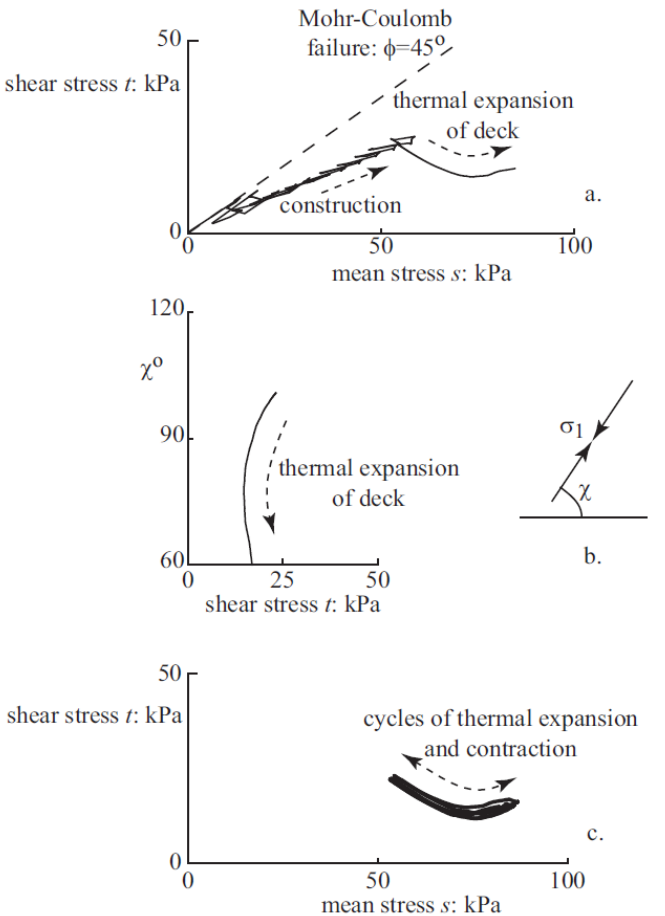

Fig. 1.8. (a) Stress path for element at mid-height behind the abutment; (b) rotation of principal axes for this element; (c) stress path during cycles of thermal expansion and contraction (Muir Wood 2004).

the understanding of the performance of IABs subjected to cyclic loading. In fact, there remains significant uncertainty on how the magnitude of lateral stresses on the abutment may be assessed for design. Lehane (2011) addressed these uncertainties using the results from a centrifuge study involving cyclic rotation of abutments for a range of soil conditions. These tests, which were performed using the beam centrifuge at the University of Western Australia (UWA) in the period 2002-2007 (Fig. 1.9), extend the database of lateral stress measurements and assist the assessment of effects such as the initial density of the granular backfill, the height of abutment, the magnitude and number of rotational cycles, the particle shape and soil structure. Combining the results, the study has confirmed that cycling loading in granular fill leads to increase in the maximum lateral stresses, and hence in the operational soil stiffness. The rate of stress increase is relatively small after about 100 typical design cyclic rotations with amplitude of $\Delta / H < 0.5\%$, at which stage the operational modulus of the fill is virtually independent of its initial relative density and angularity. Furthermore design lateral stresses may be estimated using a simple elastic FE analysis involving a linear modulus for the soil that is about 40% of the small-strain stiffness of compacted fill E_0 where this E_0 value may be measured using standard geophysical techniques. Caristo et al. (2018) with numerical analyses confirmed that the development of pressures on abutment walls can be divided into two phases: at first, an increase in pressures was exerted on the abutment wall for up to 30 consecutive load cycles and, after this point, there was an almost negligible change both in shape and maximum peaks. However, although the pressures were virtually unchanged, there was a constant increase in heaving of the backfill soil behind ; this can be explained by the non-linear behaviour of the soil, which accumulates plastic deformations and leads to increase heaving at a distance from the abutment. The authors also investigated the performance of an innovative isolation system for IABs using recycled tyres as a compressible inclusion through detailed numerical models. The proposed isolation scheme was found to be an effective and sustainable method to isolate the structure from the backfill soil, reducing the pressures experienced by the abutments and the residual vertical displacements of the backfill soil.

The design of IABs is a challenge; all the studies and efforts made so far prove this. Part of the problem is that IABs, for all their simplicity of construction, are complicated structural systems involving a

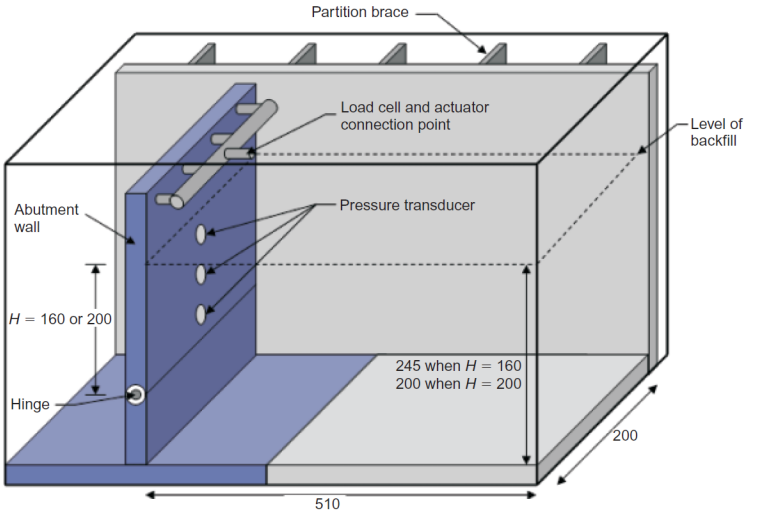

Fig. 1.9. Strongbox arrangement for UWA centrifuge tests (dimensions in mm).

soil-structure interaction problem: the deflected shape of the structure is dependent upon the soil response, and in turn the soil response is a function of the structure deformation. Moreover, to thoroughly analyse a given structure the designer must not only design for primary loads (dead, live, wind, etc.) but must also accurately account for secondary loads (creep, shrinkage, differential settlement, temperature effects, etc.) that, because of their integral construction, are so difficult to quantify. To further complicate the analysis, the response of the structure to a given set of forces is very dependent on the geometry, materials, configuration, soil interaction, and construction details of the individual system. So while IABs have been used successfully for many years, their implementation has not been an exact science, but rather a matter of intuition, experimentation and observation.

1.3.2. Design of IABs

The design of these bridges is mostly based on observations and field experiences. Although there are many types of these bridges, as already described in the section 1.2, and there are differences in design philosophies between transportation agencies worldwide, it is still possible to describe a common line of thought regarding their design and construction. The main points are reported below.

Foundations. Pile foundations on a single row are the most common solutions for these bridge. In this manner, the greatest amount of flexibility is achieved to accommodate cyclic thermal movements. There is still debate on the orientation of steel piles (Wasserman and Walker 1996, White 2007). In US for example, some states orient the piling so that the direction of thermal movements causes bending about the strong axis of the pile, while others prefer the orientation about the weak axis. Both methods have proven to be satisfactory to the respective agencies. Orienting the piling for weak-axis bending offers the least resistance but due to the potential for flange buckling, the total lateral displacement that can be accommodated is more limited than when the piling is oriented for strong-axis bending. This problem does not exist in Europe where typically symmetrical reinforced concrete section is used. However the problem of low-cycle fatigue performance of piles is not secondary and should be considered for lengths of the order of 100-200 m as appropriate; e.g. cold and temperate climates, clay or sand soil types (Dicleli and Albhaisi 2003, Dicleli and Albhaisi 2004).

Meanwhile other IABs are built with the frame abutment solution which offers a stiffer overall response. However, according to White (2007), in spite spread footings, by their very nature, restrain the rotation of the abutment stem, none of the US agencies have reported any problems related to the restrained abutment rotations.

Approach slabs. The approach slab must be anchored into the abutment backwall so that it moves in concert with the bridge. Otherwise, cyclic expansions will force the slab to move with the bridge without a mechanism to pull it back when the bridge contracts. To facilitate approach slab movements, sealed cycle-control joints should be provided between approach slabs and approach pavements to accommodate the longitudinal cycling of the approach slabs. These joints should be designed to prevent roadway drainage from penetrating the joints and flooding the sub-base. To protect these joints, effective pressure relief joints should also be provided between the joints and all rigid approach pavements. Consequently, two types of joints are required adjacent to integral bridges built in conjunction with jointed rigid approach pavements.

One (pressure relief joint) should be capable of responding to the progressive growth/pressure (G/P phenomenon, Burke 2009) of approach pavement. The other joint (cycle control joint) should facilitate the longitudinal cycling of the integral bridge and the attached approach slabs.

Approach slabs have a number of beneficial effects (Burke 2009). By spanning between abutments and approach embankments, they help prevent vehicular traffic from consolidating backfill adjacent to abutments. If approach slabs are long enough, they also eliminate live load surcharge on abutment backfill. They help to control bridge deck drainage, especially those slabs that have been provided with curbs, by conducting such drainage to approach pavements and to roadway drains. Such control of deck drainage helps prevent saturation and freezing of abutment backfill. They also help to minimise erosion of the backfill. Finally, they function as ramps from rigidly supported bridge abutments to consolidating approach embankments and thereby serve to help retain smoother riding surfaces and reduce vehicular impacts. In effect, approach slabs minimise the amount of continual maintenance that is necessary adjacent to bridges constructed without them.

On the other hand, being tied to integral bridges approach slabs become part of the bridges. Consequently, they should be explicitly considered in the definition of the overall length of the deck which is proportional to the thermal effects, thereby requiring greater movements ranges for cycle-control joints. To minimise the amount of force necessary to move the approach slabs, they should be cast on smooth, low-friction surfaces (polyethylene sheets, filter fabric, etc.)

Wing walls. A wing wall is defined as the retaining wall adjacent to the abutment stem which retains the fill behind the abutments and ensures the slope stability of the approach roadway. Wing wall orientation and connection details may have a dramatic impact on the magnitude of forces throughout the structure. Wing walls are designed to resist the forces applied to them, but the forces that wing walls may be exerting on the overall structure do not typically get a lot of attention from the bridge engineer. Cantilevered in-line wing walls (Fig. 1.10-a) behave as cantilevered beams subjected to their own vertical dead load and the horizontal pressure exerted by

the retained soil. Placing piles beneath the wing walls complicates the analysis, since the moving wing walls must not only overcome the resistance of the soil, but also the resistance of the piles. Cantilevered U-wing walls (Fig. 1.10-c) and cantilevered flared wing walls (Fig. 1.10-b) are more complicated in that because they are subjected to all of the same forces as in-line wing walls, plus an additional load from the bearing resistance of the soil beneath the rotating wing walls. As the abutment stem rotates, the wing walls are resisted by passive resistance of the retained soil and the bearing resistance of the soil beneath the wing walls. Generally, additional forces are introduced into the overall structural system when piles are placed beneath the wing walls. The piles create a moment couple that prevents rotation of the abutment stem. These restrained rotations create internal forces that must be accommodated somewhere in the structural system. Currently, (White 2008), there is little agreement among the various agencies in US and Europe regarding what limits, if any, should be placed on the wing wall type, length or support conditions.

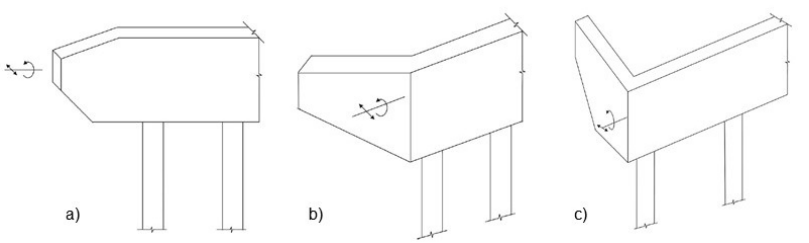

Fig. 1.10. Simple diagram of IAB with: (a) cantilevered in-line wing wall; (b) cantilevered flared wing wall; (c) cantilevered U-shaped wing wall.

1.3.3. Attributes and limitations

The superior economy of integral bridges is due to their ability, within a limited application range, to satisfy all functional requirements with safety, durability and optimal economy. As this dissertation suggests, IABs have numerous attributes and few limitations. The attributes have not been achieved without cost. Because of their aforementioned integral connection, they are subjected to a number of secondary effects (shrinkage, creep, thermal gradient, differential settlement) that are well

known but difficult to quantify. In this respect, bridge engineers have become rather pragmatic. They would rather build the cheaper IABs and tolerate these secondary stresses than build the more expensive jointed bridges with their vulnerability to deicing chemical corrosion and to the destructive pavement G/P (grow/pressure), a phenomenon not fully studied and appreciated yet (Burke 2009).

Among limitations, the most important is related to the maximum length that should be limited to minimise the bridge movements to reduce the mobilisation of high earth pressures which in turn, control the magnitude of the bending moments that arise in the abutment, resulting in fatigue problems in pile foundations. In addition, these bridges should not be used with extreme skews ($> 30°$), because for larger skews the passive earth pressure forces generated on the abutment rear faces during bridge expansion may cause a plan rotation of the bridge (Connal 2004). These forces become too large if the skew is large, and resistance to this rotation causes additional forces in the piles and can overload the wing walls if they are attached to the abutment.

Secondly, elimination of the cycle-control joints from the bridges has not eliminated the need for joints to facilitate their cyclic movement. As the joints are not incorporated in the bridge, they must be incorporated in the bridge approaches. Ignoring this can lead to problems with the approach slabs.

Nevertheless, at the moment, probably the big limitation from a practical and design point of view is the lack of codes concerning the IABs; consequently in many countries engineers refer to general design criteria. These criteria reflect the complexity of design due an insufficient knowledge of soil structure interaction phenomena.

1.4. Seismic behaviour

In recent years it was observed that a large number of bridges with integral abutments, subjected to strong ground shaking in California and New Zealand, showed a satisfactory seismic performance (Waldin et al. 2012, Wood 2015). Actually, as early as the end of the 80s, Lam and Martin (1986) foreseeing their potentials, included them in a report about the seismic design of highway bridge foundations in the US (FHWA/RD-86/102). Undoubtedly, the seismic behavior of these bridges is very complex as there are many factors that should be taken into account. Interestingly, they all relate to the presence of abutment-

embankment system that produces a kinematic and inertial interaction as well as a supplementary damping and hence energy dissipation. So, the seismic performance of these bridges has attracted the interest of many researchers and bridge engineers. Studies have been focused repeatedly on the recorded responses of two short IABs that had been instrumented with several accelerometers: these are the Painter Street Overcrossing (PSO) and the Melloland Street Overcrossing (MSO), both in California.

Werner et al. (1987) focusing on the transversal and vertical response, performed system identification analyses on the MRO response records and concluded that the abutment and soil embankments had a significant influence on the global bridge superstructure response. Wilson and Tan (1990a) and Wilson and Tan (1990b) performed the first study that presented a simple analytical model to estimate the flexible embankment contribution: they determined the static transverse and the vertical stiffness of approach embankment of typical short- and medium-span highway bridges. Their closed-form expressions that account for the sloped geometry of the embankment provide a realistic estimate of the static stiffnesses of a unit-width wedge and are consistent with the shear-wedge model (Mononobe et al. 1936, Gazetas 1987) that can be easily used to estimate the amplification functions of approach embankments. In order to obtain the total abutment stiffness, they proposed to use the embedded length of the wing walls as the multiplying factor for each of unit stiffnesses. Moreover, they recognised that part of the total superstructure damping is caused by energy dissipation in the abutment-embankment soil and that the soil damping appears to exhibit a strain dependency. As suggested by Werner et al. this study highlights the importance of the abutment-embankment soil contribution to the overall dynamic response of the bridge system. However, similar to the previous study of Werner et al., the authors did not provide any information on the embankment stiffness and damping along the longitudinal direction, nor did they include the significant effects of the nonlinear soil behaviour.

A next comprehensive study was conducted by McCallen and Romstad (1994) that studied the dynamic response of a short-span IAB employing two different modelling approaches. The first approach utilises reduced order *stick* model idealizations while the second approach, utilizes a detailed, three dimensional finite element method (Fig. 1.11), including a discretization of the soil embankment. The

Ramberg-Osgood model was used to represent the nonlinear behaviour of the soil embankment, by fitting the standard modulus reduction and damping curves developed by Seed et al. (1984). They observed that the bridge-soil system exhibits highly non linear response, even when the superstructure remains essentially elastic. The sensitivity to soil stiffness and mass becomes more pronounced as the soil becomes softer. Moreover the authors established the validity of a stick model, where the stiffness of the embankment was represented with linear spring constants. The study indicates both the substantial reduction in transverse and longitudinal frequencies and the increment of modal damping in the order of 20% to 30% when realistic soil strains are considered. However the authors noted that such damping values reflect the uncertainties inherent in the use of the modal damping ratio in a linear model to represent the energy dissipation developed in a highly nonlinear bridge-soil system. They, therefore, encouraged the potential advantages of the fully continuum model where ad hoc adjustments of the system damping are not required.

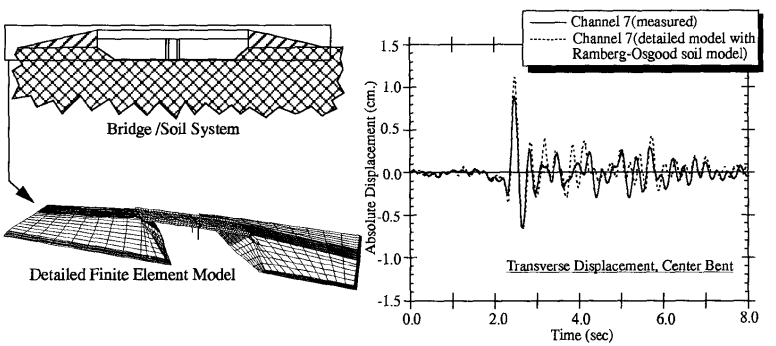

Fig. 1.11. Detailed finite element model of the PSO system used for transient seismic analysis (NIKE3D finite element model, McCallen and Romstad 1994).

Recognising the limitations of small-amplitude tests (for example those of Crouse et al. 1987) on highway bridges that are not useful in design for intense ground-motions, Goel and Chopra (1997) employed an equilibrium based approach to back-figure the abutment capacity and stiffness values at different level of shaking and to evaluate current modelling procedures. It is found that the abutment stiffness changes significantly during strong ground motions; in particular the abutment tends to be stiff for the small deformations during the build-up phase of

shaking and tends to decrease as its deformation increases. Furthermore, the abutment recovers only partially and gradually over time its stiffness as the motion becomes less intense and this recovery is especially slow after repeated cycles of large deformations. Finally they observed that adopting the current procedures (Caltrans 1988), the normal abutment capacity and stiffness may be overestimated by a factor of over two although these analyses concern only the case study of PSO. In the follow-up work Goel (1997) investigated how abutment participation affected the vibration properties of bridges with integral abutment. Through the identification of the vibration properties of PSO, he showed that the vibration period elongated and the damping ratio increased by a factor of over two as the intensity of ground shaking increased exhibiting a significant correlation. Moreover, he investigated the combined effects of the elongation in the vibration period as well as the role of the damping, stating that the first effect dominated the second.

Motivated from the need to provide a systematic procedure in estimating the stiffness of abutment, which depends strongly on the level of strains that develop in the approach embankment, Zhang and Makris (2002a, 2002b) presented a methodology based on the substructure approach, where the kinematics response functions and dynamic stiffnesses are computed separately and subsequently incorporated in a simple dynamic model where the mechanical behaviour of each of its components can be calculated with any desired level of sophistication. The model is based on the development of a kinematic response function (transfer function), which is the solution of the differential equation of motion of a truncated shear beam in the frequency domain (Fig. 1.12). The soil non-linearity is simply taken into account considering the well-known viscoelastic material where the shear modulus is written as a complex quantity. In selecting the value of G and ξ iterations are required, since their values are strain dependent and can be easily calculated by means of curves available in the literature (e.g. Seed et al. 1984). The use of a single amplification function was validated through comparisons with numerical 2D and 3D analyses and therefore applied to both transverse and longitudinal directions. They observed that typical approach embankments tend to amplify substantially the free field motions by two to three times and should not be neglected. The other ingredient of the method was the dynamic stiffness of embankments. The static solution of Wilson and Tan was so extended to take into account the frequency response; they observed that the dynamic stiffness

can be approximated in practice with frequency independent *spring* and *dashpot*. Then, they provided a closed-form expression for the critical length L_c, defined as the ratio of the transverse static stiffness of the approach embankment to the transverse static stiffness of a unit-width wedge. Note that in this study, the total stiffness and damping values along longitudinal direction are equal to those in the transverse direction. Finally, they employed these ingredients in a reduced-order stick model (Fig. 1.13) that yields seismic responses comparable to those observed in the field for MRO and for PSO. The study also confirms a significant damping ratio in the range of 10% to 20%.

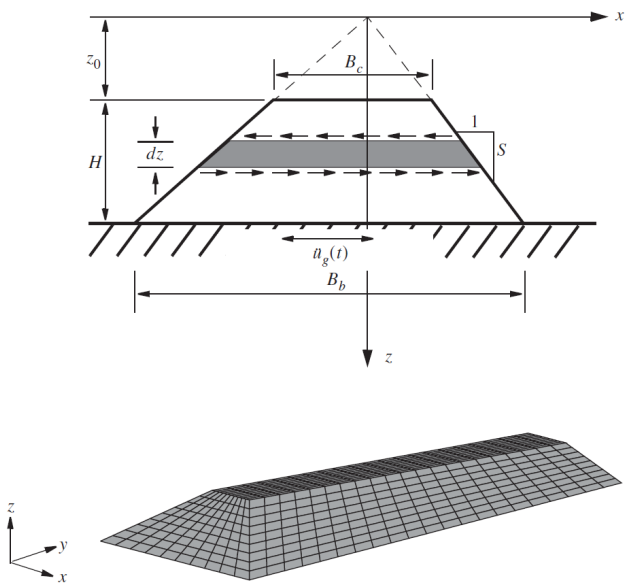

Fig. 1.12. Cross-section of infinitely long embankment and isoparametric view of approach embankment (Zhang and Makris 2002a).

This simplified approach, which uses lumped springs and dashpots, does not consider explicitly the inertial effect of embankment that instead, could be dominant when the ground motion intensity is high. In fact, the mass was considered only implicitly through a frequency-dependent stiffness. Kotsoglou and Pantazopoulou (2006, 2007a and 2007b) developed a two dimensional (2D) analytical model for the embankment and conducted equivalent elastic analyses to evaluate the transverse and longitudinal response of short IABs accounting for soil-structure inertial and kinematic interaction. Starting from the the equi-

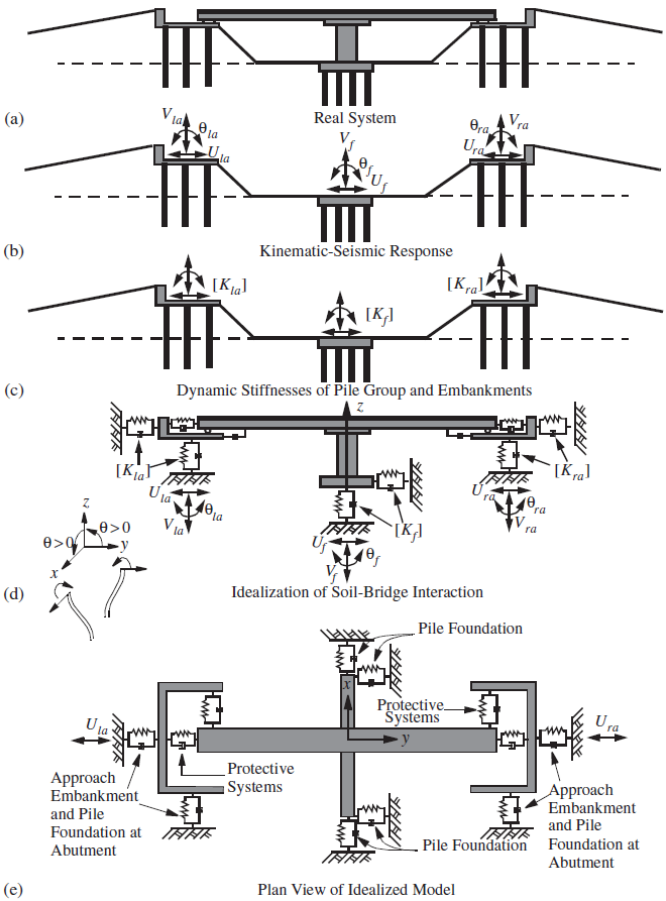

Fig. 1.13. General procedure for seismic soil-foundation superstructure interaction: (a) real system; (b) foundation input motion; (c) dynamic stiffnesses (frequency dependent springs and dashpots); (d) seismic response of the superstructure; (e) plan view of the idealised model (Zhang and Makris 2002b).

librium of forces that act on an infinitesimal rectangular soil element under transverse and longitudinal excitations, the 2D analytical model can be obtained explicitly, by incorporating in the solution of the general partial differential equations of motion, pertinent boundary conditions and constitutive laws. Estimated values of G and ξ are used to characterise the soil material properties, allowing for an equivalent viscoelastic analysis to be performed. Boundary conditions represent instead kinematic and inertial interaction (Fig. 1.14 -a). The kinematic interaction is simulated with inelastic springs, derived from a pushover analysis on the abutment-piles system, that are linearised based on the expected displacement. The inertial contribution is instead simulated establishing equilibrium of an equivalent lumped mass at the embankment edge. Forces acting on the equivalent lumped mass are the deck inertial contribution, the reaction of the linearised-elastic spring representing the abutment-pile system as well as forces owing to the embankment mobilisation. Note also that all these boundary conditions are functions of the value of displacement at the edge of the embankment. Now, performing a frequency analysis, the embankment dynamic response (generalised mass, generalised stiffness and modal damping) is evaluated using the proposed model (Fig. 1.14 -b). From a practical point of view, since only the modal mass of the first mode is significant, it would be realistic to assume that the approach embankment vibrates primarily in the first mode without introducing considerable errors into analysis. So the dynamic response of the embankment can be evaluated by performing a generalised single degree of freedom (SDOF) introducing if needed, a deck damping at the contact point as well. In parallel, dynamic analysis on the entire bridge system is conducted using springs, dashpots and lumped masses at the end-supports derived considering only the first mode (Fig. 1.15). Convergent displacement time histories provided by the two models are evaluated and compared until both time histories converge. Since calculations are performed using a linear equivalent method, a trial and error procedure is needed, as summarised below:

1. Assume a realistic target displacement of the deck. This is used to evaluate the boundary condition of the 2D analytical model for the embankment (stiffness of the pile-abutment system, participating deck mass) and the secant values of G and ξ.

2. Obtain the dynamic characteristics (generalised mass, generalised stiffness, modal damping) through a frequency analysis of the embankment.

3. Evaluate the dynamic response of the simplified embankment model and of the bridge model.

4. Revise the initial assumption and continue this procedure until the evaluated time histories converge for the two models.

With similar considerations the eventual contribution of a central pier can be simulated with an linear-equivalent spring derived from a push-over analysis. The authors also provided the critical embankment length L_c recognising that, at a long distance from the bridge support, the infinitely long embankment performs almost as a shear wedge. This value can be evaluated performing a frequency analysis of the embankment; L_c is so determined as the embankment length beyond which the rate of variation of calculated vibrating frequencies converges to zero. The order of L_c for the MRO and PSO is of 10 to 15 meters. Note that, the shear beam model for both embankments is only an approximation for the longitudinal behaviour, because, when the east embankment performs as a shear beam, shear and compressive stresses are developed in the west embankment, and vice versa. Kotsoglou and Pantazopoulou's model is rational and accurate but the model is not easy to implement in practice due to the iterative procedure of solving a set of differential equations.

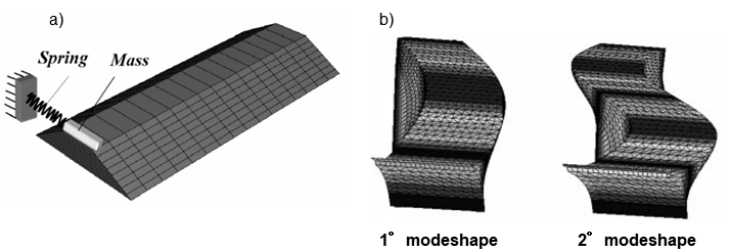

Fig. 1.14. (a) Lumped mass and equivalent spring attached at the edge of the embankment to account for inertial and kinematic soil-structure interaction; (b) dynamic characteristics of approach embankment once boundary conditions are defined (Kotsoglou and Pantazopoulou 2006 , 2007a , 2007b).

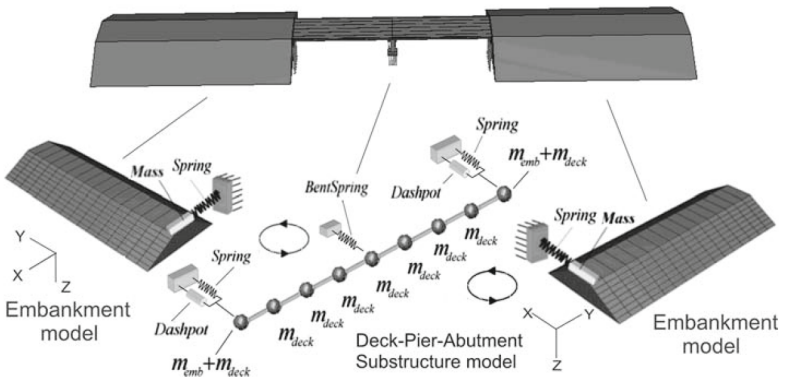

Fig. 1.15. Two semplified models employed: simplified embankment model and bridge model. (Kotsoglou and Pantazopoulou 2006 , 2007a , 2007b).

Rahmani et al. (2014), taking advantage of the on-going advances in constitutive modelling of geotechnical and structural materials, computational tools and parallel computing environment, developed a full soil-bridge model in simulating the seismic response of the MRO in OpenSees framework (McKenna et al. 2010) (Fig. 1.16). Advanced nonlinear models were used for the constitutive modelling of soil and concrete materials. The results are evaluated by comparing the computed motions at different locations of the bridge with two recorded motions, simultaneously simulating the longitudinal and transverse responses. There was generally good agreement between them; the comparison suggests that the full model is a reliable tool for studying the seismic response of large-scale soil-structure interaction problems. The authors also recognized that in this bridge (MRO), due to the relatively flexible transverse configuration, the deflection of the central bridge pier is larger in the transverse direction and especially during strong motions, the transverse peak displacement is approximately twice as large as the longitudinal one. The following research of Rahmani et al. (2016) aimed to evaluate the well-known substructuring method by comparing the response with that obtained from fully-coupled continuum model. In the substructring method the response of the foundation soil and its interaction with pile foundation and the abutment system are represented by a set of one-dimensional springs and dashpots. Three-dimensional substructure model of the bridge is developed in five consecutive steps (Fig. 1.17):

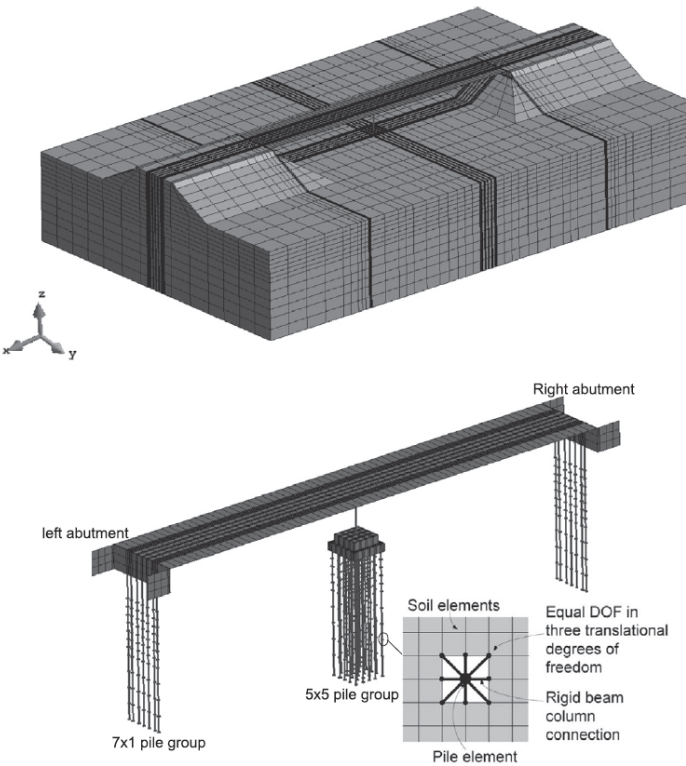

Fig. 1.16. The developed finite-element model for the MRO (Rahmani et al. 2014).

1. one-dimensional site response analysis for both the foundation soil and the embankment soil profiles in order to determine depth-varying time histories of displacement and corresponding maximum displacements.

2. p-y, t-z and Q-z nonlinear backbone curves are determined along the pile foundations following the guidelines of American Petroleum Institute (API 2007); the load-deflection backbone curves for an embedded pile cap are derived following the procedure presented by GEOSPECTRA (1997) while the guidelines of AASHTO (2012) are used to determine the group reduction factors in order to account for the group effects in the pile groups. Load-deflection curves representing the interaction between the embankment and the abutment system are determined following the guidelines of Caltrans (2013). The lateral secant stiffnesses along the piles at

the pile caps, and on top of the abutment are calculated using the previously determined force-deflection backbone curves at the corresponding maximum lateral ground displacements in the free field. Finally, the vertical secant stiffnesses are derived from the t-z and Q-z curves at a displacement equal to the settlement of the pile group under the tributary weight of the deck, the pier and the pile cap.

3. the 6x6 stiffness and damping matrices that represent the flexibility of the pile group and the energy dissipation are computed. Both matrices are composed of 6 diagonal elements representing lateral, vertical, rocking and torsional impedences (neglected in this study) with 4 more off-diagonal elements which represent the coupling effects between the lateral displacements and rocking of the foundation. To calculate the 6x6 stiffness matrix, the secant stiffnesses, obtained in the previous step, are used to create a 3D numerical model. The damping matrix is calculated as $C = (2\beta K)/\omega$ where β is damping ratio, K is the elements of the 6×6 stiffness matrix of the pile group, and ω is the predominant angular frequency of the input motion. The damping ratio (β) is taken to be 25% in both longitudinal and transverse directions following the recent observation of Lee et al. (2011). This damping ratio is meant to approximate two sources of damping in the system: (a) nonlinearity of the bridge and soil material, and (b) infinite boundaries of the soil domain.

4. In the fourth step, a massless finite element model of the 5×5 pile group supported on sets of linear springs (the secant stiffnesses) is created in OpenSees. The depth-varying time histories of displacement in the free-field are then applied to the ground nodes of the springs in the massless pile group. The kinematic motion at abutment is instead obtained in the first step from the site response analysis of the embankment without accounting for the soil-structure interaction effects.

5. In the fifth step, the global model of the bridge is developed. The model consists of the bridge deck and the pier, which are supported by the equivalent linear springs and dashpots at the base of the piers and top of the abutments. The elements and materials used to model the bridge deck and the piers are identical to those

used in the continuum model of MRO. Lumped masses for the pile cap and the abutment system are assigned at the corresponding bridge supports. The kinematic input motions in the form of displacements are applied to the ground nodes of the springs and dashpots located at the two ends of the bridge deck and the pier bases. The input motions to be applied to the two ends of the bridge deck and the pier base were already obtained in the first and fourth steps, respectively. The masses of the foundation soil and the embankment are not included in the model, as there is no information about the volume of soil affected by the response of the bridge structure under a given earthquake shaking.

Comparing the predictions of the full and substructure models in term of drifts and internal forces, the authors observed that the differences are insignificant for low intensity ground motion but, very important for strong ground motions where kinematic and inertial effects are relevant. This study clearly shows that the formulation of the substructuring method fails in representing the nonlinear hysteretic response of soil. This is in line with the findings of Liam Finn (2005). The method uses a constant dynamic stiffness matrix to represent the flexibility of the foundation system. In reality, this stiffness varies at different levels of deformation so that the prevision of seismic performance could be very altered. Thus the authors suggested the use of full soil-structure model considering that nowadays this is no longer a challenging and tedious process.

It is important to note that although Rahmani et al. focused on the limits and the inability of substructuring method to simulate the kinematic and inertial interactions, they did not include the mass of the soil foundation and the embankment due to the difficulties in estimating the volume of participating soil. Actually, especially the mass of the embankment, it should at least have been estimated in some way, as past studies have shown. In a previous study Kwon and Elnashai (2008) highlighted the importance of modelling the mass of the embankment. They modeled the MRO for which the geotechnical components, including the embankments, abutments, and pile groups, were modeled in one platform, and the structural components, including the bridge deck and the pier, were modeled in another platform. Finally, they conducted nonlinear dynamic analyses by applying the outputs from one platform as the inputs to the other one. Other authors have tried to

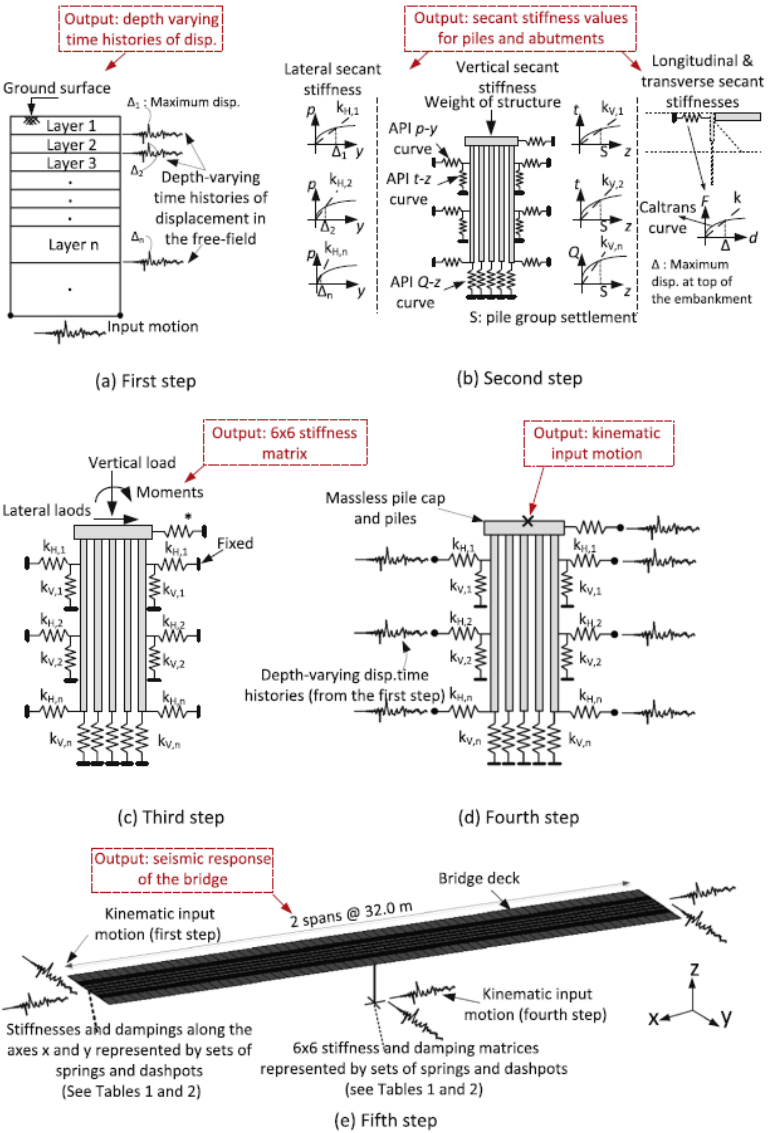

Fig. 1.17. Steps to create the substructure model of MRO; (a) determination of the depth-varying time histories of free-field displacements, (b) effective linearization of the back-bone curves, (c) determination of the 6x6 stiffness matrix (K), (d) determination of the kinematic input motion, and (e) dynamic analysis of the bridge global model (Rahmani et al. 2016).

deal with this problem with different approaches. Franchin and Pinto (2014) conducted 2D inelastic response history analysis employing a combination of one-dimensional site response analysis and inelastic Winkler-like springs as depicted in Fig. 1.18 to capture the main physical aspects of the seismic response of IABs. In order to account for the role of embankment, masses proportional to the critical length L_c were assigned to the 1D soil-column. The biggest advantage of this approach is that the model is developed to be implemented in typical commercial analysis package (SAP2000), allowing it to be generalized immediately for different case studies. Similarly Erhan and Dicleli (2017) investigated the effects of various structural and geotechnical properties such as foundation soil stiffness, pile size, abutment height and so on. Although these models are very practical to use, there has been limited validation of these methods. At the moment, in fact, their results have not been compared either with those obtained by field measurements or with full soil-structure numerical analyses (i.e. where the soil is explicitly modelled).

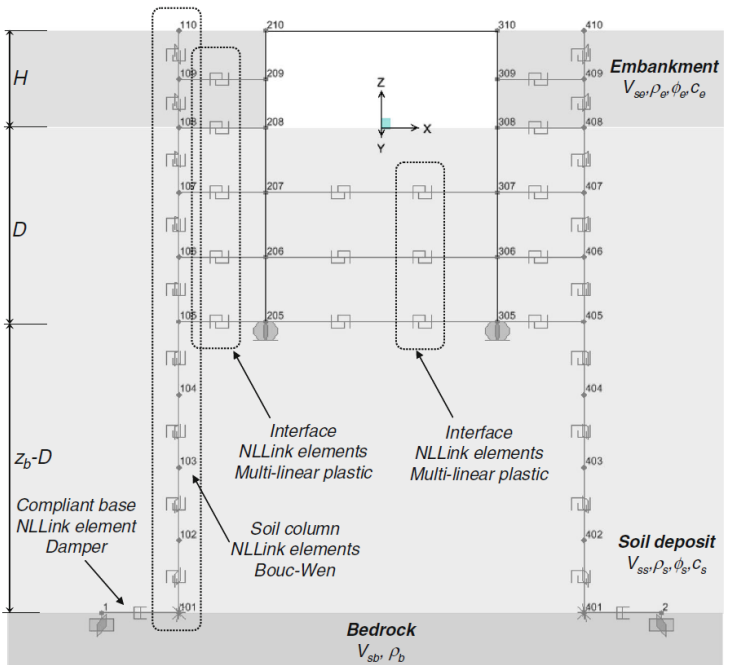

Fig. 1.18. Model components and parameters (Franchin and Pinto 2014).

1.4.1. Last developments on SSI

As stated before, in the seismic design of an integral abutment bridge an important source of uncertainty is the evaluation of the deformability and inertial effects of the bridge abutments, that in turn interact with the approach embankment. However in the current practice, it appears that there is no consensus on methods to account for the effects of soil–structure interaction on the seismic design of a bridge abutment. With the aim to evaluate the inertial effects arising form the dynamic excitation of the embankment, Gorini (2019) and Gorini et al. (2021) following the analytical approach of Kotsoglou and Pantazopoulou, provided solutions for the modal characteristics (period, mass and stiffness) of the soil-abutment system in all the three translation directions: longitudinal, transverse and vertical (Fig. 1.19). Actually this study is not specific to IABs but it is evident that it concerns them indirectly. First of all, the contribution of the embankment can be characterised by its dominant response, i.e. the first vibration modes along the three different direction of motions, and by the corresponding participating masses. These quantities may be found through the analytical expression provided by the authors, whose calibration requires some other considerations. In fact, looking at the comparison between closed-form solutions and the response of numerical simulations, they highlighted the role of the compliance of the foundation soil neglected in previous researches. Even when the behaviour of the soil can be considered reversible and thus a value of small strain shear modulus of the embankment can be used, an effective height of the embankment $H_{eff} > H$ should be employed in the close-form solutions. This effective height H_{eff} reproduces the extension of the significant soil volume interacting with the abutment foundation, whose mass is much larger than the sum of the masses of the abutment structure and of the soil above the base of the footing, roughly about 2.5 times the sum of these two masses for the considered three directions. However, it is evident that this solution strongly depends on the type of foundation and that it should then be adapted to the different abutments that are encountered in integral bridges. The authors explored the effect of the plastic response of the soil as well. Higher intensities of the external forces cause an increment in deformability and a longer dominant response of the abutment. The phenomenon becomes much difficult to study due to the non-linearities that are called into play and it is heavily dependent on the different deformation modes that develop in the soil for the three different direc-

tions. However, the analytical solutions might also provide an adequate representation using secant equivalent stiffness properties. For example the authors suggested to estimate the modulus reduction G/G_0 from a free field site response analysis or to relate it to the intensity of the ground motions as reported in many technical codes.

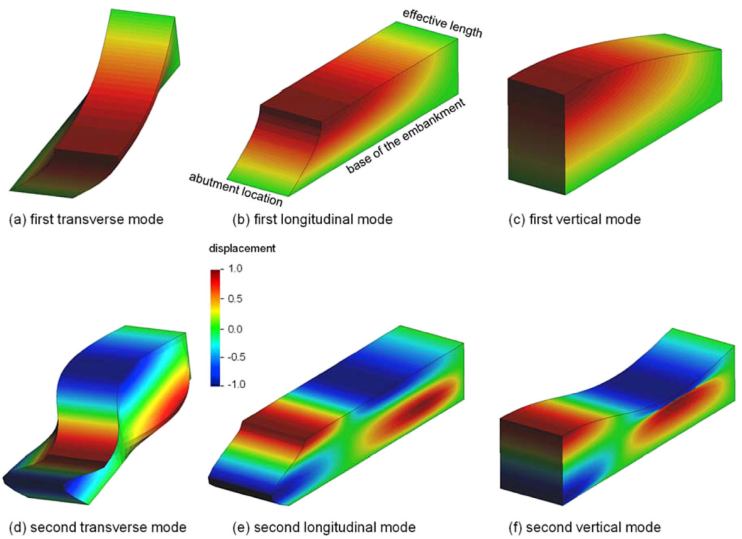

Fig. 1.19. First (a,b,c) and second (d,e,f) modal shapes of the embankment obtained with the analytical solutions (contour fill of the displacement field: blue = -1, green = 0, red = 1 (Gorini et al. 2021).

A way to deal with the soil-structure interaction problem and overcome all limitations is represented by a direct approach, entailing the development of a full three-dimensional model including the entire structure of the bridge and a substantial soil volume. In the last years, taking advantage of the high-performance computing software, the adequacy of full soil-bridge models for evaluating the seismic performance has been demonstrated in several studies (Elgamal et al. 2008, Jeremić et al. 2009, Rahmani et al. 2014, McGann 2013, Ghofrani 2018, Gorini 2019). However, the direct modelling of soil-structure interaction entails high demanding time-domain analyses that are warranted only for infrastructures of major importance. In this context, a more efficient and innovative approach, consisting in the use of macro-elements to simulate soil-structure interaction at the abutment locations, was presented by Gorini (2019) in his doctoral thesis. The macroelement approach

is aimed at reproducing the main features of interaction, that are: the inertial effects associated with a strongly frequency-dependent response and the marked nonlinear behaviour of the system.

The method proposed by Gorini (2019) and Gorini et al. (2020a) consists in the introduction of two complementary macro-elements (Fig. 1.20) in the two structural and geotechnical sub-systems that, through their internal response, define a link between the superstructure and the abutment. The two macroelements of bridge abutment and of bridge structure represent two sides of the same coin: a macro-element of the soil-abutment system for a global analysis of the bridge structure and a macroelement of the bridge structure for the local numerical model of the soil-abutment system.

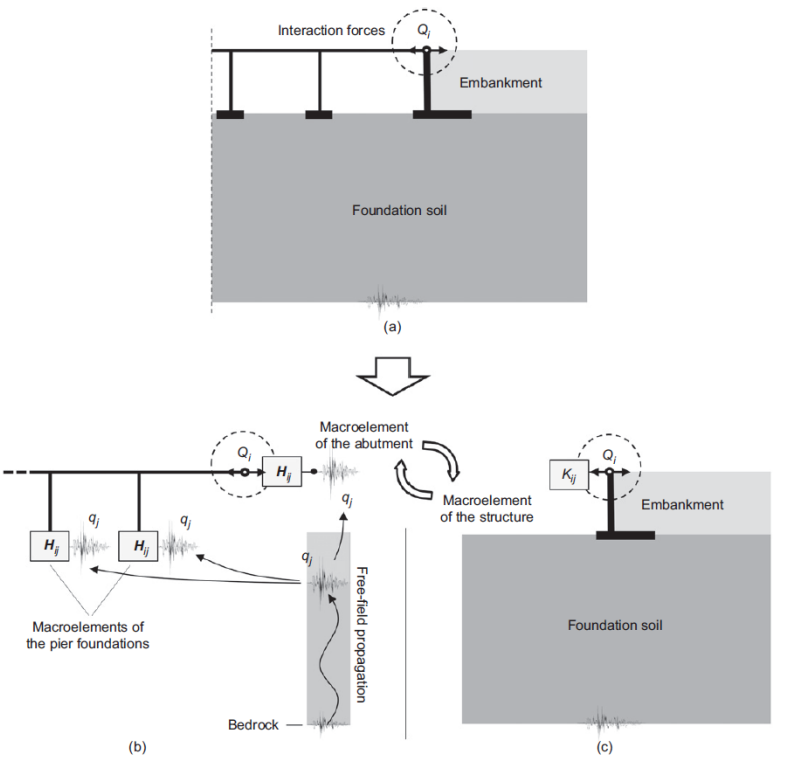

Fig. 1.20. Scheme of the semi-direct method of analysis for soil–abutment interaction: from (a) the full soil–bridge problem to (b), (c) the two sub-domains (bridge superstructure and soil–abutment system) with the complementary macroelements (Gorini et al. 2020a).

The inertial macroelement for bridge abutment has been developed according to a rate-independent multi-surface plasticity model with kinematic hardening derived with a rigorous thermodynamic formulation, using hyperplasticity (Collins and Houlsby 1997). The uniaxial (one dimensional) form of the macro-element can be employed to simulate, in an uncoupled manner, one of the three translational degrees of freedom at the deck–abutment contact (longitudinal, transverse and vertical). This is represented through an assembly of rheological elements depicted in Figure 1.21 (after Iwan 1967) comprising: an elastic spring with stiffness $H^{(0)}$, which represents the response of the soil–abutment system at small strains, and a connection of combined slider–spring rheological systems, which produces the plastic behaviour with kinematic hardening. The stiffness of the n^{th} spring and the strength of the n^{th} slider are denoted by $H^{(n)}$ and $k^{(n)}$, respectively. In order to account for the salient features of soil–abutment interaction, two significant modifications are introduced with respect to the original Iwan model: (a) the slider elements are dissymmetric, to represent the large difference in soil mass response for active and passive loading directions at the abutment; (b) a series of masses $m^{(n)}$ are associated with each plastic flow mechanism in order to simulate the dynamic response of the soil–abutment system. The plastic response of the model is so regarded as a transition phase towards the ultimate capacity. The calibration of this macroelement requires:

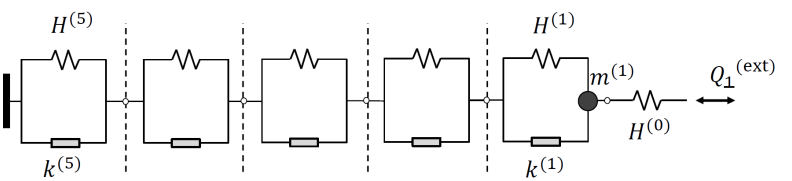

Fig. 1.21. Relation between the levels of the external force $Q_1^{(ext)}$) sliders of the macroelement (Gorini 2019).

1. The initial stiffness $H^{(0)}$, represents the small-strain stiffness of the soil–abutment system along the direction considered: it may be determined through a linear analysis of the soil–abutment interaction model or, more simply, introducing the small-strain stiffness of the soil into an available formulation for the static value of the impedance functions.

2. The ultimate strength $K_{+-}^{(N)}$ (where N is the number of dissipative devices and the term $+-$ refers to the active/passive mechanism) is the ultimate capacity of the soil–abutment system that, in a straightforward manner, may be evaluated using solutions based on perfect plasticity.

All the remaining quantities $H^{(n)}$ and $k^{(n)}$, can be derived from these two basic ingredients assuming that the strength parameters $k^{(n)}$ can vary linearly, and assuming an interpolation law to reproduce the static push-over analysis of the model (for example an hyperbolic formulation). Following these steps, the macroelement is able to reproduce quite satisfactorily the monotonic response of bridge and the static-cyclic response. In order to reproduce also the dynamic behaviour, the calibration of the masses is needed. Gorini et al. (2020a) showed that the mass $m^{(1)}$ associated with the first yield can be regarded as the modal mass of the soil-abutment system needed to the reversible system. This mass can be easily carried out from the closed-form analytical solution discussed before. It can be thought that additional masses are introduced to simulate the increase in soil mass involved in the dynamic response as the interaction and body forces in the embankment approach the ultimate capacity of the soil-abutment system. However, it has be found that a very limited number of masses combined with their other plastic flows can be sufficient to improve the dynamic response of the macroelements at medium and large strain levels. For the reference case study, a sole mass $m^{(2)}$ has been associated with the second yield surface, resulting of the same order of magnitude of the first. Now, following the logic of decoupled approach, the seismic input for the structural model is computed through a free-field site response analysis at a depth L_f of the abutment foundation (Fig. 1.22). Furthermore, in order to focus on the response of the abutment, the effects of soil–foundation interaction were neglected for the strong pier and the seismic motion computed at the foundation level was directly applied to the base of the pier. Fig. 1.22 also indicates the output quantities that were used to quantify concisely the seismic performance of the super-structure: namely, the displacement of the top of the strong abutment u_{abut} with respect to the input displacement u_{inp}; the average axial force in the deck $N_{deck} = u_{rel} * k_{deck}$ (where u_{rel} is the deformation of the deck between the strong abutment and the strong pier and k_{deck} is the axial stiffness of the deck); the shear force T_{pier} at the base of the strong pier; and the corresponding bending

moment M_{pier}. The results are directly compared to those of the full soil-bridge showing that this inertial macroelement is able to to describe the progressive accumulation of the irreversible displacements of the strong abutment, as well as the progressive increment of the permanent internal forces in the superstructure. This is evidently related to the ability of the macroelement to reproduce the irreversible behaviour of the entire soil–abutment system, but also to its ability to describe the dynamic response of the system thanks to an appropriate choice of the masses. Finally, the authors endeavored to address this problem using the classical substructure approach, showing that it is unable to reproduce important consequences of the interaction of the abutment with the foundation and the embankment soil, primarily due to the irreversible behaviour of the soil activated by the inertial forces developing in the soil-abutment system.

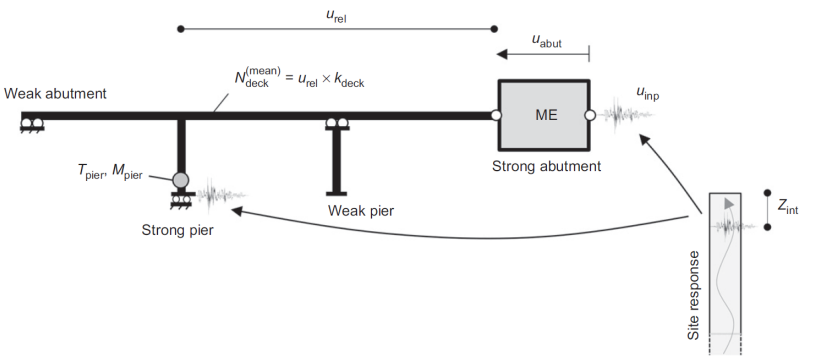

Fig. 1.22. Representation of the output quantities for the structural system: the displacements u_{abut} of the top of the strong abutment, the mean axial force N_{deck} in the deck, the internal shear force T_{pier} at the base of the strong pier in the longitudinal direction and the corresponding bending moment M_{pier} (Gorini et al. 2020a).

The extension of this model to multi-axial conditions (and so to multi-axial macroelement) is the subject of on-going researches. It follows the same approach herein described: the shape of the yield functions in the multi-axial version are taken from ultimate limit state surfaces of bridge abutments (Gorini et al. 2020b) and the inertial effects are reproduced through a number of mass tensors combined with the plastic flows.

The macroelement of bridge structure combined with the local model of the abutment (Fig. 1.20-c), is developed using a phenomenological approach for a prompt implementation in numerical simulations.

The bridge structure is simulated by a second-order transfer tensor K_{ij} to express a frequency dependent relationship between the vector of the generalised displacements u_j of the bases of the abutments and the piers, and the vector of the generalised forces Q_i exchanged at the deck–abutment contact:

$$Q_i = \mathbf{K}_{ij} u_j \tag{1.1}$$

where all the quantities depend on the vibration period T of the input motion u_j. The transfer tensor describes the filtering effect of the bridge structure on the interaction forces exchanged by the abutment and the superstructure, taking expressly into consideration their actual connection. Each term of the tensor is a transfer function: if the dynamic response of the structure is linear, the transfer functions are independent on the amplitude of the external perturbation; conversely, when the behaviour of the bridge structure is non-linear, the transfer functions depend on the amplitude of the structural response. For a bridge structure with a linear behaviour, the calibration of one of the transfer functions is obtained as follows: a numerical model of the structure, including the structural members and the abutments, is perturbed by a frequency sweep applied at the base of the piers and at the abutment foundations; for each vibration frequency, the maximum value of the interaction forces produced at the deck–abutment contact is determined; the transfer function is then evaluated at each frequency as the ratio of the interaction force to the amplitude of the input motion.

The deck-abutment contact studied by Gorini and Callisto (2019) is not referred to an IAB and there is no transmission of moments. Thus, the behaviour of the bridge structure can be described by a two-dimensional macroelements as follows:

$$\begin{bmatrix} Q_1 \\ Q_3 \end{bmatrix} = \begin{bmatrix} \mathbf{K_{11}} & \mathbf{K_{13}} \\ \mathbf{K_{31}} & \mathbf{K_{33}} \end{bmatrix} \cdot \begin{bmatrix} u_1 \\ u_3 \end{bmatrix} = \begin{bmatrix} \mathbf{K_{11}} & \mathbf{0} \\ \mathbf{0} & \mathbf{K_{33}} \end{bmatrix} \cdot \begin{bmatrix} u_1 \\ u_3 \end{bmatrix} \tag{1.2}$$

where the suffixes 1 and 3 denote the longitudinal and the vertical directions, respectively. The coupling terms $\mathbf{K_{13}}$ and $\mathbf{K_{31}}$ were set equal to zero, neglecting for simplicity the directional coupling of the structural response, but in principle there are no difficulties in the calibration of these terms, retrieving the force Q_3 induced by the displacement field u_1 applied at the foundation level to evaluate $\mathbf{K_{31}}$, and vice versa for $\mathbf{K_{13}}$. Generally, the transfer functions present a multi-modal distribution

in the frequency domain that can be easily reproduced in numerical modelling through some masses connected by simple rheological systems (1.20-c). This modelling technique is conceptually identical to the procedure used to include the inertial effects in the macro-element of the soil-abutment system: in that case the masses were calibrated to reproduce the dominant responses of the soil-abutment system representing the fundamental vibration modes. The global structure analysis shows that, in the Gorini's case study, the longitudinal transfer function $\mathbf{K_1}$ can be approximated by a mono-modal curve while the vertical transfer function $\mathbf{K_3}$ can be modelled with a two degrees of freedom system. The mass, stiffness and damping of both the SDOF representing the longitudinal transfer function $\mathbf{K_1}$ and the 2DOFs representing the vertical transfer function $\mathbf{K_3}$ can be calibrated inserting in the soil-abutment interaction model (Fig. 1.23) a SDOF for the longitudinal behaviour and a 2DOFs for the vertical behaviour following a trial and error procedure. Note that in this case, the structural constitutive model is considered elastic. Following the same procedure, effects of structural non-linearity can be taken into consideration combining for example the elastic transfer function with a perfect plastic element (fuse) calibrated to reproduce the ultimate capacity in the structural system. This solution can be particularly representative of cases in which the structural non linearity derives form deck isolating devices. This model allows for the study of the influence of the dynamic behaviour of the bridge structure on the seismic performance of the abutments and its results are in very good agreement with those of the full soil-bridge model.

The goal to reproduce with a compact model the dynamic response of a large bridge structure is quite ambitious; in fact macroelements are macro-scale constitutive relationships between the forces exchanged at the deck-abutment contact and the corresponding displacements, with no direct information about the mechanical behaviour at lower scales. Therefore, on the basis of the macroelement response the estimate of the internal forces and strains in the structural members requires a supplementary interpretative model of the local behaviour of the soil-abutment system. Nevertheless, as design is often based on the maximum internal forces in the structure and on the maximum and residual displacements of the foundation elements, the proposed approach can be deemed appropriate for the seismic design of bridge abutments.

The applicability of the Gorini's model for short bridges and for integral structural schemes needs further validation, but without any

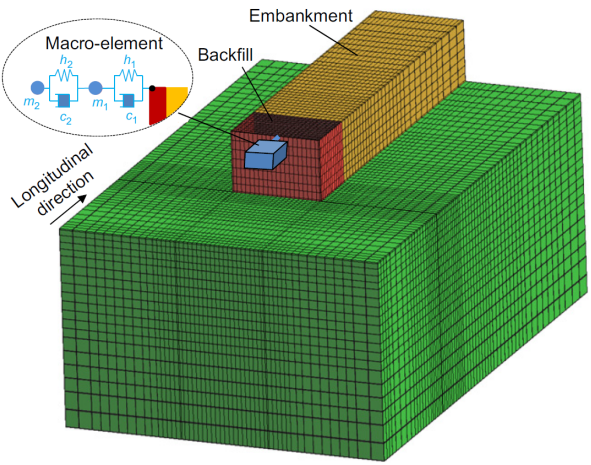

Fig. 1.23. Local soil–abutment model with indication of the longitudinal macro-element (Gorini and Callisto 2019).

doubts, it is evident that constitutes a significant step forward for the study of large-scale systems. In light of these results, bridge abutments seem to be less rigid than expected. The amplified behaviour of the abutment associated with its dominant response and its interaction with the superstructure indicates a marked effect of the plastic behaviour of soil on the overall response. The integrated macroelement approach appears as an efficient means for testing new solutions for bridge abutments, allowing for a clear definition and interpretation of the numerical models. In spite of the important reduction of the computational demand offered by macroelement approach, the calibration procedure is not so feasible and requires a thorough understanding of the problem under consideration. In fact, this approach provides a useful analysis tool for the design of infrastructure of major importance, for which the costs associated with a design based on-time domain is justifiable. Hence, for a more standard design of bridges with integral abutments, cost-effective simplified procedures must be developed.

2. The analysis framework OpenSees

One of the most interesting aspect around which the whole thesis is based is the application of principles of modelling to structural and geotechnical engineering. Nowadays, taking advantage of the continuous progress in computational tools, parallel computing environments, constitutive modelling of geotechnical and structural materials, the creation of a large-scale full three-dimensional soil-structure model is a very demanding challenge but no longer utopian.

Engineering is fundamentally concerned around modelling. Engineering is concerned with finding solutions to real problems, we cannot simply look around until we find problems that we think we can solve. We need to be able to see through to the essence of the problem and identify the key features which need to be modelled, which is to say those features of which we need to take into account and include in the design. One aspect of engineering judgement is the identification of those features which believe it safe to ignore. (Muir Wood 2004)

Precisely, with regard to the advanced numerical modelling potential that we have today, the principal skill is to find the best and appropriate level of simplification to recognise those features which are important and those which are unimportant. Along this line of thinking, this work tries to show the potential advantages offered by an open source software framework like OpenSees (McKenna 1997).

2.1. Introduction to OpenSees

The system modelling and response computation were performed by using the open source finite element analysis framework OpenSees (McKenna 1997, McKenna et al. 2010) (Open System for Earthquake

Engineering Simulation); the mesh of the models was generated with automatisated scripts in MATLAB (v 2020b) and visualised through the pre/postprocessor software GID (Ribò et al 2008). OpenSees is a software framework for developing sequential, parallel and grid-enabled finite element applications in the field of civil engineering and it offers high potentialities to reach an accurate modelling of the behaviour of both soil and structure. The continuous development of OpenSees is due to the participation to this project of a wide international scientific community that works to develop the code according to new challenges in computational engineering. One of the main advantages consists precisely in the possibility to continuously integrate the existing library with the new features needed to solve the specific problem under examination. Though it was created for structural analysis, several constitutive models and finite elements have been added during the last decade to carry out dynamic simulations of geotechnical systems. Nowadays, OpenSees represents a powerful numerical tool to investigate the dynamic behaviour of soil-structure systems, considering a variety of natural hazards. Several methods of analysis can be used to solve the governing equations according to the specific problem examined.

OpenSees is an object-oriented framework for finite element (FE) analysis. The Tcl scripting language has been chosen to support the OpenSees commands, which are used to define the problem and its solution. Each of these commands is associated with a C++ procedure that is provided by a source code included in the OpenSees library. The common structure of an input script in OpenSees can be represented by the flow chart in Fig. 2.1. As mentioned above, the scripts of very large models, such as those involved in the present research, require the use of a pre/post processor software to generate the mesh. The nodal and element information is then imported in the main Tcl script. After defining the boundary conditions, the appropriate typologies of finite elements for the problem at hand are assigned to the mesh and the relative output is set up. As a conclusive step, a model of analysis is assembled by setting the most appropriate features needed to optimise the computation.

Parallel computing can be obtained through the OpenSeesSP (Single Parallel Interpreter application) and OpenSeesMP (Multi Parallel Interpreter application) applications (McKenna and Fenves 2007) that can be built from the OpenSees source code distribution. This was an

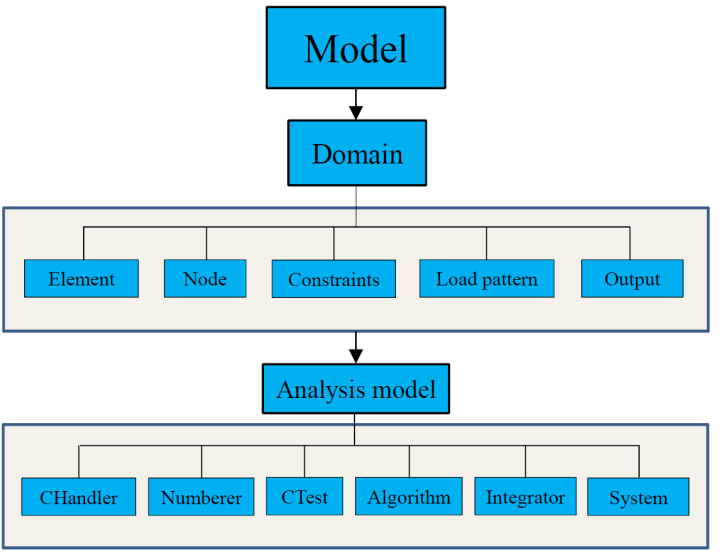

Fig. 2.1. Flowchart illustrating the common structure of an OpenSees input file.

essential feature to optimise the computation time for the non-linear time domain analyses of this research.

The OpenSeesSP interpreter is conceived for analyses of very large models with input files that take too long to run on a sequential machine (single processor). The interpreter will process the same script that the OpenSees interpreter runs on a sequential machine, except for some additional options regarding the choice of the solver. In a parallel machine, the single processor P_0, called master processor, is running the main interpreter and processing commands from the main input script. The other processors are running ActorSubdomain objects (McKenna 1997). On the first issuance of the analyze() command in the script the model is partitioned and the domain (elements, nodes, constraints, etc.) is split and distributed by the master processor to the other processors. After this, the state and solving of the system of equations is done in parallel, depending on the choice of the equation solver. To run a job on a parallel computer with this interpreter, the input script needs to be slightly modified, respect to the basic OpenSees, to make it consistent with the parallel process logic. This interpreter is particularly suitable for wide parametric studies, composed of numerous analyses running together, because able to partition the number of analyses to be run and

the number of processors to be assigned to each analysis. Hence the OpenSeesSP interpreter solves a system of equations following a highly hierarchical structure: the master processor executes the commands of the main input script and automatically partitions the solving process among the other processors, then reassembles the whole solution.

The Multi Parallel Interpreter (OpenSeesMP), instead, allows to prescribe a specific partition of the processors and to run simultaneously many simulations among different machines. The latter interpreter results to be more efficient than OpenSeesSP but requires a more substantial modification of the main input script and more knowledge of parallel computing.

2.2. OpenSees on DesignSafe

A great impetus in recent years for the execution of finite element simulations of very large-scale models is offered by the development of supercomputers. In this work we have relied on the DesignSafe cyberinfrastructure (Rathje et al. 2017, https://www.designsafe-ci.org) hosted by the Texas Advanced Computing Center (https://www.tacc.utexas.edu, TACC) at The University of Texas at Austin (http://www.utexas.edu/) that allows the execution of OpenSees, OpenSeesSP, OpenSeesMP as well as other programs.

DesignSafe is a comprehensive cloud-based natural hazards research environment for experimental, theoretical, and computational engineering and science, providing a place to steward data from its creation through publication and archive, and also the workspace in which to understand, analyse, collaborate and publish that data.

In the present research, time domain nonlinear dynamic analyses were carried out implementing large soil-structure interaction models; thus, the use of parallel computing was needed and obtained through the OpenSeesSP interpreter. The advantages of performing parallel computing on a supercomputer will be shown in the continuation of the thesis work and were fundamental for its development.

2.2.1. Stampede2

Stampede2, generously funded by the National Science Foundation (NSF) through award ACI-1134872, is one of the Texas Advanced Computing Center (TACC), University of Texas at Austin's flagship supercomputers and, precisely the one adopted for this work. Stampede2's

4,200 Knights Landing (KNL) nodes (Fig. 2.2) represent a radical break with the past of supercomputers. A Stampede2 KNL is not a coprocessor: each 68-core KNL is a stand-alone, self-booting processor that is the sole processor in its node.

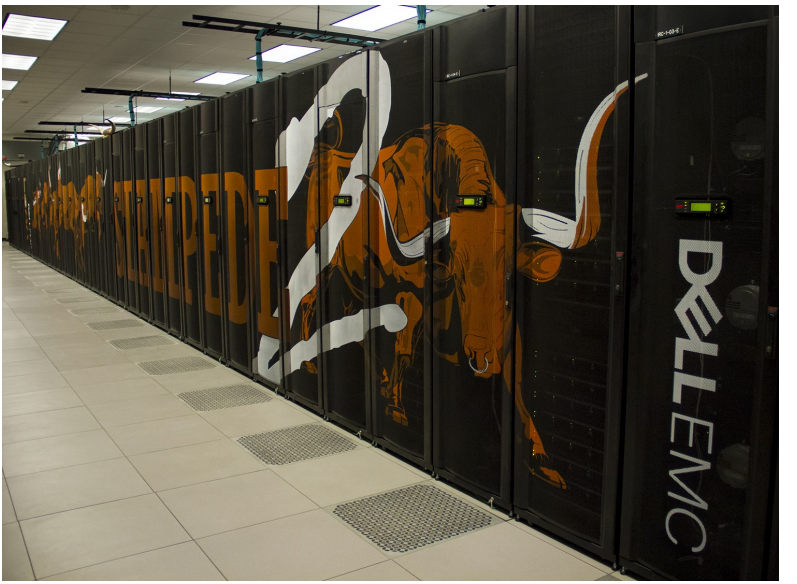

Fig. 2.2. Stampede2 System (source https://tacc.utexas.edu/systems/stampede2/).

Each of Stampede2's KNL nodes includes 96GB of traditional DDR4 Random Access Memory (RAM). They also feature an additional 16GB of high bandwidth, on-package memory known as Multi-Channel Dynamic Random Access Memory (MCDRAM) that is up to four times faster than DDR4. The KNL's memory is configurable in two important ways: there are BIOS settings that determine at boot time the processor's memory mode and cluster mode. The processor's memory mode determines whether the fast MCDRAM operates as RAM, as direct-mapped L3 cache, or as a mixture of the two. The cluster mode determines the mechanisms for achieving cache coherency, which in turn determines latency: roughly speaking, this mode specifies the degree to which some memory addresses are "closer" to some cores than to others. The main specifications of Stampede2 KNL Compute Node are summarised in Table 2.1.

Tab. 2.1. Stampede2 KNL Compute Node Specifications.

Model:	Intel Xeon Phi 7250 ("Knights Landing")
Total cores per KNL node:	68 cores on a single socket
Hardware threads per core:	4
Hardware threads per node:	68 x 4 = 272
Clock rate:	1.4 GHz
RAM:	96GB DDR4 plus 16GB high-speed MCDRAM (and it is configurable in two ways)
Cache:	32KB L1 data cache per core; 1MB L2 per two-core tile. In default config, MCDRAM operates as 16GB direct-mapped L3
Local storage:	All KNL nodes have a 107GB /tmp partition on a 200GB Solid State Drive (SSD)

3. The case study of a single-span integral abutment bridge

The case study examined in this section is inspired by an integral overpass built in Italy recently (Fig.3.1-a), along the A14 Adriatic highway in the Emilia Romagna region. The structure is composed by a single span bridge and is supported by end abutments which act as retaining walls for the approach embankments. As shown in Fig. 3.1-b/c, the abutment is of an integral type without deck joints and bearings.

The total bridge length is about 50.0 m in order to overpass the underlying highway carriageway formed by 4+4 traffic lanes and an additional deceleration lane. Its cross-section consists of a steel-concrete composite structure formed by four welded I-shaped plate girders, 1.9 m high (Fig.3.1-b), transversally connected by secondary steel beams, 1.0 m high, and by the concrete slab, 0.32 m thick and 13.2 m wide. The properties of the deck are summarised in Table 3.1, distinguishing the initial steel section used during the initial construction phases from the final steel-concrete cross section. Specifically, E is the Young's modulus, I is the second moment of inertia, A is the section area, and m is the total mass including all the permanent elements.

Tab. 3.1. Deck properties.

cross section	EA (kN)	EI (kN m^2)	m (Mg)
steel only	6.2e07	$1.0 \cdot 10^8$	225.3
composite	2.5e08	$1.4 \cdot 10^8$	956.4

The abutments are formed by reinforced concrete walls, 8.0 m high and 2.2 m width, supported by seven reinforced concrete piles with

length of 20.0 m and diameters of 1.2 m. As already seen in section 1.3.2, the choice of a single row of piles is quite common for this type of bridge and is conceived to mitigate the internal stresses produced by thermal variations.

Fig. 3.1. Integral abutment bridge which inspires the case study: (a) general view of the bridge, (b) detail of the integral connection at abutment-deck node, (c) detail of four welded I-shaped plate girders.

The idealised soil domain is inspired by a real case study and it is constituted by two different gravelly-sand soil layers. Fig. 3.2 shows the profile of the small-strain shear modulus and the correspondent approximation used for the modelling. The bedrock is located at a depth of 50 m with a shear wave velocity V_s of about 700 m/s. Additional properties of the deposit are reported in Table 3.2, namely the mass density ρ, the earth pressure coefficient at rest K_0, and the angle of shearing resistance φ'.

In absence of laboratory tests available for the real site, an advanced constitutive model is presented and calibrated in order to obtain the typical response of gravelly-sand soils.

Tab. 3.2. Soil properties.

layer	ρ	K_0	φ'
–	Mg/m^3	–	°
1	2.04	0.46	33
2	2.04	0.43	35

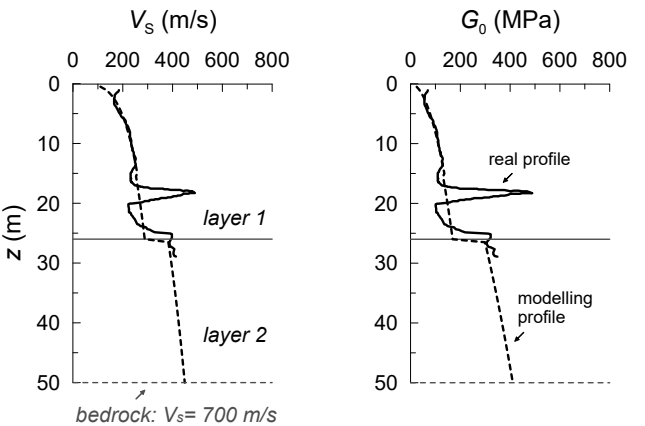

Fig. 3.2. Soil velocity profile and corresponding small-strain shear modulus.

3.1. Soil constitutive model

The mechanical behaviour of the soil is described through an advanced constitutive model: the Pressure Dependent Multi-Yield model (PDMY) developed by Yang et al. (2003). The choice of this model is aimed to get a realistic response of the soil under cyclic loading conditions. The model is available in the OpenSees library and can be combined with three-dimensional finite elements with fully coupled hydro-mechanical behaviour.

3.1.1. The PDMY model

The PDMY model is mainly conceived to reproduce the cyclic response of coarse-grained soils. It is formulated within the framework of Multi-Surface Plasticity (Iwan 1967, Mróz 1967, Prévost 1985): the model is composed of a series of conical yield surfaces with circular directrix (Prévost 1985, Lacy 1986), depicted in Fig. 3.3, that evolve in the three-dimensional principal stress space with kinematic hardening. The expression of the generic yield surface reads:

$$f = [\mathbf{s} - (p' + p'_0) \cdot \boldsymbol{\alpha}] : [\mathbf{s} - (p' + p'_0) \cdot \boldsymbol{\alpha}] - m^2 \cdot (p' + p'_0)^2 = 0 \quad (3.1)$$

where the symbol **:** denotes a doubly contracted tensor product. The quantity $\mathbf{s}$ is the deviatoric stress tensor whereas $\boldsymbol{\alpha}$ is a second-order deviatoric stress tensor that defines the center of the yield surface in the deviatoric stress subspace (back stress ratio); m defines the size of the yield surface and p'_0 represents the distance of the apex of the yield surface from the origin along the hydrostatic axis p'. A tensile cut-off is provided in order to confine the admissible states of the material for $p' \geq 0$. Although sandy and gravelly materials do not have an effective cohesion, a small value of p'_0 can be particularly useful for the stability of numerical computations and because it avoids the ambiguity in defining the normal to the yield surface at its apex. The yield surfaces have a common apex along the p' axis and the innermost surface represents the boundary of the elastic region while the outermost yield surface is designated as the ultimate surface, locus of points of attainment of the ultimate conditions of the material. Note that the PDMY model does not account for the dependence of the deviatoric plastic flow on the Lode angle since Eq. 3.1 does not include the third stress invariant. This limitation of the model can be partially overcome considering a nonzero back stress ratio $\boldsymbol{\alpha}$ of the yield surfaces in Eq.3.1 in such a way as to provide different strengths in compression and extension.

A typical response in the shear stress-strain space is shown in Fig. 3.3. The piecewise-linear curve of the model is aimed to reproduce the nonlinear shear behaviour of soil (Kramer 1996). More in detail, the hyperbolic backbone curve proposed by Duncan and Chang (1970) is taken as reference and, for a given reference confinement p'_r, it reads:

$$\tau = G_r \cdot \frac{\gamma}{1 + \gamma/\gamma_r} \quad (3.2)$$

where τ and γ are the octahedral shear stress and strain, respectively, and γ_r is the shear strain associated with a purely elastic behaviour, defined as τ_{max}/G_0. The analytical curve is reproduced through a progressive decay of the plastic modulus H_n: starting from the shear modulus at small strains G_r related to the elastic response, the plastic modulus reduces towards the ultimate surface according to the evolution of the stress ratio between the surfaces. Each linear segment of the backbone curve (continuous line in Fig. 3.3) constitutes the domain of a yield

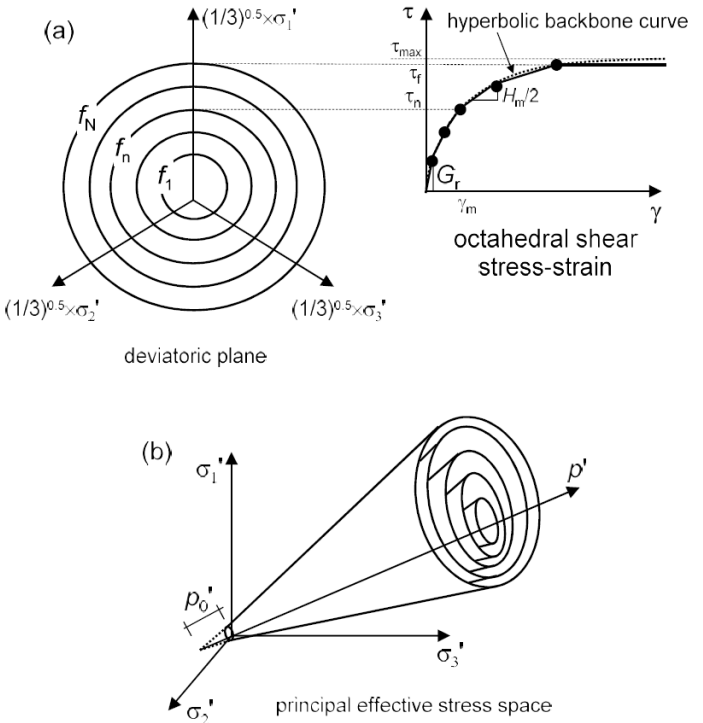

Fig. 3.3. (a) Piecewise-linear approximation of the hyperbolic backbone curve used to describe the nonlinear shear stress-strain response and, (b) representation of the conical yield surfaces in the principal stress space. (Yang et al. 2003)

surface f_n, characterised by a size M_n and by an elastic-plastic shear modulus H_n, for n from 1 to the number N of the surfaces. The size of the surfaces increases progressively according to the following expression for the n-th back stress M_n:

$$M_n = \frac{3 \cdot \tau_n}{\sqrt{2} \cdot (p'_r + p'_0)} \tag{3.3}$$

up to the ultimate surface in correspondence of which it reads $M_N = 6 \cdot \sin\varphi' / (3 - \sin\varphi')$, consistent with Critical State conditions. The CSL is described by the Li and Wang (1998) according to the Eq. 3.4 while the plastic modulus associated with the n-th surface varies according to Eq. 3.5:

$$e_c = \xi_1 - \xi_2 \cdot (\frac{p'_c}{p_{atm}})^{\xi_3} \tag{3.4}$$

$$H_n = 2 \cdot (\tau_{n+1} - \tau_n)/(\gamma_{n+1} - \gamma_n) \tag{3.5}$$

and it is bounded by the initial value $H_1 = G_0$ and the final value $H_N = 0$. Finally, the small strain shear modulus G_r, as well as all the tangent moduli H_m, is assumed to vary with the level of confinement as proposed by Prévost (1985):

$$G_0(p') = G_r \cdot \left[\frac{p' + p'_0}{p'_r + p'_0}\right]^d \tag{3.6}$$

with the exponent d taken equal to 0.5. Finally, the bulk modulus K_n of the soil skeleton is computed as $K_n = G_n \cdot [2 \cdot (1 + \nu)]/[3 \cdot (1 - 2 \cdot \nu)]$. The accuracy in reproducing the hyperbolic backbone curve increases with the number of yield surfaces employed in the computation. In the numerical analyses carried out in this study, 40 surfaces were used reaching a high level of approximation of the nonlinear behaviour.

As an important feature under dynamic conditions, a purely deviatoric kinematic hardening rule is employed, in which the yield surface translation rule proposed by Parra (1996) is developed to enhance computational efficiency. This is actually the primary aim of the model: describing with a sufficient level of accuracy the salient aspects of the soil behaviour under cyclic conditions supported by a highly stable formulation in numerical computing. Non-associativity of the plastic flow is restricted to its volumetric component.

The state of the material is simply defined by the stress ratio η in the principal stress space:

$$\eta = \frac{\sqrt{3 \cdot (\mathbf{s} : \mathbf{s})/2}}{p' + p'_0} \tag{3.7}$$

and the contractive and dilative tendency of soil depends on the position of the stress state with respect to the Phase Transformation Line (Ishihara et al. 1975), the latter characterised by a stress ratio η_{PTL} : when the stress state is inside the PTL ($\eta < \eta_{PTL}$) the material exhibits a contractive behaviour and vice versa. For coarse-grained soils, it is well known that a complete description of the material state requires the combined information on the stress and the strain levels in the $e - p'$ space, concisely expressed by the state parameter ψ (Been and Jefferies 1985). In the PDMY model, instead, only the information on the stress level η is considered to define the tendency of the behaviour, leading to

a less accurate evaluation on the development of strains. Therefore, the ratio η_{PTL} of the PTL constitutes the internal variable of the model to describe the dilation tendency.

Let $\mathbf{P}$ be the outer normal to the potential surface, respectively. This tensor can be conveniently decomposed into its volumetric $P'' \cdot \mathbf{I}$ and deviatoric $\mathbf{P}'$ part, where $\mathbf{I}$ a second-order identity matrix, such that $\mathbf{P} = P'' \cdot \mathbf{I} + \mathbf{P}'$. Different expressions for the scalar quantity P'' are used to differentiate the behaviour during contraction, dilation and neutral phase when the stress state reaches the PTL.

Shear-induced contraction occurs inside the PTL when $\eta < \eta_{PTL}$, as well as when $\eta > \eta_{PTL}$ and $\dot{\eta} < 0$. Experimental observations and micro-mechanical investigations demonstrated that the rate of contraction is significantly influenced by preceding dilation phases (Ishihara et al. 1975, Ladd et al. 1977, Nemat-Nasser and Tobita 1982 , Papadimitriou et al. 2001). In order to reproduce this effect, the parameter P'' is considered to be a function of the plastic volumetric strain ϵ_v^p accumulated during dilation (Papadimitriou et al. 2001):

$$P'' = \left[1 - \frac{\text{sgn}(\dot{\eta}) \cdot \eta}{\eta_{PTL}}\right] \cdot (c_1 + c_2 \cdot \epsilon_c) \tag{3.8}$$

where c_1 and c_2 are positive calibration constants defining the rate of contraction (or excess pore pressure increase) or, under undrained conditions, the increment of positive excess pore water pressures. The non-negative scalar quantity ϵ_c is defined following rate equation:

$$\dot{\epsilon}_c = \begin{cases} -\dot{\epsilon}_v^p, & \epsilon_c > 0 \text{ or } -\epsilon_v^p > 0 \\ 0, & \text{otherwise} \end{cases} \tag{3.9}$$

where $(\dot{\epsilon}_v^p)$ is the rate of the plastic volumetric strain. In other words, ϵ_c increases only during dilation and decreases during subsequent unloading (contraction), until it reaches zero. If no prior dilation has taken place, ϵ_c remains zero. Conversely, dilatant behaviour occurs when $\eta > \eta_{PTL}$ and $\dot{\eta} > 0$ and it is defined by:

$$P'' = \left[1 - \frac{\eta}{\eta_{PTL}}\right] \cdot d_1 \cdot \gamma_d^{d_2} \tag{3.10}$$

with d_1 and d_2 positive calibration constants and γ_d the octahedral shear strain accumulated during the current dilation phase. Finally, neutral phase occurs in correspondence of the PTL, hence when the behaviour

changes from contractant to dilative. In this condition P'' is kept equal to zero ($\dot{\epsilon_v^p}$) until the closest yield surface is reached.

The input parameters of the model are reported in Table 3.3. The parameter d defines the exponent in Eq. 3.6 and therefore the dependence of the tangent moduli H_n on the effective confinement. The peak shear strain $\gamma_{d,max}$ is the octahedral shear strain at which the maximum shear strength is reached, needed to describe completely the hyperbolic backbone curve. Finally, the stress ratio of the PTL is computed as $\eta_{PTL} = 6 \cdot sin\varphi_{PTL}/sin\varphi_{PTL}$.

Tab. 3.3. Input parameters of the PDMY model.

Constant	Variable
Elasticity	G_0 ν
Reference mean pressure	p'_r
Pressure depend coefficient	d
Peak shear strain	$\gamma_{d,max}$
shear strength	φ'
Phase Transformation Line	φ'_{PTL}
Contraction	c_1 c_2
Dilatancy	d_1 d_2
initial void ratio	e_0
Critical State	ξ_1 ξ_2 ξ_3
Number of yield surface	N

In conclusion, the PDMY model presents a robust mathematical formulation in which some peculiar aspects of the soil behaviour, such as dilation and critical state, are encapsulated into the formulation of the phenomenon through some empirical expedients. By contrast, in virtue of its simpler formulation, the PDMY model is more manageable and stable in numerical simulations, especially for big models with hundred of thousands of degree of freedoms under dynamic conditions. Last but not least, was successfully used in previous studies to simulate

soil-structure interaction problems (Elgamal et al. 2008 , Rahmani et al. 2014, McGann et al. 2017, Gorini 2019). Therefore, the PDMY model constitutes the reference material for the demanding dynamic analyses of the full soil-bridge system.

3.1.2. Calibration procedure

The parameters of the PDMY model were calibrated in order to reproduce a realistic behaviour of soil under static and dynamic conditions. As laboratory tests are not available for the real site, not all the parameters requested by the PDMY can be directly calibrated. In this context, the remaining parameters were chosen with extreme care in order to get the typical response of gravelly-sand soils.

Although the soil domain of the idealised case study is dry, the reference calibration was made for a more general case in presence of pore water pressures. In this way, on the one hand, the potential of PDMY is explored and on the other hand, a greater representativeness of the parameters is obtained. Solid eight-node brick elements with physically stabilized single-point integration (*SSPbrickUP*) were used for the element soil. Each node of these elements has three translational degrees of freedom (DoF) and one pore water pressure DoF. In addition, just one integration point at the element center is needed. According to McGann et al. (2015), SSPbrickUP elements produce results comparable with their higher-order counterparts with greater computational efficiency.

Fig. 3.4 depicts triaxial and shear tests implemented in OpenSees to reproduce the monotonic and cyclic conditions after an initial phase of isotropic consolidation. More in detail, it was found that a calibration based only on monotonic laboratory tests leads to a considerable overestimation of the excess pore water pressure under cyclic conditions and as a result, an inaccurate prediction of the mechanical response in undrained conditions. To overcome this issue, the calibration was aimed to obtain a good response for the cyclic conditions maintaining a reasonable static response in the range of strains of interest for the problem under examination. Hence, the procedure used to identify the optimum values of constitutive parameters is presented and discussed.

In the following of the discussion the influence of the parameters used for layer 1 and reported in Table 3.4 will be shown. Note that since the Drucker-Prager surface has a circular section in the octahedral plane, its aperture was calibrated under plane strain conditions to reproduce

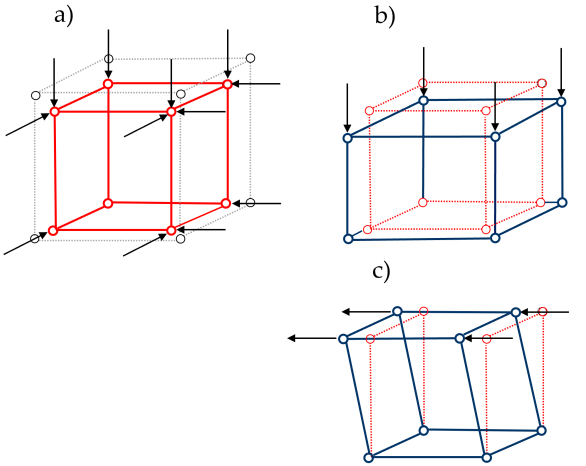

Fig. 3.4. Single element testing; (a) isotropic consolidation; (b) triaxial compression test; (c) direct shear test.

the Mohr-Coulomb criterion as depicted in Fig. 3.5. In other words, the equivalent value of the angle of shearing resistance was found so that the the two resistance criteria (Drucker-Prager and Mohr-Coulomb) coincide for a value of the lode angle equal to 0 ° (plane strain conditions). Thus, Table 3.4 reports the triaxial-compression value of the angle of shearing resistance φ' and its plane-strain equivalent value φ'_{eq}. The value of G_r, referring to a confinement stress p'_r=105 kPa, and the pressure dependence coefficient d were determined in order to match the variation of the small strain shear modulus G_0 with depth according to the Eq. 3.6. The Poisson's ratio ν is derived from the expression $\nu = K_0/(1 + K_0)$. The code available in OpenSees library neglects the dependency of the rate concentration from the previous dilative phase, thus c_2 =0. The choice of the remaining parameters is discussed below.

Fig. 3.6 reports a series of monotonic triaxial tests accounting for different configurations. Fig. 3.6-a shows the influence of drainage conditions, in particular note that for undrained conditions the resistance is reached only asymptotically. This is the reason why the model requires to define a peak shear strain $\gamma_{d,max}$ at which the maximum shear strength is reached. Fig. 3.6-b shows the influence of the phase transformation angle φ'_{PTL} and of the contraction parameter c_1. As mentioned before, φ'_{PTL} was chosen and adjusted with dilation parameters to produce desired dilation tendency while c_1 controls the contraction rate and

Tab. 3.4. Reference parameter for layer 1 (15-26 m).

Constant	Variable	Value
Elasticity	G_0	95000
	ν	0.315
Reference mean pressure	p'_r	105.0
Pressure depend coefficient	d	0.5
Peak shear strain	$\gamma_{d,max}$	0.1
shear strength	φ'_{eq} (φ')	24.1 (33)
Phase Transformation Line	φ'_{PTL}	15.1
Contraction	c_1	0.02
	c_2	0
Dilatancy	d_1	0.6
	d_2	3.0
initial void ratio	e_0	0.6
Critical State	ξ_1	0.9
	ξ_2	0.02
	ξ_3	0.7
Number of yield surface	N	40

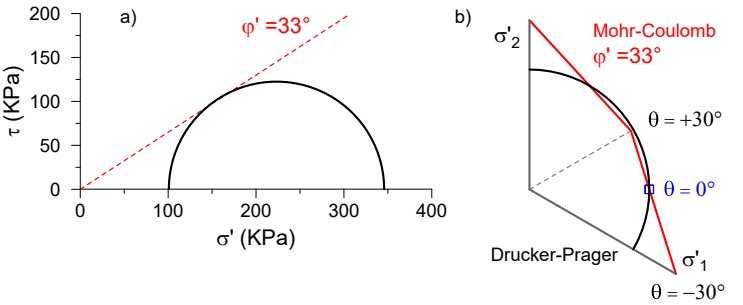

Fig. 3.5. Plane-strain failure: (a) τ-σ' plane; (b) octahedral plane.

then volumetric plastic strain rate, and therefore pore water pressure generation rate. These parameters drastically change the response of the material. Obviously, a value of φ'_{PTL} close to φ' implies only a contractive behaviour. Note that the response of green line, where both φ'_{PTL} and c_1 were varied, is completely different from the others where only one parameter was varied. Fig. 3.6-c reports the effect of dilative parameters d_1 and d_2. Larger d_1 and d_2 values result in increasingly stronger dilation. The increase in shear stress and effective confinement due to dilation is however limited by the choice of peak shear strain $\gamma_{d,max}$. Furthermore, since decreasing these parameters decreases the dilation tendency, the accumulated shear strain could increase unreasonably during a cyclic test. This aspect will be further discussed in the following.

Fig 3.7 shows the effect of confining stress p' on the response of a element subjected to cyclic shear tests for the reference set of parameters. Fig 3.7-a reports the influence of number of cycles for a $p' = 300$ kPa while, Fig 3.7-b is referred to $p' = 100$ kPa. The values of the modulus G and the damping ratio ξ are evaluated for each cycle thanks to an appropriate script developed in the Matlab environment. In particular, G is evaluated by knowing the slope of a straight line between the ends of the $\tau - \gamma$ curve as $G = 2\tau_e/2\gamma_e$, while ξ is defined as $\xi = W_d/4\pi W_e$; where $W_e = 0.5\tau_e\gamma_e$ and W_d is area of the hysteresis loop. Note that the shear modulus decay curve shows a degradation with the number of cycles starting from a value of the shear strain in accordance to that expected from experience, where the volumetric threshold of the shear strain γ_V is correlated to the value of the shear strain with a reversible response γ_L, according to the following expression: $\gamma_V = \gamma_L \cdot 10^{1.5}$

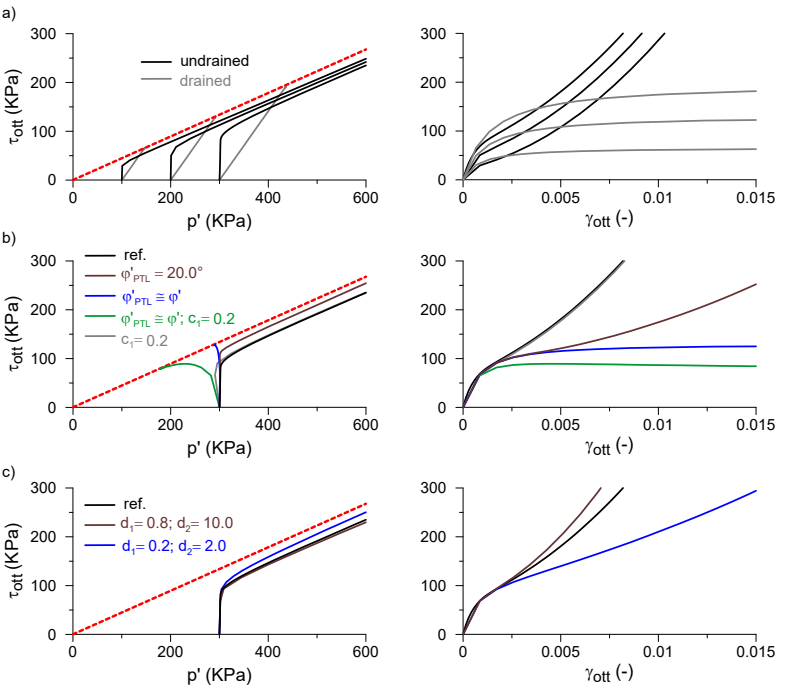

Fig. 3.6. Triaxial compression test: (a) influence of p' and drainage conditions, (b) influence of φ'_{PTL} and c_1, (c) influence of d_1 and d_2.

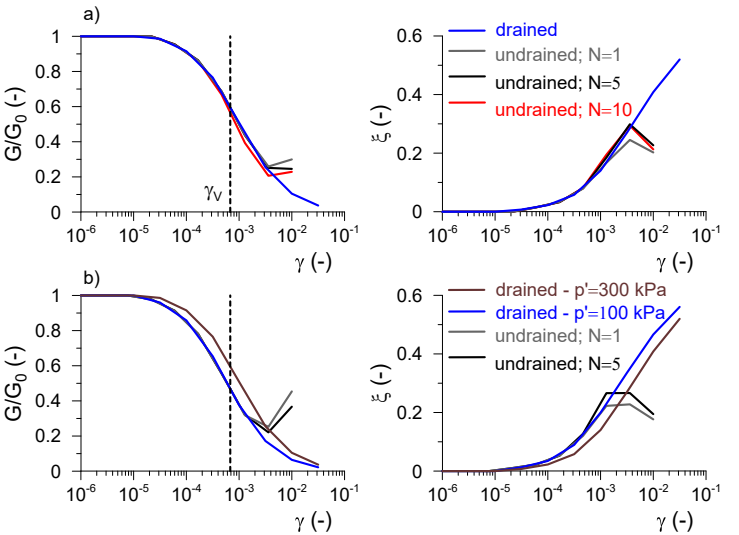

Fig. 3.7. Cyclic shear test: influence of drainage conditions and number of cycles for (a) $p' = 300$ kPa, (b) $p' = 100$ kPa.

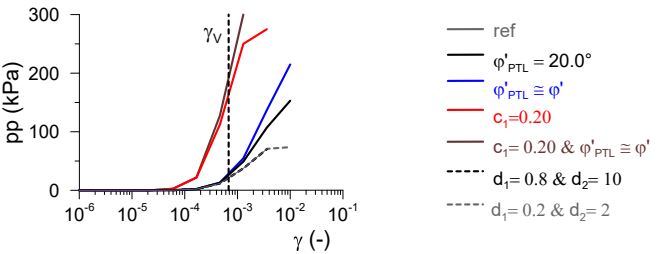

Fig. 3.8. Cyclic shear test: development of the pore water pressure according to different set of parameters.

(Vucetic and Dobry 1991). Fig. 3.7-b reports the effect of the pressure confinement on the shear modulus decay and damping curves.

In addition, Fig. 3.8 shows the development of pore water pressures according to different sets of parameters. As expected from the previous monotonic tests, the phase transformation angle φ'_{PTL} and the contraction parameter c_1 have a considerable effect while the dilative parameters produce a negligible variation.

It is worth noting that as shown in Fig. 3.7, the apparent increase in stiffness occurring for high deformation levels depends on the dilation tendency of the model. In fact, it is intuitive to think that this behaviour

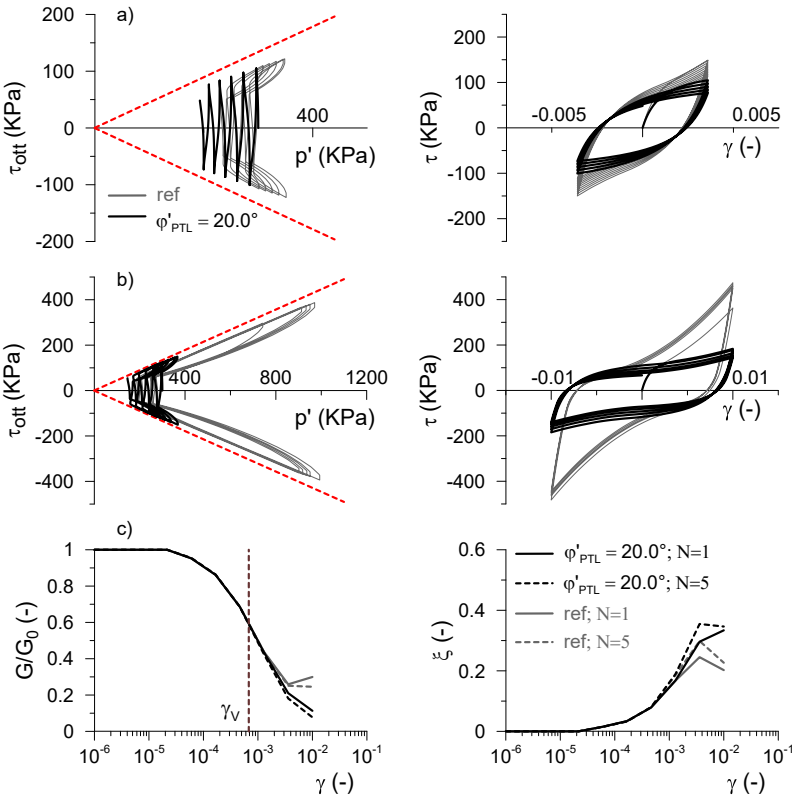

Fig. 3.9. Cyclic shear test; comparison between the reference set and the one with a different value of φ'_{PTL}: (a) γ=0.0036; (b) γ=0.01; (c) shear modulus decay and damping curves after 1 and 5 cycles respectively.

is accentuated by the development of pore water pressures as already seen for the monotonic tests. Therefore, in this case, the definitions of G and ξ as described above lose their physical meaning and remain merely a convention. The modification of the shape of the $\tau - \gamma$ cycles observed during several cyclic shear tests due to increasing deformation is presented from Fig. 3.9 to Fig. 3.14.

More in detail, Fig. 3.10 and Fig. 3.12 show the response of only contractive behaviour. In these cases, the development of pore pressures, already reported in Fig. 3.8, is so large that the confinement stress goes to zero after only a few cycles. This effect is certainly pronounced in Fig. 3.12 where a bigger value of c_1 was employed. Fig 3.9 reports the effect of a different value of φ'_{PTL}. It can be seen that with a bigger value of φ'_{PTL},

the phase transformation line is reached later and a greater development of pore water pressures is produced. Fig. 3.11 shows the influence of a bigger value of c_1 while Fig. 3.13 and 3.14 report the effects of the dilative parameters. Note that in these latter figures, although both the shear modulus decay and damping curves are very similar to the reference set, the response in the plane τ - γ is quite different. Finally, Fig. 3.15 reports the comparison between undrained and drained conditions related to cyclic shear tests. As expected, the response is quite different, especially at higher level of deformations, where the *butterfly effect* develops under undrained conditions.

The final set of parameters is therefore chosen by accounting for the above considerations, reaching the best calibration choice between static and cyclic conditions.

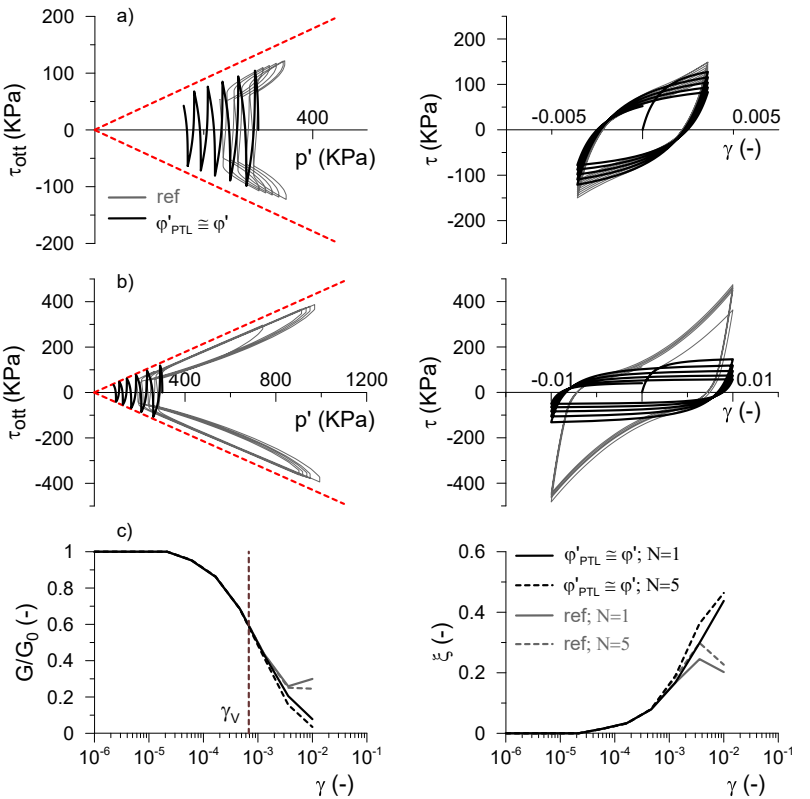

Fig. 3.10. Cyclic shear test; comparison between the reference set and the one with a different value of φ'_{PTL}: (a) γ=0.0036; (b) γ=0.01; (c) shear modulus decay and damping curves after 1 and 5 cycles respectively.

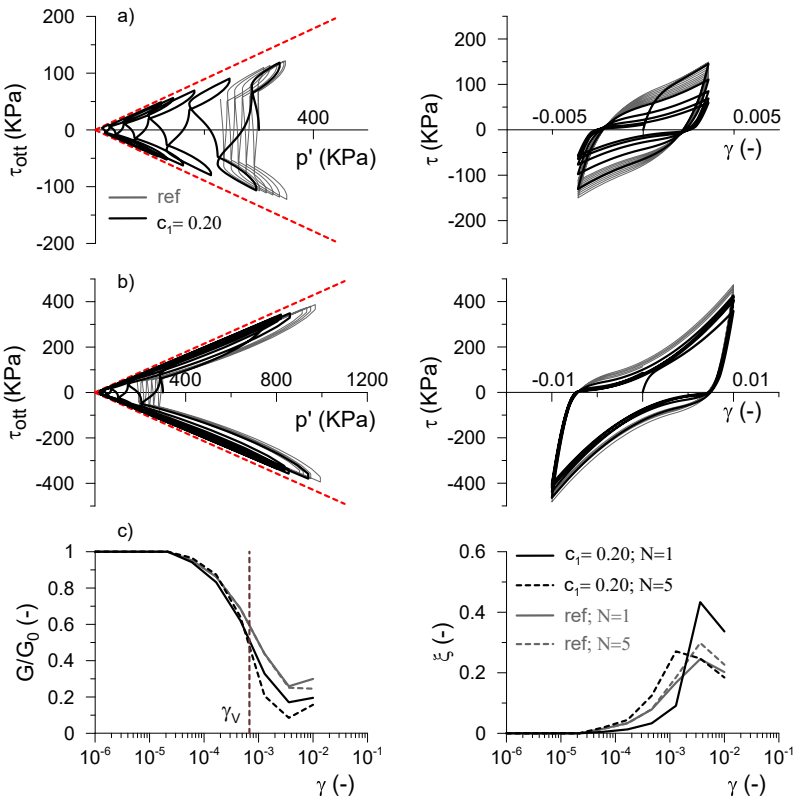

Fig. 3.11. Cyclic shear test; comparison between the reference set and the one with a different value of c_1: (a) γ=0.0036; (b) γ=0.01; (c) shear modulus decay and damping curves after 1 and 5 cycles respectively.

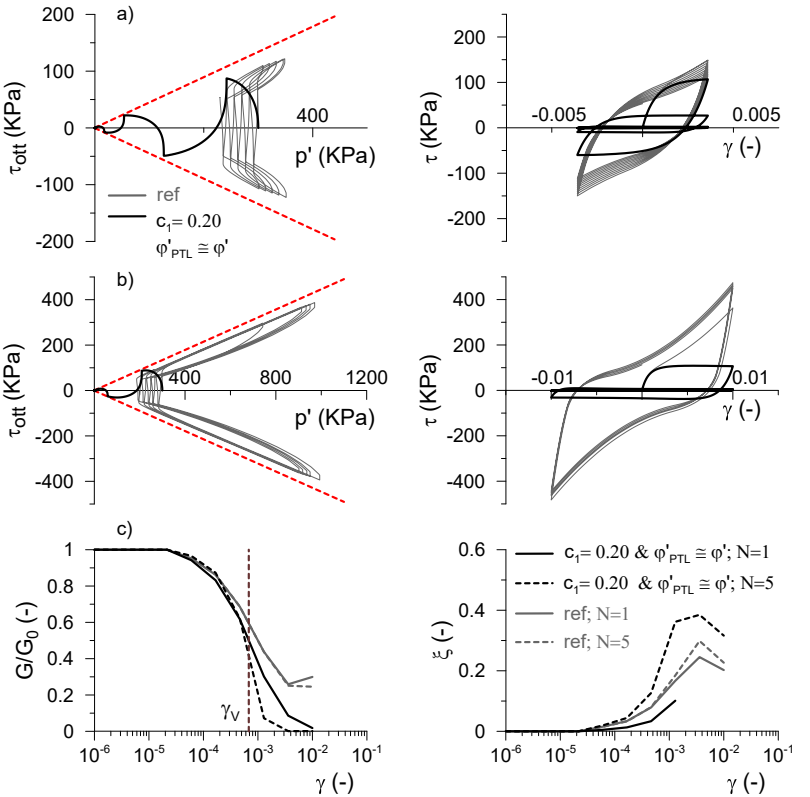

Fig. 3.12. Cyclic shear test; comparison between the reference set and the one with a different value of c_1 and φ'_{PTL}: (a) γ=0.0036; (b) γ=0.01; (c) shear modulus decay and damping curves after 1 and 5 cycles respectively.

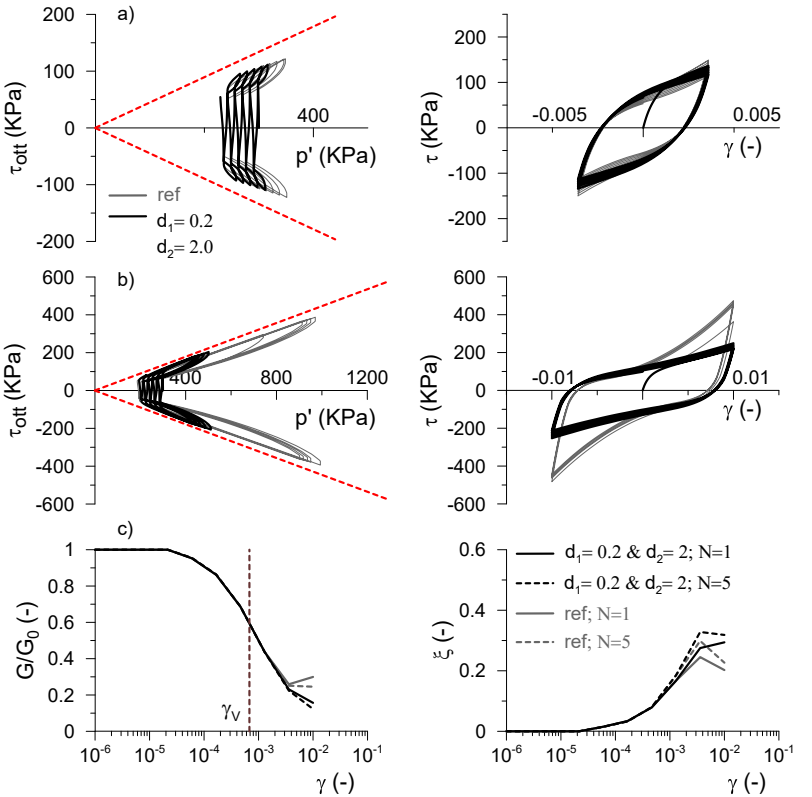

Fig. 3.13. Cyclic shear test; comparison between the reference set and the one with a different value of dilative parameters d_1 and d_2': (a) γ=0.0036; (b) γ=0.01; (c) shear modulus decay and damping curves after 1 and 5 cycles respectively.

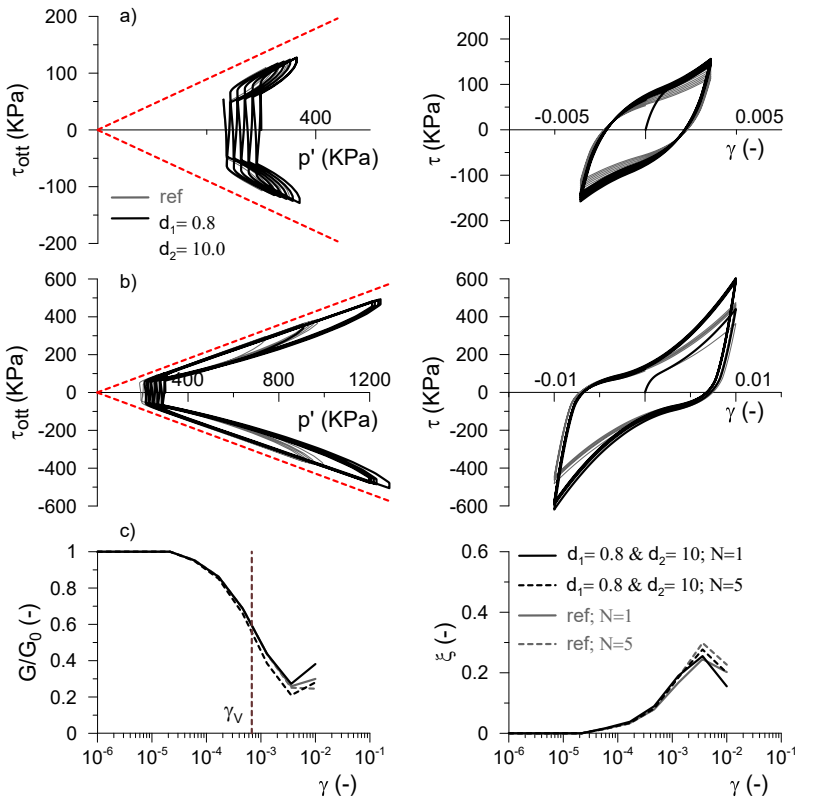

Fig. 3.14. Cyclic shear test; comparison between the reference set and the one with a different value of dilative parameters d_1 and d_2': (a) γ=0.0036; (b) γ=0.01; (c) shear modulus decay and damping curves after 1 and 5 cycles respectively.

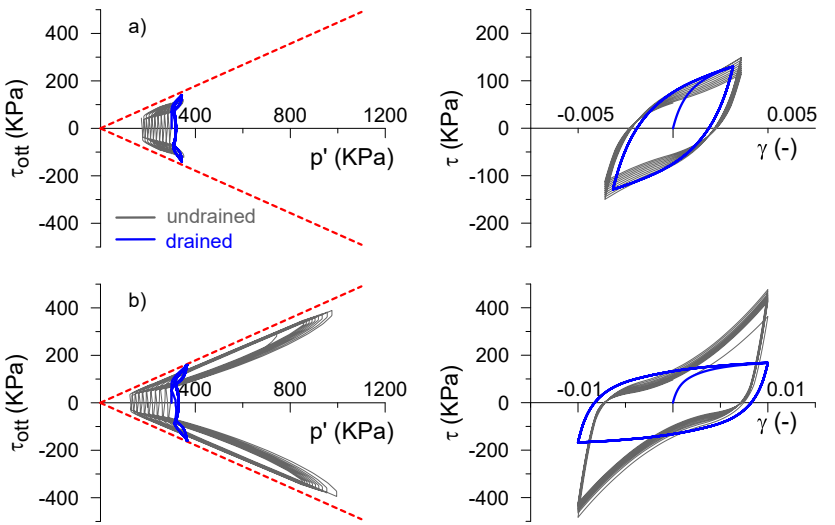

Fig. 3.15. Cyclic shear test; comparison between drained and undrained conditions: (a) γ=0.0036; (b) γ=0.01.

3.2. From the real case study to a simplified model

A simplified full 3D soil-bridge model was developed with the aim to evaluate the seismic performance of such complicated systems through time-domain dynamic analyses. The simplified model, depicted in Fig. 3.16, is composed of an idealised structure scheme, inspired by the Gatteo Overpass scheme but located in an idealised soil domain. The full model is composed by about 51000 solid elements for the soil and about 2400 structural elements, for a whole extension of 116 x 68 m^2 in plan and 50 m in depth. The model was implemented in the analysis framework OpenSees while the mesh generation was developed with an automatised script in Matlab (2020) according to a parametric procedure. Finally the visualisation of the results was performed both in Matlab and in the pre/post processor software GiD (Ribó et al. 2008).

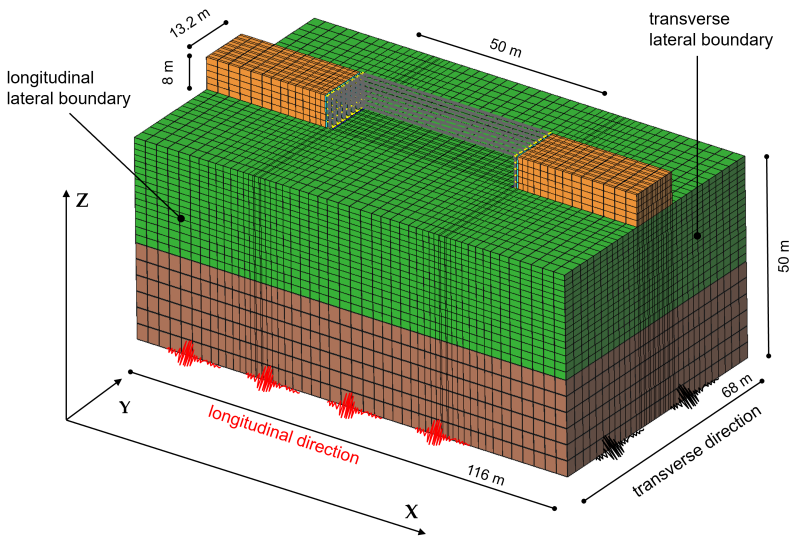

Fig. 3.16. Full 3D model of the soil-bridge system.

3.2.1. Bridge structure

The bridge superstructure is composed of a single-span of continuous deck with integral abutments that carry most of the longitudinal inertial forces developing into the superstructure. The span has a length of 50 m while the abutment is massive reinforced concrete structure with 8 m height wall, with 2.2 m thickness and with 13.2 m width. It rests on deep foundations composed by seven reinforced concrete piles with lengths

of 20.0 m and diameters of 1.2 m placed on a single row. The design solution based on the choice a of single row of piles is quite common for IABs an it is conceived to mitigate the internal forces in the structure produced by thermal gradient changes.

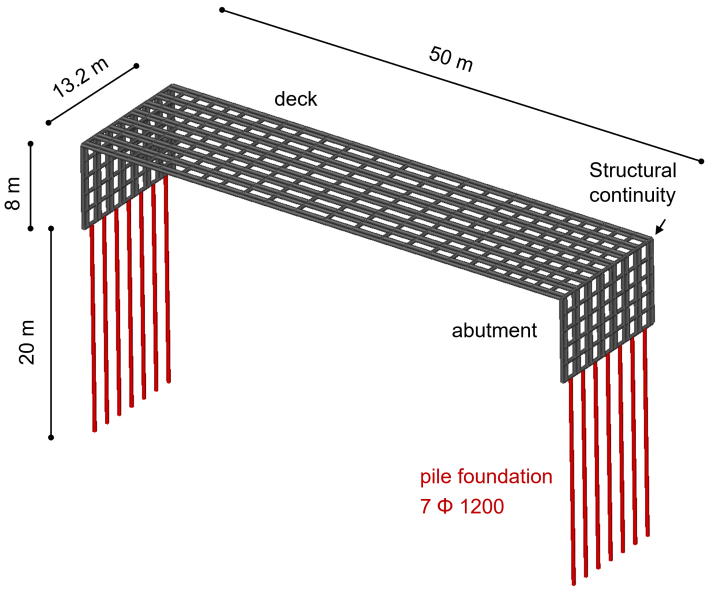

Fig. 3.17. Bridge structure modelled through beam elements.

Since the seismic design of IABs aims to guarantee the structural integrity, the strength of the structural members was designed to remain in the elastic range under the maximum seismic forces. Therefore, a linearly elastic behaviour was assigned to the piles, abutment walls and deck. More in detail, a grillage modelling approach was adopted to model the abutment walls and the deck (see Fig. 3.17), where the properties of each beam are proportional to its tributary area.

The properties of the deck are summarised in Table 3.1 distinguishing the initial steel-only section from the final composite section, whereas a homogenization procedure was used to get the equivalent parameters in terms of axial and bending stiffness.

The pile foundations that support the piers were designed by the application of standardized procedures (in particular following the Italian Building Code 2018) considering all the static actions (traffic loads, shrinkage, creep, thermal variations, earth pressures) and maintaining

an adequate safety margin for seismic conditions. The modelling of static actions (herein non reported for sake of brevity) was performed in SAP2000 following the *Non linear staged construction* and describing the soil-structure interaction with non linear spring. Finally the elastic material assigned to the pile foundations and abutments was calibrated for a *C32/40* strength class concrete according to the European standards.

3.2.2. Foundation soil and embankment

The foundation soil represents an idealised deposit. The mechanical behaviour of the foundation soil was described through the PDMY model and the relative constitutive parameters associated with each layer have already been discussed in section 3.1.

The use of dry soil in the full soil-bridge model, allowed to adopt the SSPbrick eight node hexahedral elements (Zienkiewicz and Shiomi 1984) to discretise the entire soil domain. These elements use a physically stabilized single-point integration, resulting in an element which is free from both volumetric and shear locking. As well as for the SSPbrickUP elements, SSPbrick elements produce results comparable with their higher-order counterparts with great computational efficiency (McGann et al. 2015).

The PDMY model is able to reproduce the dependence of the energy dissipation on the strain amplitude as seen in section 3.1. Nonetheless, an additional small damping ratio not grater than 2% for the frequencies of interest was introduced in the soil domain using the Rayleigh formulation, in order to attenuate the effects of spurious high frequencies.

The coarse-grained embankment was designed according to the procedure proposed by Gorini (2019) to have stiffness and strength properties respectful of the corresponding limit values imposed by Italian technical provisions (Italian Building Code 2018). The technical provisions herein taken as reference were the *Capitolato Ferrovie and Testo Unico* currently in force in Italy. The design requirements for bridge embankment allow to minimize the settlements of the embankments due to the traffic loads that might compromise the serviceability of the infrastructure. Specifically, it is prescribed that the Young's modulus E_{min} be not less than $7.2 \cdot 10^4$ kPa for the embankment body with a dry unit weight $\gamma_{d,min}$ not less than $0.95 \cdot \gamma_{d,max}$, where $\gamma_{d,max}$ is the maximum value of γ_d evaluated by a modified Proctor compaction test.

These requirement are therefore used as constraints for the choice of constitutive parameters of soil of the embankment.

The embankment was modelled in the finite element analysis framework OpenSees as an equivalent single-phase body, by using PDMY model to simulate its cyclic behaviour. The properties of the mix design and the effects of suction were implicitly taken into account by assigning appropriate parameters to the constitutive models (Gorini 2019). Finally, as done for the foundation soil, the same small damping ratio was added to these elements using the Rayleigh formulation.

A schematic representation of the case study is illustrated in Fig. 3.18-a. The profile of the small strain shear modulus G_0 with depth, provided by the PDMY model, is shown in Fig. 3.18-b. The black dashed line in the figure considers the increase in effective stresses produced by the presence of the embankment. Table 3.5 reports the PDMY parameters for the soil domain. Note that the layer 1 was divided in two parts in order to better follow the experimental profile of G_0 reported in Fig. 3.2. In other words, it was necessary to adjust the parameters G_0 and p'_r.

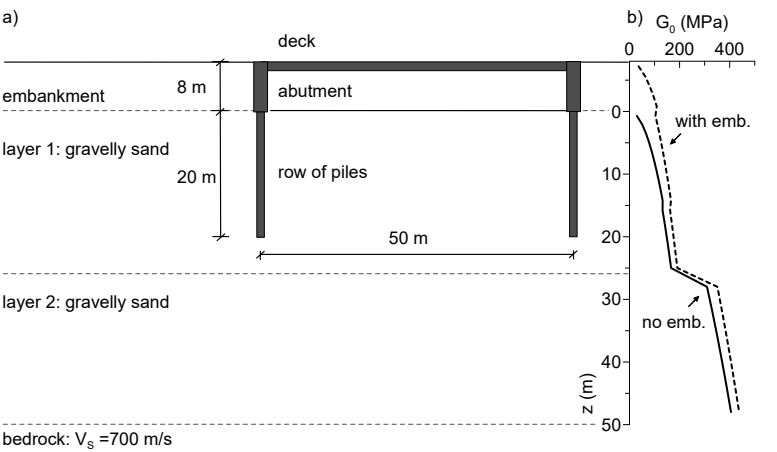

Fig. 3.18. (a) Schematic representation of the case study; (b) profile of the small strain shear modulus G_0 with depth.

Tab. 3.5. PDMY parameters for the soil domain.

Variable	Unit	embank.	layer 1 (0-15 m)	layer 1 (15-26 m)	layer 2 (26-50 m)
G_0	kPa	115 000	98 000	95 000	165 000
ν	-	0.3	0.315	0.315	0.3
p'_r	kPa	100	100	105	100
d	-	0.5	0.5	0.5	0.5
$\gamma_{d,max}$	-	0.1	0.1	0.1	0.1
φ'_{eq} (φ')	°	25.8 (36)	24.1 (33)	24.1 (33)	25.2 (35)
φ'_{PTL}	°	12	15	15	18
c_1	-	0.02	0.02	0.02	0.02
c_2	-	0	0	0	0
d_1	-	0.6	0.6	0.6	0.6
d_2	-	3.0	3.0	3.0	3.0
e_0	-	0.6	0.6	0.6	0.6
ξ_1	-	0.9	0.9	0.9	0.9
ξ_2	-	0.02	0.02	0.02	0.02
ξ_3	-	0.7	0.7	0.7	0.7
N	-	40	40	40	40

3.2.3. Soil-structure contact

The soil-structure contact was modelled by means of thin layers of solid elements interposed between the structure and the soil. Fig. 3.19 shows an enlarged view of the soil-structure contact. The interface elements of the abutment are represented in cyan in Fig. 3.19-a while interface elements of the pile foundations in blue in Fig. 3.19-b/c. The main objective of the interface elements is to describe the strain concentration occurring in the soil in close proximity to the structural elements. The behaviour of the interface elements was reproduced with the same advanced constitutive model used for the soil domain.

More in detail, two-node beam elements with three translational and three rotational degrees of freedom at each node were used to model all the structural elements: piles, abutments and bridge deck. To connect the pile elements to the surrounding soil elements, solid elements in the region occupied by the piles were removed (see Fig. 3.19-b/c), and at each elevation the pile nodes were connected horizontally to the soil nodes using four rigid link elements reproducing the dimensions of the circular section. Between the terminal nodes of the rigid links and the corresponding soil nodes with the same coordinates, constraints of equal displacements were used for the translational degree of freedoms, named equal-DoF constraints, while the rotational DoFs of the rigid links were left free. A schematic representation of the employed procedure is depicted in Fig. 3.20. Finally a thin layer of elements next to the pile was used to describe the frictional behaviour at the soil-pile interface, characterised by a friction angle equal to 2/3 the one of the soil to simulate the strength reduction along the soil-pile contact. Note that the interaction between piles is permitted by a thin layer of soil (in green in Fig. 3.19-a) left in the transverse direction between one pile and another.

As reported by Jeremić et al. (2009), connecting piles to soil using the above described method has a number of advantages and disadvantages. On a positive side, geometry of soil–pile system is modeled very accurately and the presence of a thin layer of elements next to pile is useful to mimic frictional behavior at soil–pile interface. In addition to that, the deformation modes of the pile (axial, bending, shearing) are accurately transferred to surrounding soil by means of connection rigid-link elements. On a negative side, discrepancy of displacement approximation fields between pile and soil will lead to incompatibility of displacements between nodes of pile-soil system. However, this in-

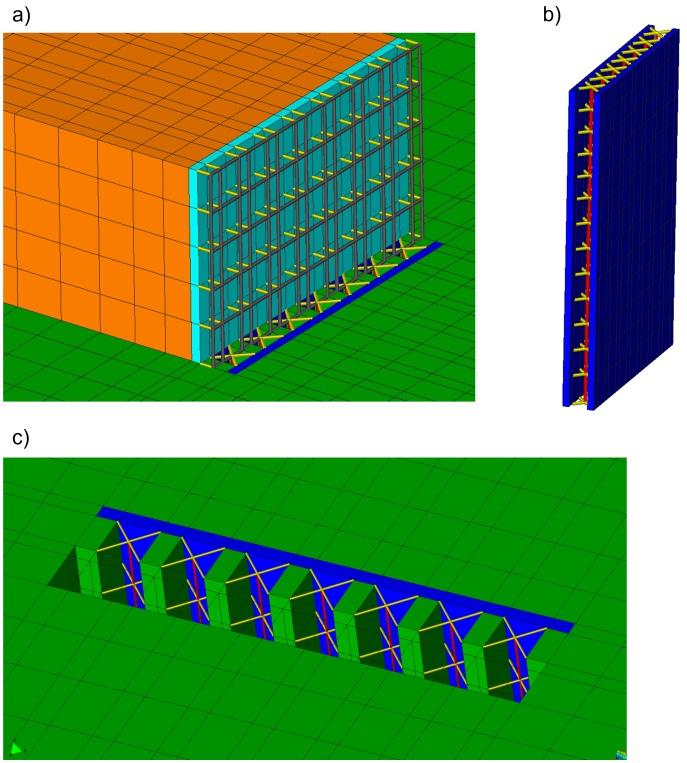

Fig. 3.19. Enlarged view of the soil-structure contact for (a) abutment and (b-c) pile foundation.

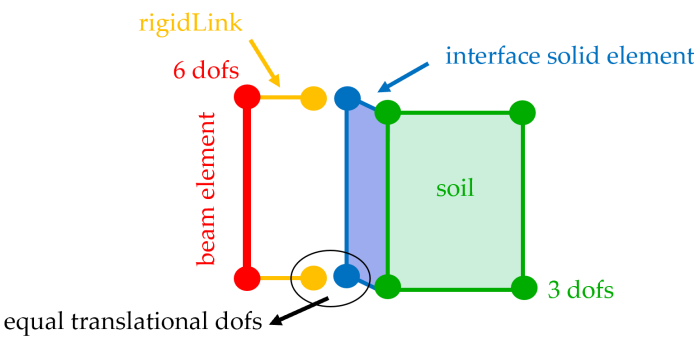

Fig. 3.20. Modelling of soil-structure contact.

compatibility was deemed acceptable in view of advantages described above.

The same procedure was also applied to connect the abutment elements to the correspondent embankment elements (see Fig. 3.19-a), and a friction angle equal to 2/3 the one of the embankment was assigned to the interface elements.

Finally, taking into account the way in which the abutments and pile foundations were constructed, it was assumed that only the abutment-embankment interface could have a dilative behaviour. On the contrary, since the piles are rotary drilled into the ground, only a contractive behavior is expected at the pile-soil interface. Thus, in the soil-pile interface the parameter φ'_{PTL} is considered equal to $\varphi'_{eq,interface}$.

3.2.4. Embankment modelling and wing walls

In this work, two assumptions were made about the abutment-embankment interaction: presence or absence of the wing walls. The case without wing walls assumes that the wing walls are disconnected from the abutment so that the behaviour of the abutment can be considered independent. Thus, the lateral boundaries of the embankment were constrained through equal-DOFs to undergo the same motions of the opposite side, reproducing a *shear beam* behaviour, as depicted in Fig. 3.21. In fact, the main idea was to focus on the global behaviour of the embankment rather than on the possible local instabilities of the slopes. From an engineering perspective, the embankment behaves like a reinforced earth wall.

Conversely, section 1.3.2 have reported some observations on the wing walls design. In details, White (2008) and White et al. (2010) observed that wing walls did not get the necessary attention from the designers although the wing walls orientation and connection details could have an impact on the forced induced in, and the distribution of, the forces through the structure. The survey results indicated that there is a little agreement among the various US and European transportation agencies regarding the wing walls design.

The type of the wing wall chosen for the case study is the one called *cantilivered-U wingwall* in section 1.3.2. The wing walls extend along the length of the embankment for about 10.5 m.

They were considered in a simple way by using an appropriate choice of equal-DOFs. Looking at the Fig. 3.22, the slave nodes at each eleva-

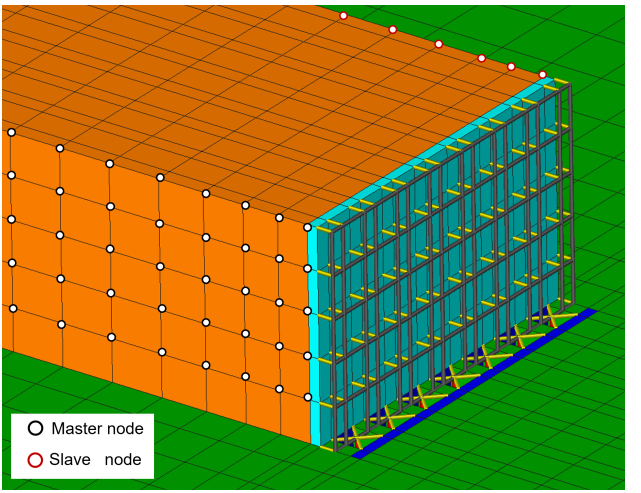

Fig. 3.21. Embankment modelling.

tion follow the translational displacements of the master node at the correspondent elevation. It is assumed therefore that the abutment and wing walls behave like a U-shaped rigid box. No foundation has been provided under the wing walls so that the abutment can continue to have a flexible behavior. Moreover, using only equal-DOF constraints, the modelling did not require additional elements such as interfaces and soil-structure contacts. This allows to keep the exact same mesh of the previous case with only small changes to be applied to the boundary conditions on the side walls of the embankment. As made for the abutment, a thin layer of elements next to the wing walls was used to describe the frictional behaviour.

Finally, in the remaining part unoccupied by the wing walls, the embankment continues to behave like a shear beam as the previous case.

3.3. Simplifying the full 3D model

3.3.1. Solution procedure

Non-linear dynamic analyses in the time domain were carried out on the numerical models after a staged construction procedure that will be discussed in depth in section 3.4. Velocity time-histories are applied to the bottom boundary through the interposition of viscous dampers (Lysmer and Kuhlemeyer 1969) to simulate a compliant bedrock (Joyner and Chen 1975). In addition, precisely because the bedrock is de-

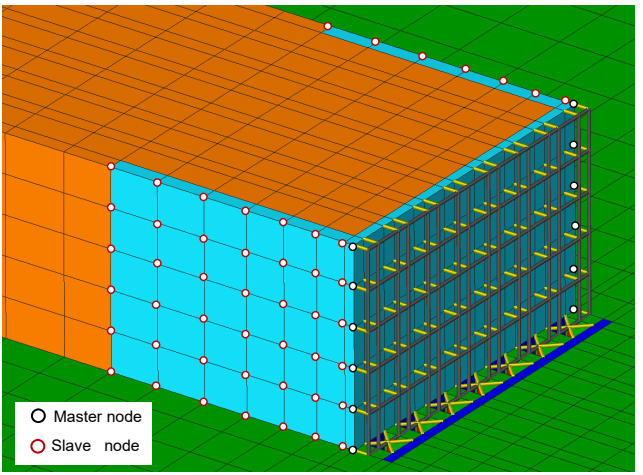

Fig. 3.22. Wing wall modelling.

formable, the displacements at the base of the model will be subtracted from those of the structural nodes. Specifically, at each structural node of coordinates (x,y), in the global reference system illustrated in Fig. 3.16, corresponds one node at the bottom with the same coordinates (x,y).

Periodic constrains were applied to the lateral boundaries of full 3D soil-bridge model depicted in Fig. 3.16. The nodes placed at the same elevation on the two longitudinal lateral boundaries, including the embankment, are forced to undergo the same displacements. The same relationship is applied to the two transverse boundaries. The base assumption is that the lateral boundaries are located far enough from the bridge to ensure the free field response. These assumption has been however checked and will be discussed in section 4.4.

The use of the parallel computing, obtaining with the OpenSeesSP (McKenna and Fenves 2007) interpreter, was needed to get reasonable computation times starting from the staged construction. The system solver Multifrontal Massively Parallel sparse direct Solver (MUMPS) was adopted to solve the large sparse system of equation in the analysis. A Newmark time-stepping method with γ equal to 0.5 and β equal to 0.25 was used to integrate the equation of motion (with no additional numerical damping) while the Newton-Raphson algorithm was employed to solve the nonlinear residual equation.

In spite of the aid of parallel computing, the dynamic analysis of the system depicted in Fig. 3.16 is not easy and immediate to handle. Thus, to validate simplified procedures, models with greater simplifications were introduced.

Moreover, just to facilitate the development of these models, a parametric mesh has been developed with MATLAB taking into account different geometries and schemes. At the same time, the automated procedure allows for defining the properties of the structural elements which substantially depend on the tributary areas (see section 3.2.1). Once the mesh and the properties of the various elements have been generated, minor changes to the OpenSees script are necessary to consider the new boundary conditions to apply to the structural and soil nodes.

3.3.2. Longitudinal behaviour

To focus on the longitudinal response of the bridge, only half of the bridge can be modelled, as shown in Fig. 3.23, taking advantage of the symmetry of the problem about the vertical longitudinal plane.

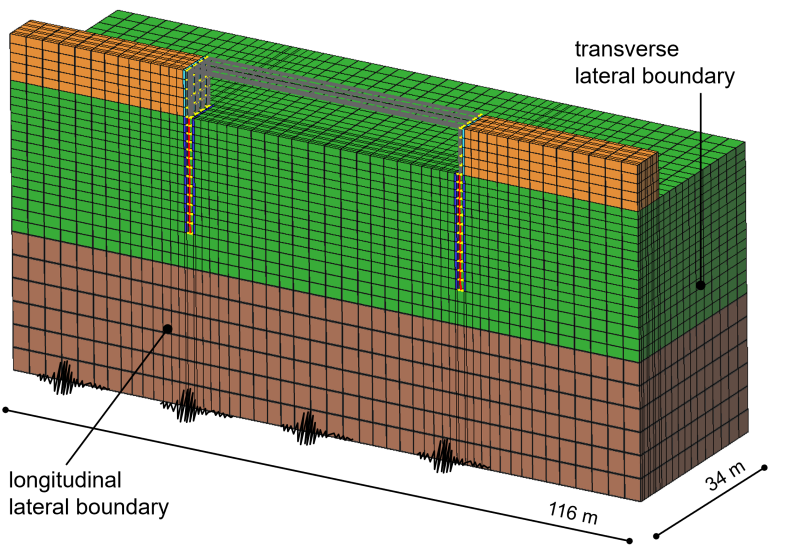

Fig. 3.23. Half of the 3D soil-bridge model used in the longitudinal analysis.

In addition, a simpler mesh was developed, as shown in Fig. 3.24, aimed at defining an equivalent two-dimensional representation, called 2D model, of the full system layout. This model includes the soil con-

tained between two longitudinal planes spaced by 1.8 m, equal to the pile spacing, and therefore incorporates a single pile connected to the surrounding soil in the same manner as in the 3D model, as show in detail in Fig. 3.25. Basically, it can be thought as a plane-strain model for the soil, and a plane-stress model for the bridge structure.

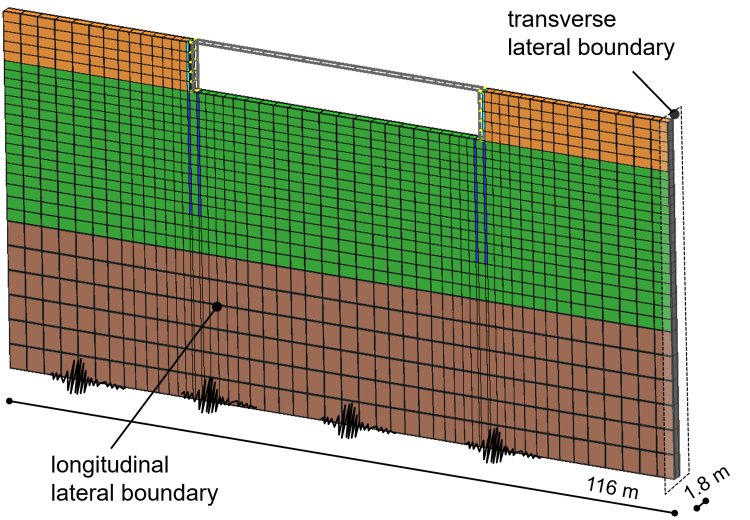

Fig. 3.24. Equivalent 2D model.

The above models have the same discretization of the full model depicted in Fig. 3.16 in both the vertical and longitudinal directions. The 2D model includes about 4100 brick elements and about 300 beam elements, while the half 3D model has about 26000 brick elements and 700 beam elements. A parametric study carried out on the 2D model with a much more refined mesh (up to 11000 brick elements) will be presented in the next chapter, indicating that the discretization adopted in the finite element mesh of Fig. 3.24 provides an acceptable approximation for the system at hand.

Finally, periodic constrains were applied to the transverse lateral boundaries, forcing the nodes placed on both sides of the soil and the embankment at the same elevation to undergo the same displacements. The nodes along the longitudinal lateral boundary were constrained in the normal direction only. In addition, the rotation of the structural nodes out of symmetry planes was impeded.

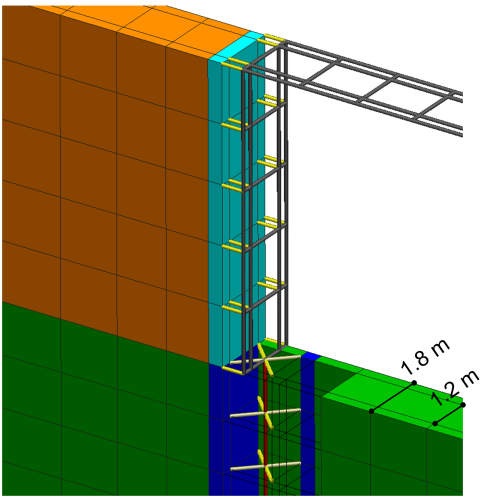

Fig. 3.25. Enlarged view of the soil-structure contact for the equivalent 2D model used in the longitudinal analysis.

3.3.3. Transverse behaviour

Similar considerations can be made for the development of the half 3D model in the transverse direction depicted in Fig. 3.26. In this case, we took advantage of the symmetry of the problem about the vertical transverse plane to excite the model with only the transverse component of the seismic action. The half 3D model has about 26000 brick elements and 700 beam elements.

The periodic constrains were applied to the longitudinal lateral boundaries, forcing the nodes placed on both sides of the soil at same elevation to undergo the same displacements. The nodes along the transverse lateral boundaries were constrained in the normal direction only. Furthermore, the rotation of the structural deck nodes out of symmetry planes was impeded. In closing, this model as well as the full model depicted in Fig. 3.16, allows to consider or not the presence of wing walls as explained in section 3.2.4.

3.4. Staged construction

A very important modelling challenge in soil-structure interaction problems is that of staged construction because the construction sequence has a strong influence on the static and seismic response of the bridge.

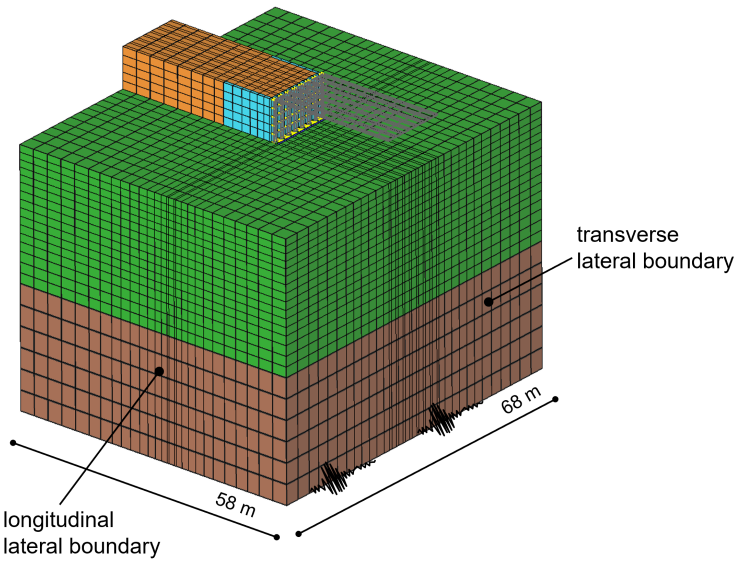

Fig. 3.26. Half of the 3D soil-bridge model used in the transverse analysis.

Different construction sequences may be envisaged for an integral abutment bridge. The procedure modelled herein mimics that employed in the construction of the prototype bridge, that was aimed at minimising the internal forces in the deck and in the foundation piles under static conditions. The relative numerical modelling is composed of the several stages depicted in Fig. 3.27 which are:

stage 0: initialisation of the effective stress state in the soil deposit (layer 1 and 2), done by performing an elastic analysis in which the soil is loaded by its own weight and desired earth pressure coefficient is obtained by adjusting the Poisson's ratio. Subsequently, the elasto-plastic behaviour in the soil element material is activated.

stage 1: construction of the soil embankment. The embankment was built gradually in the model by adding progressively the five horizontal rows of solid elements for a more accurate reproduction of the stress state in the soil. The vertical boundary in correspondence of the abutment location was restrained in the longitudinal direction to avoid any local instability.

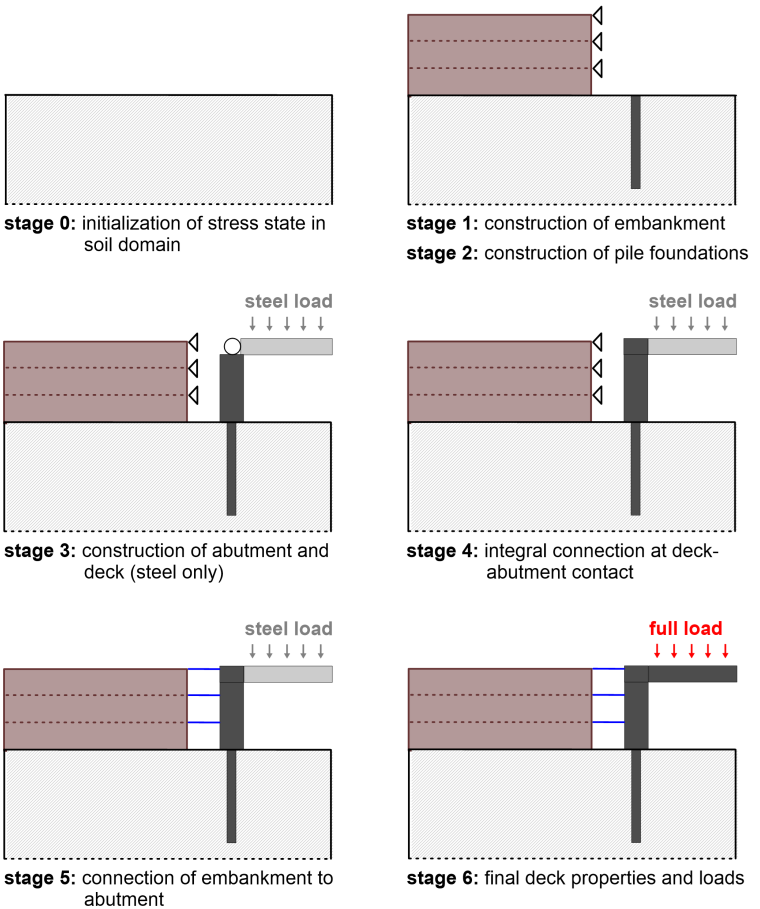

Fig. 3.27. Representation of the construction stages of the reference soil-bridge model.

stage 2: construction of the piles through the removal of soil elements and simultaneous installation of the pile elements, that are connected to the surrounding soil by means of rigid links.

stage 3: construction of the abutment and the deck. During this stage, the deck is simply supported at the abutments through a hinged connection and includes only the steel girder and the secondary beams (see Table 3.1).

stage 4: integral connection of the deck-abutment contact, obtained by impeding relative rotations between the respective nodes.

stage 5: embankment in contact with the abutment front wall. The longitudinal restraints along the embankment face are removed and the soil nodes are connected to the abutment nodes according to the technique described in section 3.2.3.

stage 6: updating the stiffness and loads of the deck; the deck stiffness is changed to that of the final composite steel-concrete structure and the final permanent loads are applied to the deck.

Fig. 3.28-a shows the evolution of the bending moments in the piles, in the front wall and in the deck during the bridge construction, while the corresponding displacement field is illustrated in Fig. 3.28-b; note that in the latter figure the scale of the horizontal displacements of the abutment and pile is of one order of magnitude smaller than that of the vertical settlements of the deck. Stage 6 represents the end of construction and is therefore the initial state for the subsequent dynamic analyses. It is worth noticing that, with respect to the previous stages, at this stage the increment of the loads on the deck causes a counter-rotation of the abutment-pile system towards the embankment, changing the sign of the moment at the deck-abutment contact.

Fig. 3.29 reports the evolution of the bending moments and of the longitudinal displacements carried out on the 3D model. The abutment forces the piles to undergo the same displacement (Fig. 3.29-b), therefore as a consequence of three dimensional effects, the external pile (No.4) is the most loaded (Fig. 3.29-a) because it is the pile that exhibits the stiffer response. Nonetheless, the values of the internal forces and displacements obtained with the 2D and 3D model are comparable.

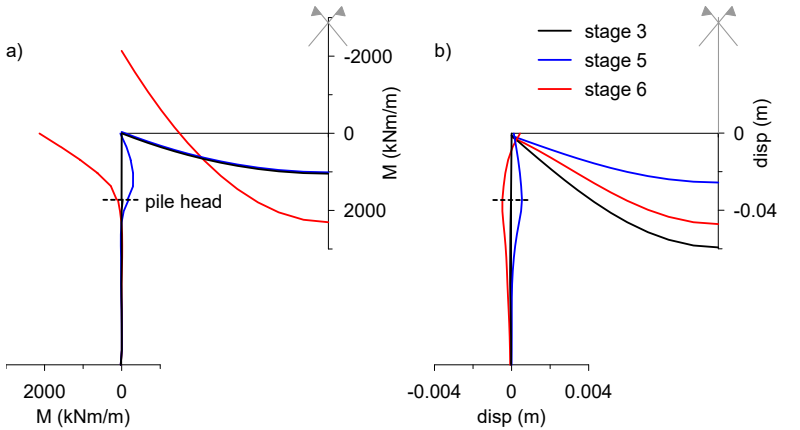

Fig. 3.28. 2D model: (a) bending moment evolution in the structure during the bridge construction and (b) corresponding deformations.

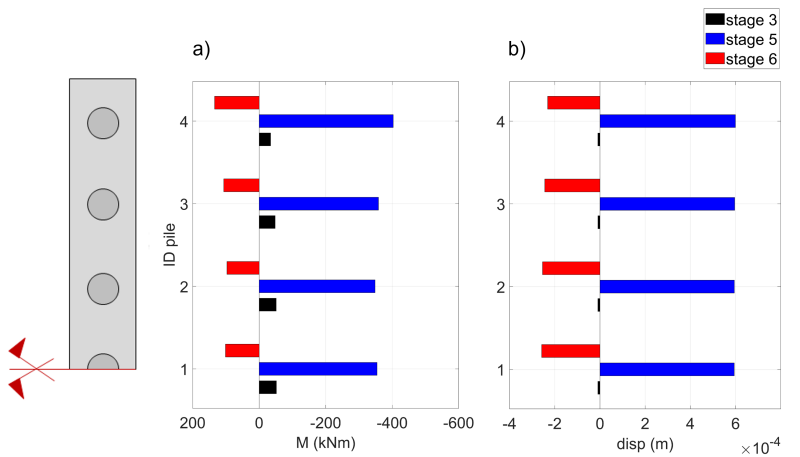

Fig. 3.29. 3D model: evolution of (a) bending moments and displacements (b) in correspondence of the pile heads during the bridge construction.

4. Dynamic response of the soil-bridge system

This chapter focuses on the dynamic response of the soil-bridge system taking advantage of the modal analysis tool. Starting from the soil column model, the dynamics of the overall system is described step by step up to the full 3D model. Subsequently, the main modes provided by the modal analysis are used to choice two essentially mono-frequency input motions. Finally, some intriguing results of the dynamic analyses are discussed.

4.1. Modal analysis

This section illustrates a novel approach for the application of the modal analysis to a soil-structure interaction problem. These results will be used to develop simplified design procedures aimed at evaluating the seismic performance of the bridge examined.

4.1.1. Analysis of the soil column

In order to perform the modal analysis of the soil column, a three-dimensional soil column was implemented in OpenSees, representing the soil deposit with the double hypothesis of presence and absence of the embankment. The two soil columns are depicted in Fig. 4.1.

The *Elastic-Isotropic nDMaterial* constitutive model, available in the OpenSees library, was used to model the soil elements. Since this model does not account for the stress and strain dependent stiffness, the stiffness used for the modal analyses is precisely the one at small strains. This procedure can be implemented in OpenSees once the stress tensor for each Gauss point is known. Then, the small-strain stiffness is defined according to the Eq. 3.6; in other words, an elastic material is

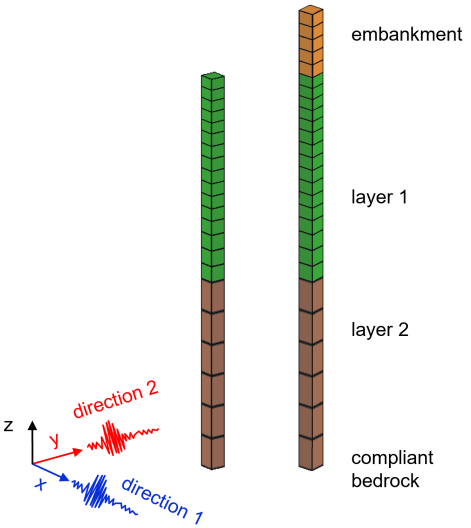

Fig. 4.1. Soil columns for site response analysis: (a) soil deposit without embankment and (b) with embankment.

defined for each soil element. Regarding the mass term, a mass density ρ can be assigned to the elements, or alternatively, the nodes can be assigned masses proportional to the volumes of influence. The results of modal analysis carried out with OpenSees are validated using MARTA (https://luigicallisto.site.uniroma1.it/attivita); a computer program for the equivalent-linear site response analysis. In order to perform a modal analysis with MARTA, for each layer the values of the shear modulus are set constant and equal to the ones at small strains whereas, the values of the damping ratio are set close to zero (0.5%). The periods of the modes can be obtained looking at the amplification function at ground level. Fig. 4.2-a and Fig. 4.2-b report an excellent correspondence between the normalised amplification functions carried out with MARTA and the periods provided by OpenSees.

With the aim of quantifying the importance of the modes, a very important parameter in the modal analysis is the participating mass M%. This parameter, associated to each mode, is evaluated through a post-processing script written in MATLAB environment. In a very simple way, it is possible to calculate for each mode the modal participation factor γ_j once the mass matrix M and the eigenvectors ϕ_j (modal shapes) are known. The eigenvectors and the eigenvalues (periods T)

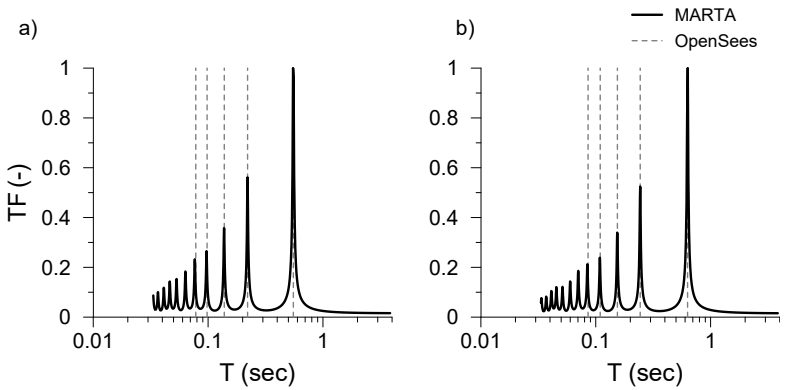

Fig. 4.2. Comparison between MARTA and OpenSees: (a) soil column, (b) soil column with embankment.

are provided by OpenSees in the output quantities; in contrast, the calculus of the participating mass requires a post-processor evaluation. In fact, the nodal masses must to be known by the user. In this regard, the development of a parametric mesh, presented in section 3.3, was of great importance because it facilitated the determination of the volumes/areas of influence associated with the individual nodes. Furthermore, if this operation seems trivial for a model like the soil column, it can become particularly tedious for more complex systems that will be presented later. Currently in OpenSees, the only possibility is to develop in-house pre and post processing scripts, possibly automated.

The modal participation factor γ_j is defined as:

$$\gamma_j = \frac{\phi_j^t \cdot M \cdot R}{\phi_j^t \cdot M \cdot \phi_j} \tag{4.1}$$

where R is a directional vector that in this case is a unit vector. At this point, the definition of the participating mass $M\%_j$ is immediate:

$$\tilde{M}_j = \gamma_j^2 \cdot (\phi_j^t \cdot M \cdot \phi_j) \tag{4.2}$$

$$\tilde{M}_{tot} = \sum_{j=1}^{Nmodes} \tilde{M}_j \tag{4.3}$$

$$M\%_j = \frac{\tilde{M}_j}{\tilde{M}_{tot}} \tag{4.4}$$

The results of modal analysis are reported in Table 4.1. Looking at the response of the soil column with embankment, it can be seen that the embankment plays a pivotal role mainly influencing the first mode. In fact, in terms of periods, the first modes of the two columns are quite different, whilst a slight difference in terms of both periods and participating masses is observed for the subsequent modes. The results of the soil columns in term of eigenvectors are reported in Fig. 4.3 and in Fig. 4.4 after a trivial stage of post-processing in MATLAB which allows for a subsequent visualization in GiD.

Fig. 4.3. Modal analysis of soil column without embankment.

Tab. 4.1. Modal analysis of soil column with and without embankment.

	soil column		soil column with embank.		
mode	$T(sec)$	$M_{tot}(\%)$	$T(sec)$	$M_{tot}(\%)$	$M_{emb}(\%)$
1	0.55	73.4	0.63	72.9	31.4
2	0.22	15.7	0.24	15.3	30.4
3	0.14	4.5	0.15	5.3	24.1
4	0.10	2.2	0.11	2.0	6.7
5	0.08	1.7	0.09	1.5	0.0

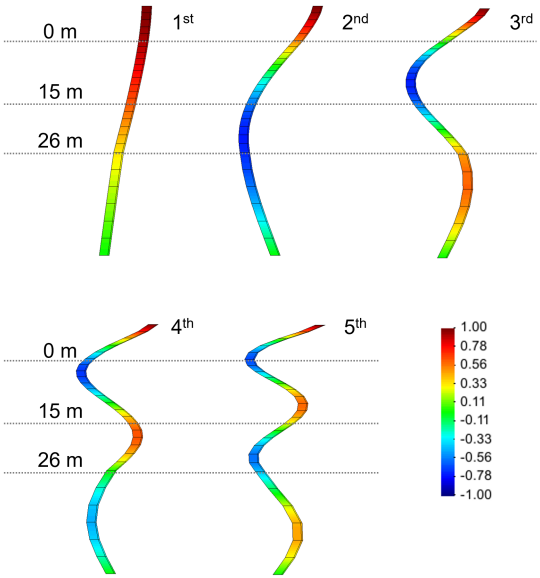

Fig. 4.4. Modal analysis of soil column with embankment.

4.1.2. Towards the 3D model

Before developing the final model of the system, let us to wonder what would happen to the two soil columns (one with embankment and another without it) if they are placed side by side and the size of the mesh (and thus of the degrees of freedom) is then increased. Now the goal is to evaluate the effect of the transverse extension of the system, which reproduces the half complete model depicted in Fig. 3.23, on the modal response. In order to simplify the physic interpretation of the modal analysis, only the longitudinal displacement is left free. The displacements in the transverse and vertical directions are therefore constrained. In other words, the models behave like a *shear beam* along the longitudinal direction.

Firstly, the response of the two soil columns (one without the embankment and another without it) placed side by side and reported in Fig. 4.5-a is evaluated and compared with the that of the soil column with the embankment presented in section 4.1.1; as reported in Table 4.2 the response of the *model A* appears very similar. It is worth noting that the the first three modes of the *model B* (Fig. 4.5-b) are in exact correspondence with the *model A*, but a new mode (the 4^{th} in Fig. 4.6-a) appears with no participating mass. This is a completely symmetric

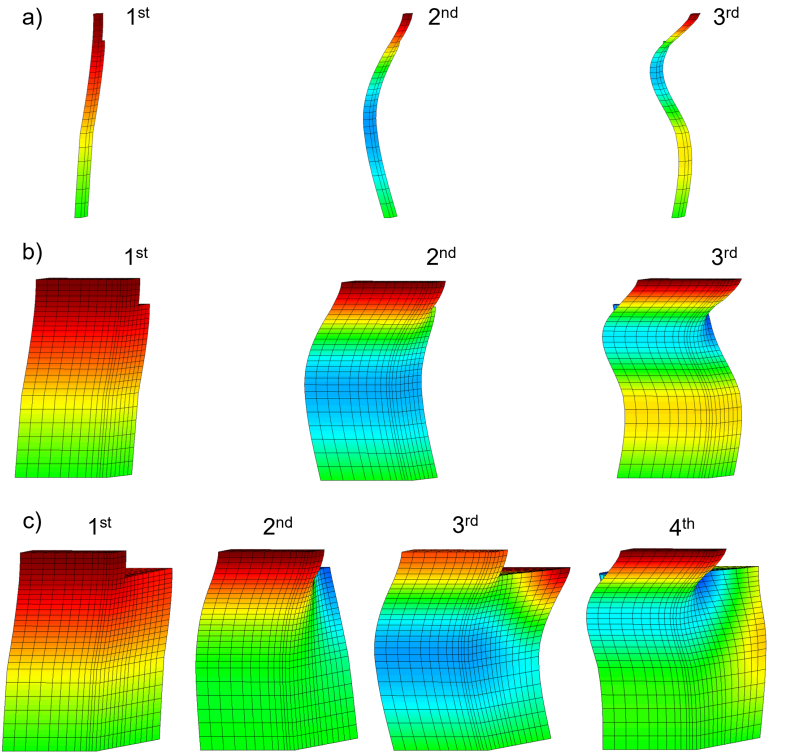

Fig. 4.5. Towards the 3D model: soil column and soil column with embankment placed side by side with a progressive extension of the size of the model; (a) *Model A*, (b) *Model B*, (c) *Model C*.

mode respect to a vertical plane crossing the center of the model. This mode corresponds to the 5^{th} of the *model C* (Fig. 4.6-b). Furthermore, we can see that in the *model C* (Fig. 4.5-c), the 2^{nd} mode of the soil column is split into two modes, while the first mode continues to be substantially the same.

This easy example is very important in order to understand the modal analysis of the full system. In fact, even if the same model is addressed, different results are provided depending on the refinement of the mesh. In details, *Model A* and *model B* share the same geometry ratio in the transverse direction and differ only due to the refinement of the mesh, while *model C* has the same refinement as *model B* but features a larger dimension in the transverse direction. Generally with a more refinement mesh, dummy modes can develop and the understanding of

the phenomenon may become more difficult. Thus, it is important to recognize the principal modes of the system distinguishing from those with no practical interest.

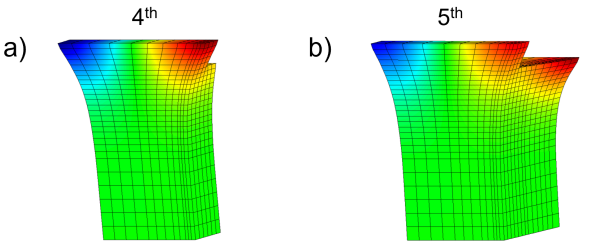

Fig. 4.6. Example of modes with no participant mass.

Tab. 4.2. Towards the 3D model: soil column and soil column with embankment placed side by side with a progressive extension of the size of the model.

	model A			model B			model C		
mode	T (sec)	M_{tot} (%)	M_{emb} (%)	T (sec)	M_{tot} (%)	M_{emb} (%)	T (sec)	M_{tot} (%)	M_{emb} (%)
1	0.60	72.6	29.1	0.60	75.0	29.3	0.57	76	16.2
2	0.24	14.8	28.2	0.25	14.5	28.4	0.30	2.5	16.0
3	0.16	5.2	23.7	0.17	5.6	24.9	0.23	12.9	15.5
4	0.12	2.4	10.3	0.16			0.19	2.9	14.6
5	0.09	1.7	0.2	0.12	2.7	12.8	0.16		
6	0.07	1.2	1.1	0.12			0.16		8.5

4.1.3. Modal longitudinal response

In this section the behaviour of the full system without the structure is studied for both the 2D and the 3D models in the longitudinal direction. In both models, the longitudinal displacement is the only degree of freedom left free; the results are reported in Table 4.3. This procedure can be implemented in OpenSees carrying out the stress tensor for each soil element at the end of the embankment construction, which is built in a later stage than the deposit domain. The small-strain stiffness is defined according to the Eq. 3.6 and constitutes the reference stiffness for the modal analysis.

These results, provided in Table 4.3, can be directly compared to the ones seen in section 4.1.2. In particular in the case of the 2D model (Fig.

4.7-a), the first mode is quite similar to that of *model A* and *B* (Fig. 4.5-a/b), while there are two different modes (T=*0.27 s* and T=*0.21 s*) that correspond to the second mode of the *model A/B*. Similar considerations can be made for the 3D model (Fig. 4.7-b) that may be compared with *model C* of Fig. 4.5-c. Note that for both models there are modes with zero participating mass (Fig. 4.8).

Tab. 4.3. 2D and 3D model without structure: longitudinal direction.

	2D model			3D model		
mode	$T(sec)$	$M_{tot}(\%)$	$M_{emb}(\%)$	$T(sec)$	$M_{tot}(\%)$	$M_{emb}(\%)$
1	0.60	75.0	23.2	0.56	79.0	13.0
2	0.44			0.40		
3	0.27	8.5	22.5	0.30	1.5	12.8
4	0.22			0.28		
5	0.21	8.7	7.1	0.24	0.7	11.5
6	0.17			0.23	10.6	12.5
7	0.16	2.6	18.4	0.21	4.8	11.5
8	0.15			0.20		
9	0.15			0.18		
10	0.14	2.1	15.8	0.18	0.7	10.8
11	0.13			0.18		
12	0.12	1.2	9.2	0.16		
13	0.12			0.16		9.7
14	0.11	0.1	0.1	0.15	0.2	3.2
15	0.11			0.15		

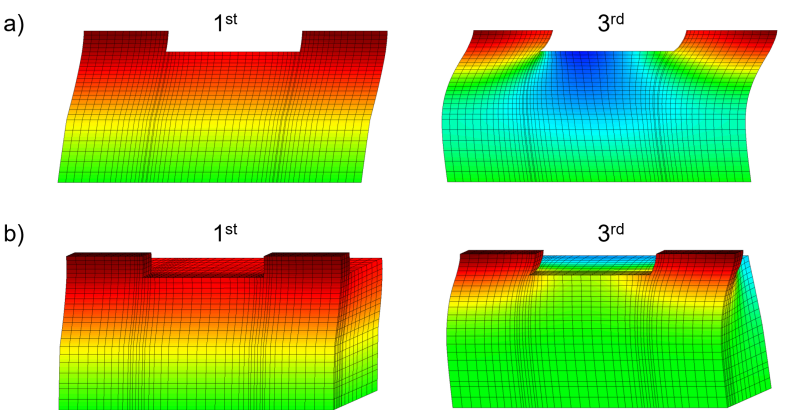

Fig. 4.7. 2D and 3D model without structure: longitudinal direction.

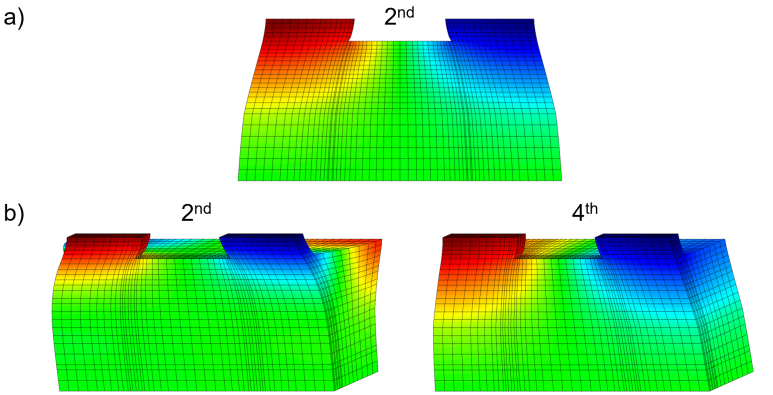

Fig. 4.8. Example of 2D and 3D modes with zero participating mass: longitudinal direction.

When examining the full system considering the soil-structure interaction, some additional expedients for the implementation in OpenSees need to be considered. In fact, the knowledge of the stress tensor for each soil element at the end of the static construction (following the stages discussed in section 3.4) is required. The small-strain stiffness is then defined according to the Eq. 3.6 and it follows the same procedure used for the previous cases. The elastic beam elements presented in section 3.3 are implied for the structure according to a grillage modelling approach for which the definition of the areas of influence is necessary for assigning the mass and the stiffness.

With reference to the boundary conditions, the longitudinal displacement is left free for the entire system: soil and structure nodes. In addition, the rotation of the structural nodes about a transverse axis and the vertical displacement of the deck-nodes are allowed. On the other hand, in modelling the soil-structure contact, it was decided not to employ any rigid link to avoid a potential ill-conditioned stiffness matrix. In their place, constraints of equal displacements (equalDOFs) for the translational degree of freedoms between soil and structural nodes at the same height are chosen.

Table 4.4 reports the modal characteristics of the vibration modes obtained for the 2D and 3D models, indicating the corresponding participating masses of the full system M_{tot}, of the embankment M_{emb} and of the structure M_{str}. The results of the the 2D models are reported in Fig. 4.9. Note that the presence of the structure and the structural continuity between the abutments and the deck makes this problem very similar

Tab. 4.4. 2D and 3D model with soil-structure interaction: longitudinal direction.

	2D model				3D model			
mode	T (sec)	M_{tot} (%)	M_{emb} (%)	M_{str} (%)	T (sec)	M_{tot} (%)	M_{emb} (%)	M_{str} (%)
1	0.62	74.6	29.1	17.8	0.57	78.7	15.0	17.5
2	0.39				0.38			
3	0.28				0.31	2.2	14.8	14.2
4	0.27	10.2	28.3	9.9	0.29			
5	0.22	6.4	0.1	14.5	0.26			
6	0.21				0.24	0.9	13.7	5.3
7	0.19	2.7	0.1	11.4	0.23	8.2	12.7	11
8	0.16				0.21	6.9	13.1	9.1
9	0.16	1.5	13.4	16.6	0.20			
10	0.14	1.7	9.6	1.2	0.19	0.5		12.0
11	0.14				0.18			
12	0.13	1.2	1.5	2.1	0.17			
13	0.12				0.17	0.1	4.6	11.6
14	0.12	0.5	11.1	0.4	0.16		6.3	11.6
15	0.12				0.16			
16	0.11	0.5	2.9	11.2	0.15	0.2	6.8	
17	0.10		0.1	2.4	0.15			
18	0.10	0.6	3.2	1	0.15	0.2	6.4	1.4
19	0.10	0.1	0.5	11.6	0.15		0.9	4.0
20	0.10			0.1	0.14	2.1	5.7	2.2

to the simple soil column which includes the embankment, represented in Fig. 4.4. The modes 1^{st}, 4^{th}, 9^{th}-10^{th} are immediately comparable with the first three modes of the soil column. Being a more complex model, now there are more modes of interest as the 5^{th} and the 7^{th} but, basically the physics of the problem is the same. In fact, the deformation modes for such a system are mainly controlled by the soil response. In addition, it can be seen that except for the first mode that concerns the main mode of the deposit, the next modes are all related to the presence of the embankment. It is evidently that a high participation of the embankment produces much more pronounced flexural deformations in the structure.

The results of the 3D model are reported in Fig. 4.10. As predictable, the response of the system is less intuitive than the 2D model. For example the same mode can show a synchronous or asynchronous movement between the soil behind the bridge (back of the model) and

the soil in contact with the bridge (front of the model). This can produce different modes for a similar structure deformation, as for the case of the modes 6^{th}, 7^{th}, 8^{th}, 10^{th}. Nevertheless for our purposes, the 3D model confirms the importance of the dynamic role of the embankment as well. Fig. 4.11 in turn, shows examples of modes with zero participating mass.

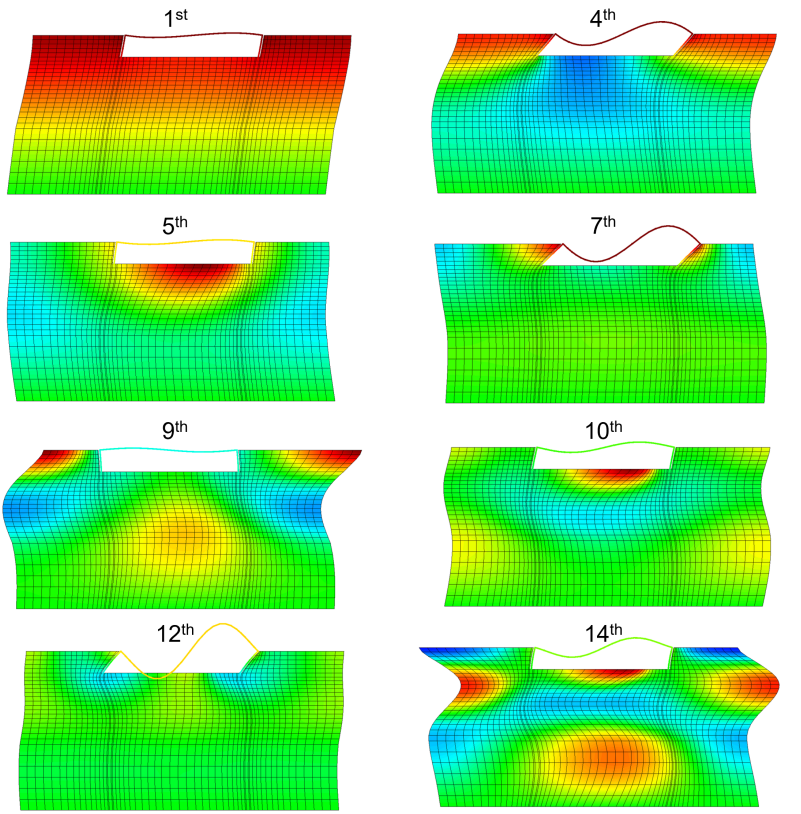

Fig. 4.9. 2D soil-structure interaction: longitudinal direction.

In summary, the information obtained from the modal analysis suggests that the dynamics of the system is correctly analysed whether at least the first two significant modes are considered. These are respectively the 1^{st} and the 4^{th} mode of the 2D model (Fig. 4.9), or alternatively the 1^{st} and the 2^{nd} modes of the soil column which includes the embankment (Fig. 4.4). In fact, it is believed that these modes involve more the flexural behaviour of the structural members.

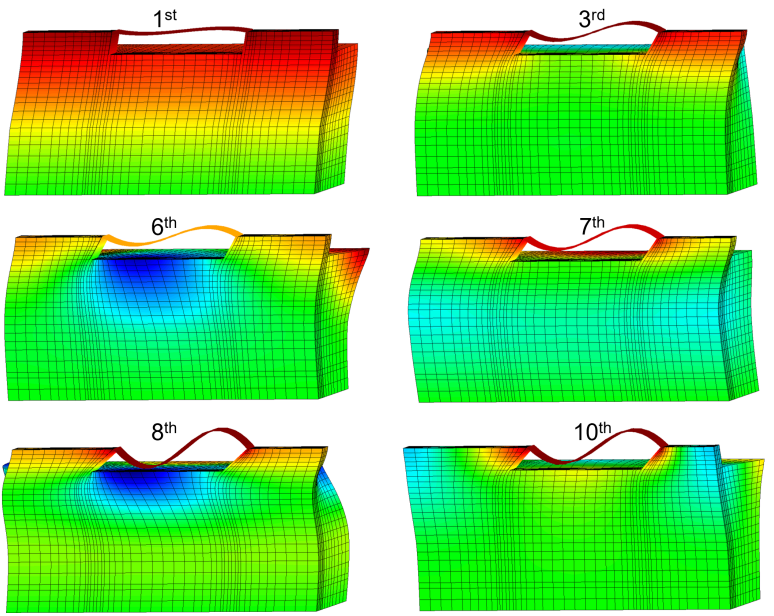

Fig. 4.10. 3D soil-structure interaction: longitudinal direction.

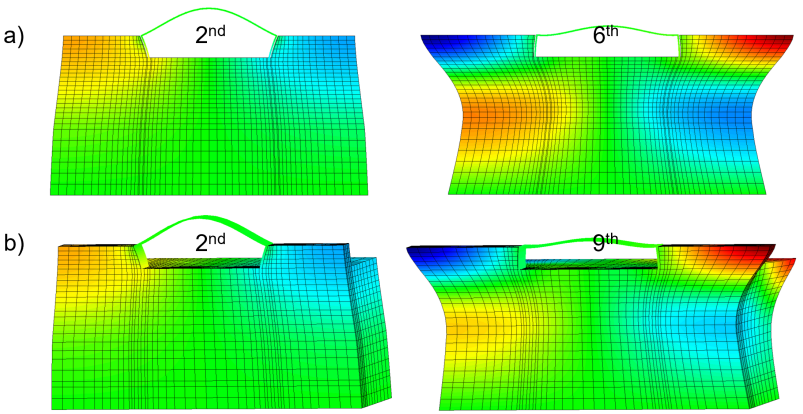

Fig. 4.11. Example of 2D and 3D modes with zero participating mass: longitudinal direction.

4.1.4. Modal transverse response

The behaviour of the system without the structure is investigated in the transverse direction. Now, the transverse displacement of the system is the only DoF left free.

Fig. 4.12 reports the response of the 2D model. Some similarities can be observed between this model and the soil column with the embankment (Fig. 4.4). Also in this case, the presence of the embankment plays a crucial role. A careful observation of the modal shapes shows that the 3^{rd} together with the 4^{th} modes as well as the 6^{th} together with the 7^{th} modes correspond respectively to the 2^{nd} and 3^{rd} modes of the soil column.

Fig. 4.13 shows the response of the 3D model. It can be seen that the 2^{nd} is actually very similar to the first mode on both the front and back sides of the model. Obviously this mode involves deformation along the longitudinal development of the embankment that the 2D model cannot predict. In general, the deformation of the embankment roughly follows the shape of the soil beneath it. Note also that the 6^{th} and the 7^{th} modes are basically very similar.

It is evident that in the transverse direction the embankments plays a significant role as well. In fact, it is involved in all the significant modes affecting the system. Table 4.5 collects the results discussed so far.

Tab. 4.5. 2D and 3D model without structure: transverse direction.

	2D model			3D model		
mode	$T(sec)$	$M_{tot}(\%)$	$M_{emb}(\%)$	$T(sec)$	$M_{tot}(\%)$	$M_{emb}(\%)$
1	0.57	75.7	22.6	0.56	79.5	20.4
2	0.26			0.37	0.3	17.2
3	0.24	10.9	22.0	0.27		
4	0.20	6.8	21.0	0.24	1.8	9.1
5	0.16			0.24		
6	0.14	2.3	16.0	0.24	8.5	17.8
7	0.13	2.0	11.8	0.21	7.0	17.3
8	0.12			0.20		
9	0.11			0.19	0.5	1.9
10	0.11	0.2	4.8	0.18	0.1	1.3

As already done for the analysis in the longitudinal direction, the soil-structure interaction in the transverse direction is investigated. The modelling procedure follows the steps reported in section 4.1.3: briefly,

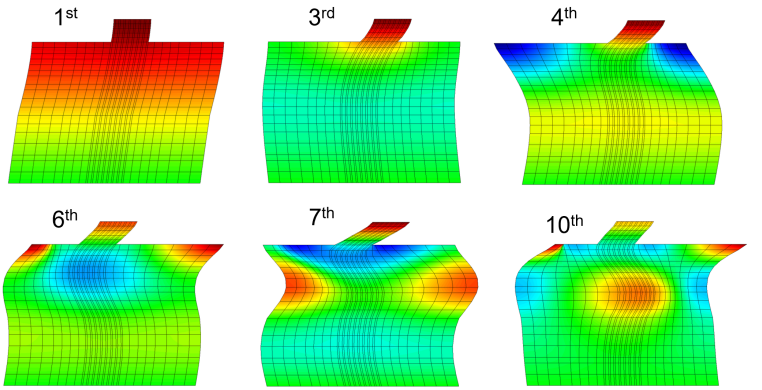

Fig. 4.12. 2D soil model without structure: transverse direction.

the soil-stiffness at small strains is defined after a staged construction while the properties and the mass of each structural node are defined proportional to its area of influence.

The transverse displacement is left free for both the soil and the structure nodes. In addition, the rotation of the structural nodes about an axis parallel to the longitudinal direction of the model as well as the vertical displacement of the deck-nodes are allowed. EqualDoF conditions are used for modelling the soil-structure contact. Finally, the eventual presence of the wing walls, whose modelling is already explained in section 3.2.4, is investigated.

Table 4.6 reports the comparison between the cases with and without the wing walls. The results are substantially the same as also shown in the Fig. 4.14 and in the Fig. 4.15. This result should not surprise, because it derives directly from the initial choice to impede the vertical displacements of the nodes. In this case, therefore, the information obtained from the modal analysis does not allow us to distinguish the behaviour with or without the wing walls. This however goes beyond the reason why these modal analyses were conducted so far; it would have complicated the interpretation significantly because numerous dummy modes would have been generated. Notwithstanding, the modal analysis is still able to provide different deformations (modal shapes) of the soil bridge system in these two cases (Fig. 4.15).

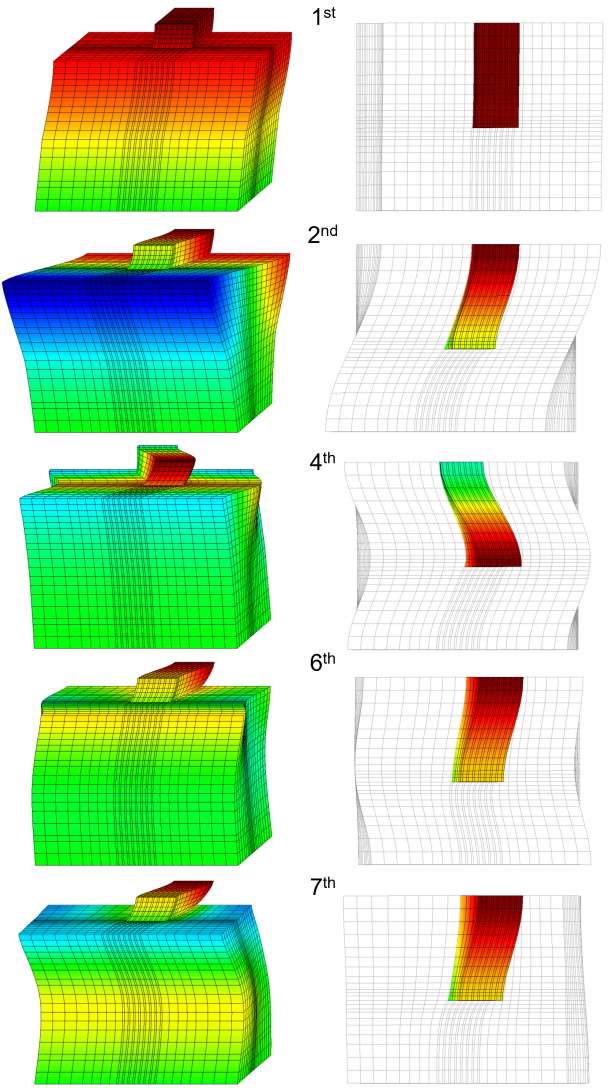

Fig. 4.13. 3D soil model without structure: transverse direction.

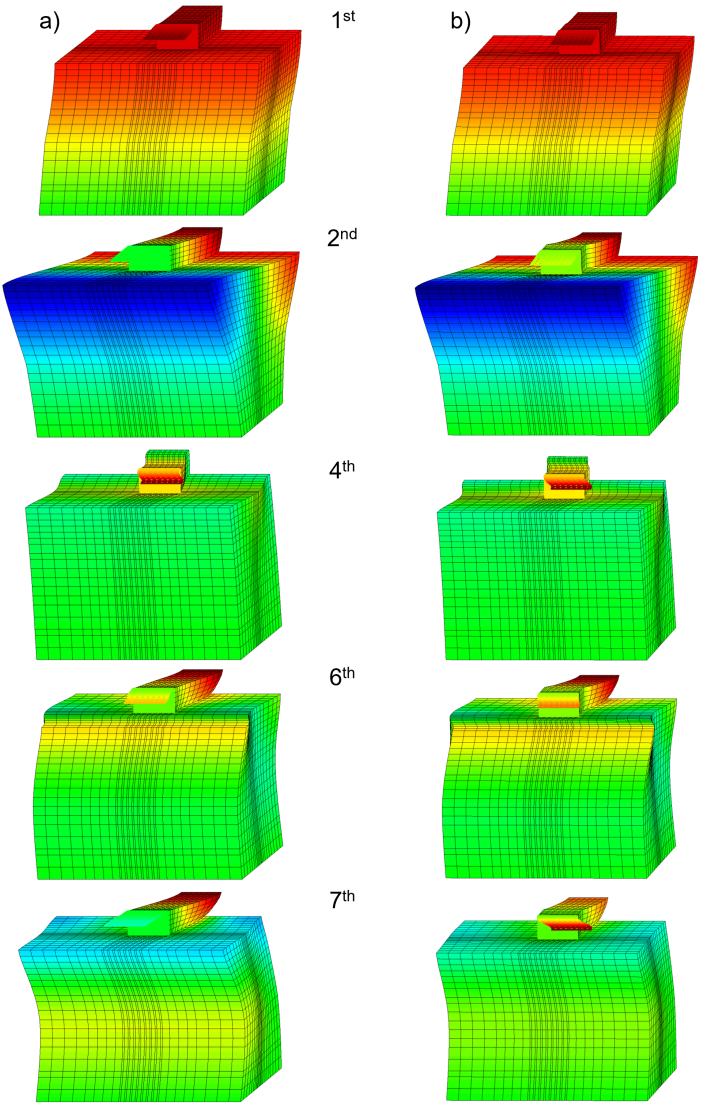

Fig. 4.14. 3D soil-structure interaction (transverse direction): model without (a) and with (b) wing walls.

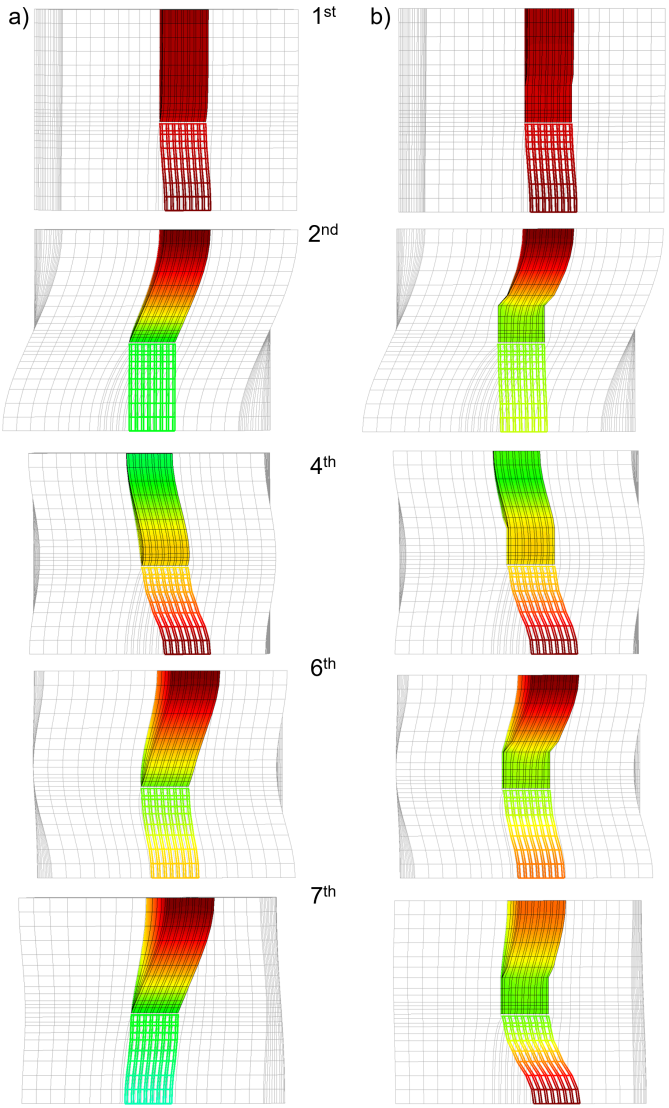

Fig. 4.15. 3D soil-structure interaction (transverse direction and top plan view): model without (a) and with (b) wing walls.

Tab. 4.6. 3D model with soil-structure interaction with and without the wing walls: transverse direction.

	without wingwall				with wingwall			
mode	T (sec)	M_{tot} (%)	M_{emb} (%)	M_{str} (%)	T (sec)	M_{tot} (%)	M_{emb} (%)	M_{str} (%)
1	0.57	77.6	15.8	20.2	0.57	77.6	15.4	19.5
2	0.37	0.2	12.1	11.3	0.37	0.2	11.5	8.1
3	0.27				0.27			
4	0.25	2.2	6.8	14.7	0.25	2.5	7.8	14.1
5	0.24				0.24			
6	0.24	8.4	12.6	8.4	0.23	8.4	11.4	9.0
7	0.21	5.7	11.4	5.1	0.20	6.2	11.3	7.4
8	0.20	1.1	0.8	7.1	0.20	0.2	1.9	6.0
9	0.19				0.19			
10	0.18	0.4	12.1	3.0	0.18	0.3	11.0	2.5

4.2. Seismic demand

In this section, two site-specific ground motions compatible with the seismic demand for the site of the bridge are defined. The idealised bridge is located along the A14 Adriatic highway close to Gatteo, a small town in the Emilia Romagna region.

In details, the seismic demand is evaluated with a *semi-direct* approach essentially in accordance with Italian technical provisions (Italian Building Code 2018) in which four limit states must be taken into account under seismic conditions: two serviceability limit states and two ultimate limit states. A probability of exceedance P_R is associated with each limit state. In order to investigate the response of the system when the soil exhibits a pronounced nonlinear response, the focus of the present study is on the last ultimate limit state, namely the No-Collapse Earthquake (NCE) with ($P_R = 5\%$). Being an infrastructure of a certain importance, a design life T_L of 100 years can be considered. Hence, for a given P_R and T_L, the seismic hazard (Table 4.7) can be expressed in terms of return period T_R according to the Poisson's model:

$$T_R = \frac{-T_L}{\ln(1 - P_R)} \tag{4.5}$$

Tab. 4.7. Case study seismic hazard.

T_L $(years)$	P_R $(\%)$	T_R $(years)$
100	5	1950

It is also common to see seismic hazard defined in terms of P_R and T_L or in terms of T_R, or both. Finally once the location has been defined, the site http://esse1-gis.mi.ingv.it/ (Stucchi et al. 2011) provides uniform hazard spectra associated with different probabilities of exceedance P_R (or equivalently return periods T_R). For each value of P_R, the seismic hazard model defines the median estimated spectrum ($50th$ percentile) and its uncertainty, expressed as the spectra corresponding to the $16th$ and $84th$ percentile. Then, according to the Italian technical provisions (Italian Building Code 2018), the spectrum referring to the $50th$ percentile constitutes the design motion on a stiff outcrop (soil category A). In this logic, the site effects are evaluated through dynamic analyses that simulate explicitly the propagation of the seismic waves through the foundation soil. However, this approach has been previously defined

semi-direct because, unlike the direct approach, the seismic records were not selected to follow the design spectrum.

Focusing mainly on the longitudinal response as the one significantly affected by dynamic soil-structure interaction (Elgamal et al. 2008, Gorini and Callisto 2020, Gorini et al. 2020a), the modal analysis of the full system showed basically two significant modes that cause the major internal forces in the structure. The idea here is to look for two mono-frequency ground motions that can independently excite the correspondent modes according to an approximate procedure respectful of the seismicity of the site. As a consequence, the only information carried out from the seismic hazard study was a representative value of the Peak Ground Acceleration PGA (Fig. 4.16-a).

Considering that one of the two modes (see Table 4.4) is at low frequencies (about 1.7 Hz) while the other at high frequencies (about $3-4$ Hz), it is intuitive to think that the former can be associated with ground motions at a greater distance than the latter. In order to maintain a rigorous approach, the attenuation model of Sabetta and Pugliese (1987) has been employed to carry out the magnitude-distance pairs required for searching, selecting and downloading ground motion data from the web-based Pacific Earthquake Engineering Research Center (https://ngawest2.berkeley.edu/). The Sabetta-Pugliese empirical predictive equation is based on a regression of the Italian database containing 95 accelerograms from 17 earthquakes of magnitude 4.6 to 6.8:

$$\log(PGA) = -1.562 + 0.306 \cdot M - \log(\sqrt{R + 5.8^2}) \qquad (4.6)$$

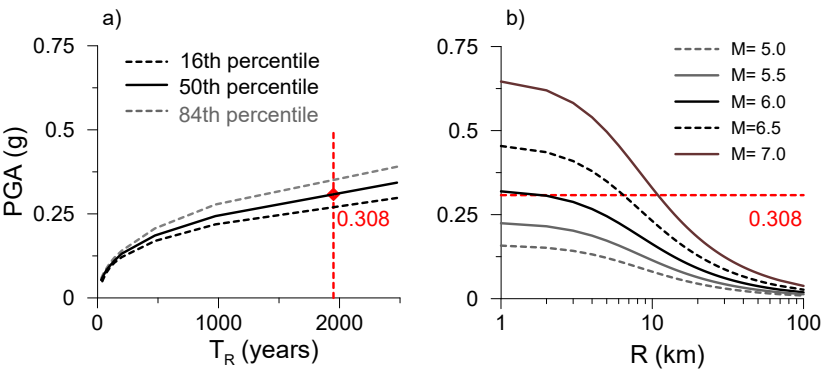

Fig. 4.16. (a) PGA hazard curve; (b) Sabetta-Pugliese attenuation model (1987).

The pairs magnitude-distance corresponding to PGA 0.308 g ($T_R = 1950$) are respectively: $M = 6.0$ and $R < 5$ km for the high-frequency, and $M = 6.5 \div 7.0$ and $R > 10$ km for the low-frequency ground motion (Fig. 4.16-b). Accordingly, two seismic records were selected as representative of the seismic demand, relative to the events reported in Table 4.8. The average shear wave velocity $V_{S,30}$ in the first 30 m of depth at the station location is entirely compatible with the bedrock velocity of the site ($V = 700 m/s$); moreover, Mw is the moment magnitude and R_{JB} the Joyner-Boore distance.

Tab. 4.8. Properties of the seismic records selected to represent the NCE limit state.

Event	*Record*	$V_{S,30}$	R_{JB}	Mw
Parkfield (US, 2004)	RSN 4064	656.8	4.25	6.0
Yamakoshi (Japan, 2007)	RSN 4868	655.5	22.23	6.8

Because of the main scope of this work is to study the seismic behaviour of the full soil-bridge model, both the ground motion plane-directions were considered. Actually in such 3D models, could be very interesting to consider the vertical component of the motion as well. However, the study of the latter component needs further validation that is beyond the scope of the work. Therefore, the seismic performance of the model is first evaluated separately in longitudinal and transverse direction, and finally, both the components are applied simultaneously. This requires firstly, the search for the minimum correlation between the two components of the motion and subsequently, the search for the maximum correlation. This procedure follows the *theory of the earthquake intensity tensor* proposed by Arias (1996). Briefly, the main underlying assumption at the basis, is the idea that earthquake intensity, conceived as the capacity of ground motion to produce damage, can be represented by the amount of energy dissipated in the production of permanent effects on the structures belonging to some representative set. According to the original definition, earthquake intensity at a point 0 is a tensor quantity represented by the matrix:

$$\begin{bmatrix} \mathbf{I_{11}} & \mathbf{I_{12}} \\ \mathbf{I_{21}} & \mathbf{I_{22}} \end{bmatrix} \tag{4.7}$$

whose elements are given by:

$$I_{ij} = \frac{\pi}{2g} \cdot \int_0^{t_0} a_i(t) \cdot a_j(t) \quad dt, \qquad i,j = 1,2 \tag{4.8}$$

here $a_i(t)$, for $i = 1,2$ are the components of accelerations recorded at 0 in the directions of the axes of a rectangular system of coordinate $0xy$, t is time, and t_0 is the total duration of the record. The diagonal terms I_{11} and I_{22} are the intensities at 0 in the 1-,2- axis, respectively. In general, the intensity at 0 in the direction of the unit vector $\bar{e}$ is given by the product $\bar{e}^T \cdot \bar{I} \cdot \bar{e}$, where the superscript T denote transpose. Therefore, the intensity at 0 contains all the information necessary to determine the intensity in any direction through 0.

It is always possible to diagonalise the intensity matrix by a suitable rotation of the coordinate axes, leaving 0 fixed. This transformation is essentially unique. When the motion is referred to the principal axes of ground acceleration, the variance terms (diagonal terms) have stationary values, whereas the cross-variance terms (off-diagonal terms) become equal to zero. This means that the components of accelerations along the principal axes are uncorrelated.

All the procedure is easily explained looking at the Fig. 4.17 whereby the directions of maximum correlation and uncorrelation (minimum correlation) are defined for both the ground motions. Finally, the properties of the ground motions with the minimum correlation are reported in Table 4.9 and the corresponding spectra are depicted in Fig. 4.18. Conversely, the properties of the ground motions with the maximum correlation are reported in Table 4.10 and the corresponding spectra are depicted in Fig. 4.19.

In particular PGA is the peak ground motion, I_A is the Arias intensity (Arias 1970), T_s is the significant duration between 5% and 95% of the Arias intensity (Bommer and Martinez-Pereira 1999), and T_m is the mean quadratic period (Rathje et al. 1998).

Summarising, these two ground motions were specifically chosen to excite the fundamental modes of the system following the so-called *semi-direct approach* herein discussed. Even though this approach is not totally *rigorous*, it should be remarked that the goal is simply finalised to study the actual behavior of the system during dynamic analyses adopting two *representative* mono-frequency seismic input-motions. Nonetheless, at a later time, many other ground motions will be selected according to a *classical approach*, i.e. reproducing in the average the elastic spectrum provided by the technical codes for a stiff soil (rock). These records will

be presented in the following of the discussion and will be employed to validate the results provided by the simplified procedures presented in the next chapters.

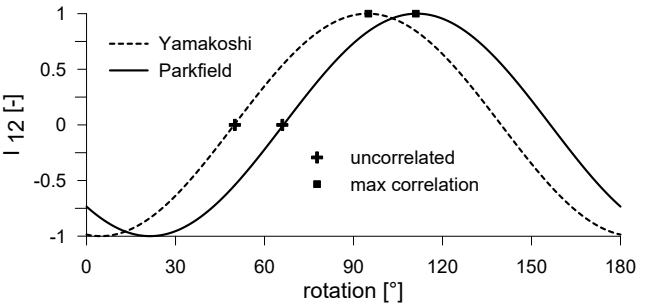

Fig. 4.17. Variation of the normalized off-diagonal elements of Arias intensity tensor with the rotation of the coordinate axes.

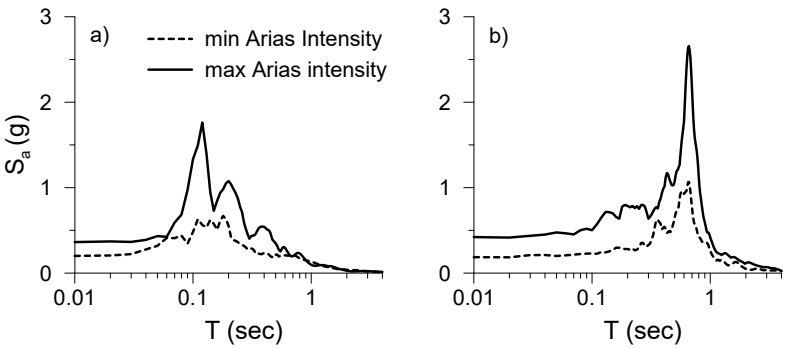

Fig. 4.18. 5%-damped elastic response spectra for (a) Parkfield and (b) Yamakoshi. The correlation between the two directions is minimum.

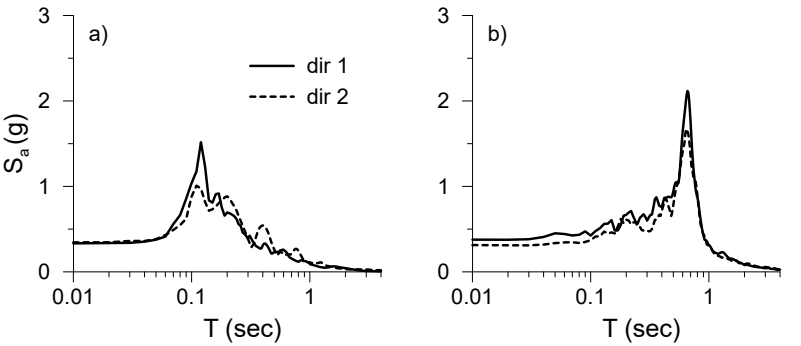

Fig. 4.19. 5%-damped elastic response spectra for (a) Parkfield and (b) Yamakoshi. The correlation between the two directions is maximum.

Tab. 4.9. Properties of the uncorrelated directions.

Event	$PGA(g)$	$I_A(m/s)$	$T_m(s)$	$T_s(s)$
Parkfield	0.36	0.79	0.23	4.9
Yamakoshi	0.42	4.12	0.66	13.6

Tab. 4.10. Properties of the max correlated directions.

Event	*direction*	$PGA(g)$	$I_A(m/s)$	$T_m(s)$	$T_s(s)$
Parkfield	1	0.33	0.53	0.23	5.77
	2	0.35	0.53	0.27	5.10
Yamakoshi	1	0.37	2.82	0.65	15.03
	2	0.31	2.80	0.66	14.54

4.3. Site response analysis

As a first evaluation of the dynamic response of the soil domain, the one-dimensional site response is investigated. A three-dimensional soil column was implemented in OpenSees, representing the soil deposit with and without the embankment (see Fig. 4.1). As it will be shown in the next chapters, the soil column with the embankment is of crucial importance to take into account the dynamics of the overall system. The PDMY model was used to model the soil behaviour, according to the calibration described in Section 3.1.2, whereas the soil domain was discretised through the SSPbrick elements available in the OpenSees library.

A first gravity analysis recreated the lithostatic stress state in soil, which is allowed to settle under its self weight. In a second stage, periodic constraints in the global x- and y-directions were assigned to the nodes at the same depth. A Lysmer and Kuhlemeyer (1969) dashpot was utilized to account for the finite rigidity of an underlying elastic medium, and the loading was applied in a manner consistent with that proposed by Joyner and Chen (1975).

The one-dimensional site response analyses is carried out on the soil column without the embankment and performed with the most severe seismic scenario corresponding to the ground motions of Table 4.9. For brevity, the focus is mainly on Yamakoshi and the results of Parkfield are only briefly reported.

Fig. 4.20 shows the 5%-damped elastic response spectra obtained through a seismic response analysis in correspondence of two different depths. It is clear that amplification begins to be important only in the first few meters of deposit. A further comparison between the response at these two depths is reported in Fig. 4.21 in terms of $\gamma - \tau$ cycles evaluated in correspondence of the Gauss points. We can observe the same cyclic behaviour observed at the level of the single element discussed in Section 3.1.2. The study of these cycles, allows to define the profile of the maximum values of the shear strain γ with depth. Fig. 4.22-b reports a satisfactory comparison of this profile with that obtained carrying out a visco-elastic analysis with MARTA. In MARTA, the behaviour of each layer is completely described by the mass density ρ_s, the shear modulus G_0 at small strains and by the evolution curves of the normalised shear modulus G/G_0 and the damping ratio ξ with the level of shear strain attained. The profile of G_0 follows the profile chosen

in OpenSees (Fig. 3.18) while the shear modulus decay and the variation of the damping ratio reported in Fig. 4.23 were carried out from the PDMY calibration considering a representative mean effective stress p' for each layer. Moreover, Fig. 4.22-a reports the excellent overlap of the spectra obtained with MARTA and OpenSees in correspondence of the top of the soil column.

Fig. 4.24 shows the results of Parkfield record. Since this scenario is less intense, the differences are even smaller. Finally, Fig. 4.25 shows the spectra evaluated at the top of the soil column with embankment for both ground motions.

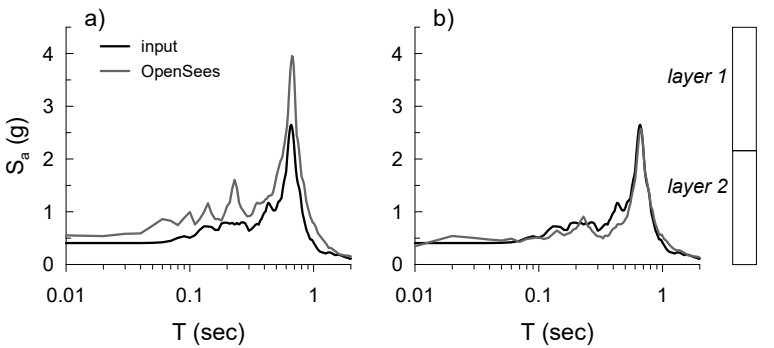

Fig. 4.20. Yamakoshi record: 5%-damped elastic response spectra at different values of depth: (a) z=0 m; (b) z=-15 m.

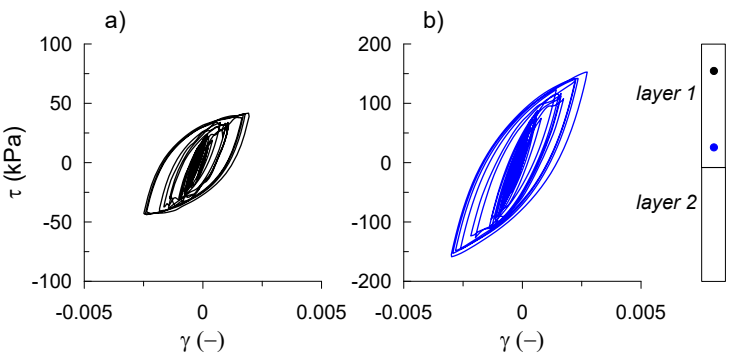

Fig. 4.21. Yamakoshi record: $\gamma - \tau$ cycles for two Gauss points placed at different depths: (a) z=-4.9 m; (b) z=-21 m.

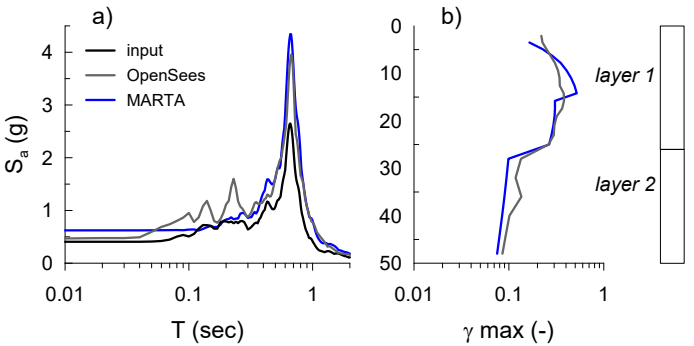

Fig. 4.22. Yamakoshi record: (a) 5%-damped elastic response spectra at z=0 m ; (b) profile of the maximum values of strain γ with depth.

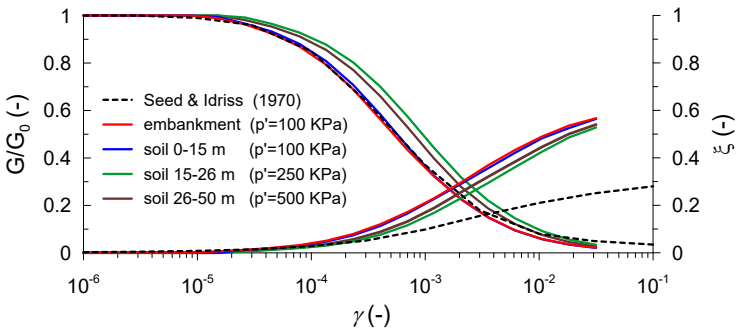

Fig. 4.23. Shear modulus reduction and damping ratio curves carried out from the PDMY calibration.

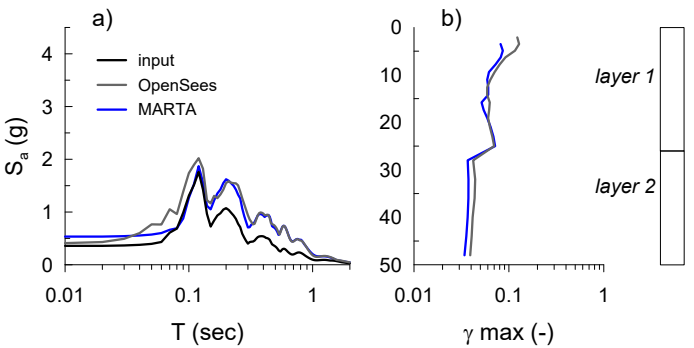

Fig. 4.24. Parkfield record: (a) 5%-damped elastic response spectra at z= 0m ; (b) profile of the maximum values of strain γ with depth.

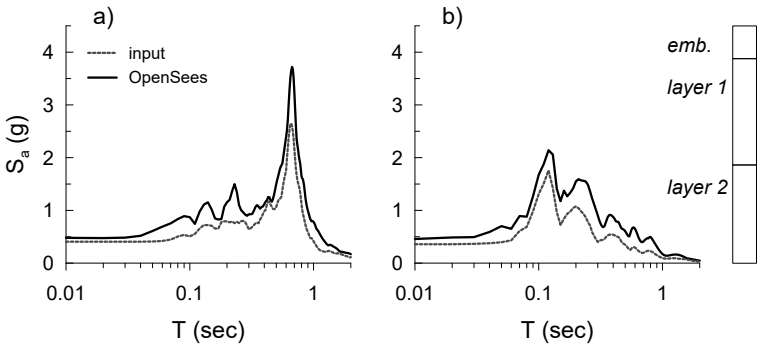

Fig. 4.25. 5%-damped elastic response spectra at the top of the soil column with embankment for (a) Yamakoshi and (b) Parkfield.

4.3.1. Two-directional analysis on the 3D soil column

Site response analyses of the 3D soil column without embankment and depicted in Fig. 4.1 were performed in order to have some preliminary information about the effects induced by a two-directional motion. With the aim of having a comparable response in longitudinal and transverse direction, ground motions with the maximum correlation reported in Table. 4.10 were used. The motion was applied in the horizontal plane *xy* at the base of the soil column. In particular, the *direction 1* and *direction 2* of Table 4.10 are applied respectively along the x- and y-directions (see Fig. 4.1).

In order to show the effects of the bidirectional motion, Fig. 4.26-a reports, for the Yamakoshi ground motion (Table 4.10), a comparison between the 5%-damped elastic spectra evaluated at the top of the column in both the monodirectional and the bidirectional analyses along the first direction, while Fig. 4.26-b, represents the same comparison along the second direction. First and second directions of the soil column correspond respectively to the longitudinal and transverse direction of the full 3D model employed for the analyses described in Chapter 6 and 7. It can be noted that the spectra of the one-directional analyses are slightly higher due to the greater non linear effects developed during the bidirectional analyses.

The same analyses, performed for Parkfield record (Table 4.10), are reported in Fig. 4.27. In this case however, due to the lower intensity, the spectra show a smaller the difference between the one-directional and two-directional analyses.

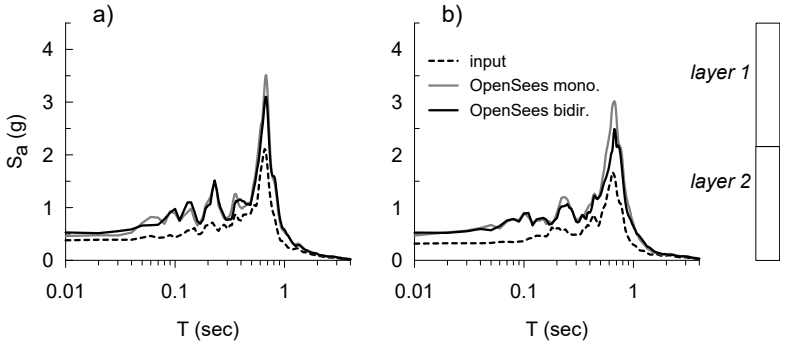

Fig. 4.26. Yamakoshi record: site response analysis of the soil column considering a one-directional and two-directional motion; (a) first and (b) second direction.

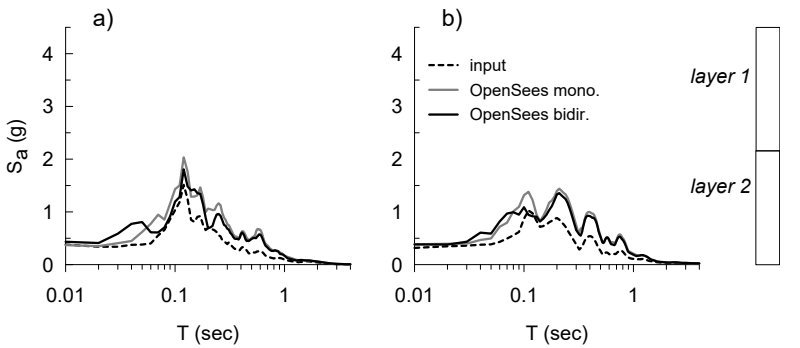

Fig. 4.27. Parkfield record: site response analysis of the soil column considering a one-directional and two-directional motion; (a) first and (b) second direction.

4.4. Some considerations about the numerical model

In order to have consistent results in the dynamic analyses, some checks are addressed in this section. Dealing with soil-structure interaction problems for bridge abutments, Gorini (2019) suggested a minimum distance of the lateral vertical boundaries equal to 4 times the height of the embankment. In addition, preliminary modal analysis (herein omitted for sake of brevity) with a double distance (8 times the height of the embankment), showed completely similar results in terms of shapes, periods and participating masses.

In this section, the accuracy of the mesh discretization in the vertical longitudinal plane, as well as the transverse distance of the lateral boundaries in the 3D model, are examined in depth. In both cases, the input motion is applied along the longitudinal direction.

Finally, the volumetric behaviour of the PDMY model is investigated.

4.4.1. Checking the accuracy of the mesh

The mesh discretization in the vertical longitudinal plane used for the *half 3D* and *2D* models reflects the mesh used to describe the full 3D soil-bridge model. The mesh refinement is then constrained by the number of degrees of freedom of the full 3D model for which time demanding analyses are expected. With the aim of investigating the accuracy of the mesh, a further 2D model, depicted in Fig. 4.28, was developed. This model consists of about 11000 brick elements and 600 beam elements. The detail of the enhanced mesh in correspondence of the abutment system is illustrated in Fig. 4.29-a while the target mesh is reported in Fig. 4.29-b.

Fig. 4.30 reports the comparison between the time histories of the bending moment evaluated in both the enhanced and the target mesh for some scrutiny points: in details, the pile heads and the abutment-deck nodes. Moreover, Fig. 4.31 provides the bending moment distributions in the piles for different instants of interest. The direct comparison between the target and the enhanced mesh, shows that from a practical and design standpoint, the target mesh is sufficiently accurate to describe the overall behaviour of the system.

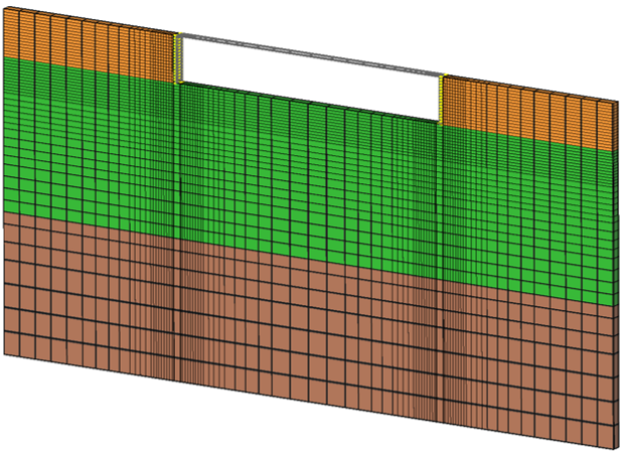

Fig. 4.28. Refined mesh considered for the 2D model.

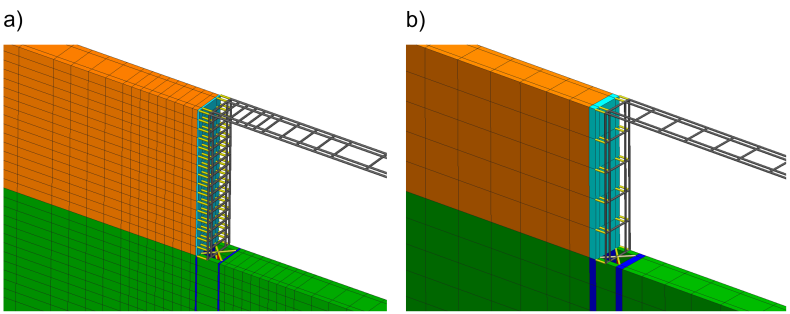

Fig. 4.29. Detail of the enhanced (a) and of the target mesh (b).

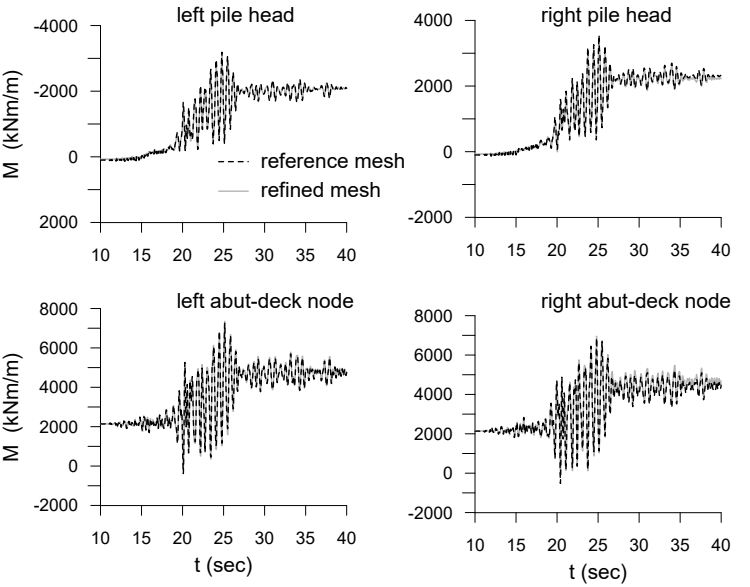

Fig. 4.30. Yamakoshi record: comparison between the time histories of the bending moment evaluated in the enhanced and the target mesh in some scrutiny points.

4.4.2. Checking the distance of the transverse boundaries in the 3D model

The distance of the transverse boundaries in the 3D model (Fig. 3.16) is now investigated; indeed, reflection waves can be generated and could be affect the soil-structure interaction problem. A distance of 68 m (and then 34 m in the half 3D model depicted in Fig. 3.26) was considered remote enough from the system. Even though the motion is applied only in the longitudinal direction, the discontinuity created by the presence of both the embankment and the bridge could generate waves that are not parallel to the direction of the motion, which, in turn, could be reflected at the transverse lateral boundaries. However, the effects of these waves become weaker as the transverse distance increases due to combined effect of greater dissipation exerted by the hysteretic soil-damping and the absorbing base boundary.

A further half 3D model, depicted in Fig. 4.32 was then considered where the lateral distance of the back transverse boundary has been doubled (70 m). In the current half 3D model the same boundary conditions of the half 3D model described in section 3.3.2 are applied.

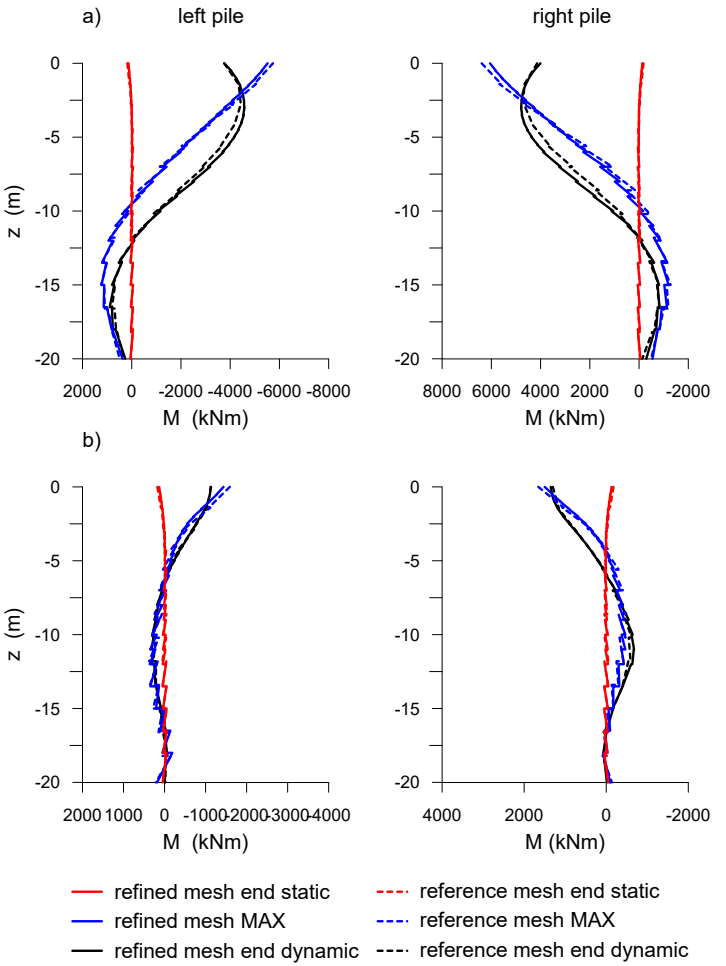

Fig. 4.31. Comparison between the spatial distributions of the bending moment in the piles evaluated in the enhanced and in the target mesh; (a) Yamakoshi, (b) Parkfield ground motions.

In order to run the analyses on the 3D full model in a reasonable time, the ground motions of Table 4.9 have been appropriately shortened on the basis of the significant duration T_s (based on the Arias intensity Arias (1970)). Furthermore, after applying the baseline correction, it was verified that the response of the system was approximately the same as that of the original ground motions.

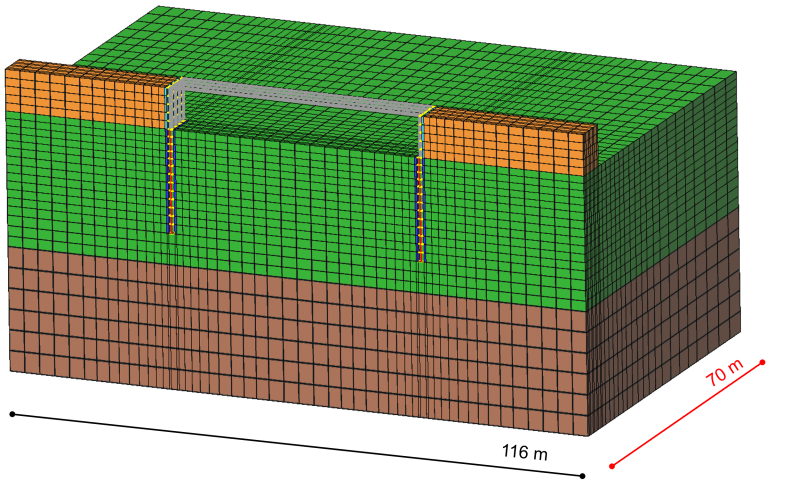

Fig. 4.32. Half 3D model with farther boundary.

The time histories of the bending moment are evaluated in correspondence of the pile heads and of the deck-abutment nodes for the three models examined: the target full 3D model, the target half 3D model and the current half 3D model with farther back boundary. Fig. 4.33 shows that the three models produce very similar response suggesting that the lateral distance chosen for the target half 3D model (34 m and then 68 m for the target full 3D model) was far enough from the structural system.

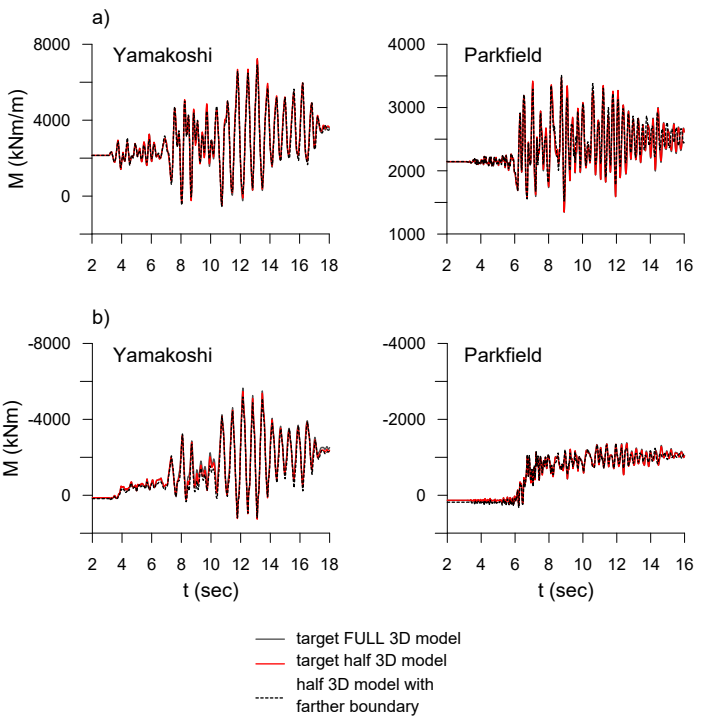

Fig. 4.33. Comparison of the bending moment time histories between the target full 3D model, the target half 3D model and the half 3D model with farther back boundary; (a) deck-abutment node, (b) pile head.

4.4.3. Volumetric-deviatoric coupling

As a last observation on the numerical modeling, it is important to dwell on the effects of the volumetric-deviatoric coupling of the PDMY model. Despite the efforts of calibrations aimed at obtaining a set of parameters that reproduces the typical hydro-mechanical coupling response of gravelly-sand soils, this model tends to excessively overestimate the volumetric deformations induced by the deviatoric component.

This behavior is even observable at the level of the seismic response analysis of the soil column reported in Fig. 4.34-a. Looking at the profile of the vertical displacements of the column at the end of the earthquake, it is possible to observe a generalised subsidence of the entire deposit. In this regard, Fig. 4.34-b shows the evolution of the vertical displacements of two points placed respectively at the top of the embankment and at the bottom of the pile foundation. This effect is obviously accentuated as the number of cycles and the intensity of the earthquake increase. Therefore, the results carried out with Yamakoshi represent an extreme case.

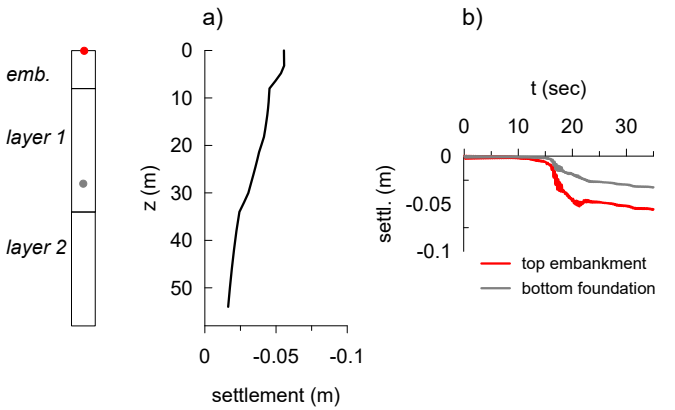

Fig. 4.34. Yamakoshi record: (a) profile of the permanent vertical displacement obtained in the soil column; (b) time histories of the vertical displacements at two different depths.

The same phenomenon is present in the numerical model that describes the soil-structure interaction. Fig. 4.35 shows the contour of the permanent vertical displacements evaluated with the Yamakoshi record in the 2D soil-bridge model. The same values obtained from the analysis of the column can be observed at the edges of the model (about 5 cm) where free field conditions have been imposed. These values are even greater in correspondence of the structure, as a consequence of the kine-

matic and inertial effects of the soil-structure interaction. However, it is noted that they are quite uniform along the structure and therefore not such as to condition the distribution of the internal forces. Nonetheless, these effects should be taken into account in the definition of the axial forces in the piles which may be influenced by such settlements. This is the main reason why in chapter 6 and 7 the rocking moment at the bottom of the abutment, induced by the transverse component of the seismic motion, is used to characterize the *strut and tie* effect in the pile foundation rather than the mere axial forces in the piles.

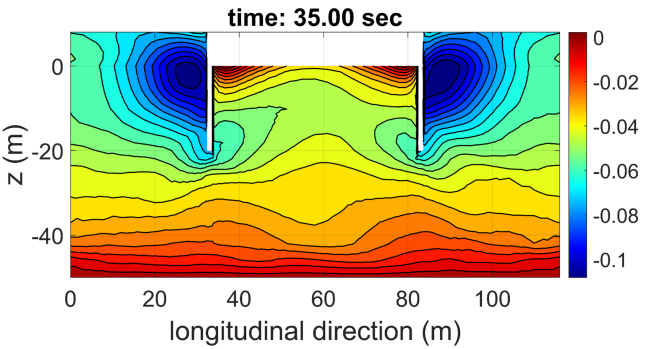

Fig. 4.35. Yamakoshi record - 2D soil-bridge model: contour of the permanent vertical displacement (in meters).

5. Seismic behaviour in longitudinal direction

This chapter provides a contribution to the interpretation of the seismic behaviour of a single-span integral bridge in the longitudinal direction that, typically, is the direction that dominates the design. With the aid of the modal analysis discussed in the previous chapter, a simplified design procedure, aimed at evaluating the deformation and the internal forces in the structure, is developed. This design procedure is based on the well-established *capacity spectrum method* and can be conceived as an extension of the nonlinear static analysis applied to geotechnical systems. Finally, the proposed method is validated against the results of several time-domain dynamic analyses on the global numerical models.

5.1. Seismic behaviour of the integral abutment bridge

After the construction stages illustrated in section 3.4, time-domain dynamic analyses were carried out on the *half 3D* and *2D* models in the manner described in section 3.3.

As the 2D model was seen to provide similar results as the 3D model, it was taken as reference for the discussion of the results of this section. However, a direct comparison between 2D and 3D model will be provided at the end of the chapter. Significant increases of the bending moment are obtained at the deck-abutment contact and at the pile head, which constitute therefore the critical locations to consider for a direct assessment of the seismic performance. The bending moment at the deck-abutment node elongates the top fibers of the deck and the internal fibers of the abutment. Conversely, at the top of the piles, the bending moment elongates the external fibers (away from the embankment). It is paramount to note that the internal forces in the structure at the end

of the dynamic analysis can also be much greater than the static ones especially for the pile foundations.

These observations are also confirmed by the bending moment distributions in the piles of the corresponding half 3D model reported in Fig. 5.2 for the Yamakoshi input motion. Moreover, the external piles (No.4 for the left abutment and No.8 for the right abutment) are always the most loaded, because these are the piles that exhibit the stiffer response as a consequence of three-dimensional effects.

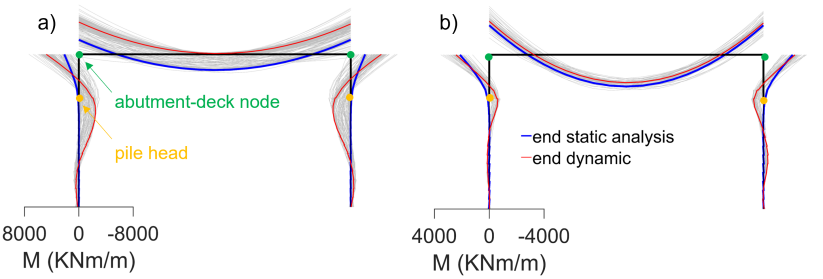

Fig. 5.1. 2D model: critical locations for a direct assessment of the seismic performance: (a) Yamakoshi; (b) Parkfield.

The final deformed configuration of the structure for both the ground motions is showed in Fig. 5.3. The pile-abutment system moves inward, away from the embankment, as a consequence of the increase of the soil pressure behind the abutments. The longitudinal displacement contours of the soil at the end of the dynamic analyses, depicted in Fig. 5.4, confirm this behaviour as well.

Fig. 5.5 and Fig. 5.6 report, for both records, the bending moment distributions in the structure in the instants when the maximum bending moment is reached respectively for: left and right pile head and, left and right abutment-deck node. As already showed in Fig. 5.1, the bending moment at the deck-abutment node elongates the top fibers of the deck and the internal fibers of the abutment while, at the top of the piles, the bending moment elongates the external fibers. Note that when a large value of the bending moment is reached in the left pile head, a large value in the right abutment-deck node is reached as well and vice versa. Same considerations can be made for both the right pile head and left abutment-deck node. This behaviour was observed for both records, characterised on purpose by different frequency contents as described in section 4.2. These asymmetric distributions appear related to the modes

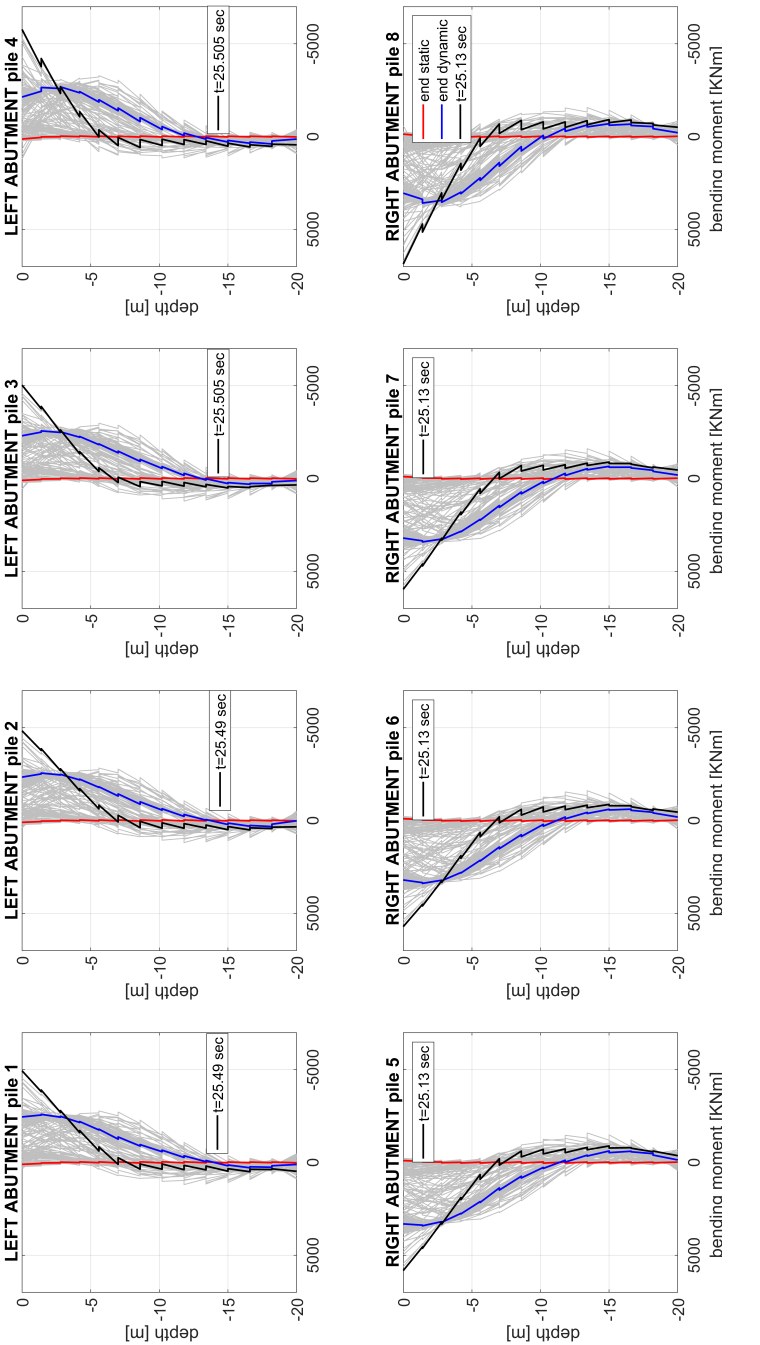

Fig. 5.2. 3D model: distributions of bending moment in the piles during the Yamakoshi record.

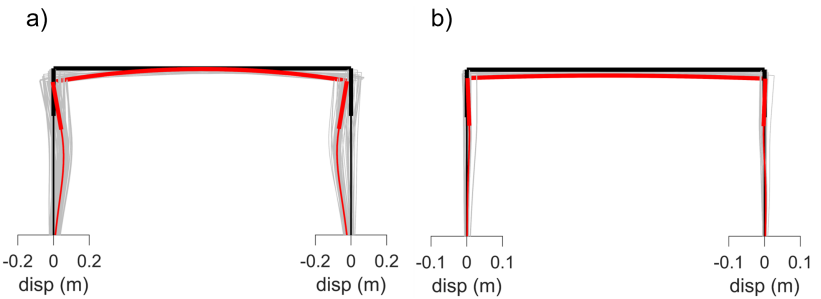

Fig. 5.3. 2D model: structural configurations at the end of the dynamic analysis; (a) Yamakoshi, (b) Parkfield.

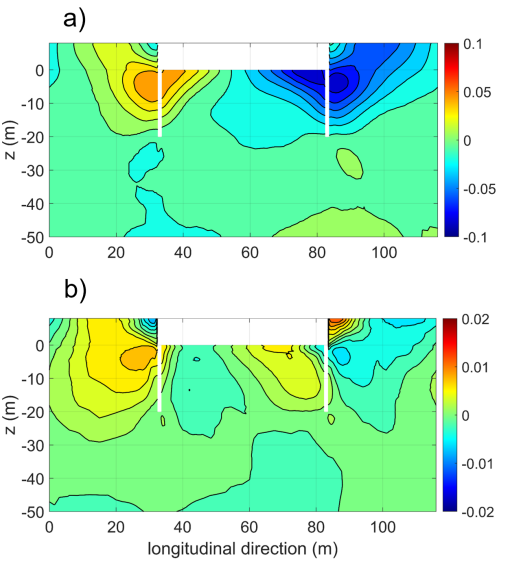

Fig. 5.4. 2D model: longitudinal displacement contours (in meters) of the soil at the end of the dynamic analyses; (a) Yamakoshi, (b) Parkfield.

that produce the most pronounced flexural behaviour in the structure (see section 4.1.3).

This interpretation can be further validated by observing the deformations of the structure (Fig. 5.7 and Fig.5.8) in the instants when the maximum bending moment is reached in the scrutiny points. In all cases indeed, the maximum bending moments are reached in correspondence of asymmetric deformation patterns.

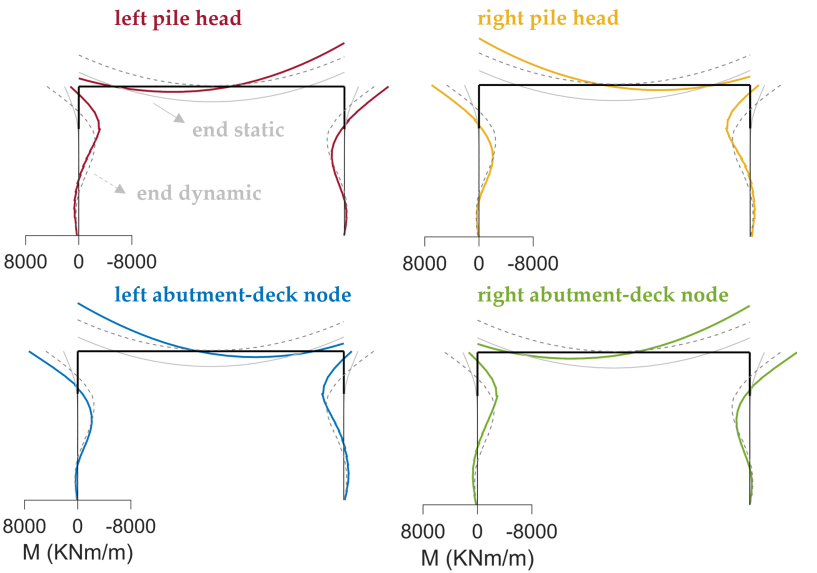

Fig. 5.5. 2D model - Yamakoshi record: bending moment distributions in the structure in the instants when the maximum value is reached for each considered scrutiny point.

5.2. Validation of the response obtained from the modal analysis

The previous section has shown the salient aspects of the dynamic analysis for the integral abutment bridge herein examined highlighting the deformation shapes that produce the paramount internal forces in the structure. In this section, the effects of the main modes affecting the dynamic soil-structure interaction are quantified. Fig. 5.9 reports the normalised frequency contents of both ground motions considered, distinguishing between the input signal and the response of the site response analysis evaluated at the top of the embankment. As already

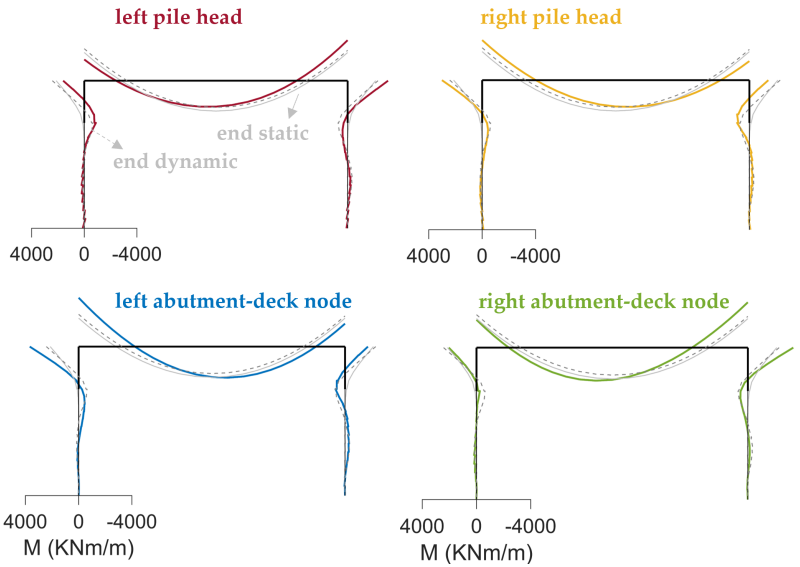

Fig. 5.6. 2D model - Parkfield record: bending moment distributions in the structure in the instants when the maximum value is reached for each considered scrutiny point.

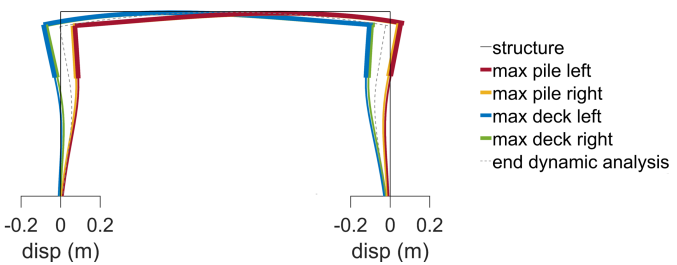

Fig. 5.7. 2D model - Yamakoshi record: structure deformation in the instants when the maximum value is reached for each considered scrutiny point.

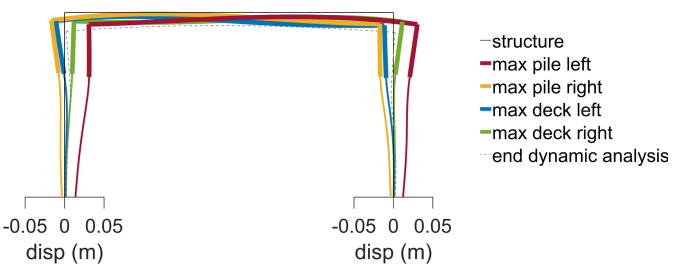

Fig. 5.8. 2D model - Parkfield record: structure deformation in the instants when the maximum value is reached for each considered scrutiny point.

shown in Fig. 4.18, the frequency content of the Yamakoshi record is mainly concentrated around the main mode of the soil column (about $1.7Hz$), while the Parkfield signal also produces a significant amplification in correspondence of the second mode (about $3.3Hz$).

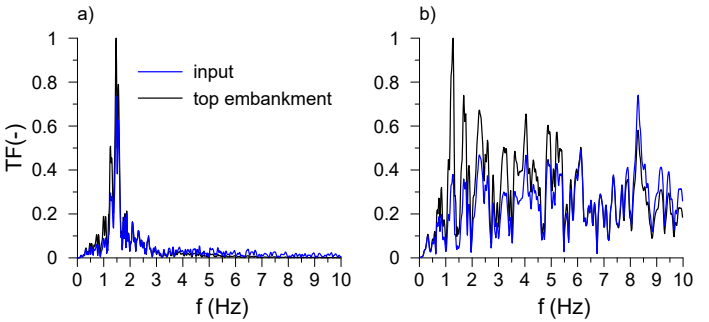

Fig. 5.9. Normalised frequency contents of (a) Yamakoshi and (b) Parkfield after a site response analysis of the soil column with embankment.

Fig. 5.10-b shows, for Yamakoshi record, the normalised frequency contents of the bending moment increments in the left pile head and in the left abutment-deck node (Fig. 5.10-a). As expected, the main contribution is offered by the first mode; however for the abutment-deck node there is an amplification of around 30% in correspondence of the second mode that cannot be neglected. A smaller amplitude instead is observed for the pile head in correspondence of the second mode. The behaviour of the pile foundation in fact, being embedded in the soil domain, is barely affected by the second mode. Note that the normalised frequency contents of the correspondent accelerations reported in Fig. 5.10-c are very similar to the frequency contents of Fig. 5.9-a and do not allow to distinguish the effect of the second mode. The normalised frequency content of the bending moment is, in fact, influenced by the combined effect of both the horizontal and vertical accelerations.

Same illustrations are reported for Parkfield record in Fig. 5.11. In this case the frequency content is affected by a greater *noise* due to the presence of the higher frequencies in the input signal. Nevertheless, Fig. 5.11-b shows that in correspondence of the first mode a more pronounced amplification occurs at the pile head than at the abutment-deck node, whilst a high amplification around the second mode affects both the responses, though it is slightly lower for the pile head. These observations confirm the importance of taking into account the second

mode in the development of a simplified procedure. Considering only the main mode of the system (the first) may be not sufficient to describe the dynamic behaviour of the system, especially in the critical location of the abutment-deck node.

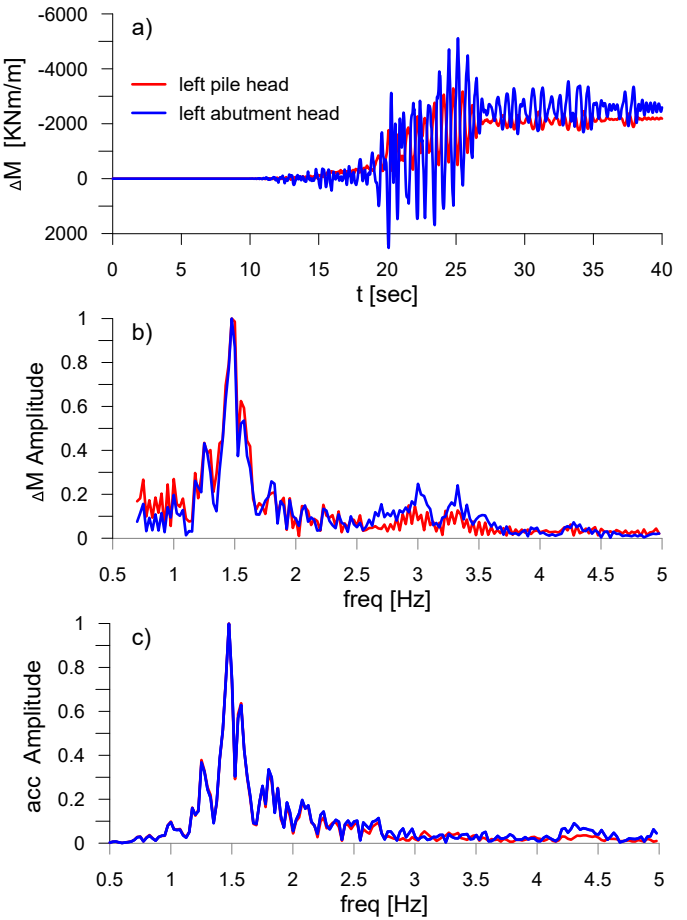

Fig. 5.10. Yamakoshi record: (a) time histories of the bending moment increments for left pile head and left abutment-deck node; (b) normalised frequency content of the bending moment increment; (c) normalised frequency content of the longitudinal acceleration.

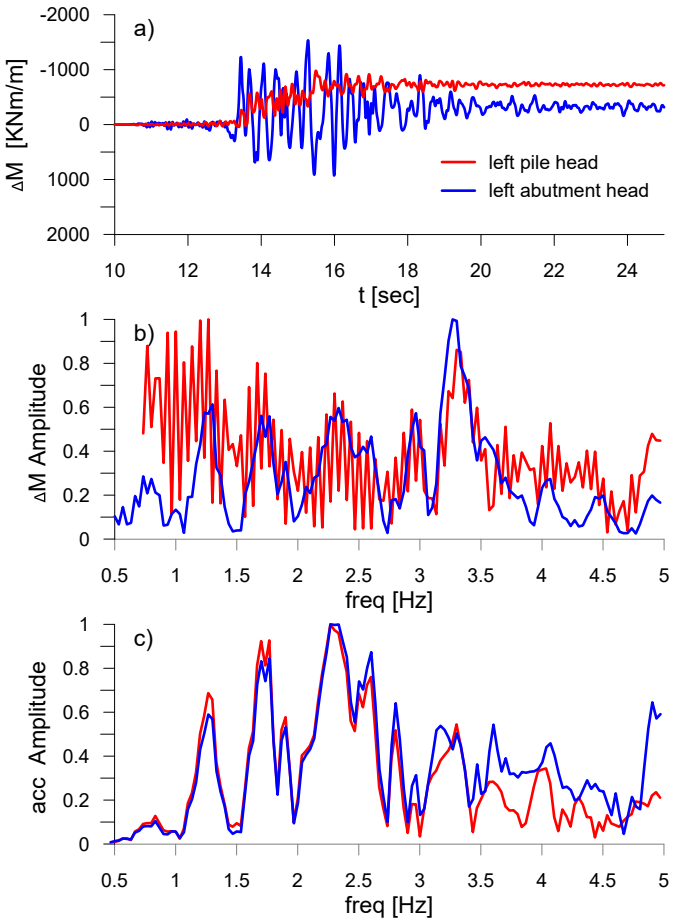

Fig. 5.11. Parkfield record: (a) time histories of the bending moment increments for left pile head and left abutment-deck node; (b) normalised frequency content of the bending moment increment; (c) normalised frequency content of the longitudinal acceleration.

5.3. A novel seismic design approach based on the nonlinear static analysis

This section proposes an application of a novel seismic design method for integral abutment bridges. In the proposed method, the seismic capacity of the bridge is obtained through a nonlinear static analysis of the entire soil-structure system, in which the soil domain is perturbed by a distribution of equivalent forces aimed at reproducing the effects associated with the significant modes of the bridge. This method, validated against the results of several dynamic analyses carried out on the full soil-structure model, demonstrates that the proposed design approach is able to reproduce quite satisfactorily the performance of the structure, in terms of maximum internal forces and displacements, with a very low computational demand.

5.3.1. Use of the 2D model

The *half 3D* and *2D* models were subjected to the longitudinal motions for a direct comparison between the two modelling strategies. Fig. 5.12 shows, for the two selected seismic inputs, the time histories of the bending moment calculated at the deck-abutment node (per unit deck length), and the histograms of the maximum bending moment at the top of the foundation piles (pile No. 1 is located on the plane of symmetry, pile No. 4 at the edge of the abutment). In the 3D model, since the abutment forces the piles to undergo the same displacement, the external pile (No. 4) is the most loaded, because it is the pile that exhibits the stiffer response. Although the 2D model cannot reproduce this edge effect, the bending moments computed at the top of the piles with this simplified model reproduce reasonably well the response of the internal piles, while the error on the external pile is of the order of 6 and 23 %, respectively for Yamakoshi and Parkfield. The time histories of the bending moment at the deck-abutment contact are very similar for the 3D and the 2D models; for the Parkfield signal the peak bending moment in the 3D model is slightly larger than that of the 2D model (order of 20 %), while the Yamakoshi accelerogram yields comparable results.

Overall, the two models show a very similar response, and the limited differences in the internal forces at the top of the pile can probably be accommodated by any non-linearity of the structural response of real piles. The computation times of the dynamic simulations on the 2D model are reduced to a couple of hours of execution using OpenSeesSP,

representing an efficient modelling technique for extensive studies on the longitudinal seismic performance of integral bridges. Therefore, the equivalent 2D model is taken as the reference model for the development and validation of the simplified design method discussed in the following.

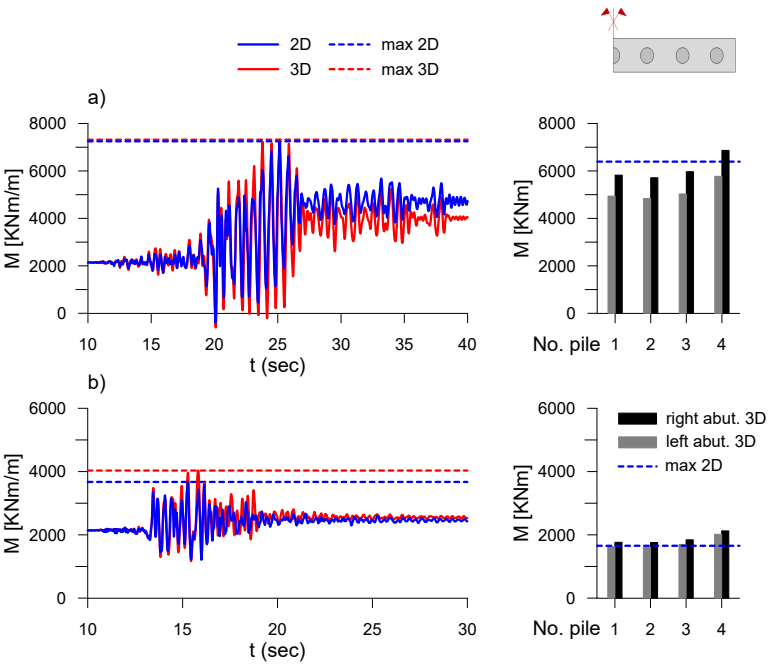

Fig. 5.12. Time histories of the bending moment in correspondence of left abutment head (left column) and histograms of the maximum earthquake-induced bending moment on pile foundation (right column) for (a) Yamakoshi and (b) Parkfield records.

5.3.2. Introduction to nonlinear static analysis

The non-linear dynamic analyses discussed in the previous section provide a detailed description of the seismic response of the soil-bridge system, but these are too complex and time-consuming for a routinary use in bridge design. Therefore, the results obtained in this study were used as a benchmark to calibrate a simplified design method. An interesting question to this effect is what an acceptable degree of complexity in the design practice could be: it was felt that for the type of bridge considered in this study the development of a static numerical model is indeed essential, because the design under gravity loading should con-

sider the effects of the construction sequence which are strongly affected by soil-structure interaction. Therefore, the design method proposed in this paper is based on the 2D model described above, and the simplification consists in the use of this same model to perform static nonlinear analyses of the seismic response of the bridge. The static nonlinear analysis, commonly used for the seismic design of structural systems, was recently extended to geotechnical systems, including multi-propped excavations, by Laguardia et al. (2020) and Jiang et al. (2021). Following Laguardia et al. (2020), the method employed in this work derives from the Capacity Spectrum Method (CSM) used for structural analysis (Freeman et al. 1975, Freeman et al. 1998, Freeman 2004) and already implemented in international design codes (ATC-40 1996, FEMA 440 2005). The method requires the independent definitions of the capacity of the system and of the seismic demand. The capacity is expressed by a nonlinear capacity curve, while the demand is provided by an elastic response spectrum plotted in the acceleration-displacement plane (ADRS). The capacity curve of the soil-bridge system is herein evaluated through the push-over analysis proposed by Callisto (2014, 2019) for earth-retaining structures: equivalent inertial forces are applied to all the nodes of the 2D model, including the structural nodes, of a non-linear numerical model of the system. These inertial forces are proportional to the nodal masses through a seismic horizontal coefficient k_h, representing the ratio of the horizontal acceleration to the gravity acceleration, and are increased progressively while simultaneously monitoring the corresponding displacements of significant points of the system. For the case of earth-retaining structures, Laguardia et al. (2020) assumed that the seismic horizontal coefficient was constant in space, because was thought to represent the deformation pattern associated with the fundamental vibration mode of the entire system, that typically governs its dynamic response. However, it was shown previously that the dynamic behaviour of the integral bridge at hand is actually controlled by two dominant modes, the first and fourth modes of the 2D soil-structure model, or equivalently the first and second mode of the soil column. The application of the nonlinear static analysis for this system requires therefore some changes and considerations that will be explained in the following.

5.3.3. Application of nonlinear static analysis

To consider in a simplified manner this bi-modal response represented in Fig. 5.13, k_h was taken to vary linearly along the height of the model with a distribution chosen to approximate the deformation patterns observed in these two dominant modes. To reproduce the deformation obtained in the first mode, the distribution depicted in Fig. 5.14-a was used, where k_h varies linearly from its maximum value, at the top of the embankment, down to zero at the bottom of the model. The deformation obtained in the second significant mode (No. 4) was reproduced by the linear distribution shown in Fig. 5.14-b extended only along the thickness of the embankment.

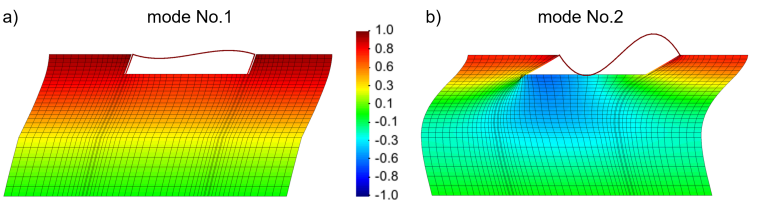

Fig. 5.13. (a) First and second (b) modal shapes of the 2D model, with representation of the contours of the normalised longitudinal displacements.

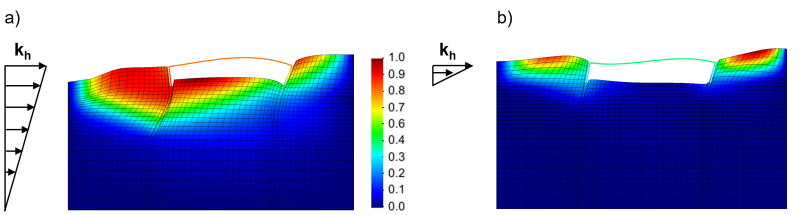

Fig. 5.14. Distributions of the seismic coefficient, k_H, deformed mesh and contours of normalised longitudinal displacement to reproduce the first (a) and the second (b) modal shapes.

5.3.4. Layout of the method

Fig. 5.15-a shows the capacity curves of the 2D model for the two different distributions of k_h, expressed as relationships between k_h at the top of the embankment and the corresponding horizontal displacement u of the deck. For a given point on the capacity curve, the vibration period T^* corresponding to the secant stiffness of the system can be obtained as:

$$T^* = 2\pi\sqrt{\frac{u}{k_h g}} \tag{5.1}$$

where g is the gravity acceleration. Fig. 5.15-b plots this secant period as a function of the displacement u (in a logarithmic scale) for the two capacity curves. The tangent initial periods obtained from the two capacity curves, equal to 0.55 s and 0.32 s, are reasonably close to the first two vibration periods of the soil-bridge system, equal to 0.62 and 0.27 s (see Table 4.4), confirming that the two distributions of k_h in Fig. 5.14 can be conceived to represent in a simplified manner the seismic loading associated with the dominant modes.

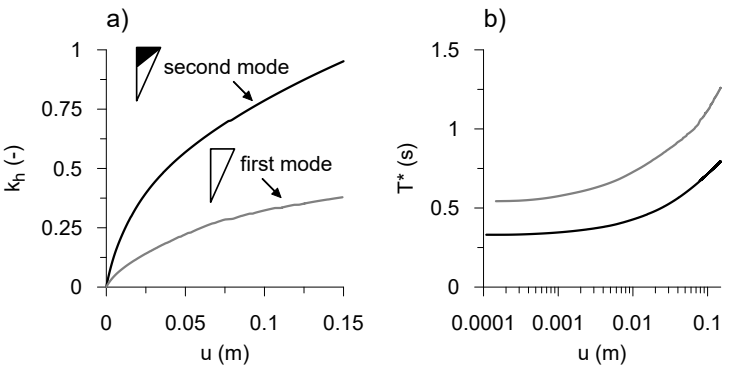

Fig. 5.15. (a) Capacity curve of the system; (b) evolution of the secant period T^* with the displacement u.

Fig. 5.16 shows the progressive deformation of the structural elements obtained in the push-over analyses, indicating that the deformation patterns obtained with the two distributions of k_h are indeed very similar to the modal shapes of Fig. 5.13. Fig. 5.17 reports the increments of the bending moment in the structure as the intensity of k_h rises, due to the two adopted distributions of k_h. Note that Fig. 5.17-b refers only to the increments induced by the nonlinear static analysis, while Fig. 5.17-a shows the total values. In terms of shape, the distributions of Fig. 5.17-a are immediately comparable with the distributions of the bending moment in the instants when maximum values are reached, illustrated in Fig. 5.5 and in Fig. 5.6.

In the present simplified method, the seismic demand is defined with a decoupled approach and it is expressed by the ADRS. Specifically, this demand is derived from a one-dimensional ground response analysis,

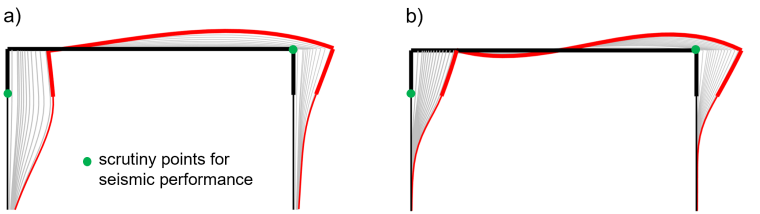

Fig. 5.16. Progressive deformations of the structure as the intensity of k_h rises due to the distributions of k_h that simulate the (a) first and (b) second modes.

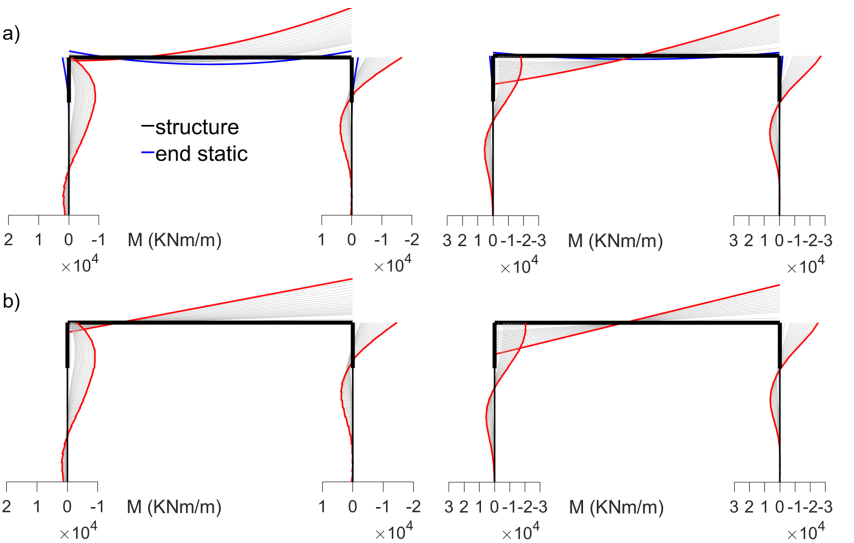

Fig. 5.17. Increments of the bending moment in the structure as the intensity of k_h rises due to the distribution of k_h that simulates the first (left) and second modes (right); (a) refers to the total values of bending moment while (b) to the increments due to the nonlinear static analysis only.

considering the soil column that includes the embankment. Conversely, for the practical application of the method, the seismic demand may be represented by a code-defined response spectrum.

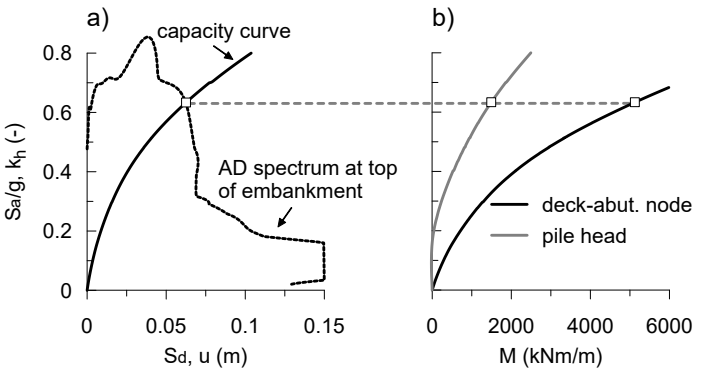

Fig. 5.18. Application of the proposed design method: (a) evaluation of the intersection point (or performance point, squared symbol); (b) moment-seismic coefficient curves.

In Fig. 5.18-a the capacity curve of the bridge is superposed onto the A-D elastic spectrum computed at the top of the embankment, where S_d is the spectral displacement and S_a is the spectral acceleration, which is divided by g for compatibility with the capacity curve. Fig. 5.18-b shows the relationships obtained in the push-over analysis between the seismic coefficient and the bending moments at two representative points of the structural elements, namely, the deck-abutment connection and the top of the pile. As in the original CSM, the equivalent damping ratio ξ of the A-D spectrum is found by an iterative procedure, i.e., by evaluating the damping ratio at the intersection of the capacity curve with the A-D spectrum and re-plotting the spectrum accordingly. The iterative procedure is therefore aimed at identifying an equivalent linear soil-structure system, characterised by a decreasing secant stiffness and an increasing equivalent viscous damping ratio. The value of the equivalent damping ratio, at each iteration, can be found assuming an elliptic shape for the hysteresis cycle as depicted in Fig. 5.19 such that:

$$\xi = \frac{W_D}{4\pi \cdot W_E} = \frac{\pi b \cdot S_d}{2\pi \cdot S_d \cdot k_h} \tag{5.2}$$

where $W_E = 0.5 \cdot u \cdot k_h$ is the recoverable energy and W_D is the dissipated work in each loading cycle. Due to the symmetric behaviour of the system at hand, W_D is calculated according to the Masing (1926)

unloading-reloading rule, with the intersection b easily determined by knowing the value that the k_h function assumes for the intersection displacement s and $s/2$:

$$b = -k_h(s) + 2 \cdot k_h\left(\frac{s}{2}\right) \tag{5.3}$$

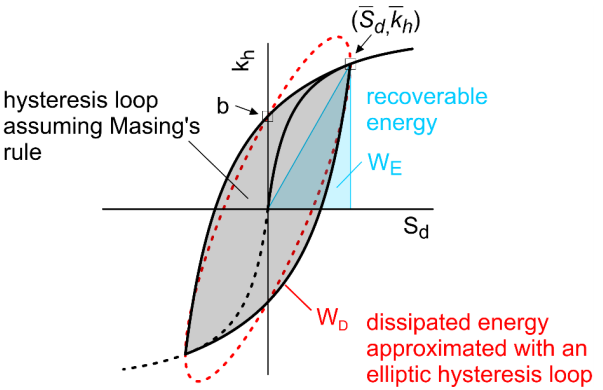

Fig. 5.19. Definition of the b parameter following the Masing rule.

Once convergence is attained (the damping ratio computed at two successive iterations is the same), the procedure provides the following quantities:

- acceleration, expressed as the spectral acceleration S_a/g or the seismic coefficient k_h at the intersection between the capacity curve and the seismic demand;
- the maximum displacement of the system;
- the corresponding internal forces at selected points of the structural elements.

The following is a brief summary of the proposed procedure:

1. An appropriate two-dimensional numerical model of the soil-bridge system is developed, and is used to analyse the construction sequence.
2. The seismic capacity is obtained by carrying out two static push-over analyses that adopt the two distributions of the seismic coefficient k_h associated with the dominant vibration modes (Fig. 5.14).

3. The seismic demand is expressed by an elastic response spectrum, that is either obtained from a construction code, or is evaluated as a site-specific spectrum through appropriate ground response analyses. In both cases the properties of the embankments should be taken into account in the derivation of the seismic demand.

4. The capacity curves obtained with the two k_h distributions are superposed onto the AD response spectrum, and iterations are needed to plot the elastic spectrum at the correct damping ratio value.

5. The performance point yields the maximum displacement of the system and, at the same time, provides the internal forces in the structural elements.

6. The procedure is applied to both pushover analyses, and the most conservative value of each output quantity is used for design.

5.3.5. Validation

The seismic records acting in the longitudinal direction of the bridge were selected through the web-based PEER ground motion database (https://ngawest2.berkeley.edu/) and are listed in Table 5.1. Although some of the signals were recorded on deformable ground, as evidenced by the equivalent shear wave velocity in the first 30 m of depth V_{s30}, they were seen to reproduce in the average the Type 1 elastic spectrum on soil type A according to the current Eurocode (2003). Table 5.1 also lists the peak ground acceleration PGA of the signals, the Arias intensity Arias (1970) I_A, the significant duration T_s (between 5 % and 95 % of the Arias intensity), the mean quadratic period Rathje et al. (1998) T_m, the moment magnitude M_w of the earthquake, and Joyner-Boore distance R_{JB} of the recording station. The 5 %-damped elastic response spectra of the longitudinal components of the selected records are shown in Fig. 5.20-a, together with the corresponding average response spectrum. All ground motions are used with their actual recorded amplitudes, with the exception of the RSN 4345 and RSN 4868 records, that were scaled by a factor of 1.65 and 0.5, respectively. Therefore, note that the results that will be shown for Yamakoshi from now on, will refer to the scaled ground motion and not to the original, as shown so far.

Fig. 5.20-b shows the elastic response spectra obtained propagating the signals of Fig. 5.20-a through a one-dimensional sub-model includ-

Tab. 5.1. Characteristics of the selected seismic records.

Event	*Record*	PGA (g)	I_A (m/s)	T_s (s)	T_m (s)	$V_{S,30}$ (m/s)	R_{JB} (km)	M_w $(-)$
Parkfield	RSN 4064	0.35	0.78	4.9	0.23	657	6.0	4.3
L'Aquila	RSN 4477	0.15	0.40	8.4	0.25	488	6.3	6.4
Assisi - scaled	RSN 4345	0.28	0.75	4.3	0.25	377	6.0	16.6
Tolmezzo	RSN 125	0.35	0.80	4.2	0.41	505	6.5	15.0
Montenegro	RSN 4455	0.22	0.73	10.9	0.41	585	7.1	23.6
Loma Prieta	RSN 753	0.64	3.24	6.9	0.49	462	6.9	0.2
Superstition Hill	RSN 725	0.47	2.07	13.7	0.49	317	6.5	11.2
Christchurch	RSN 8124	0.29	1.13	9.5	0.61	293	6.2	9.4
Yamakoshi - scaled	RSN 4868	0.20	1.03	13.6	0.66	655	6.8	22.2
Corinth	RSN 313	0.24	0.69	15.4	0.71	361	6.6	10.3
Cape Mendocino	RSN 3749	0.33	1.31	11.5	0.71	355	7.0	16.5
Kocaeli-Gebze	RSN 1161	0.24	0.55	7.4	1.21	523	7.5	7.6

ing the foundation soils and the embankment. Fig. 5.20-c indicates that, as a result of the ground response, the spectral accelerations are, on average, amplified by a factor (MF: magnification factor) ranging from 1.5 to 2.0 in the period interval of interest for the dynamic response of the soil-bridge system at hand, as described in more detail in chapter 4.

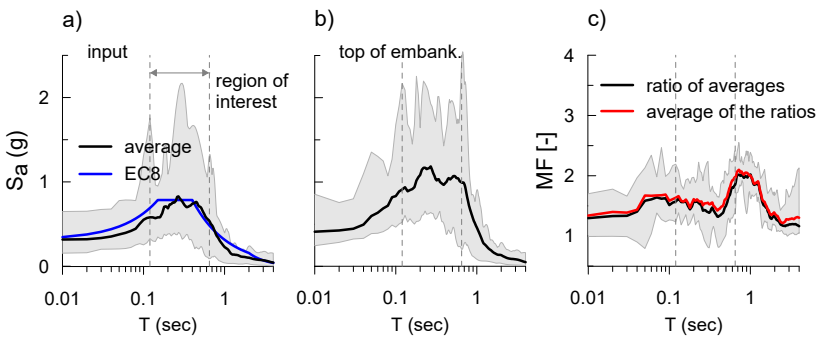

Fig. 5.20. (a) 5%-damped elastic response spectra of the longitudinal components of the input ground motions; (b) 5%-damped elastic response spectra at the top of embankment after seismic response analyses; (c) dynamic amplification factor (MF) between the top of the embankment and the input motion as a function of the period T.

The simplified method was validated by comparing its results with those obtained with the full dynamic analyses carried out using the seismic records of Table 5.1. The comparison was carried out for each individual seismic signal, and considering the average of the results obtained for all the signals. In the former case, the simplified procedure was applied considering the response spectrum of each record after its propagation through a soil column. Conversely, the comparison with the average results of the dynamic analyses was carried out using the average response spectrum of Fig. 5.20-b, which had to be recalculated for each value of the damping ratio obtained during the iterations.

The results of this validation are collected in Fig. 5.21, which shows, for each record and on average, the ratios of the output quantities obtained from both the simplified non-linear static analysis (NLSA) and the full dynamic analyses (DYN) using the two different distributions of k_h (mode 1 and mode 2). It should be noted that the average of the results obtained for each ground motion with the proposed procedure (NLSA) has not been superimposed in Fig. 5.21, as it substantially corresponds to the value obtained with the average spectrum. Table 5.2, Table 5.3 and Table 5.4 report this comparison for clarity; the application of the NLSA considering the average spectrum is defined by the term *average spectrum*, while the average of the results of the NLSA applied to the individual ground motions is indicated as *average*.

Tab. 5.2. Maximum bending moment (kNm/m) at the abutment deck-node.

	DYN	$NLSA - 1°mode$	$NLSA - 2°mode$	$NLSA - 1°mode\ /\ DYN$	$NLSA - 1°mode\ /\ DYN$
average	2889	2202	4297	0.76	1.49
average spectrum	2889	2367	4301	0.82	1.49

Tab. 5.3. Maximum bending moment (kNm/m) at the pile head.

	DYN	$NLSA - 1°mode$	$NLSA - 2°mode$	$NLSA - 1°mode\ /\ DYN$	$NLSA - 1°mode\ /\ DYN$
average	1720	1707	1227	0.99	0.71
average spectrum	1720	1855	1239	1.08	0.72

Tab. 5.4. Maximum displacement (in meters) at the deck-abutment node.

	DYN	*NLSA* – 1°*mode*	*NLSA* – 2°*mode*	*NLSA* – 1°*mode* / *DYN*	*NLSA* – 1°*mode* / *DYN*
average	0.057	0.072	0.053	1.28	0.93
average spectrum	0.057	0.079	0.052	1.40	0.92

Fig. 5.21-a refers to the bending moment at the deck-abutment connection, Fig. 5.21-b to the bending moment at the top of the piles, and Fig. 5.21-c to the horizontal displacement at the top of the abutment. All these results quantify the effect of the seismic actions only, that should be added to the effects computed at the end of the construction sequence. As a general result, inspection of Fig. 5.21 indicates that the first-mode distribution of k_h provides a better approximation of the bending moments at the pile top, while the results obtained with second-mode distribution are more effective in predicting the maximum displacements at the top of the abutment. The bending moment at the deck-abutment connection is effectively bounded by the two distributions of k_h, suggesting the use of the maximum value or alternatively, the average of the values found with the two procedures for design purposes. Overall, the predictive capability of the simplified method appears rather good, considering the substantial simplifications introduced in the analysis.

In Fig. 5.21, as in Table 5.1, the input seismic records are sorted according to a decreasing frequency content. In general, effects of the frequency content of the seismic input are not apparent. However, Fig. 5.21-b shows that both distributions of k_h tend to underestimate the benchmark results for the first three records. Fig. 5.22 reports the deformation of the structure in the instants when the maximum bending moment is reached at the pile head, respectively for record No. 2 (RSN 4477) and No.3 (RSN 4345). Fig. 5.23 shows for the same instants the contours of the longitudinal displacements in the soil model. These records are characterised by a high average frequency (about 5 Hz) and the underestimation obtained for these high-frequency records could be due to the occasional excitation of modes (as for example the ones reported in Fig. 4.11) not considered in the non linear static analysis. In fact, the actual values of the moment produced by these three records reported in Fig. 5.21-b, are quite small and not particularly relevant for design purposes. In addition, this underestimation is quite marked for

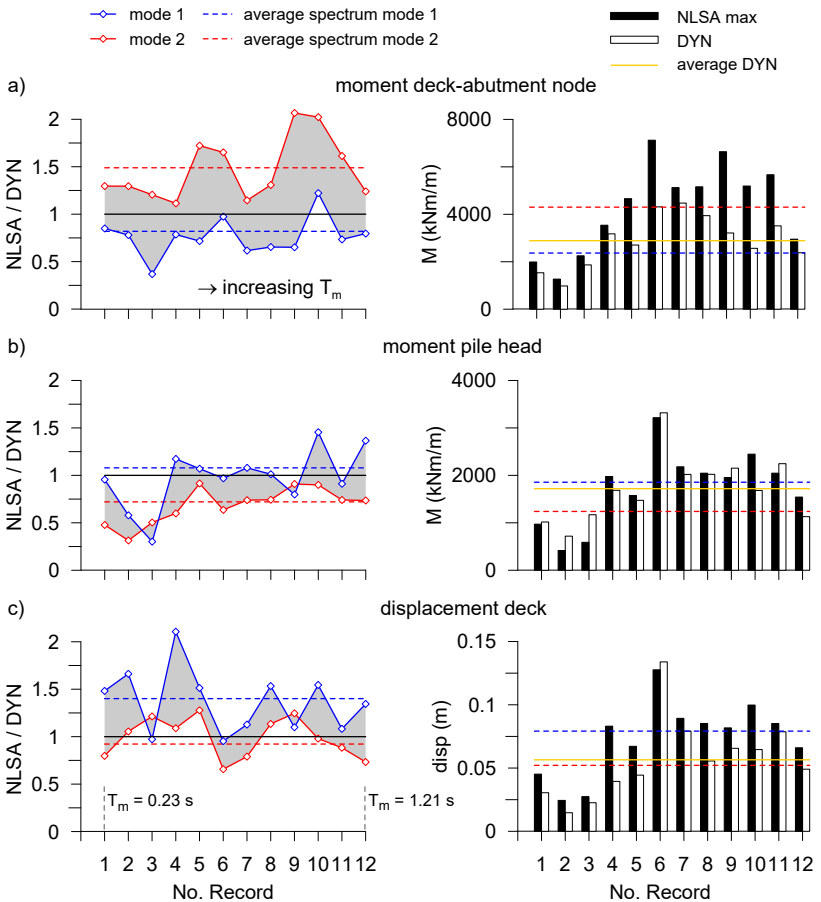

Fig. 5.21. Comparison between the prediction of the proposed design approach and the results of the dynamic analyses: (a) maximum moment at the abutment-deck node, (b) maximum moment at the pile top; (c) maximum displacement at the abutment-deck node.

record No. 3 (RSN 4345) because it is unrealistically emphasised by the large scaling factor (equal to 1.65) considered to make it compatible with the seismic demand. Although this discrepancy is somewhat smoothed out using the average response spectrum, it confirms the necessity of selecting the seismic input using a realistic range of frequencies, avoiding excessive multiplying factors when scaling the signal for spectral compatibility.

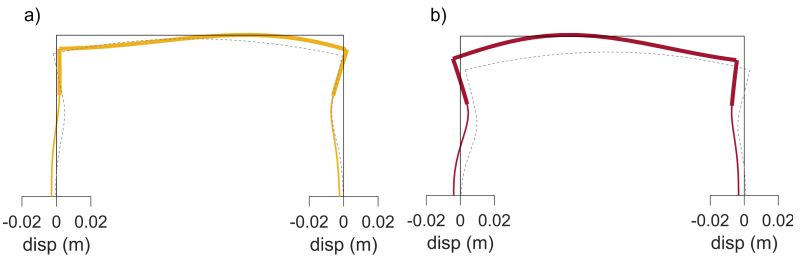

Fig. 5.22. Deformations of the structure in the instant when the maximum values of bending moment are reached at the (a) right pile head (L'Aquila) and at (b) left pile head (Assisi).

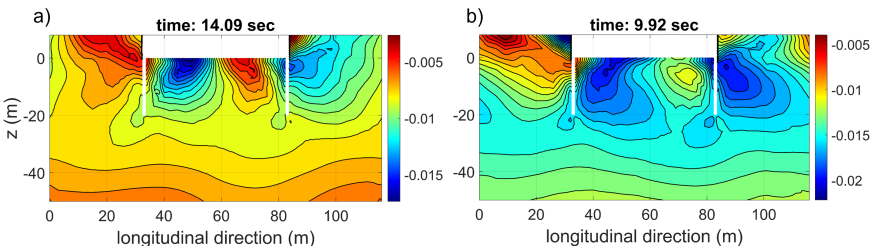

Fig. 5.23. Contours of the longitudinal displacement (in meters) in instants when the maximum values of the bending moment are reached at the (a) right pile head (L'Aquila) and at (b) left pile head (Assisi).

5.3.6. Additional checks

As a further validation of the procedure discussed so far, Fig. 5.24 and Fig. 5.25 report the contours of the longitudinal acceleration in instants when the maximum bending moment values are reached at each considered scrutiny point, respectively for L'Aquila and Assisi records. As a general result, the concentration of high values of the acceleration in correspondence of the embankments is evident. Focusing on the contours associated with the deformation described in Fig. 5.22-a,

Fig. 5.24 shows that the distribution of acceleration near the abutment-pile system, which yields the greatest internal forces at the *right pile head*, is very irregular, with negative values in correspondence of the embankment and positive values underneath. A similar phenomenon can be appreciated for the contours depicted in Fig. 5.25 associated with the deformation depicted in Fig. 5.22-b where the acceleration changes direction above and below the *left pile head*.

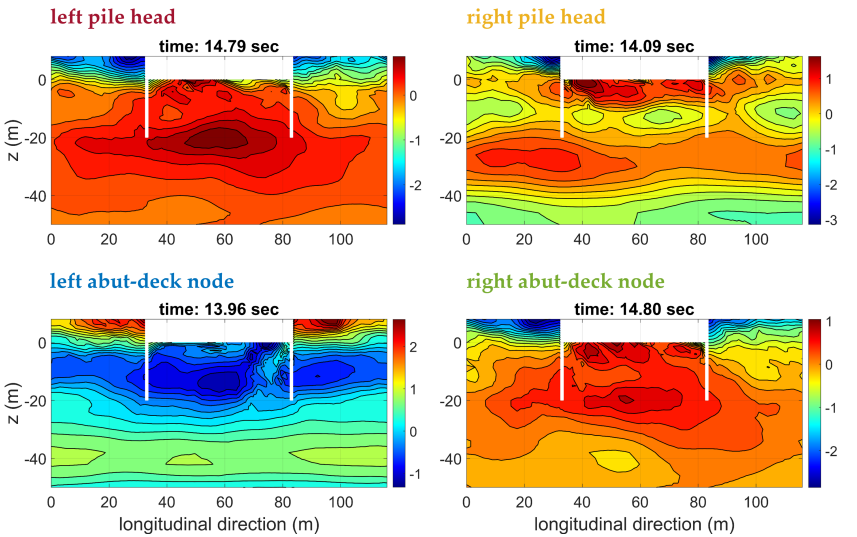

Fig. 5.24. L'Aquila record: contours of the longitudinal acceleration (in m/s^2) in instants when the maximum bending moment values are reached at each scrutiny point considered.

In the light of simplification, a decoupled approach involving a simple site response analysis can be employed to verify whether the inertial forces/accelerations applied to the system (Fig. 5.14) are comparable with the patterns of accelerations at the instants when maximum moment is reached at the the scrutiny points. In other words, the acceleration profiles in the soil column neglect soil-structure interaction effects. This assumption can be conceived as a good compromise because introduces the same level of approximation used in defining the seismic demand according to the decoupled approach. Last but not least, it greatly simplifies the interpretation of the results.

Fig. 5.26 shows, for the first six ground motions of Table 5.1, the direct comparison between the normalised acceleration patterns applied to the system in the non-linear static procedure and the normalised

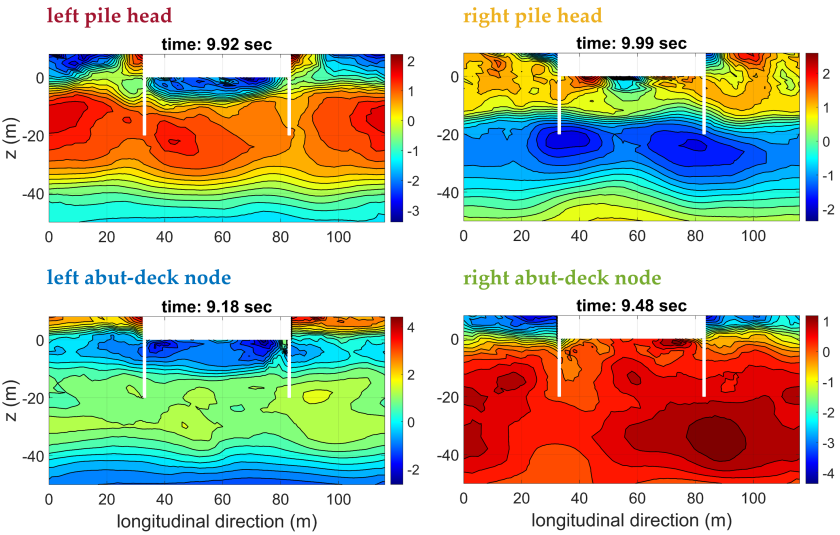

Fig. 5.25. Assisi record: contours of the longitudinal acceleration (in m/s^2) in instants when the maximum bending moment values are reached at each scrutiny point considered.

acceleration patterns evaluated on the soil column in instants when maximum values of bending moment are reached for each scrutiny point. In addition the same figure, reports the maximum values of the increment of bending moment in the structure evaluated in the dynamic analyses in correspondence of the pile head and of the deck-abutment node, using different colors for the left and for the right abutment. For example, for the record RSN 4477, the maximum bending moment is reached for the right pile head and for the left deck-abutment node. The acceleration pattern profile associated with the right pile head (orange line) for the record RSN 4477 closely follows the acceleration pattern profile of the second mode (applied only to the embankment), but then assumes a negative value under the pile head. This represents therefore, a worse condition in terms of flexural behavior for the structure than the one hypothesised considering the second mode. At the same way, the acceleration pattern profile for the right pile head (red line) for the record RSN 4345 is quite different from the hypothesised distribution. As already explained before, this is mainly attributed to the occasional excitation of higher modes, shown in chapter 4, neglected in the current procedure.

Nevertheless in most cases the comparison is very good. For example, the record RSN 125, suggests that the first mode is able to describe the maximum bending moment in the pile head (red line) while the second mode describes well the maximum bending moment in the deck-abutment node (green line). In fact, the procedure in this case approximates in a very satisfactory way the results of the dynamic analyses as shown in Fig. 5.21. Looking at the record RSN 753, it is evident that the first distribution approximates well the maximum bending moment at pile head (red line) and at the deck-abutment node (green line); Fig. 5.21 confirms this interpretation as well.

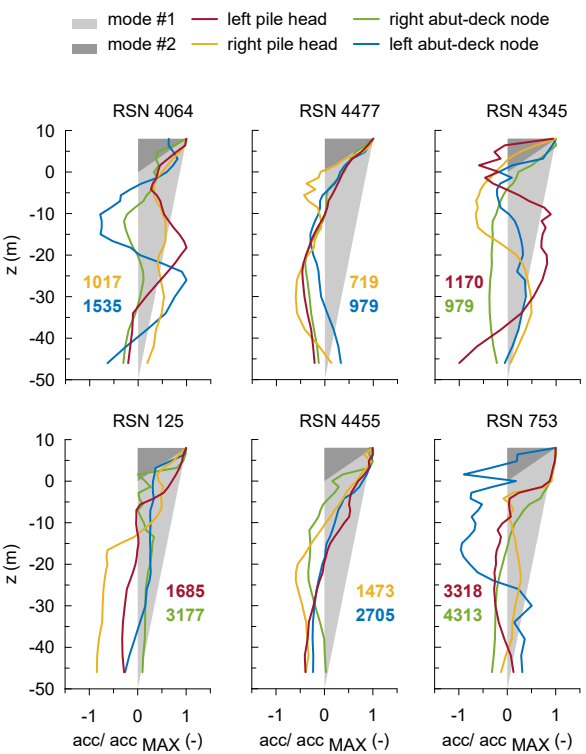

Fig. 5.26. Patterns of the longitudinal acceleration evaluated in the soil column in instants when the maximum values of bending moments are reached for each scrutiny point considered and comparison with the hypothesised inertial acceleration patterns; first six ground motions of Table 5.1.

Fig. 5.27 shows the same results, for the last six ground motions of Table 5.1. The record RSN 4868 shows that the pattern distribution

of the first mode is able to provide good results for the evaluation of the maximum bending moments for both pile head and deck-abutment node. Overall, the hypothesised distributions of the inertial acceleration are very similar to the acceleration pattern profiles evaluated during the site response analysis of the soil column. This therefore represents a further confirmation of the representativeness of the results already described in Fig. 5.21.

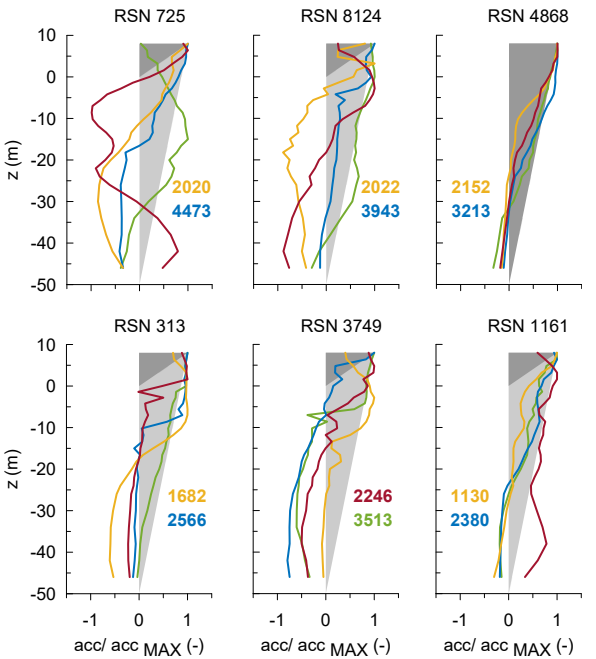

Fig. 5.27. Patterns of the longitudinal acceleration evaluated in the soil column in instants when the maximum values of bending moments are reached for each scrutiny point considered and comparison with the hypothesised inertial acceleration patterns; last six ground motions of Table 5.1.

As a last consideration, Fig. 5.28 reports the comparison between the acceleration patter profiles evaluated on the soil column for Yamakoshi (RSN 4868) assuming the real ground motions and a scale factor of 0.5. This record was actually scaled for the application of the procedure in the attempt to make it compatible with the seismic demand of the site in question. Even though these patterns occur in different instants, the patterns that produce the maximum internal forces differ significantly from each other. This confirms again, as already discussed for the record RSN

4345, the necessity of selecting the seismic input using a realistic range of frequencies, avoiding excessive multiplying factors when scaling the signal for spectral compatibility.

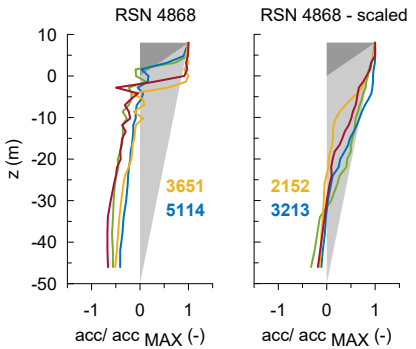

Fig. 5.28. Patterns of the longitudinal acceleration evaluated in the soil column in instants when the maximum values of the bending moments are reached for each scrutiny point considered and comparison with the hypothesised inertial acceleration patterns; Yamakoshi vs Yamakoshi scaled.

5.4. Validation with different set of ground motions

The proposed simplified procedure is now validated against two new sets of ground motions referred to two different seismic scenarios. The seismic hazard on stiff outcrop for the site of the bridge (Gatteo, Italy) is defined by elastic response spectra referring to soil type A, evaluated in accordance with Italian technical provisions (Italian Building Code 2018). In the present study, the two investigated seismic scenarios are: Damage Limit State (DLS), with a probability of exceedance PR = 63 %, and No-Collapse Earthquake (NCE), with PR = 5%. Several seismic records were selected through the web-based PEER ground motion database (https://ngawest2.berkeley.edu/) as compatible seismic actions with the seismic demand discussed above. Fig. 5.29-a shows the lower and upper envelopes and the average elastic response spectra of the selected records, relative to the longitudinal direction of the bridge, for the DLS and the NCE, for which 9 and 7 records, listed respectively in Table 5.5 and in Table 5.6 were considered. Fig. 5.29-a refers instead to the ground motions at the top of the embankment, evaluated separately through a free field site response analysis on a soil column including the embankment.

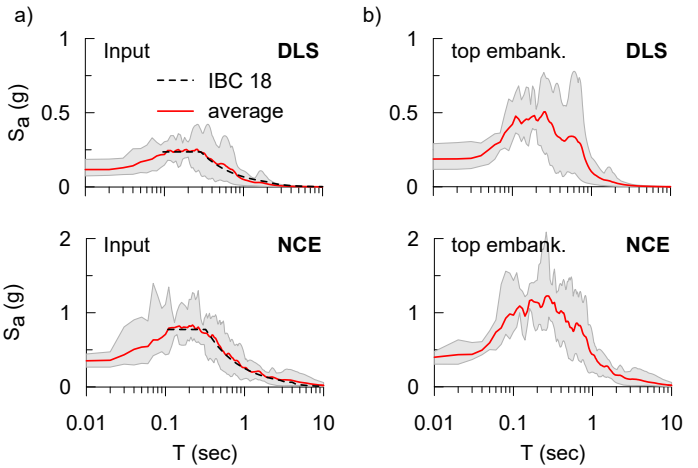

Fig. 5.29. Lower and upper envelopes (shadowed area) and average trend of the 5%-damped elastic spectra of the longitudinal components of the selected seismic records for the limit states DLS and NCE; (a) relative to the input motion (outcrop); (b) relative to the motion computed at the top of the embankment.

Tab. 5.5. Characteristics of the seismic records for DLS.

Record	SF $(-)$	PGA (g)	I_A (m/s)	T_s (s)	T_m (s)	$V_{S,30}$ (m/s)	R_{JB} (km)	Mw $(-)$
RSN 2019	0.65	0.14	0.04	2.5	0.16	730	4.9	2.2
RSN 146	0.75	0.07	0.04	6.8	0.20	1428	5.7	10.2
RSN 23	1.25	0.11	0.04	5.0	0.23	875	5.3	9.7
RSN 80	0.80	0.08	0.07	14.1	0.28	969	6.6	21.5
RSN 3774	1.00	0.08	0.04	2.8	0.33	740	5.3	13.0
RSN 4083	0.75	0.18	0.10	8.8	0.36	907	6.0	4.7
RSN 8709	1.60	0.11	0.11	4.1	0.45	710	5.5	12.8
RSN 680	1.25	0.14	0.14	3.5	0.46	969	6.0	6.8
RSN 4513	1.30	0.12	0.10	13.4	0.61	717	5.6	5.1

The assessment of the seismic performance of the reference bridge is reported in Fig. 5.30. The figure shows a systematic comparison between the results obtained with the proposed method (NLSA) and with the full dynamic analysis (DYN) for the two limit states considered. As already explained before, since the proposed method provides an estimate of the maximum effects induced by the seismic action, the results of the dynamic analyses only refer to the variations computed with respect to the end of the static conditions.

Tab. 5.6. Characteristics of the seismic records for NCE.

Record	*SF* $(-)$	*PGA* (g)	I_A (m/s)	T_s (s)	T_m (s)	$V_{S,30}$ (m/s)	R_{JB} (km)	*Mw* $(-)$
RSN 8165	0.50	0.52	3.34	13.3	0.26	760	7.1	4.2
RSN 1633	0.50	0.26	1.16	28.7	0.36	724	7.4	12.6
RSN 763	0.85	0.30	0.66	5.0	0.38	730	6.9	9.2
RSN 879	0.60	0.44	2.51	13.2	0.46	1369	7.3	2.2
RSN 989	1.40	0.30	1.22	9.0	0.51	740	6.7	9.9
RSN 5618	1.35	0.30	2.39	19.7	0.52	826	6.9	16.3
RSN 1161	1.65	0.43	1.50	7.5	1.19	792	7.5	7.6

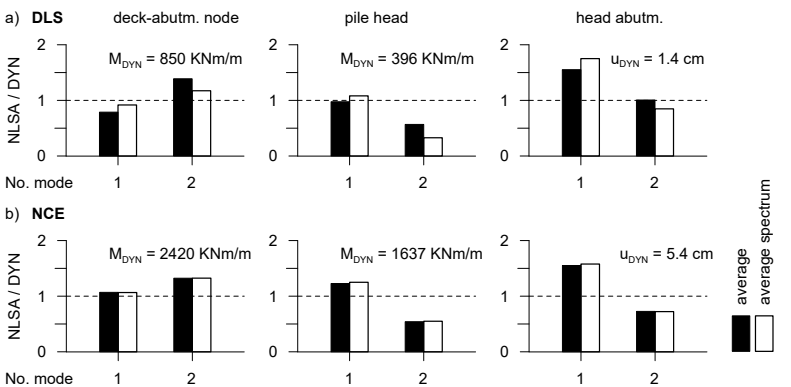

Fig. 5.30. Results of the proposed design method for the DLS (a) and NCE (b): ratios NLSA/DYN of the maximum bending moment at the deck-abutment node, pile head, and of the maximum displacement of the deck.

The same three output quantities are considered: the maximum bending moments at the deck-abutment node and at the pile head, and the maximum deck displacement. For each output quantity the average value obtained from the dynamic analyses is reported above each plot. In particular, the application of the procedure considering the average spectrum (Fig. 5.29) is defined by the term *average spectrum*, while the average of the results of the procedure applied to the individual ground motions is indicated as *average*. The comparison between these two different ways to characterise the seismic demand is also reported in Table 5.7, Table 5.8 and Table 5.9. It is evident that this choice does not influence significantly the average results yielded by the proposed method, suggesting the possibility to use a code-design spectrum straightforwardly.

Considering the simplicity and rapidity of the NLSA, the comparison with the results of the dynamic analyses is quite satisfactory.

From an engineering perspective, the following considerations can be inferred: the internal forces at the deck abutment node may be calculated using the capacity curve associated with the second mode while, the curve associated to the first mode may be used to evaluate the internal forces in the pile foundation. Finally, the first mode provides systematically greater displacements of the deck, whilst a limited underestimation is provided by the second mode solution.

Tab. 5.7. Maximum bending moment (kNm/m) at the abutment deck-node.

DLS	*DYN*	*NLSA* – 1°*mode*	*NLSA* – 2°*mode*	*NLSA* – 1°*mode* / *DYN*	*NLSA* – 1°*mode* / *DYN*
average	850	670	1179	0.79	1.39
average spectrum	850	779	997	0.92	1.17
NCE					
average	2420	2586	3201	1.07	1.32
average spectrum	2420	2578	3204	1.07	1.32

Tab. 5.8. Maximum bending moment (kNm/m) at the pile head.

DLS	*DYN*	*NLSA* – 1°*mode*	*NLSA* – 2°*mode*	*NLSA* – 1°*mode* / *DYN*	*NLSA* – 1°*mode* / *DYN*
average	396	386	221	0.98	0.57
average spectrum	396	428	130	1.08	0.33
NCE					
average	1637	2010	886	1.23	0.54
average spectrum	1637	2046	899	1.25	0.55

Tab. 5.9. Maximum displacement (in meters) at the deck-abutment node.

DLS	DYN	$NLSA - 1°mode$	$NLSA - 2°mode$	$NLSA - 1°mode\ /\ DYN$	$NLSA - 1°mode\ /\ DYN$
average	0.014	0.022	0.014	1.55	1.01
average spectrum	0.014	0.025	0.012	1.75	0.85
NCE					
average	0.054	0.083	0.039	1.55	0.73
average spectrum	0.054	0.085	0.039	1.58	0.72

5.5. Final remarks about the application of the procedure

Soil-structure interaction effects cannot be neglected in the design of integral abutment bridges because they are particularly affected by the presence of the foundation soil and of the approach embankment. Since full-dynamic analyses can rarely be used to study the soil-structure interaction under seismic loading, as they require a large computational effort and a complex control of the response of the numerical model under dynamic loading, this chapter has proposed a simplified procedure for the ordinary seismic design.

Three- and two-dimensional numerical models of an idealised integral bridge were developed to investigate, with the aid of dynamic and modal analyses, the main characters of the dynamic response of the reference bridge, leading to the development of the simplified design method. The results of the dynamic analyses, obtained using a significant number of seismic records, were also used as a benchmark to demonstrate the validity of the simplified procedure.

Considering that non-linear numerical models for the study of the soil-structure interaction under gravity loads will soon become routinary developed in the design practice, the method herein developed extends the use of these same models to the seismic design of the bridge. This extension is obtained by performing a push-over analysis, according to two different distributions of equivalent seismic forces, and using the resulting capacity curves in the context of the capacity spectrum method, generalising the non linear static approach for geotechnical systems. Finally, it is really important to remark that these two employed distributions, reproducing the deformation patterns associated with the dominant vibration modes, have an extremely general character and are not case-study dependent. In fact, they respectively reproduce the main modes of both the soil-deposit and the embankment in a simple manner (linear distributions).

The encouraging results demonstrate that the proposed design method may be efficiently used for a direct assessment of the seismic performance of single-span integral bridges. This requires the sole application of the nonlinear static analysis methodology, as a robust framework that, if properly validated, generalised and systematised, may be also extended for the seismic design of similar soil-structure systems as already demonstrated by previous studies (Callisto 2014, Callisto 2019, Laguardia et al. 2020, Jiang et al. 2021). In addition, the procedure herein implemented

can be straightforwardly employed in commercial software, using common elastic-plastic constitutive models for soil and defining the seismic demand with code-defined response spectrum. Therefore, this tool needs a much more limited computational effort with respect to more advanced nonlinear dynamic analyses.

5.6. An extensive comparison between 2D and 3D models

The direct comparison between the 2D and 3D models was shown in the section 5.3.1 for the two reference ground motions, Yamakoshi and Parkfield. The two different models provided comparable results so that, the 2D model was taken as the reference model for the validation of the proposed model. In this regard, this section provides an extensive comparison between the two models, using *a posteriori*, all the ground motions of Table 5.1.

The time histories of the bending moment at the abutment-deck contact as well as the maximum values of the bending moment reached in the pile foundation are depicted for both models in Fig. 5.31, in Fig. 5.32 and in Fig. 5.33.

Fig. 5.34 reports the comparison between the maximum increments of bending moment evaluated at the deck-abutment node (Fig. 5.34-a) and in the pile foundation (Fig. 5.34-b/c). As a general result the average of the increments of the maximum bending moment at the deck-abutment node are about 19 % higher respect to the 2D model. In addition, it appears that the 2D model is able to capture the maximum value in the central pile with a slighter underestimation of 9 %, while the underestimation in the external pile reaches the 26 % on average. The underestimations associated with the 2D model can be ascribed to the transverse deformation pattern of the 3D model. In addition, since the aperture of the Drucker-Prager surface was calibrated in plane strain to reproduce the Mohr-Coulomb criterion (section 3.1), the resistance in the 3D model may be lower than in the 2D model.

Finally, in terms of displacements, the discrepancies are smaller and in the order of 15 and 12 % respectively for the abutment head (Fig. 5.35-a) and for the pile foundation (Fig. 5.35-b).

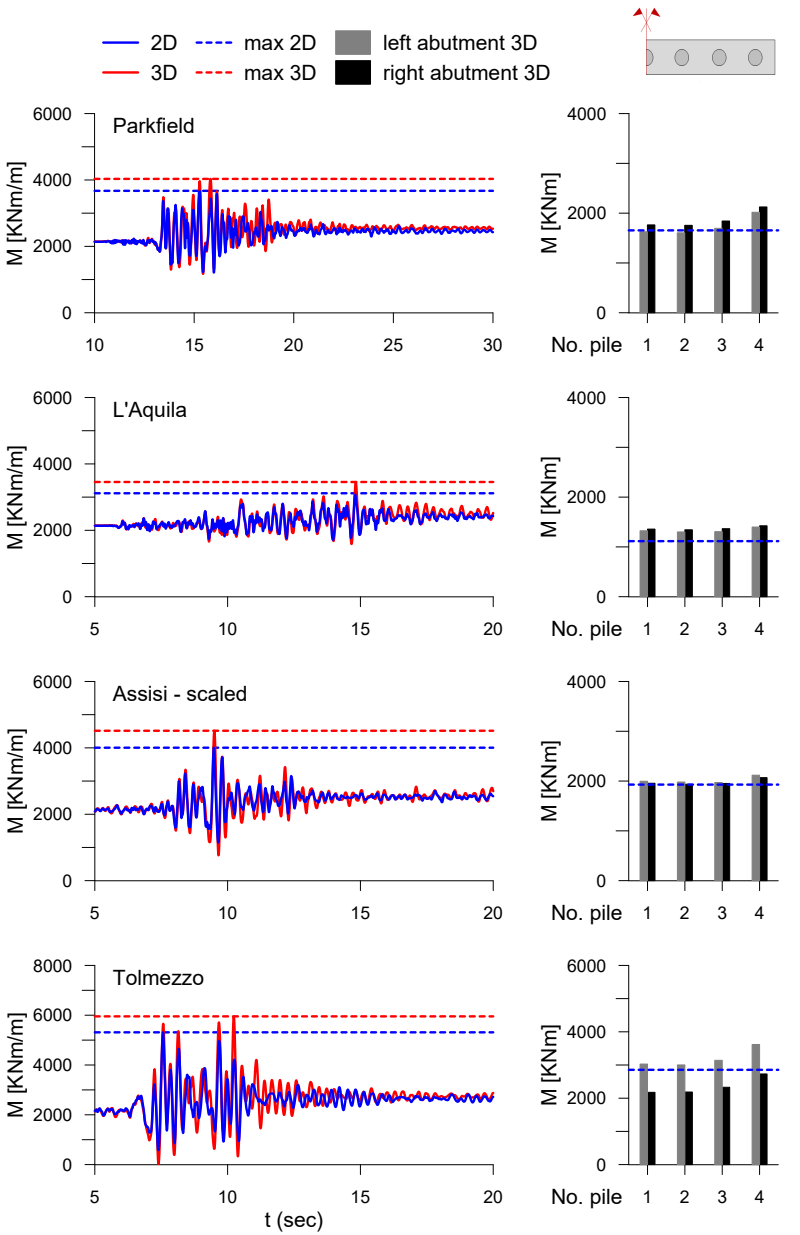

Fig. 5.31. Time histories of the bending moment at deck-abutment node and maximum earthquake-induced bending moment on piles of ground motions listed in Table 5.1 (from 1^{st} to 4^{th}).

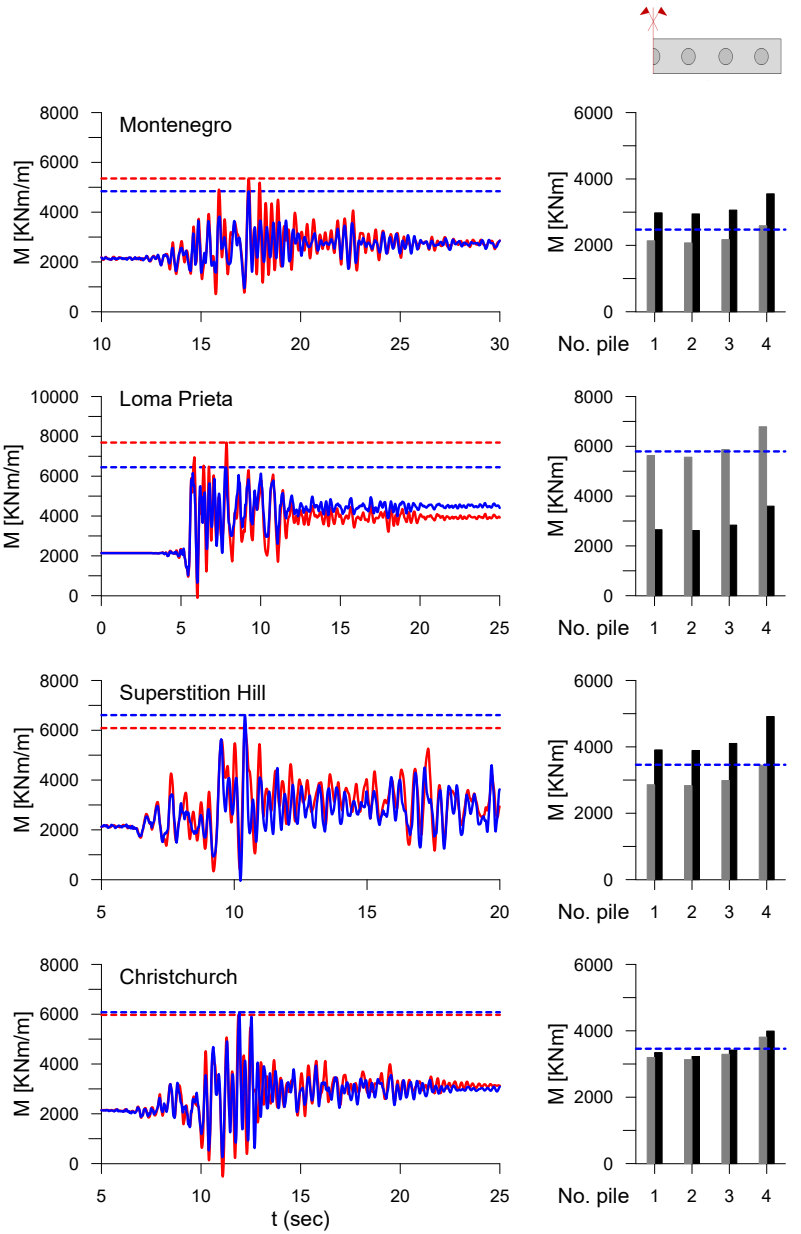

Fig. 5.32. Time histories of the bending moment at deck-abutment node and maximum earthquake-induced bending moment on piles of ground motions listed in Table 5.1 (from 5^{th} to 8^{th}).

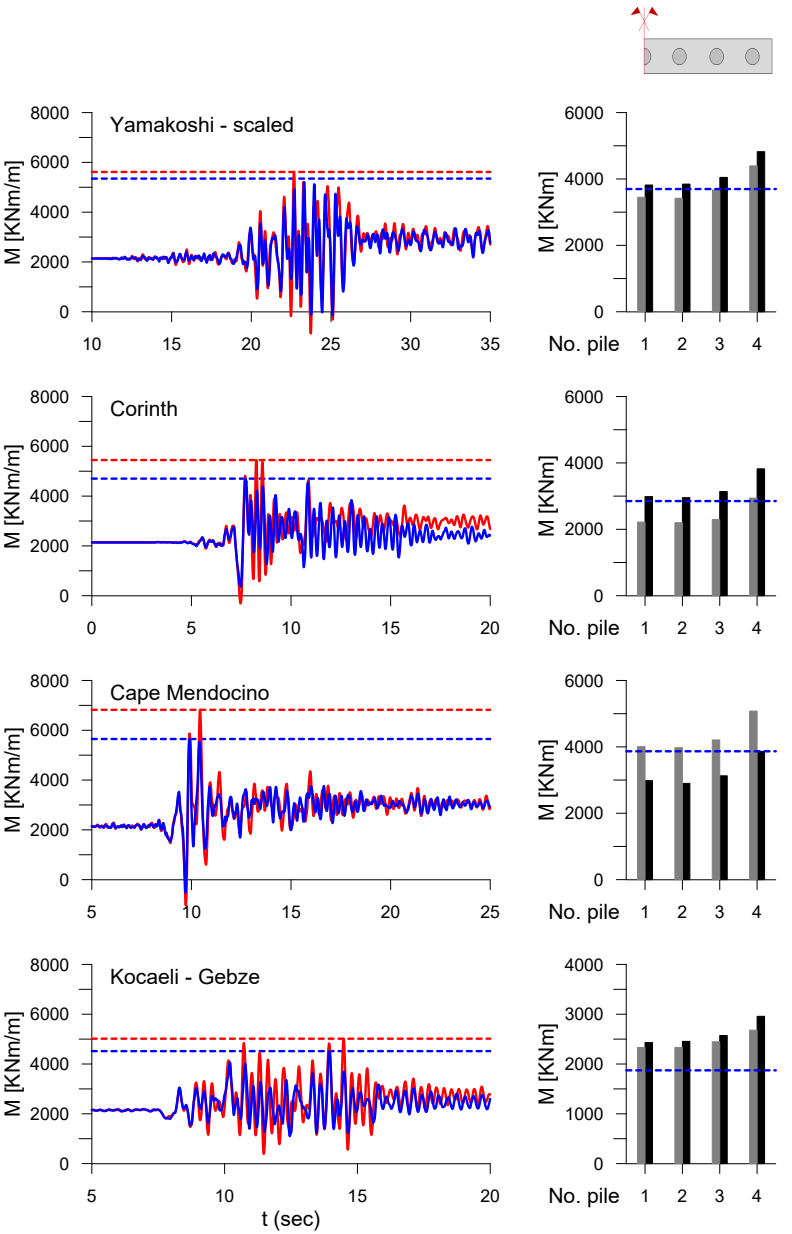

Fig. 5.33. Time histories of the bending moment at deck-abutment node and maximum earthquake-induced bending moment on piles of ground motions listed in Table 5.1 (from 9^{th} to 12^{th}).

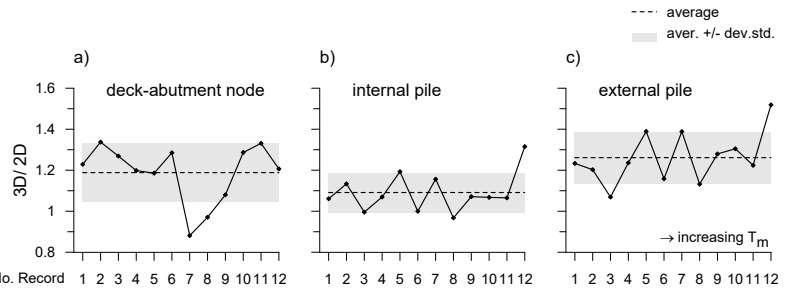

Fig. 5.34. Comparison between the maximum values of bending moment of the 2D and 3D models reached at (a) deck abutment node, (b) internal pile and (c) external pile.

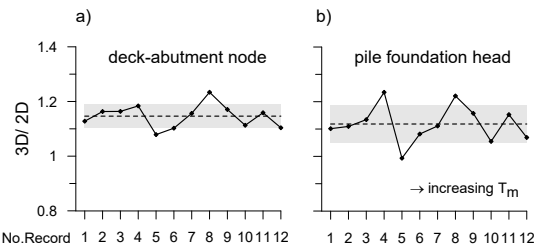

Fig. 5.35. Comparison between the maximum longitudinal displacement of the 2D and 3D models reached at (a) the abutment head and at (b) pile foundation head.

6. Bidirectional effects

This chapter addresses the effects of the bidirectional motion on the seismic performance of the integral abutment bridge herein examined. Specifically, the response of the bridge in the transverse direction produces additional internal forces that cannot be provided by the longitudinal analysis. In the present case study with a regular geometry, these effects are seen to be basically independent from those computed for the longitudinal seismic action; therefore, they can be evaluated separately and then superimposed. In this regard, a further simplified method, easily implementable, is provided for the evaluation of earthquake-induced effects in the transverse direction. The combination of this method with the one proposed in the previous chapter provides a complete tool for the design of these bridges under bidirectional seismic actions without significant underestimations.

6.1. Evaluation of bidirectional effects

Bidirectional effects are evaluated in the full 3D soil-bridge model reported in Fig. 6.1. The global reference system is employed to represent the output quantities such as forces and displacements. The *X-axis* describes the longitudinal direction, the *Y-axis* describes the transverse direction while the *Z-axis* describes the vertical direction. Finally, the definition of the moments follows the convention of the rotation about the respective axes. For example the moment MY, that is the moment about the *Y-axis*, and the force FX are precisely the internal forces involved in the longitudinal response discussed in the previous chapter.

With the aim of having a comparable response in longitudinal and transverse direction, ground motions with the maximum correlation,

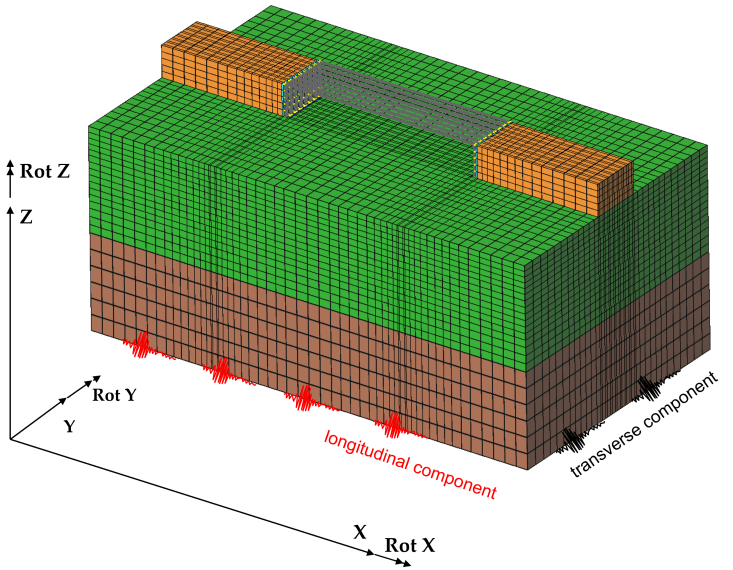

Fig. 6.1. Full 3D soil bridge model for the evaluation of bidirectional effects with the correspondent global reference system.

reported in Tab. 4.10, were used. Furthermore, as already explained in section 4.4, these input motions have been suitably shortened and processed to obtain reasonable analysis times.

The pile foundations are considered the structural elements of major interest for the evaluation of the bidirectional effects. Therefore, from now on, most of the considerations are restricted to these elements. For simplicity, just three piles (Fig. 6.2) for each pile foundation (left and right) are considered in the output quantities: the external piles (No. 1 and No.7) and the central pile (No.4).

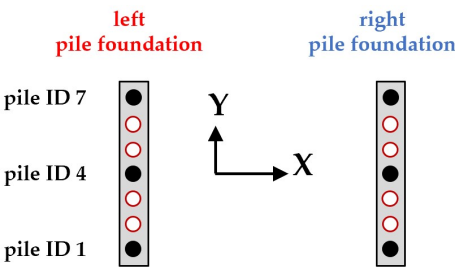

Fig. 6.2. Piles considered in the full 3D soil bridge model for the direct comparison between analyses performed in longitudinal, transverse and bidirectional directions.

As a first evaluation of the bidirectional effects, we first focus on the behavior of the pile foundation in both the longitudinal and transverse direction when subjected to a two-directional motion. The distributions of the bending moments computed for Yamakoshi and acting in the longitudinal and transverse plane, in correspondence of the pile No.1 of the right foundation, are depicted in Fig. 6.3-a. The differences in the two configurations can be obviously ascribed to the different degree of constraint in correspondence of the pile cap. The corresponding curvatures, computed in correspondence of the Gauss points of the beam elements, are reported in Fig. 6.3-b. Fig. 6.3-c instead indicates the distributions of the longitudinal and transverse displacements in the right pile foundation in the same instants. The time histories of the displacement at the top of both pile foundations are reported in Fig. 6.4. Fig. 6.4-a shows that the two foundations move closer in the longitudinal direction, as already observed in chapter 5. In fact, the permanent displacement assumes a positive value for the left foundation and negative for the right one. Conversely, in the case of the transverse direction, the two foundations seem to have undergone the same displacement.

The piles depicted in Fig. 6.2 are now used for a direct comparison between three different analyses performed on the full 3D soil-bridge model: the one-directional analysis along the longitudinal direction, the one-directional analysis along the transverse direction and the two-directional analysis. In addition, unless otherwise specified, all the reported internal forces refer to the pile heads.

Fig. 6.5 shows the time histories of the longitudinal force FX at the head of the examined piles in the left (Fig. 6.5-a) and right (Fig. 6.5-b) pile foundations for the Yamakoshi ground motion. The effect of the one-directional transverse analysis on these forces is negligible; in fact, the time histories relating to the two-directional analysis are only slightly larger than those evaluated from the one-directional longitudinal analysis. In addition, the same observation can be made about the time histories of the bending moment MY depicted in Fig. 6.6. It is evident that the internal forces FX and MY are essentially related to the longitudinal component of the seismic motion only, as discussed in the previous chapter.

Conversely, the bidirectional effects become evident for the purpose of evaluating the internal forces related to the transverse motion component, such as FY, MX and FZ. In this regard, Fig. 6.7 reports the time histories of the transversal force FY at the head of the examined piles in

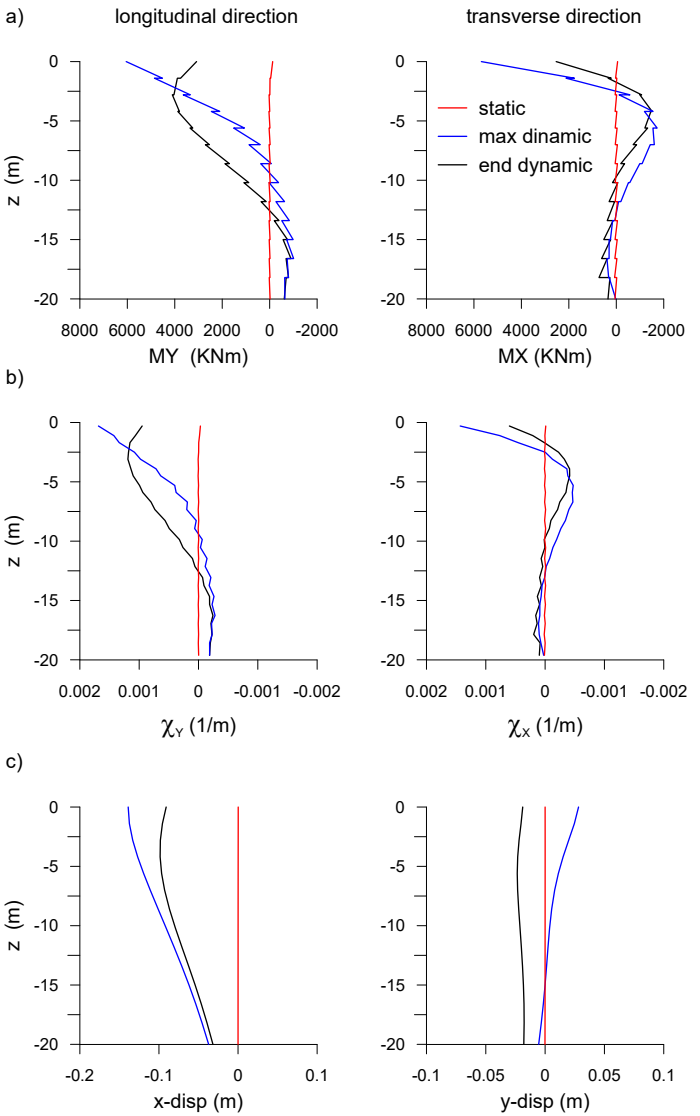

Fig. 6.3. Distribution of the (a) bending moments MY and MX in the pile No.1 of the right foundation and corresponding (b) curvatures. Distribution of the (c) displacements in the right pile foundation.

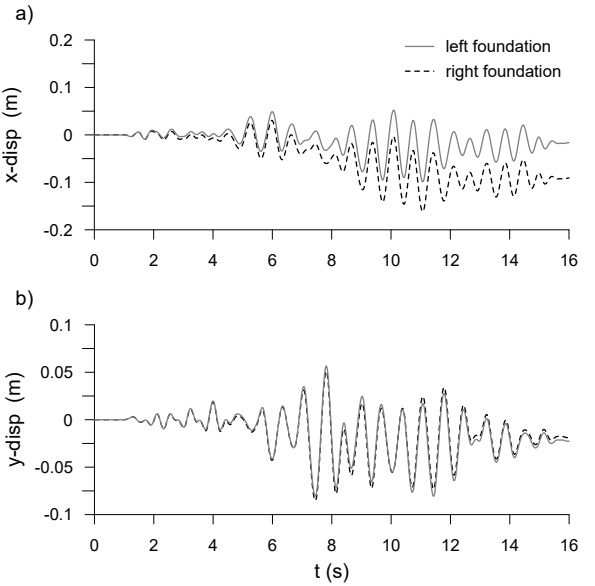

Fig. 6.4. Time histories of the (a) longitudinal displacement and of the (b) transverse displacement computed for both pile foundations.

the left (Fig. 6.7-a) and (Fig. 6.7-b) right pile foundations. As expected the one-directional longitudinal analysis cannot provide these forces; however, the time histories obtained from the two-directional analysis appear to be reasonably reproducible from the one-directional analysis that only considers the transverse motion component.

Similar considerations can be made about Fig. 6.8 that reports the time histories of the moment MX, representing the moment around the longitudinal axis at the pile heads due to the effect of impeded rotation. From this point of view, the FY forces and the MX moments can be considered two sides of the same coin.

Finally, the assumption that the behavior of this system is essentially given by the superimposition of the one-directional longitudinal and transverse analysis is confirmed in Fig. 6.9, reporting the time histories of the axial forces FZ at the head of the examined piles. The evaluation of these forces is paramount, not only for the geotechnical design of the piles but also for the design of the resistance and ductility of a concrete cross section like the one considered in this case study. This variation of the axial forces in the external piles can be attributed to the rocking mechanism in the transverse direction. In fact, the axial forces in the

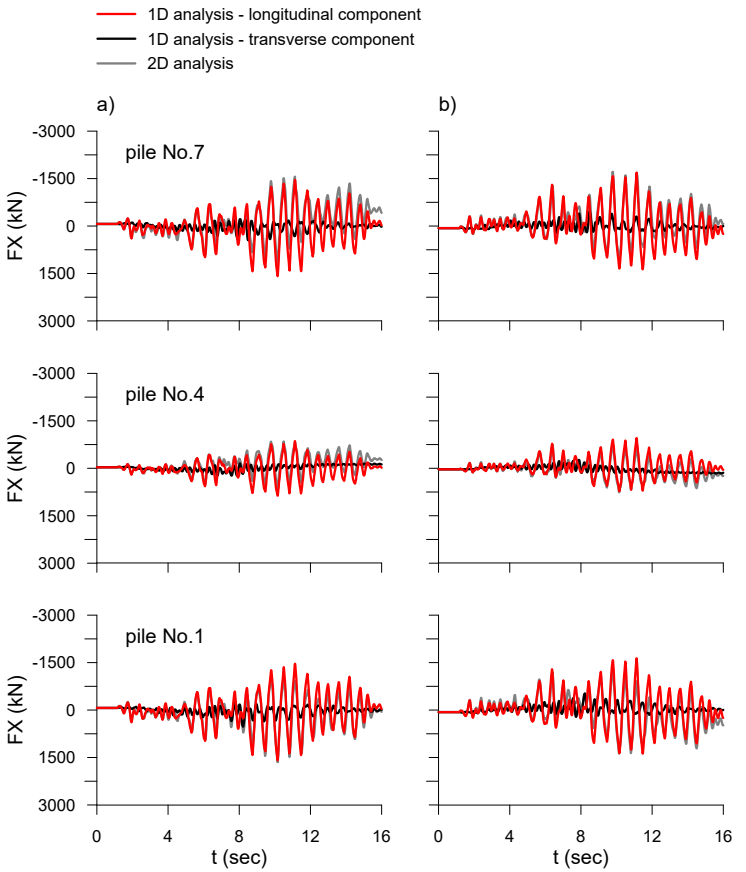

Fig. 6.5. Yamakoshi record: comparison between the time histories of the forces FX in the (a) left foundation and (b) right foundation, assuming one-directional (longitudinal or transverse) and two-directional analyses.

central piles oscillates slightly with respect to the values reached at the end of the static conditions.

In the light of these considerations, it is clear that the internal forces can be provided by the combination of both the one-directional longitudinal and transverse components of the seismic motion, applied individually. The bidirectional effects only involve small increments that could be neglected for ordinary design purposes. In particular, FX and MY are reasonably provided by the longitudinal analysis while FY, MX and FZ are given by the transverse analysis. For this reason, from now on, it makes sense to compare the two-directional analysis with

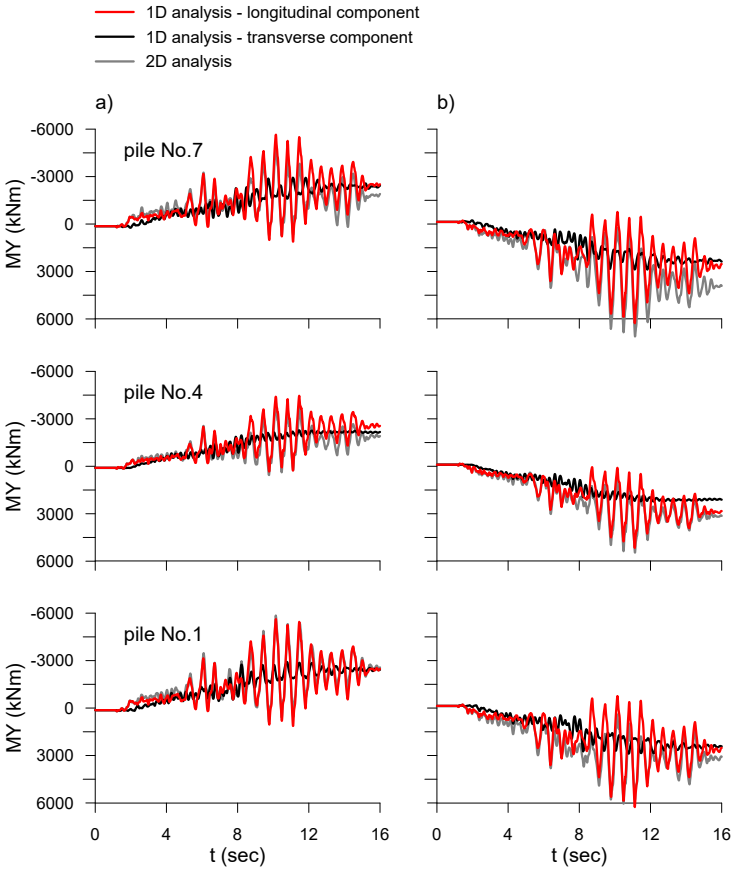

Fig. 6.6. Yamakoshi record: comparison between the time histories of the bending moment MY in the (a) left foundation and (b) right foundation, assuming one-directional (longitudinal or transverse) and two-directional analyses.

the one-directional longitudinal analysis for FX and MY and with the one-directional transverse analysis for FY, MX and FZ.

Fig. 6.10 reports a summary of the variation of the internal forces in correspondence of the scrutiny piles due to the bidirectional effects respect to the one-directional analyses for the Yamakoshi ground motion. In particular the comparison is made with reference to the one-directional longitudinal analysis (FX and MY) in Fig. 6.10-a and to the one-directional transverse analysis (FY, MX and FZ) in Fig. 6.10-b. Regarding the numbering shown on the x-axis, piles No. 1 and No. 3 indicates the external ones, while pile No.2 is the central pile in the left

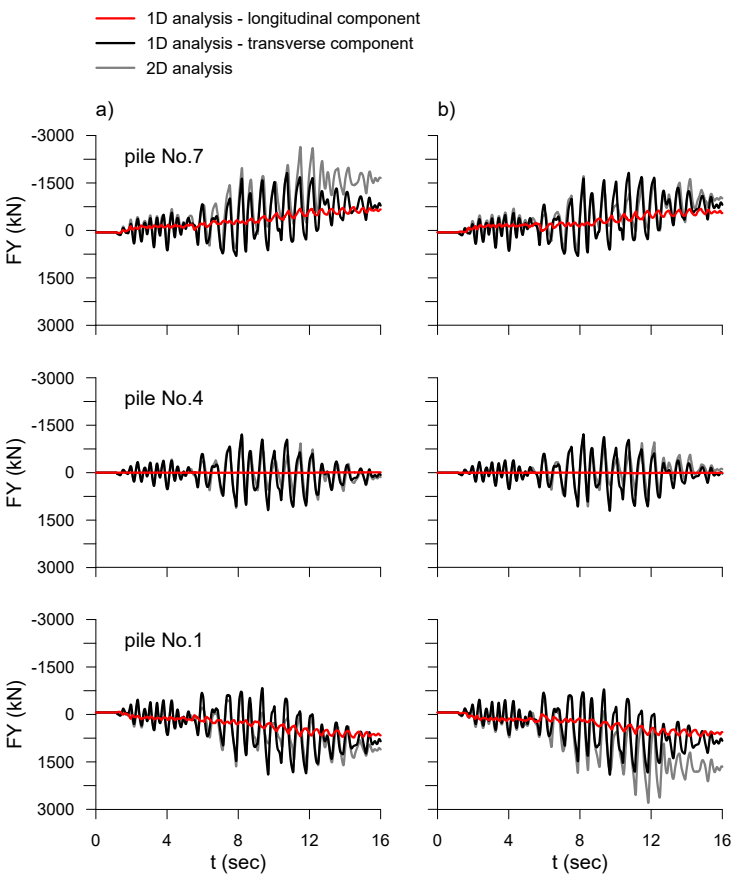

Fig. 6.7. Yamakoshi record: comparison between the time histories of the forces FY in the (a) left foundation and (b) right foundation, assuming one-directional (longitudinal or transverse) and two-directional analyses.

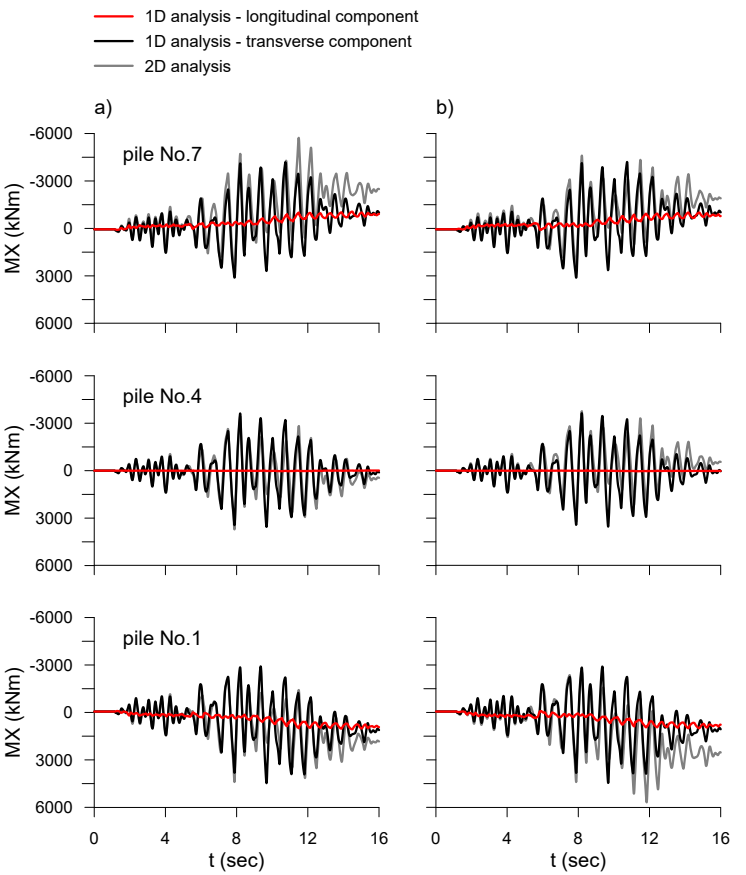

Fig. 6.8. Yamakoshi record: comparison between the time histories of the bending moment MX in the (a) left foundation and (b) right foundation, assuming one-directional (longitudinal or transverse) and two-directional analyses.

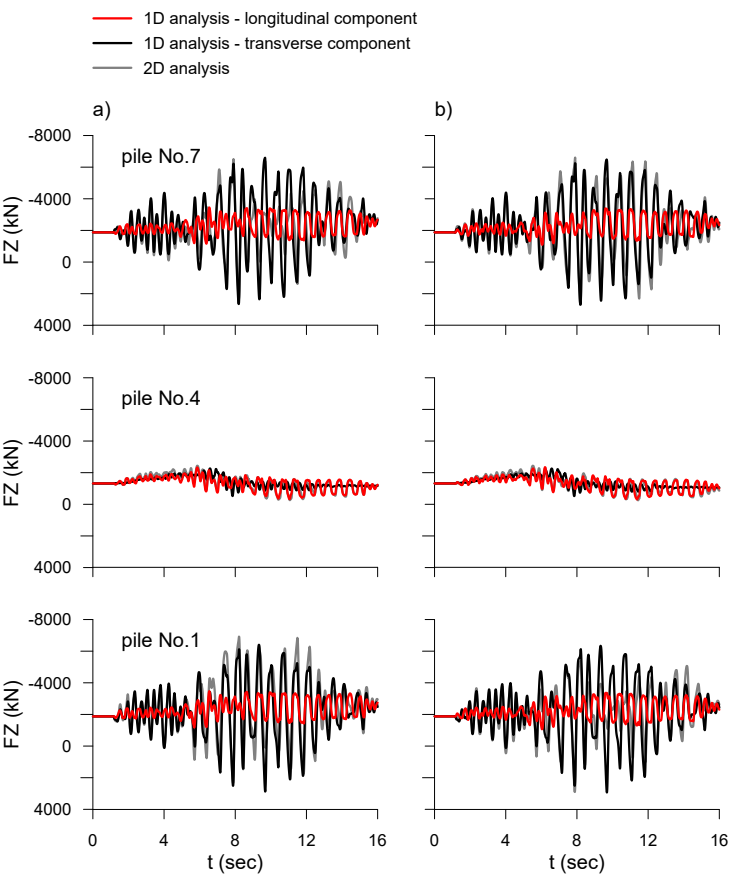

Fig. 6.9. Yamakoshi record: comparison between the time histories of the forces FZ in the (a) left foundation and (b) right foundation, assuming one-directional (longitudinal or transverse) and two-directional analyses.

foundation. Similarly, piles No. 4 and No. 6 represent the external ones, with pile No.5 being the central one in the right foundation. The percentage variations refer to the maximum values of the seismic increments evaluated for each pile, while the term *average* indicates the average of these maximum values.

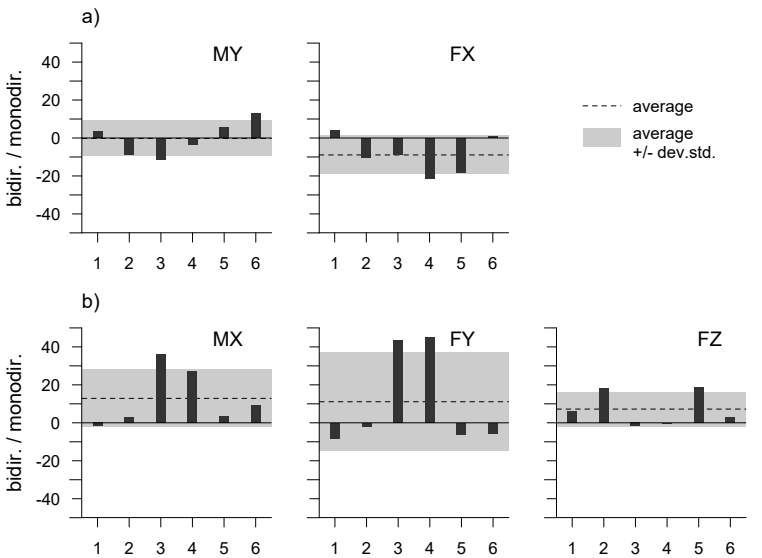

Fig. 6.10. Yamakoshi record: variations (%) of the internal forces in the scrutiny piles due to the bidirectional effects compared to the one-directional (a) longitudinal and (b) transverse analyses.

Fig. 6.10-a shows that the maximum values provided by the one-directional longitudinal analysis for MY are quite close to the maximum values of the two-directional analysis; the average variation is almost nil and the standard variation is smaller than 10 %. In the case of FX, the one-directional analysis produces an average overestimation of the force in the order of 10 % and the standard variation of about 10 %. Generally, it appears that the variations observed in the piles for FX are bigger. In fact, the internal force MY can be conceived as a *global quantity* affected by the overall response of the pressure behind the abutment; on the contrary, FX is really influenced by local stress concentrations. Nevertheless, from a practical standpoint, performing just the one-directional longitudinal analysis, as suggested in the previous chapter, leads to a reasonable evaluation of MY and FX at the pile heads.

Regarding MX and FY, both represented in Fig. 6.10-b, local variations of about 30-45 % are registered for the piles No. 3 and 4 (respectively the No.7 in the left foundation and the No. 1 in the right foundation showed in Fig. 6.7 and in Fig. 6.8). Nevertheless, the differences in the other piles are negligible and the average variation is in the order of 10 %. The variations of the axial forces FZ are reported in Fig. 6.10-b; the one-directional transverse analysis provides satisfactory results with an average variation less than 10 %. Note also that, the piles where these variations are higher (No. 2 and 5) are precisely the central piles of the left and right foundations (reported in Fig. 6.9) whose absolute values are much lower than those of the external piles.

Fig. 6.11 reports a summary of the variations of the same quantities for the Parkfield record. As for the Yamakoshi record, the one-directional longitudinal analysis showed in Fig. 6.11-a provides a good estimation of MY and FX with an average error less than 5 %.

The variations of MX, FY and FZ induced by the two-directional analysis respect to the one-directional transverse analysis are illustrated in Fig. 6.11-b. Also in this case, the average differences are negligible and in the order of 10 %.

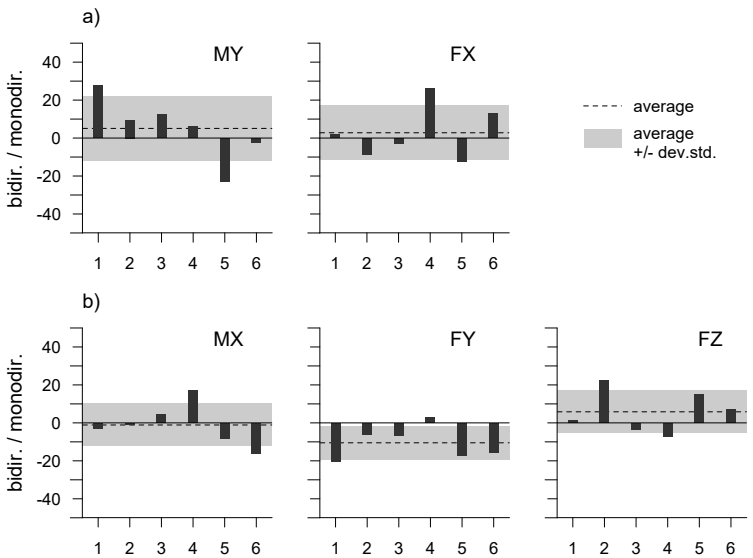

Fig. 6.11. Parkfield record: variations (%) of the internal forces in the scrutiny piles due to the bidirectional effects compared to the one-directional (a) longitudinal and (b) transverse analyses.

6.2. Development of a simplified method for the transverse motion

This section describes a simplified method aimed at evaluating the internal forces in the pile foundation caused by the one-directional transverse component of the seismic motion. Since the longitudinal and transverse responses of the bridge under examination can be considered decoupled, the proposed application can be conceived as complementary to the procedure illustrated in chapter 5. This approach is validated against the results of several dynamic analyses carried out on the half 3D transverse model described in section 3.3.3, and all seven piles are considered in the output quantities.

6.2.1. Seismic input

The seismic records are selected through the PEER database and are listed in Table 6.1, where they are sorted for a decreasing frequency content according to the mean quadratic period T_m (Rathje et al. 1998). Parkfield and Yamakoshi records correspond to the ground motions of Table 4.10 along the *direction 2*, while the others were already presented in Tab. 5.1. The 5 %-damped elastic average response spectrum of the transverse components of the selected records, shown in Fig. 6.12-a, reproduces in the average the Type 1 elastic spectrum on soil type A according to the current Eurocode (2003). All ground motions are used with their actual record amplitudes, with the exception of *Assisi* (RSN 4345), that was scaled by a factor of 1.65. Fig. 6.12-b shows the elastic average response spectrum obtained propagating the signals of Fig. 6.12-a through a one-dimensional sub-model including the foundations soil and the embankment.

6.2.2. Schematic interpretation

In order to evaluate the transverse effects, a schematic interpretation with all the inertial forces involved is depicted in Fig. 6.13: *F deck* is the inertial force associated to the excitation of the mass of the deck, *F abutment* is associated to the mass of the abutment while *F embankment* is the inertial force associated to the mass of the embankment, proportional to the length of the embankment in the longitudinal direction *L embankment*. The latter quantity is unknown because depends on the participating mass of the embankment involved in this mechanism. These inertial forces, in turn, generate a transverse force *FY* at the head of each pile

Tab. 6.1. Characteristics of the selected seismic records for analyses in the transverse direction.

Event	*Record*	PGA (g)	I_A (m/s)	T_s (s)	T_m (s)	$V_{S,30}$ (m/s)	R_{JB} (km)	Mw $(-)$
Parkfield	RSN 4064	0.35	0.53	5.8	0.23	657	6.0	4.3
Assisi	RSN 4345	0.28	0.75	4.3	0.25	377	6.0	16.6
Tolmezzo	RSN 125	0.35	0.80	4.2	0.41	505	6.5	15.0
Loma Prieta	RSN 753	0.64	3.24	6.9	0.49	462	6.9	0.2
Christchurch	RSN 8124	0.29	1.13	9.5	0.61	293	6.2	9.4
Yamakoshi	RSN 4868	0.31	2.80	14.5	0.66	655	6.8	22.2
Cape Mendocino	RSN 3749	0.33	1.31	11.5	0.71	355	7.0	16.5

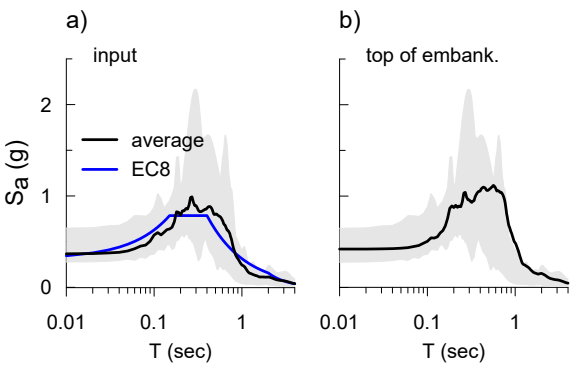

Fig. 6.12. (a)5 %-damped elastic response spectra of the input ground motions reported in Table 6.1 and (b) 5 %-damped elastic response spectra evaluated at the top of the embankment through a site response analysis.

and a rocking moment, inducing a cyclic variation of the axial force FZ in the piles. As already explained in the previous section, the bending moment MX is a derived quantity that arises at pile heads due to the effect of the impeded rotation. Finally, the development of the angular acceleration $\ddot{\theta}$ in the bridge-abutment system generates an additional moment that increases the axial forces in the piles.

Fig. 6.14 shows the normalised frequency content of the internal forces induced by the one-directional transverse analysis at the head of an external pile. The vertical load FZ appears slightly more stressed by the higher frequencies, likely due to the effects induced by the rotational motion of the bridge-abutment system. However, the frequency

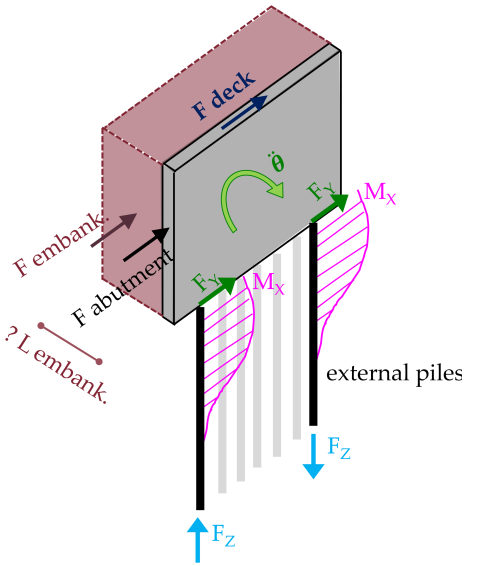

Fig. 6.13. Schematic interpretation of the transverse mechanism along with a description of the involved inertial forces and the generated internal forces.

contents are very similar, suggesting that all these internal forces may be evaluated with a single calculation scheme.

The rocking moment is effectively illustrated by the time-history of the axial forces of Fig. 6.15. The external piles are the more interested by this effect (No. 1 and 7) while the axial force in the central pile (No.4) tends to slightly oscillate about the value reached at the end of the static analysis. The increments of the axial forces in the external piles are in phase opposition: for example a positive variation in the pile No. 1 corresponds to a negative variation in the pile No.7. This means that in the pile cross section, from an initial state of compression, a state of tension could be generated.

The development of the transverse forces FY at the pile heads and of the corresponding bending moments MX is depicted in Fig. 6.16. Generally, these internal forces are distributed roughly equally between all the piles. However, in the right column of the Fig. 6.16, a deviation of the time histories with the time is observed. Let us consider that the pile No.1 and the pile No. 7 are respectively placed in the right and left edge of the left foundation (Fig. 6.2), with reference to an observer who looks in the direction of the positive X. Applying now a force in the direction

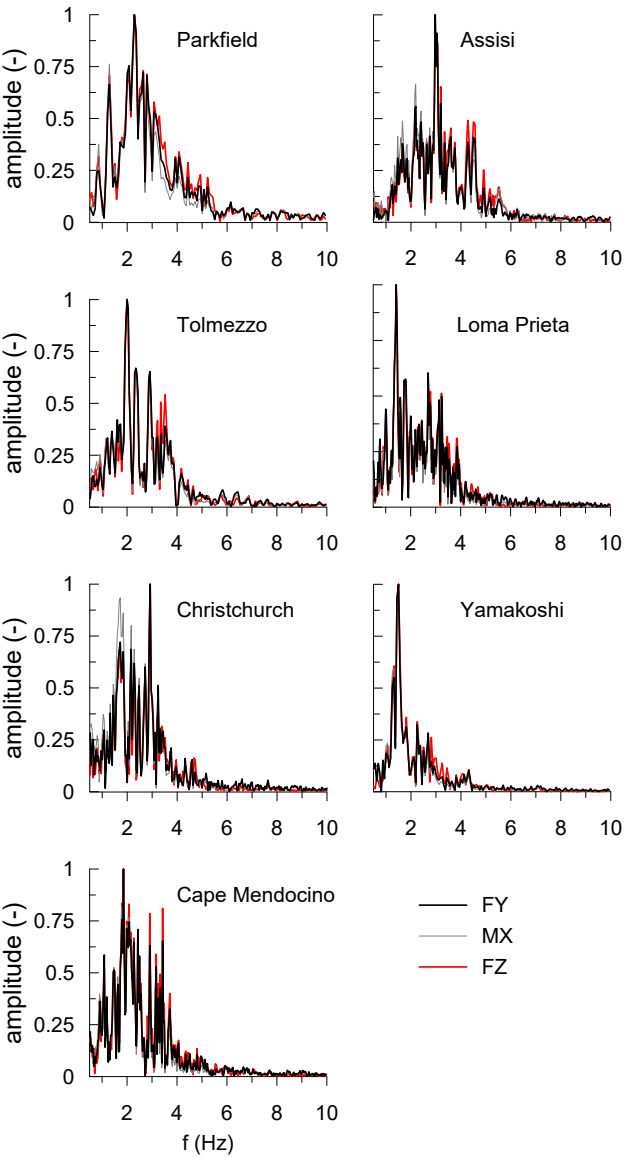

Fig. 6.14. Normalized frequency contents of the internal forces (FY, MX, FZ) belonging to the transverse mechanism.

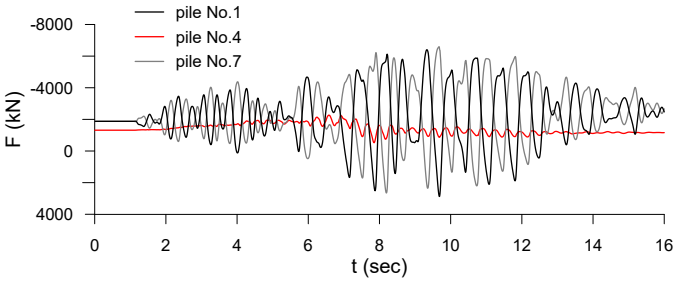

Fig. 6.15. Yamakoshi record: time histories of axial forces in the piles in the same foundation.

of the increasing Y, the pile No. 1 will be slightly more loaded than pile No. 4 which in turn, will be slightly more loaded than pile No. 7. By reversing the direction of the force, the pile No.7 will be obviously the most loaded. As cycles go by, these small differences tend to accumulate. This explains why at the end of the analysis an appreciable difference in residual forces is generated. Finally, note that these differences are a results of non-linearity effects in the soil. In fact, these discrepancies are imperceptible in the first 8 seconds.

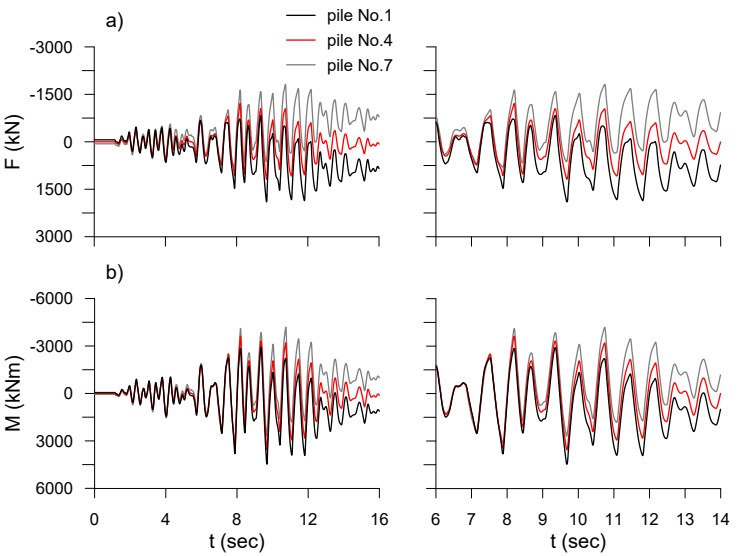

Fig. 6.16. Yamakoshi record: time histories of (a) forces FY and (b) bending moments MX in the piles. The right column shows a zoom of these time histories.

The correlation between the internal forces FY and MX is reported in Fig. 6.17 for Yamakoshi (Fig. 6.17-a) and Parkfield (Fig. 6.17-b) records. Because in this direction the pile is restrained to rotate at the top and subjected to a horizontal force FY, the bending moment MY that develops at the pile heads to restrain the rotation may be computed, assuming a Winkler's subgrade model, with the following expression:

$$MX = C_M \cdot \lambda \cdot FY = const \cdot FY \tag{6.1}$$

where λ is the characteristic length. For a infinitely long pile, the coefficient C_M assumes the value of 0.93. For the pile foundation in question the value of λ is about 3.0 and hence the constant coefficient is about 2.8. Once this coefficient and the time history of FY are known, it is possible to compare the bending moment obtained with the Eq. 6.1 with the bending moment actually observed in the analysis. This comparison, reported in Fig. 6.18-a/b, respectively for Yamakoshi and for Parkfield, confirms the previous hypothesis.

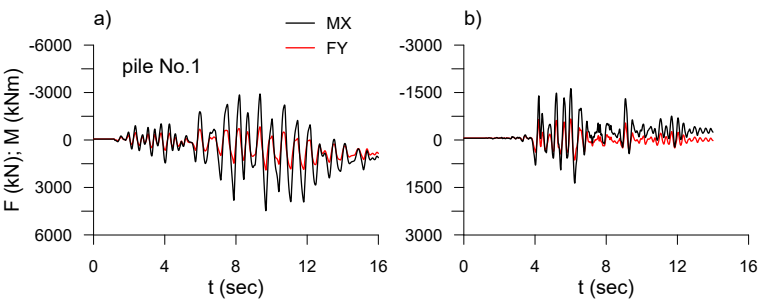

Fig. 6.17. Time histories of forces FY and bending moments MX in the pile No.1 for (a) Yamakoshi and (b) Parkfield.

Finally, looking at the time histories of the force FZ and the bending moment MX reported in Fig. 6.19 and evaluated in correspondence of the top of the pile No.1, it appears that these two internal forces are perfectly in phase, demonstrating once again that both derive from the same mechanism analysed so far.

6.2.3. Expeditious evaluation of angular acceleration

An expeditious evaluation of the angular acceleration $\ddot{\theta}$ illustrated in Fig. 6.13 is now illustrated. In fact, the presence of the embedment foundation, represented by the pile foundation and the abutment itself,

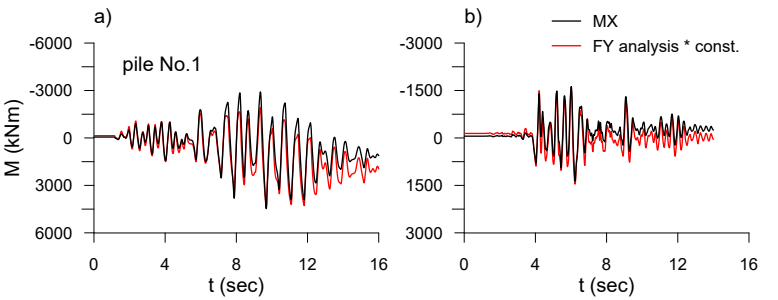

Fig. 6.18. Relationship between forces FY and bending moments MX in the same pile using Winkler coefficient for (a) Yamakoshi and (b) Parkfield.

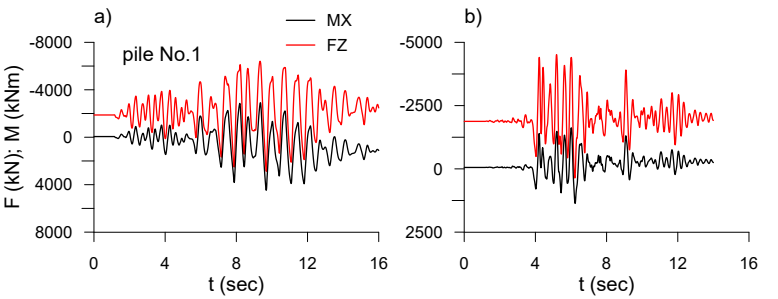

Fig. 6.19. Time histories of forces FZ and bending moments MX in the pile No.1 for (a) Yamakoshi and (b) Parkfield.

combined with the monolithic deck-abutment connection, induces an additional moment that should be considered.

Fig. 6.20 shows the contours of vertical acceleration on the abutment for different ground motions at selected instants of interest. In general, since the gradient is approximately parallel to the transverse direction, the abutment is subjected to a rotation. This rotation can be computed once the time histories of the vertical acceleration at the nodes belonging to the external vertical beams of the abutment have been obtained. At this point, as illustrated in Fig. 6.21, the definition of the angular acceleration $\ddot{\theta}$ is straightforward. It can be shown that the time histories of the angular acceleration do not vary along the height of the abutment; therefore, the entire abutment including the abutment-deck node, can be thought as a single rigid body. The time histories, determined with the scheme of Fig. 6.21 and reported in Fig. 6.22, show that the angular acceleration is in the range of 5-15 deg/s^2.

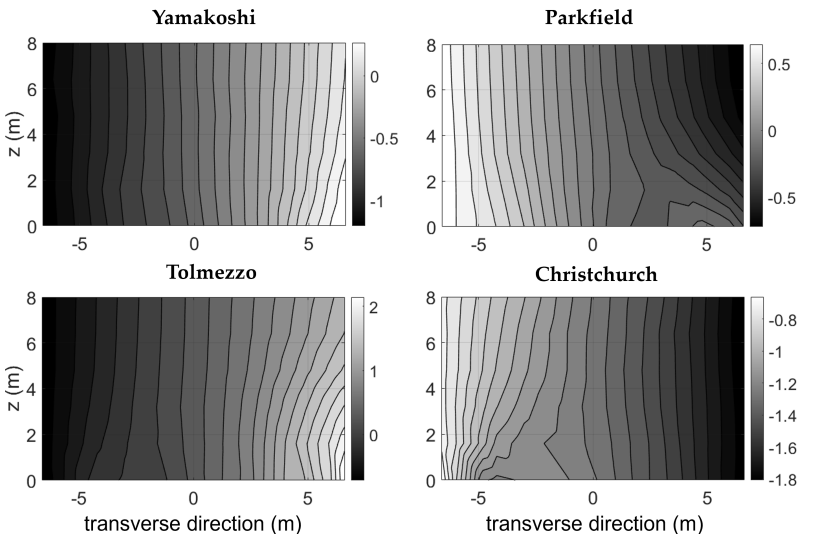

Fig. 6.20. Contours of vertical acceleration (m/s^2) in the abutment for Yamakoshi (t=9.685 s), Parkfield (t=5.185 s), Tolmezzo (t=5.56 s) and Christchurch (t=9.9375 s).

In the absence of a numerical analysis, the rotational acceleration of the abutment-deck system may be evaluated using solutions proposed in the literature regarding the rotational motion induced in embedded foundations by kinematic interaction effects. The available solutions apply to rigid massless cylinders embedded in a uniform soil of finite or

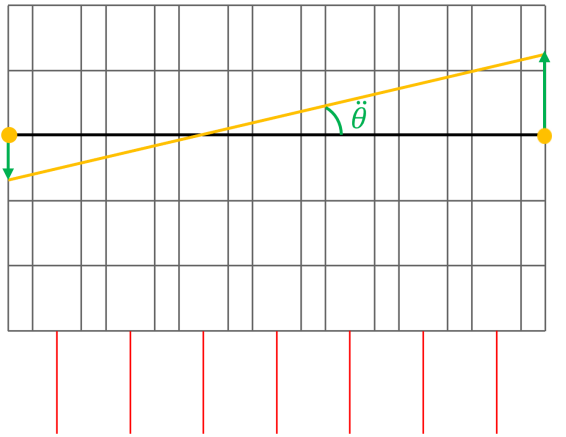

Fig. 6.21. Computation of the angular acceleration starting from the time histories of the vertical acceleration at the nodes of the external vertical beams of the abutment.

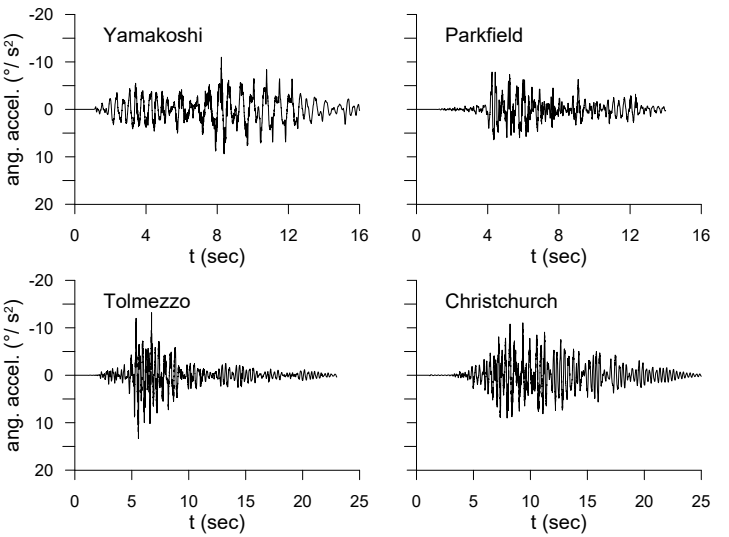

Fig. 6.22. Time histories of angular acceleration of the abutment for different input motions.

infinite thickness (halfspace). When subjected to vertically propagating coherent SH waves, the embedded cylinders experience a reduction in base-slab translational motion relative to the free-field due to ground motion reductions with depth and wave scattering effects. In addition, rotations in the vertical plane are introduced.

Elsabee and Morray (1977) and Day (1978) developed analytical transfer functions relating base-slab translational and rotational motions to free-field translations for an incident wave field consisting of vertically propagating, coherent SH waves. The amplitude of the halfspace and finite soil layer transfer functions are shown together in Fig. 6.23-a for foundation *embedment/radius* ratio $e/r = 1.0$ while Fig. 6.23-b shows similar results for the rocking component of the foundation input motion. In this case, the approximate transfer function is given by:

$$|H_\theta(\omega)|\, r = 0.257 \cdot [1 - \cos\left(\frac{e}{r}\right) a_0] < 0.257 \qquad (6.2)$$

where H_θ indicates the FIM/free-field transfer function , e = foundation embedment, r = effective foundation radius, $a_0 = \omega r / V_S$ with ω circular frequency in rad/sec and V_S = soil shear wave velocity.

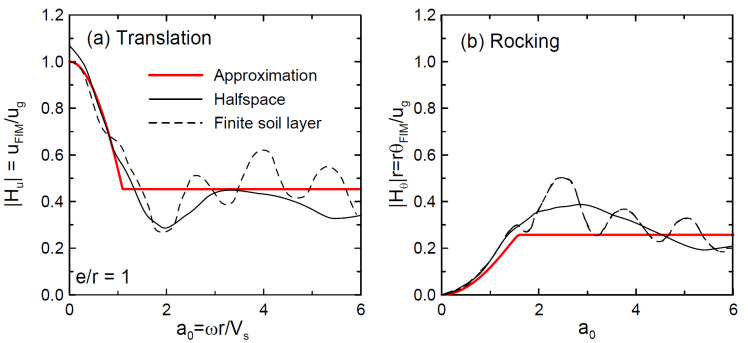

Fig. 6.23. Solutions for the transfer functions between foundation input motions and free-field motions for translation and rocking of embedded rigid cylinders. Halfspace solution is from Day (1978) and finite soil layer case is from Elsabee and Morray (1977).

Regarding non circular foundations, Mita and Luco (1989) found that an embedded square foundation could be replaced by an equivalent cylinder without introducing significant error. The radius of the equivalent cylinder was defined as the average of the radii necessary to match the area and moment of inertia of the square base.

The embedded foundation of the present case study can be conceived as a combination of the abutment and the pile foundation; the foundation

embedment e is therefore equal to 28 m $(20 + 8)$. In addition, being rectangular in shape, the equivalent cylinder radius r_{eq} was defined on the basis of an equivalence with the second moment of inertia. Table 6.2 lists the additional parameters used for the calculation: V_S is the average soil shear velocity below the pile foundation and ω_0 is the circular frequency corresponding to the first mode of the soil column.

Tab. 6.2. Parameters for evaluating the kinematic interaction.

B (m)	t (m)	I (m^4)	r_{eq} (m)	e (m)	V_S (m/s)	T_0 (s)	ω_0 (rad/sec)	a_0 (rad)
13.2	2.2	421.7	4.8	28.0	300	0.6	10.5	0.17

The angular acceleration can be determined once the horizontal acceleration a_{ff} is obtained from a free field analysis, according to the following expression:

$$\ddot{\theta} = \frac{|H_\theta(\omega)|\, r \cdot a_{ff}}{r} \tag{6.3}$$

In turn, the horizontal acceleration a_{ff} represents the spectral acceleration $S_{a\,(\xi)}$ computed at the top of the embankment, relative to the period T_0 of the first mode of the soil column at small strains (0.6 sec) and to a representative damping value obtained from an equivalent-linear site response analysis (Fig. 6.24). In this regard, it was considered the average damping mobilised in the embankment (first 8 m). Table 6.3 reports these damping-ratio values with the correspondent spectral accelerations. Actually, the damping associated with the average spectrum is indicative only, because the spectral acceleration is obtained averaging the single values of each motion. In the end, the angular accelerations are finally determined by using Eq. 6.3.

Fig. 6.25-a shows a comparison between the angular accelerations evaluated with this simplified procedure and the angular accelerations obtained from dynamic analyses. The blue line refers to the maximum angular accelerations, while the red one corresponds to the angular accelerations values evaluated at the instants when the maximum rocking moment is reached in the pile foundation. Considering the simplicity of the method, the comparison offers satisfactory results, especially if the average acceleration is considered. A better correspondence would be obtained if the periods T_m (Rathje et al. 1998) of each ground motion were used for the definition of the circular frequency ω_0 in Eq. 6.3.

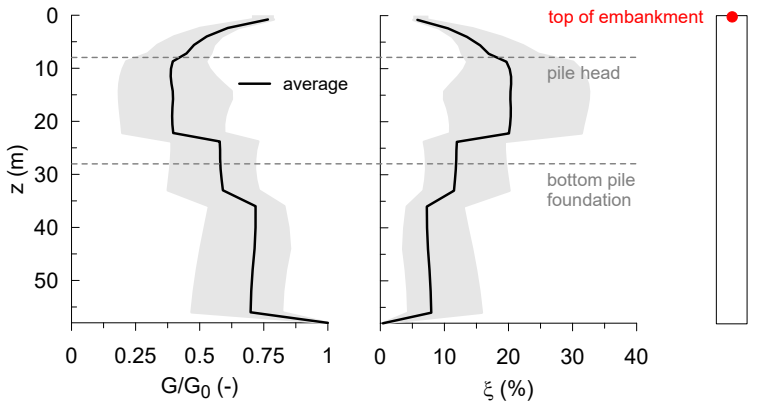

Fig. 6.24. Average shear modulus and damping mobilised in the equivalent-linear site response analysis.

However, thinking of a simplified method based on the use of a design spectrum, the use of the first mode of the soil column for the definition of the circular frequency ω_0 is more easily applicable. This value is therefore taken as reference in the rest of the discussion.

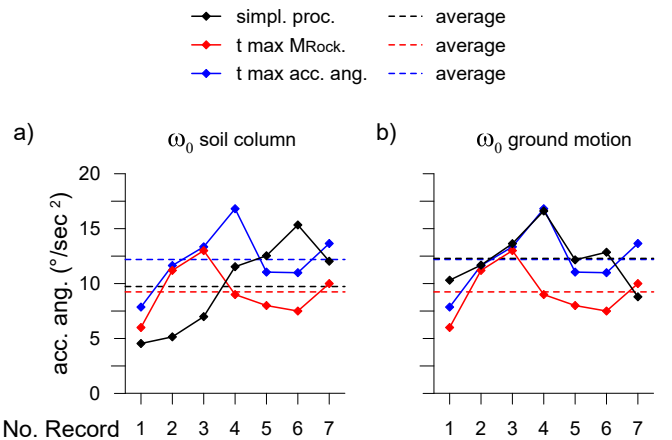

Fig. 6.25. Comparison between the angular accelerations provided by the simplified procedure and the angular accelerations obtained in the dynamic analyses. Circular frequency ω_0 correspondent to the first period of the soil column (a) and to the frequency content T_m (Rathje et al. 1998) of each ground motion (b).

Once the angular acceleration has been evaluated, it is necessary to proceed with the determination of the polar moment of inertia. An appropriate clarification must be made regarding the point of application

Tab. 6.3. Evaluation of horizontal and angular accelerations. Note that the damping associated with the average spectrum is indicative only because the spectral acceleration is obtained averaging the values of each motion.

	$S_{a\ 5\%}$ (g)	ξ $(\%)$	$S_{a\ (\xi)}$ (g)	$\ddot{\theta}$ $(^\circ/sec^2)$
Parkfield	0.43	11.1	0.34	4.5
Assisi	0.51	10.1	0.39	5.1
Tolmezzo	0.68	11.6	0.53	7.0
Loma Prieta	1.24	17.6	0.87	11.5
Christchurch	1.46	11.9	0.95	12.5
Yamakoshi	1.96	13.1	1.16	15.3
Cape Mendocino	1.32	11.9	0.91	12.0
average spectrum	1.09	$(12.5)^*$	0.74	9.7

of the forces shown in Fig. 6.13. Since the abutment-deck contact is of the integral type, the abutment-deck-embankment system can be regarded as a single macro-system (Fig. 6.26-a/b) with the forces applied in just one point. However, the center of gravity of this system indicate with G in Fig. 6.26 depends on the involved embankment length. Fig. 6.27-a shows the variation of the center of gravity (h_G) with the length of the embankment. By varying this height, the contribution of the transport polar moment of inertia varies as well. Table 6.4 shows the values of the barycentric and overall polar moment of inertia of the deck and abutment for a length of embankment equal to $L = 0$. Fig. 6.27-b shows that in reality this polar moment of inertia $(J_{p\,abut.+deck.})$ remains almost constant, while, obviously, the contribution of the embankment increases with the increase of L. The same figure also shows the evolution of the additional rotational moment $(M = J_{p,TOT} \cdot \ddot{\theta})$ considering an average angular acceleration of 10°.

Tab. 6.4. Polar moment of inertia of the abutment-deck system $(L_{embank.} = 0)$.

h_G (m)	$J_{pG,deck}/2$ (Mgm^2)	$m_{deck}/2$ (Mg)	d_{deck} (m)	$J_{pG,abutm.}$ (Mgm^2)	$m_{abut.}$ (Mg)	$d_{abutm.}$ (m)	$J_{p,TOT}$ (Mgm^2)
5.79	7024.0	478.2	2.21	11754.1	592.0	1.79	23106.5

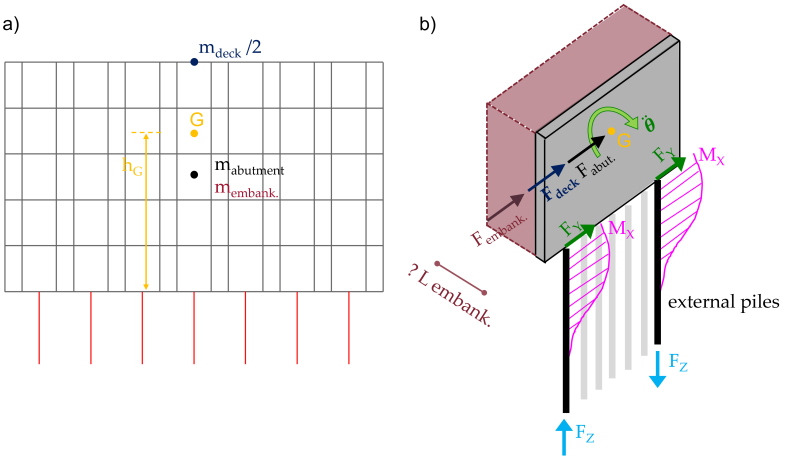

Fig. 6.26. (a) Definition of the center of gravity of the system; (b) improved schematic interpretation of the transverse mechanism.

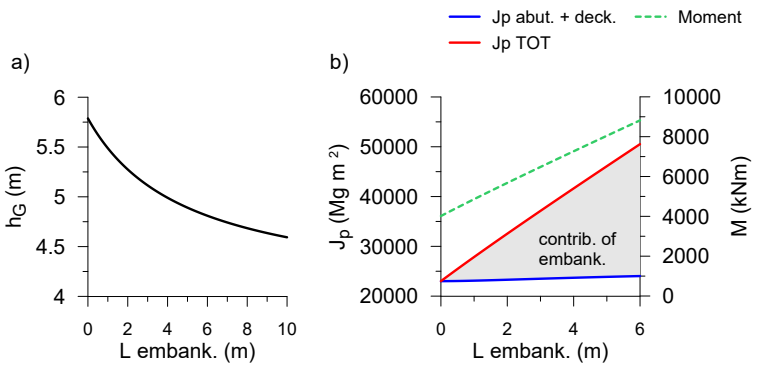

Fig. 6.27. (a) Dependence of the center of gravity of the system on the length of the embankment involved in the transverse mechanism; (b) variation of the polar moment of inertia and of the correspondent additional moment with the length of the embankment.

6.2.4. Layout of the simplified method

The design method presented in this section stems from the idea of providing a complementary tool to the procedure already proposed for the longitudinal direction. However, unlike the analysis in the longitudinal direction for which a 2D numerical model had to be developed to take into account the static conditions, the need for an *ad hoc* numerical model for the analysis in the transverse direction is not justifiable, except for special cases. Hence, the main idea is to provide a procedure that is easily implementable.

Fig. 6.28 shows the comparison between the normalised frequency content of the accelerations evaluated at the top of the soil column with embankment, obtained from the site response analysis (SRA), and the normalised frequency content of the forces FY. Although there are discrepancies, the frequency content obtained from the SRA reasonably reproduces the frequency content of the internal forces in the structure. It can also be noted that this consideration is all the more satisfactory the more the ground motions in question have the frequency content centered around the first mode of the system (approximately $1.67Hz$) such as Yamakoshi, and to a lesser extent Loma Prieta. This comparison shows that the seismic demand can be obtained with a decoupled approach, i.e. without taking explicitly into account the effects of soil-structure interaction.

The inertial horizontal acceleration requested for the system depicted in Fig. 6.26-b can be therefore carried out from a SRA of the soil column which includes the embankment, considering the spectral acceleration computed at the top of the embankment relative to the period T_0 of the first mode (0.6 sec) and to a representative damping value obtained from an equivalent-linear site response analysis (Fig. 6.24). As done for the evaluation of the angular acceleration, it was considered the average damping mobilised in the embankment.

In summary, the spectral acceleration evaluated according to this procedure, can be used for two purposes. On the one hand, it allows the determination of the inertial forces of the simplified model (FY, MX, and rocking moment); on the other hand, it allows for the definition of the rotational acceleration using Eq. 6.3, as described in Section 6.2.3. Following this approach, the seismic demand can be obtained from a design building code, provided that it accounts for the presence of the embankment and a representative soil damping ratio.

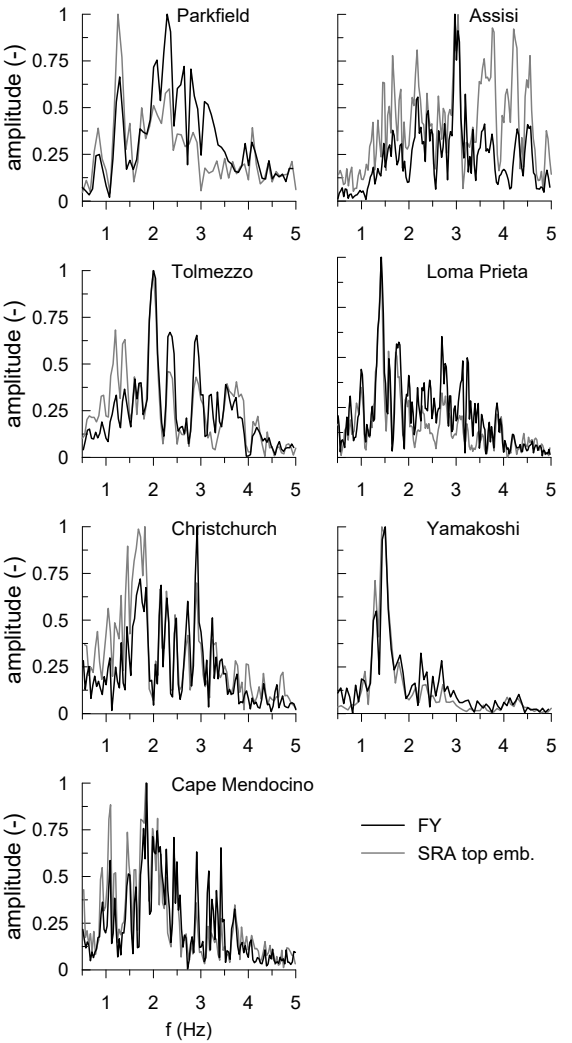

Fig. 6.28. Comparison between the normalised frequency contents of the acceleration evaluated at the top of the soil column with embankment after a site response analysis and the normalised frequency contents of the forces FY.

Once the seismic action has been defined, the internal forces in the structure can be determined by equilibrium conditions (Eq. 6.4), where for simplicity a participating mass of 100 % is assumed for each component of the system: abutment, deck and embankment. Note that, the beneficial moment contribution arising at the top of the piles was cautiously neglected.

$$
\begin{aligned}
F_{deck} &= m_{deck}/2 \cdot a_{ff} \\
F_{abutm.} &= m_{abutm} \cdot a_{ff} \\
F_{embank.} &= m_{emb}\left(L_{embank}\right) \cdot a_{ff} \\
F_{TOT} &= F_{deck} + F_{abutm} + F_{embank} \\
FY &= \frac{F_{TOT}}{n^{\circ} piles} && \text{(6.4a)} \\
MX &= FY \cdot C_M \cdot \lambda && \text{(6.4b)} \\
M_{Rocking} &= F_{TOT} \cdot h_G && \text{(6.4c)} \\
M_{Rocking,TOT} &= M_{Rocking} + J_{p,TOT}\left(L_{embank}\right) \cdot \ddot{\theta} && \text{(6.4d)}
\end{aligned}
$$

The SRA already performed for the longitudinal direction, makes this method immediately applicable. The only difference is the definition of the damping, provided in any case by the SRA. For simplicity, the first mode of the soil column is considered to derive both the spectral acceleration and the angular acceleration. Actually, the modal analysis carried out in section 4.1.4 as well as the frequency content of Fig. 6.14, shows possible contributions of higher modes. Nevertheless, with the aim of making this method simple and intuitive, the contribution of higher modes has not been addressed.
A brief summary of the proposed procedure is provided in the following together with the flow chart depicted in Fig. 6.29:

1. The seismic demand is expressed by an elastic response spectrum, that is either obtained from a design building code, or is evaluated as a site-specific spectrum through appropriate equivalent-linear site response analyses. In both cases the properties of the embankments and an average soil damping ratio should be taken into account in the derivation of the seismic demand.

2. Assuming that the first mode of the column is the most significant, the spectral acceleration in correspondence of this period can be obtained.

3. The angular acceleration can be evaluated from the spectral acceleration through literature solutions, as the one illustrated in this work.

4. The spectral and angular accelerations are now applied to an appropriate schematic model, as the one proposed in Fig. 6.26-b, to evaluate the internal forces FY, MX and rocking moment.

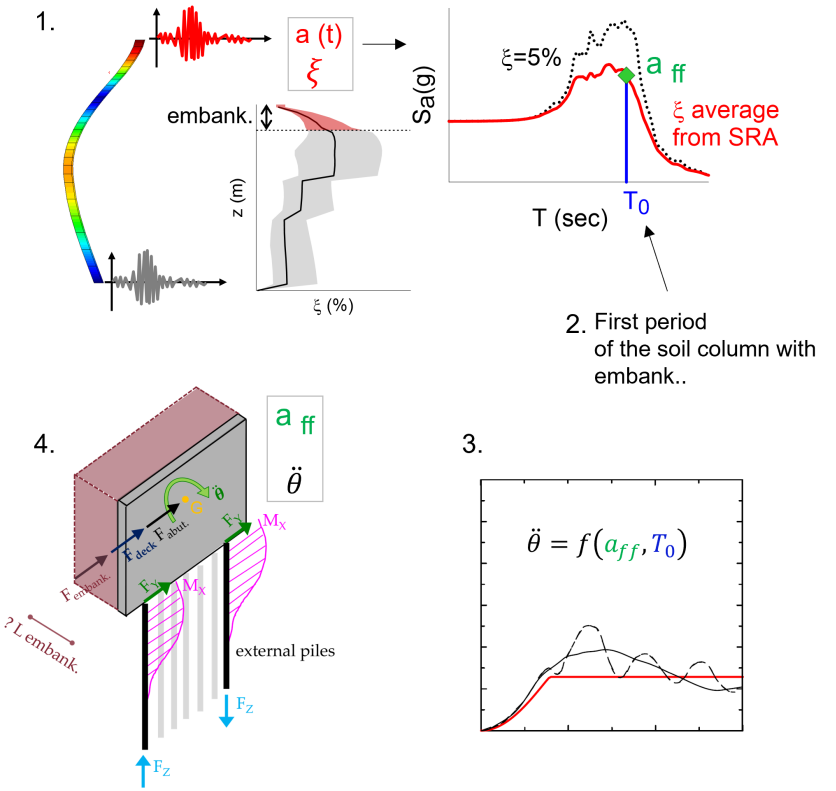

Fig. 6.29. Flow chart of the simplified method: (1.) definition of the seismic demand, (2.) evaluation of the first mode of the soil column with embankment and of the spectral acceleration, (3.) evaluation of the angular acceleration, (4.) reference calculation model for the application of the inertial forces.

6.2.5. Validation and discussion

The analyses carried out with the seismic motion of Table 6.1 allow for the validation of the proposed method. With the aim to make immediately comparable the results, it is useful to consider a single value of

the internal forces that can be representative of the entire pile foundation, taking into account that the maximum increments are approximately the same for all piles. For this reason, firstly the average of the time histories of the seven piles is calculated. Secondly, the maximum value reached by the average time history is considered. Following this procedure, it is possible to obtain for each record, a representative value of FY and MX.

Following the same logic, it is possible to characterize the rocking moment in the pile foundation, representing the axial forces FZ. The rocking moment at the bottom of abutment can be evaluated in three steps. In the first step, the average increase of the axial force in all the seven piles is computed. In the second step, the moment given by each pile is evaluated for each time step, multiplying the increment of the axial force respect to the average value by its distance from the central pile. Finally, the sum of the contributions of the individual piles provides the time history of the rocking moment. Therefore, the use of the rocking moment involves a global equilibrium of the whole abutment-pile foundation system. At the same time, the average increase of the axial forces in the pile foundation is not considered for our purposes, because this quantity may be markedly influenced by the excessive volumetric-deviatoric coupling offered by the constitutive model employed for the soil, as already extensively explained in section 4.4.3.

The validation of the simplified procedure (SP) is shown in Fig 6.30 with a systematic comparison with the dynamic analyses (DYN) in terms of the variations of the internal forces MX, FY and of the rocking moment for the ground motions listed in Table 6.1. In details, Fig. 6.30-a refers to the transverse force FY, Fig. 6.30-b to the bending moment MX and Fig. 6.30-c to the rocking moment.

Considering the extreme simplicity of the method, the application of the average spectrum produces satisfactory results. It appears that in general a length of the embankment of 2 m is sufficient to describe the internal forces obtained in the dynamic analyses. For the purpose of the seismic design, this length may be related to the height of the embankment and in this case it is of about 25 %. The method applied to the average spectrum would seem to overestimate the internal stresses FY and MX by about 50 %. However, it is important to highlight that these values are in any case in line with the maximum instantaneous seismic increments reached in the most loaded pile, as shown in Fig. 6.31. Table 6.5 reports the results provided by the simplified procedure together with the values of the rocking moment obtained by the only

kinematic interaction (M_{rot}), as well as the maximum dynamic values registered in the most loaded pile (DYN_{MAX}). Finally note that, given the linearity of the method, in Table 6.5 there was no need to distinguish between the average results and the results of the average spectrum.

Tab. 6.5. Internal forces provided by the simplified procedure and comparison with the dynamic values; FY (in kN), MX and rocking moment (in kNm). (M_{rot}) indicates the rocking moment obtained from the kinematic interaction only.

	DYN	$SP_{L=0}$ (M_{rot})	$SP_{L=2}$ (M_{rot})	$var_{L=0}$ %	$var_{L=2}$ %	DYN_{MAX}
FY	984	1103	1547	12.1	57.3	1287
MX	2877	3079	4317	7.0	50.1	3226
rock. M	61573	48609 (3909)	62660 (5527)	−21.1	1.8	

Despite its simplicity, the proposed method provides satisfactory results. When combined with the method for the longitudinal direction, it leads to the seismic design of the bridge under consideration considering the bidirectional motion. From an engineering practitioners' perspective, it only requires a SRA and equilibrium considerations.

6.2.6. Additional analyses: contribution of the deck and embankment

When examining the seismic behavior of the system in question, soil-structure interaction considerations are unavoidable. It has been seen that the dynamics of the soil-embankment system plays a fundamental role. Now, the idea is to evaluate the contribution of the single components of the system on its overall response. In particular, the set up of two new models allows to investigate the inertial contribution of the deck and the role of the embankment. The comparison of these two models with the reference one have benefited from the use of the half 3D model, illustrated in section 3.3.3.

In order to isolate the contribution of the deck mass, in a first analysis the mass of the deck was removed while the static loads were reproduced through assigned forces.

The role of the embankment was evaluated in a second model, by disconnecting the rigid links that relate the transverse displacements of the abutment and the embankment. From an operational point of view, the periodic constraints (described in Fig. 3.20) between the final nodes

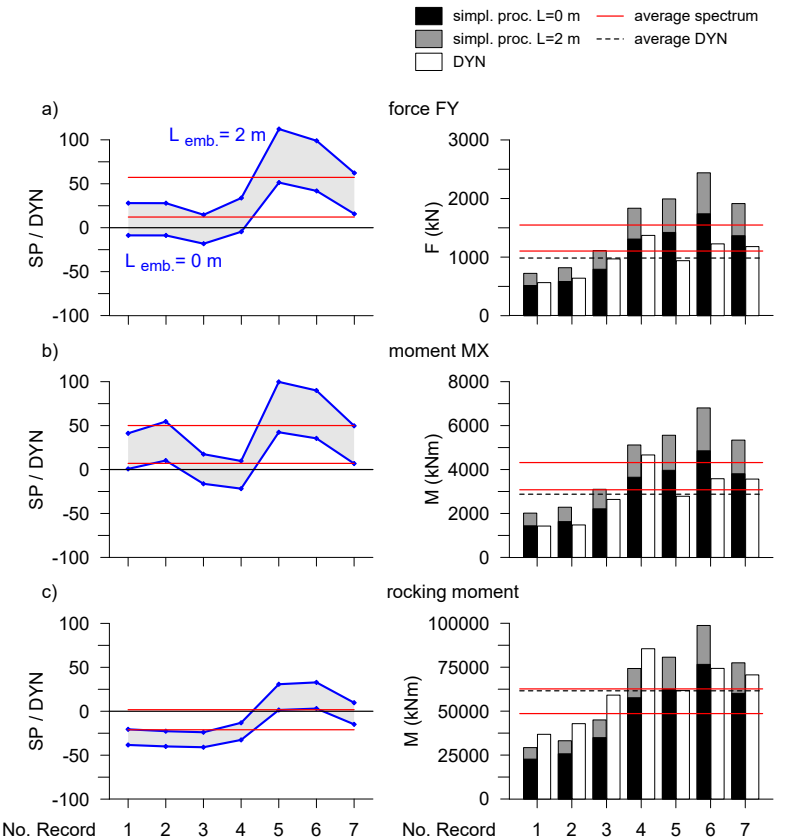

Fig. 6.30. Comparison (%) between the simplified procedure (SP) and the results of the dynamic analyses; (a) *FY*, (b) *MX* and (c) rocking moment.

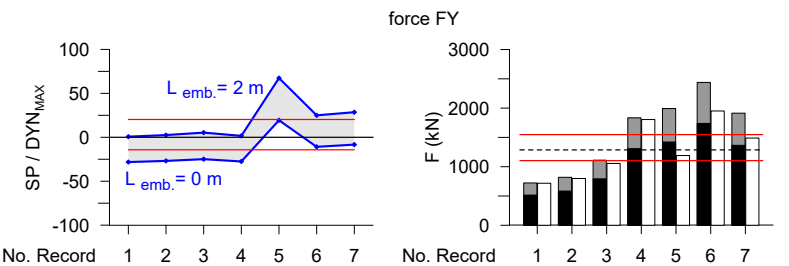

Fig. 6.31. Comparison (%) between the simplified procedure (SP) and the results of the dynamic analyses for *FY*. In this case, it was considered the maximum value recorded in the most loaded pile and not the maximum value of the average time history increments.

of the rigid links and the nodes of the embankment are considered only in the longitudinal and vertical direction. The embankment therefore keep collaborating with the abutment for the vertical loads.

The comparison between the three different models in terms of the quantities described in the previous section is illustrated in Fig. 6.32 for two ground motions with high (Assisi - Fig. 6.32-a) and low (Cape Mendocino - Fig. 6.32-b) frequency content. Fig. 6.33 shows that the differences between the three analyses do not depend on the frequency content of the ground motion. The inertial mass of the deck (Fig. 6.33-a) produces an increase of the order of 20-25 % for MX and FY, and about 35 % for the rocking moment. On the contrary, the embankment (Fig. 6.33-b) induces 15-20 % increase for MX and FY, and 15 % for the rocking moment.

The time histories shown in Fig. 6.32 clearly show that in the three models the response period is essentially the same. This means that the mass of the deck, while being important, is not able to modify the response of the overall system. Nevertheless, the deck mass cannot be neglected for the evaluation of the maximum internal forces. On the other hand, it was observed that the embankment in the transverse direction plays a minor role, suggesting that the volume involved in the transverse direction is modest.

Finally, the analyses carried out without the inertial contribution of the embankment allow us to validate the proposed method considering null the L of the embankment of Fig. 6.26-b. The results of the simplified approach, provided in Fig. 6.34, shows that the application of the average spectrum produces an overestimation of FY and MX of the order of 25-30 % and a slight underestimation of the rocking moment of about 5 %. As in the previous case, a better result not reported here for the sake of brevity, would be obtained if FY and MX were referred to the most loaded pile. This check substantially confirms the ability of the model to appropriately take into account the contribution of the abutment-deck system eliminating the uncertainties relating to the inertial soil mass of the embankment involved in the transverse motion.

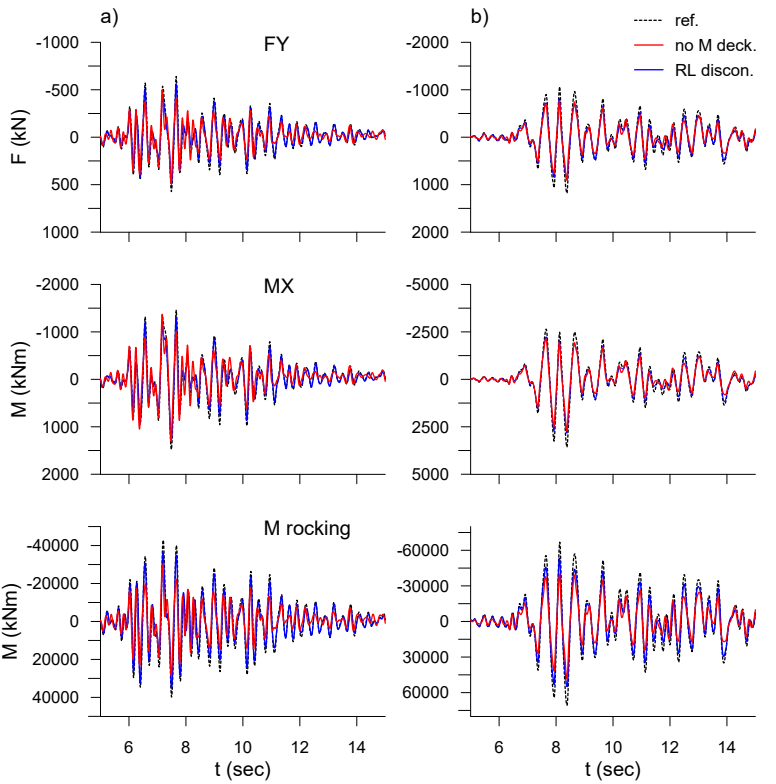

Fig. 6.32. Comparison between the time histories of the internal forces in three different models: reference model, model without inertial mass of the deck, model with disconnected rigid links between the abutment and embankment; (a) Assisi and (b) Cape Mendocino ground motions.

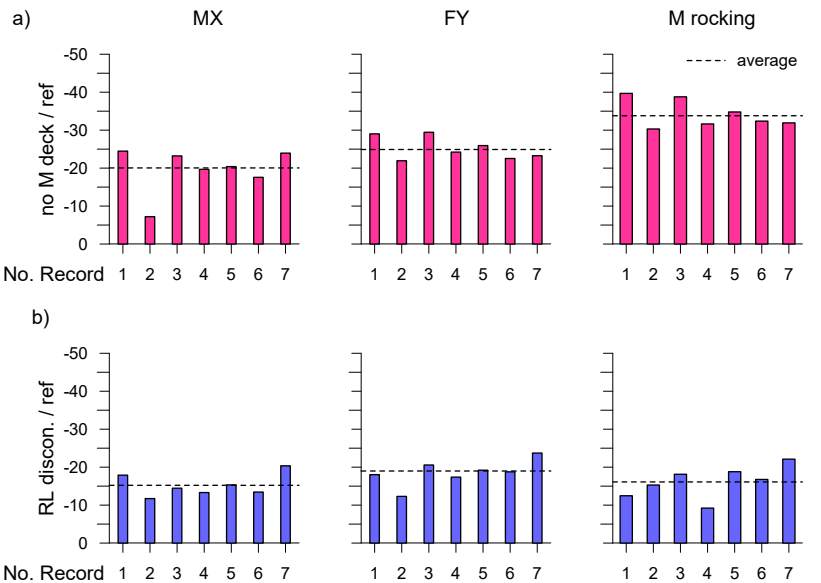

Fig. 6.33. Variations (%) of the internal forces in two different models respect to the reference model; (a) model without inertial mass of the deck, (b) model with disconnected rigid links between the abutment and embankment.

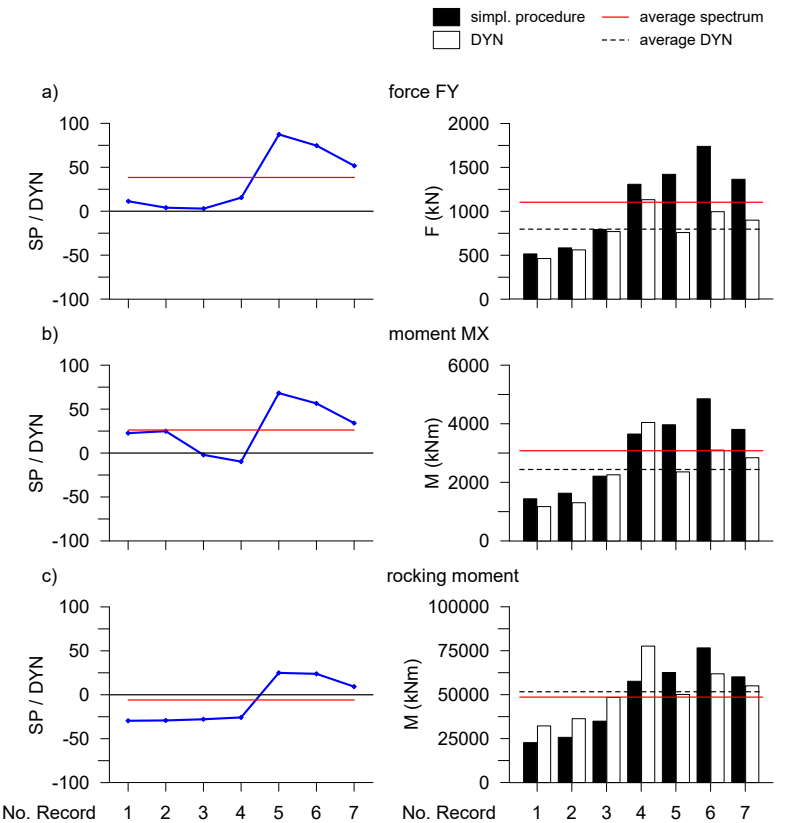

Fig. 6.34. Comparison (%) between the simplified procedure (SP) and the results of the dynamic analyses; (a) *FY*, (b) *MX* and (c) rocking moment. The reference model here is the model with disconnected rigid link between the abutment and embankment.

6.3. Torsional effects

In addition to the the effects interpreted with the calculation scheme of Fig. 6.26-b and illustrated in the previous section, the transverse component of the seismic motion produces further effects, that are herein termed "torsional". These effects are produced by the fact that the inertial force of the deck is applied at a distance L from the abutment (see Fig. 6.35). In this way, the generated moment produces an increase in the axial force N in the beam elements of the deck, according to a *strut and tie model*. These forces are partly transferred to the abutment, modifying the normal stresses at the contact with the embankment, while the remaining part is transferred as shear forces FX to the head of the piles, generating in turn a distribution of bending moments MY. Since the quantities FX and MY are already involved in the longitudinal analysis; these effects may overlap with the response computed for the longitudinal seismic action. As already done for the previous mechanism, we examine the results deriving only from the one-directional transverse analysis.

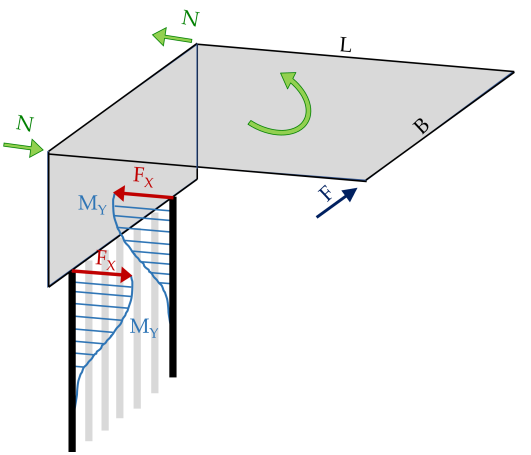

Fig. 6.35. Schematic interpretation of the torsional mechanism along with description of the inertial forces involved and the generated internal forces.

The variation of the axial forces in the beams of the deck at the deck-abutment contact is reported in Fig. 6.36-a where the alignment No.1 and No.3 are the external ones while the alignment No.2 is referred to the average of the two central ones. A positive variation in one of the external alignments corresponds to a negative variation in the other one, as best shown in Fig. 6.36-c. Fig. 6.36-b depicts instead, the configuration

of the axial force in the abutment-deck contact in different instants. Note the *butterfly* patterns in the two instants and the final increment at the end of the analysis as a result of greater mobilisation of the soil pressure behind the abutment.

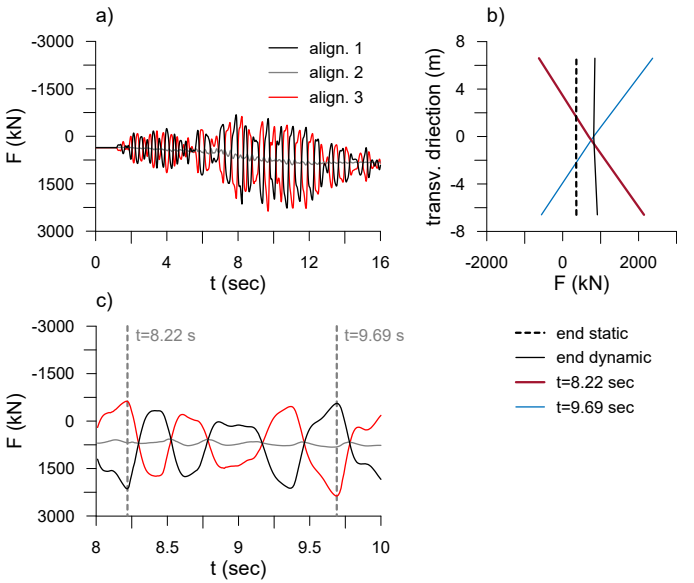

Fig. 6.36. Yamakoshi record: (a) time histories of axial forces in different alignments of the deck and an enlarged view (c); (b) configuration of the axial forces in the abutment-deck contact in some instants.

The correlation between the internal forces belonging to this mechanism is illustrated in Fig. 6.37. The forces FX at the pile heads (Fig. 6.37-b) are easily associated with the axial forces (Fig. 6.37-a) of the beams of the deck; the external pile No. 1 corresponds to the alignment No. 1, the pile No. 7 is related to the alignment No. 3 and the pile No. 4 is the central.

On the other hand, the study of the evolution of MY (Fig. 6.37-c) deserves a broader discussion. Although the central pile should not be affected by the strut and tie mechanism, it is in any case subject to an increase of the moment MY. In other words, it seems that all the piles undergo an increase of the moment MY as a consequence of the increase in pressure behind the abutment.

This phenomenon is immediately shown in Fig. 6.38-a; for each soil column depicted in Fig. 6.38-c, the evolution of the soil pressure during

the transverse analysis is illustrated. Note that the configuration of the soil pressure follows the strut and tie mechanism generated at the abutment-deck contact. Nevertheless, with the repetition of the cycles, a generalized pressure increase is observed over the whole abutment so that the soil pressure at the end of the dynamic analysis is greater than the static one. In this regard, Fig. 6.39 reports the detail of the contours of the normal stresses on the abutments in the same instants.

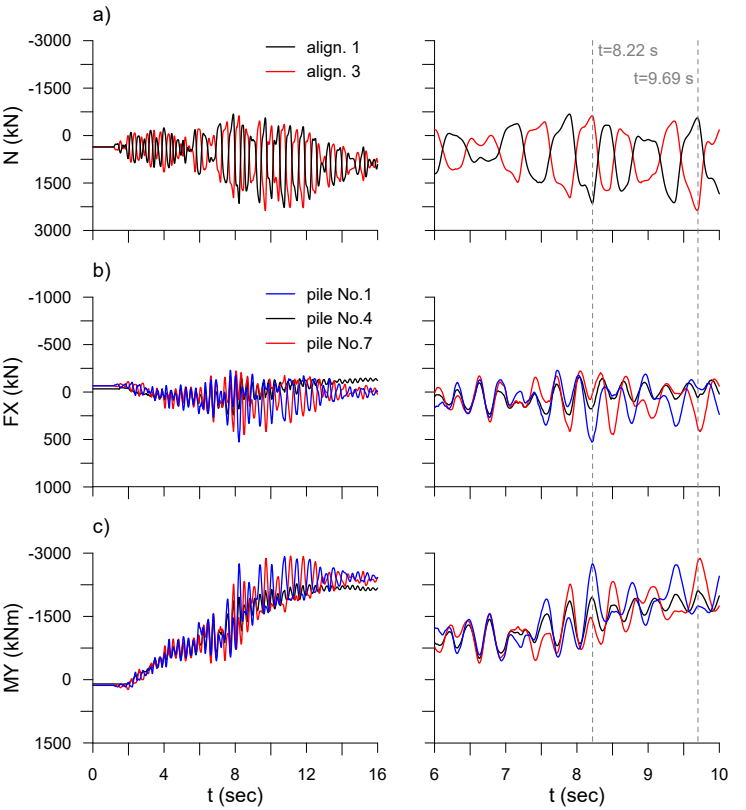

Fig. 6.37. Time histories of (a) forces N, (b) forces FX and (c) bending moments MY in the piles for Yamakoshi record. The right column presented an enlarged view.

The effect of the increase in pressure behind the abutment produces the deformation patterns shown in Fig. 6.40-a. The abutment-pile system tends to deform inward in the longitudinal direction, away from the embankment. This is exactly the same configuration that the system assumes during the longitudinal analysis. It is therefore now clear that this mechanism is coupled with what happens during the analysis in

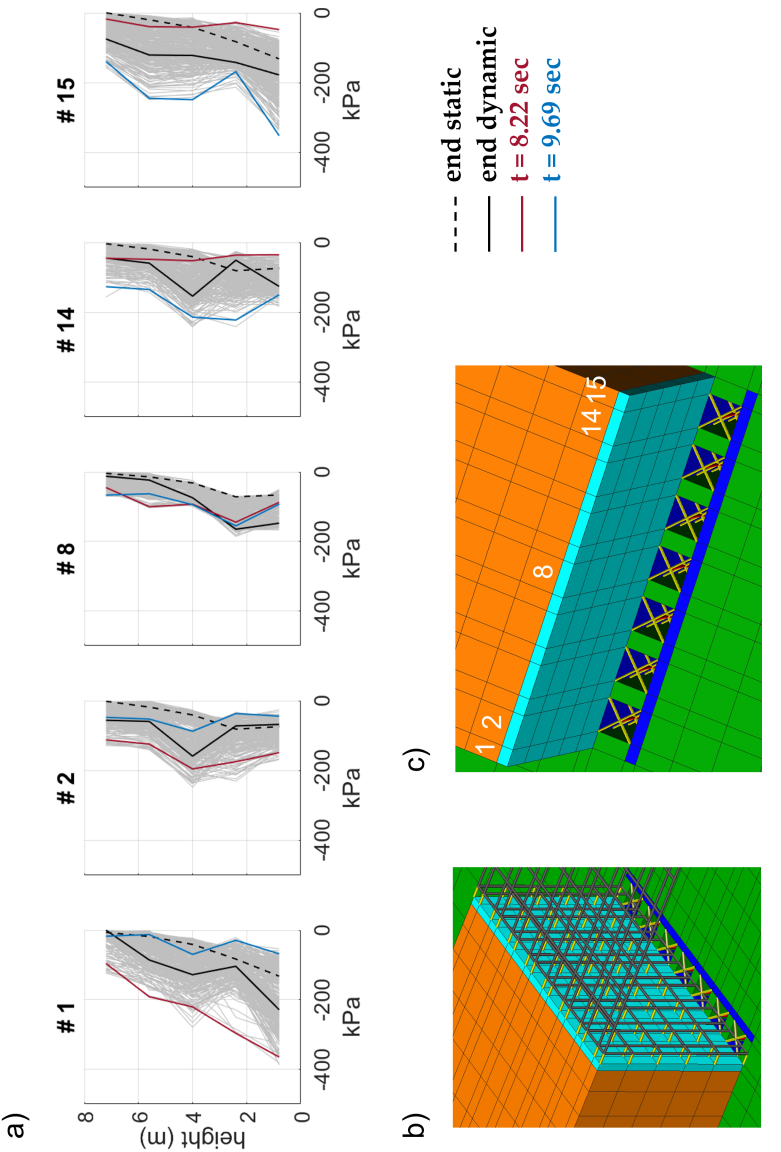

Fig. 6.38. Yamakoshi record: (a) soil normal stresses (kPa) in different instants, (b) abutment detail, (c) numbering of the soil columns depicted.

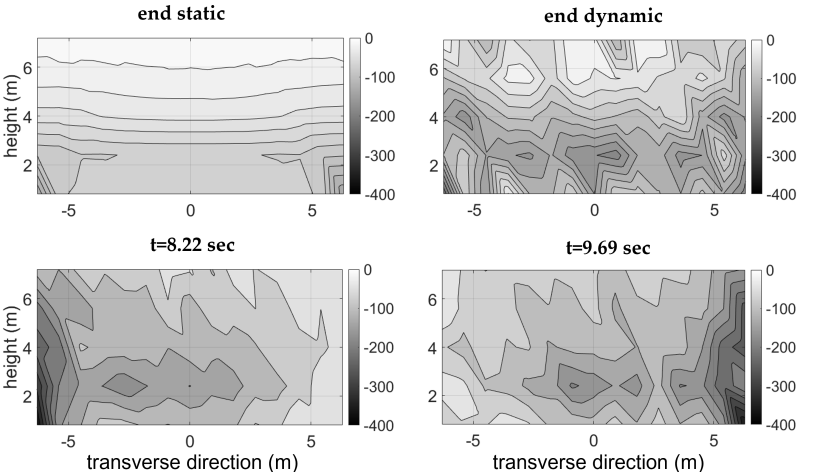

Fig. 6.39. Yamakoshi record: contours of the normal stresses (kPa) on the abutments in different instants.

the longitudinal direction. In detail, Fig. 6.40-a corresponds to the alignment No.1, however Fig. 6.40-b and Fig. 6.40-c clearly show that the entire abutment-pile system is subjected to this deformation. In fact, the relative displacement between the three different alignments considered is small and can be neglected.

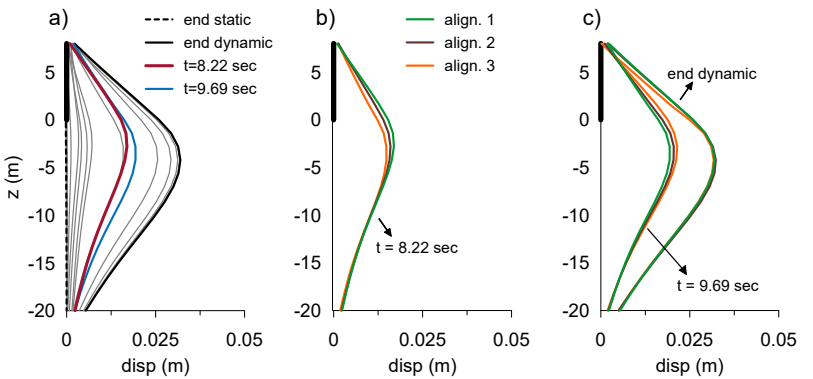

Fig. 6.40. (a) Deformation of the abutment-pile system during dynamic analysis in correspondence of the alignment No.1 (pile No.1); (b) and (c) displacement in the external and central alignments of the abutment-pile system in some instants of interest.

Nevertheless, the case study examined in this work characterised by a regular geometry, appears to be little affected by this behaviour. In fact,

as shown in Fig. 6.10 and in Fig. 6.11 the one-directional longitudinal analyses provides reasonable values of the internal forces FX and MY.

7. Influence of wing walls

The influence of the wing walls on the global seismic behaviour is investigated in this chapter. The modelling of the wing walls, depicted in Fig. 3.22, was already discussed in the section 3.2.4. The two-directional analyses performed on the 3D full soil-bridge model with the wing walls show that the behavior of the system continues to be essentially decoupled in the longitudinal and transverse direction. However, the presence of the wing walls raises further considerations.

Moreover, the comparison between the models with and without the wing walls in both the directions indicates that the influence of the wing walls is significant only for the transverse direction. Thus, the presence of the wing walls was incorporated in a straightforward manner in the simplified procedure conceived for the transverse seismic behaviour and, in closing, validated against the results of additional dynamic analyses carried out on the transverse half 3D soil-bridge model.

7.1. Bidirectional effects on the model with wing walls

In this section, the effects of the two-directional analyses on the seismic performance of the full 3D soil-bridge model with wing walls are investigated. As done in chapter 6, just three piles (Fig. 6.2) for each pile foundation (left and right) are considered in the output quantities.

Fig. 7.1 reports, for the Yamakoshi ground motion, a summary of the variation of the internal forces in correspondence of scrutiny piles due to the bidirectional effects respect to the one-directional analyses. This comparison is made with the one-directional longitudinal analysis in Fig. 7.1-a and with the one-directional transverse analysis in Fig. 7.1-b. Fig. 7.1-a shows that the maximum values provided for MY by the

one-directional longitudinal analysis are really close to those provided by the bidirectional analysis; the average variation is almost nil with the standard variation less than 10 %. In the case of FX, the one-directional longitudinal analysis produces an average overestimation of the forces of the order of 10 %. Note that, these result are in good agreement with what has already been observed in the model without wing walls, as discussed in Section 6.1.

Regarding MX and FY, both represented in Fig. 7.1-b, except some local variations of about 30 %, the average variation is around 10 %. In the case of the axial forces FZ (Fig. 7.1-b) the one-directional transverse analysis produces an overestimation of about 4 %. As discussed for the model without wing walls, the one-dimensional analysis carried out with the sole transverse motion component provides satisfactory results with an average variation less than 10 %.

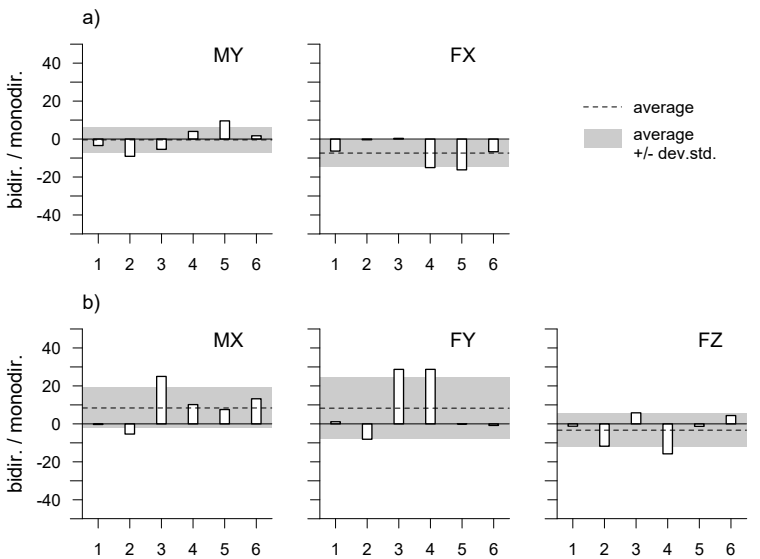

Fig. 7.1. Yamakoshi record: variations (%) of the internal forces in the scrutiny piles (in the model with wing walls) due to the bidirectional motion compared to those evaluated in the one-directional analysis: (a) longitudinal and (b) transverse.

Fig. 7.2 reports a summary of the variation of the same quantities for the Parkfield record. Contrary to what has been observed for Yamakoshi, Fig. 7.2-a shows that the bidirectional effects lead to an important increment of the bending moment MY in the order of 40 % in the left pile foundation. Fig. 7.3-b shows, in fact, that the time histories

evaluated as the difference between the two-directional analysis and the one-directional longitudinal analysis are comparable with the time-histories of the two-directional analysis. This effect was not observed for Yamakoshi (Fig. 7.3-a).

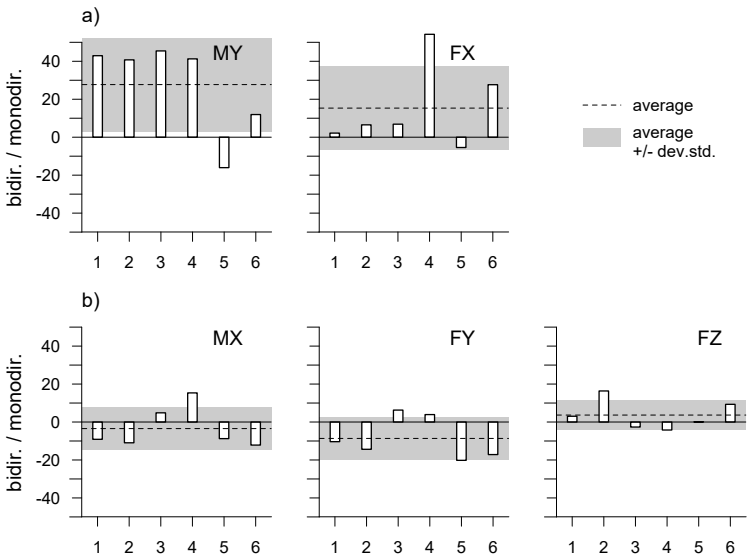

Fig. 7.2. Parkfield record: variations (%) of the internal forces on the scrutiny piles (in the model with wing walls) due to the bidirectional motion compared to those evaluated in the the one-directional analysis: (a) longitudinal and (b) transverse.

Actually, this is due to two concurrent phenomena. The analysis in the longitudinal direction is not strong enough to mobilise the resistance of the soil behind the abutment. On the other hand, the presence of the wing walls in the transverse analysis produces a greater moment than that produced by the longitudinal analysis (Fig. 7.4), as an effect of the torsional deformation pattern discussed in section 6.3. For the same reasons, an important variation in two external piles of the right foundation is observed for FX in Fig. 7.2-a. This phenomenon, under the same ground motion, does not occur in the model without wing walls precisely because it is the presence of the wing walls themselves that calls into play the behaviour of the abutment in the longitudinal direction.

Finally, regarding the internal forces involved in the transverse direction and depicted in Fig. 7.2-b, the bidirectional effects induces a slight

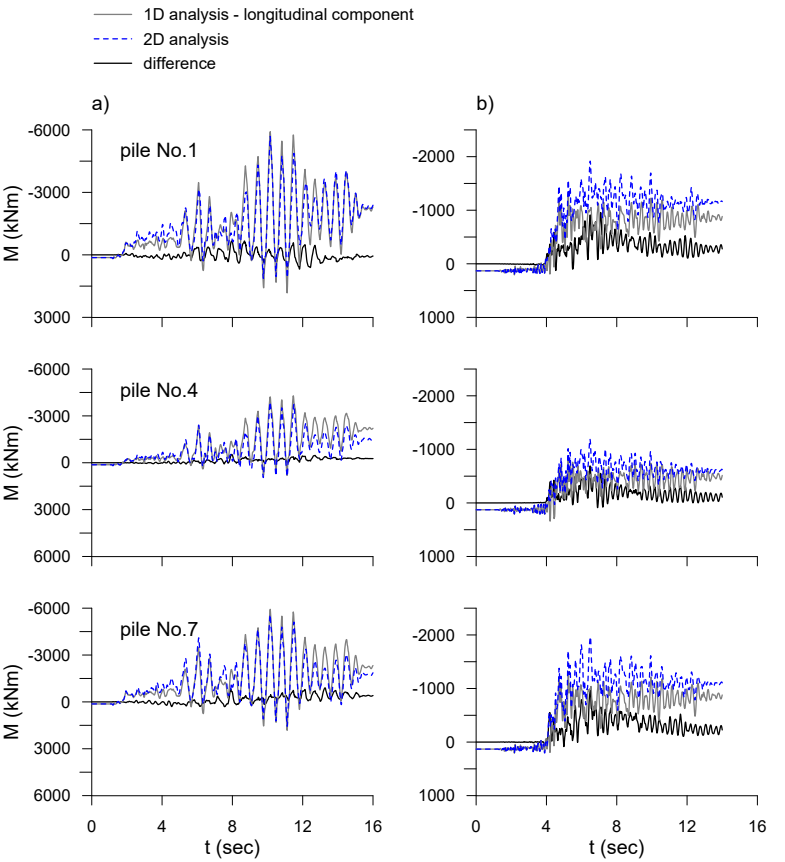

Fig. 7.3. Time histories of the bending moments MY in the left pile foundation for (a) the Yamakoshi and (b) the Parkfield ground motions.

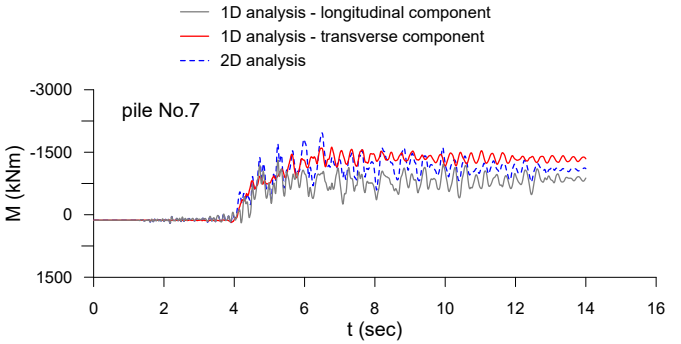

Fig. 7.4. Parkfield record: time histories of the bending moments *MY* in the pile No.7.

increment for *FZ* and a variation less than 10 % for *MX* and *FY* respect to the one-directional transverse analysis.

In closing, this section showed that the behavior of the model with the wing walls continues to be essentially decoupled. However, there may be cases where the presence of the wing walls can accentuate the torsional effects, increasing the stresses computed along the longitudinal direction. This situation occurs when the two components of the seismic motion in the longitudinal and transverse direction are similar and, at the same time, in the longitudinal analysis no significant mobilisation of the pressure behind the abutment is achieved. In fact, it should be noted that while in Yamakoshi a value of the bending moment of about 6000 kNm is reached (Fig. 7.3-a), the maximum value obtained in Parkfield (Fig. 7.3-b) is approximately one third.

7.2. Comparison between models with and without wing walls

Recognizing that the behavior of the system continues to be essentially decoupled even in the presence of the wing walls, this section shows the comparison between the 3D full models with and without the wing walls, separating the longitudinal and transverse behaviour.

7.2.1. Longitudinal behaviour

The typology of the wing walls used in the present study is the one defined *cantilivered-U wing wall* in section 1.3.2. This type does not involve any significant additional mass of the embankment because the wing walls are placed parallel to the direction of the embankment itself.

Moreover, it is important to underline that in the model without the wing walls, the two longitudinal faces of the embankment were modeled like *shear beam* simulating basically a reinforced earth wall. This means that from a practical point of view, the boundary constraints out of the longitudinal-vertical plane applied on the two models are very similar. Consequently, the one-directional longitudinal analysis is minimally affected by the modelling of the wing walls.

Fig. 7.5 reports the comparison between the time histories of the internal forces evaluated at the pile heads for Yamakoshi in the one-directional longitudinal analysis. Fig. 7.5-a refers to FX while Fig. 7.5-b refers to MY. Fig. 7.6 instead, reports the same comparisons for the pile head No.7 for Parkfield. The figures indicates that the differences are negligible.

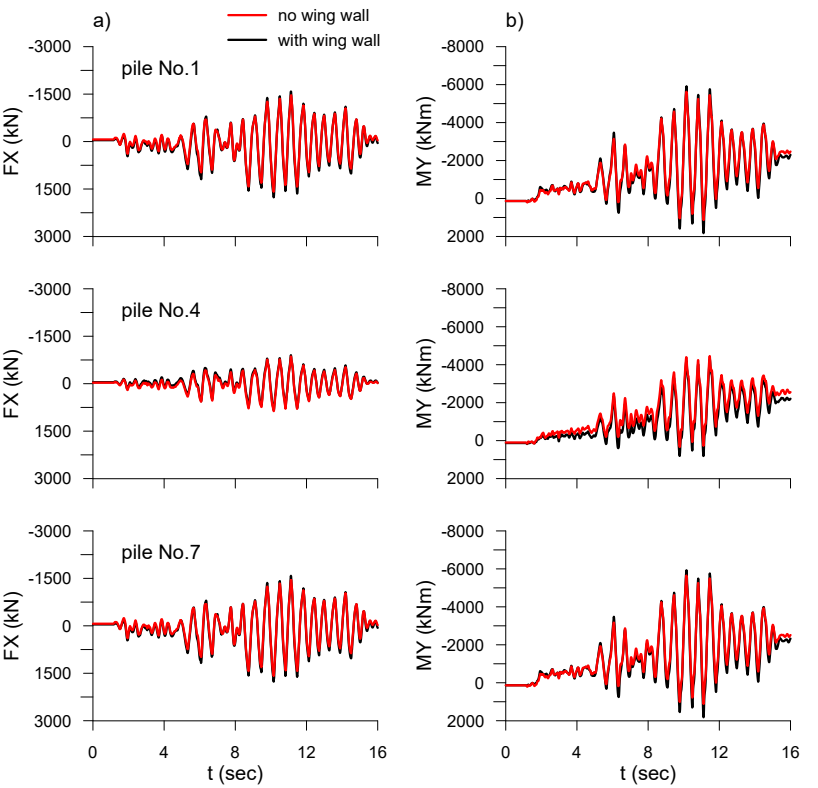

Fig. 7.5. Yamakoshi record: comparison between the models with and without the wing walls in the one-directional longitudinal analysis. Time histories of the internal forces FX (a) and MY (b) evaluated at the pile heads in the left foundation.

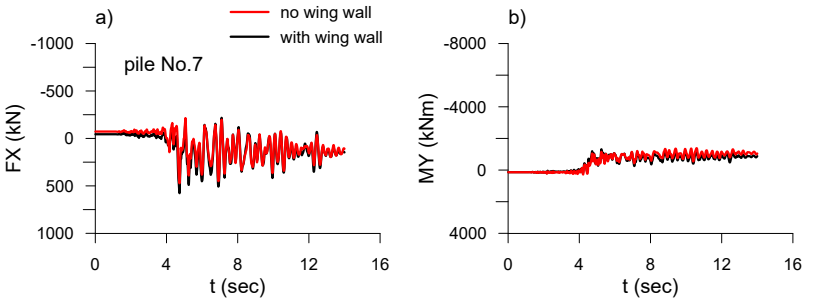

Fig. 7.6. Parkfield record: comparison between the models with and without the wing walls in the one-directional longitudinal analysis. Time histories of the internal forces FX (a) and MY (b) evaluated at the pile No. 7 head in the left foundation.

Fig. 7.7 reports a summary of the variation of the internal forces FX and MY due to the presence of the wing walls, respectively for the Yamakoshi (Fig. 7.7-a) and the Parkfield ground motion (Fig. 7.7-b). In order to have a single value of the internal forces that can be representative of the entire pile foundations, the average of the maximum increments in the six scrutiny piles is considered. In particular this comparison in made with reference to the one-directional longitudinal analysis and the two-directional analysis performed with both models.

Regarding Yamakoshi (Fig. 7.7-a), the presence of the wing walls induces a slight increment of the internal forces less than 5 % for both the comparisons.

For the Parkfield record (Fig. 7.7-b), it is interesting to note that the model with the wing walls produces an underestimation of approximately 10 % for MY in the one-directional longitudinal analysis, while an overestimation of the same magnitude is obtained in the two-directional analysis. A posteriori, this could explain the reason why in the Fig. 7.2-a a significant increase in stresses was recorded in the two-directional analysis compared to the one-directional analysis. In fact, comparing the models with and without the wing walls in the two-directional analysis, this increment is only 10 %. Thus, in the one-directional longitudinal analysis the presence of the wing walls probably makes the abutment-embankment system stiffer, resulting in a slight increase in the stresses in the lateral piles and a more significant decrease in the central one due to the arc effect. Finally, regarding the other quantity FX, small differences of around 5 to 10 % are observed.

In light of these results, the analyses confirm that for the purposes of the seismic design of the system in the longitudinal direction, the adop-

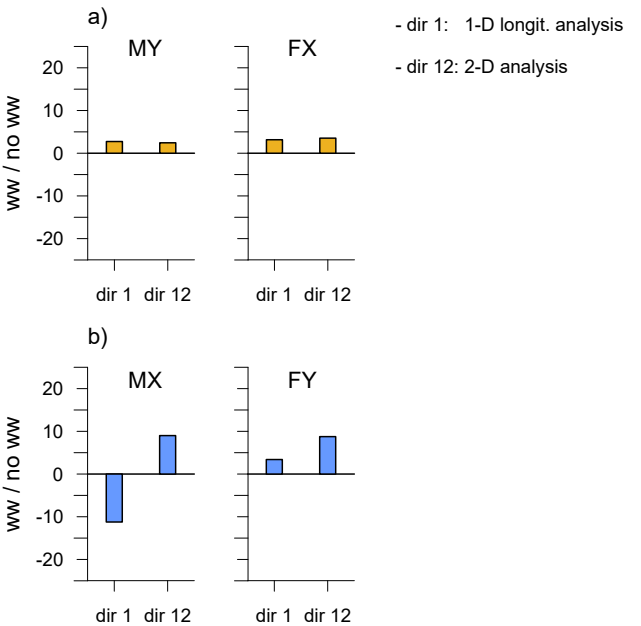

Fig. 7.7. Comparison (%) between the one-directional longitudinal analyses and the two-directional analyses carried with and without the wing walls for (a) Yamakoshi and (b) Parkfield.

tion of the cantilevered U-type wing wall produces slight increments. Therefore, the simplified 2D model, proposed in chapter 5, can be used with no need of further changes.

7.2.2. Transverse behaviour

In the previous chapter, it was highlighted that in the transverse direction the contribution of the embankment was modest and quantifiable with a couple of meters. Conversely, the presence of the wing walls may increase the volume, and hence the mass, of the embankment involved in the transverse direction.

Fig. 7.8 reports the comparison between the model with and without the wing walls in terms of time histories of the internal forces evaluated at the pile heads with one-directional transverse analysis for the Yamakoshi ground motion; Fig. 7.8-a and Fig. 7.8-b refer respectively to the internal forces FY and MX. As expected, the internal forces induced in the model with the wing wall are bigger, given the greater masses involved. However, the behavior of the system is quite similar, indicating that not all the mass of the embankment included in the wing walls is participating. The same comparisons are presented in Fig. 7.9 referring to the Parkfield seismic record.

Fig. 7.10-a shows for the Yamakoshi seismic record and for both models, with and without the wing walls, the increments of the axial forces FZ in the pile No. 1 and 7 with respect to the central pile of the foundation. The effect of the presence of the wing walls is unequivocal. Moreover, taking advantage of the transverse half 3D model illustrated in section 3.3.3 where all the seven piles were considered in the output quantities, Fig. 7.10-b/c reports, respectively for the Yamakoshi and the Parkfield seismic records, the former comparison in term of the rocking moment.

Fig. 7.11 reports a summary of the variation of the internal forces FY, MX and rocking moment due to the presence of the wing walls, respectively for the Yamakoshi (Fig. 7.11-a) and the Parkfield ground motion (Fig. 7.11-b). The average of the maximum increments in the six scrutiny piles is considered for FY and MX, while the rocking moment is chosen for characterizing the increment of the axial forces in the piles. This comparison is provided for both the one-directional transversal analysis and for the two-directional analysis.

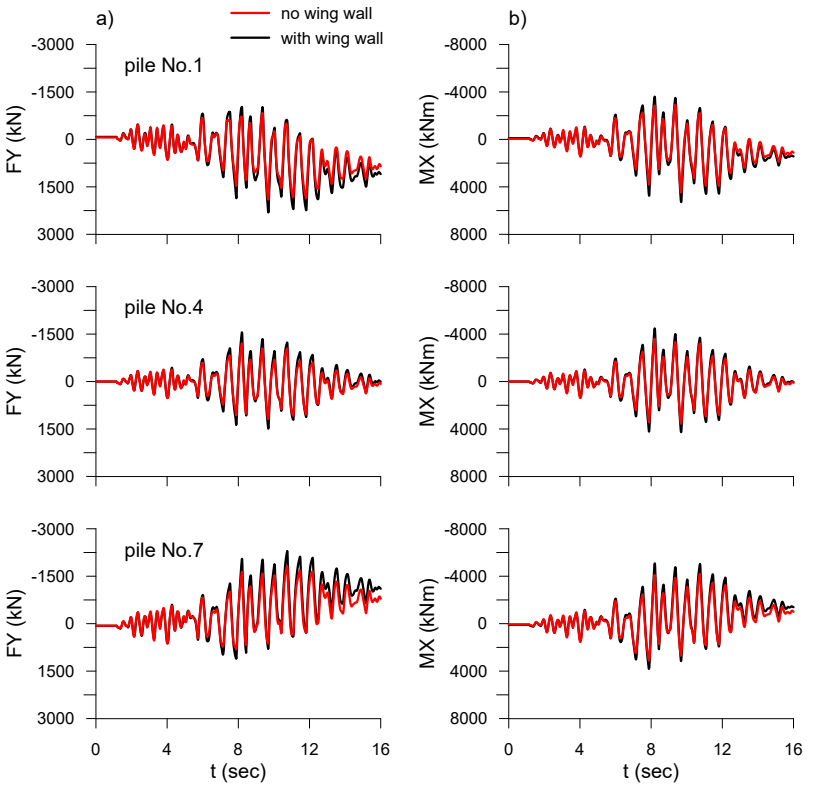

Fig. 7.8. Yamakoshi record: comparison between the models with and without the wing wall in the one-directional transverse analysis. Time histories of the internal forces FY (a) and MX (b) evaluated at the pile heads in the left foundation.

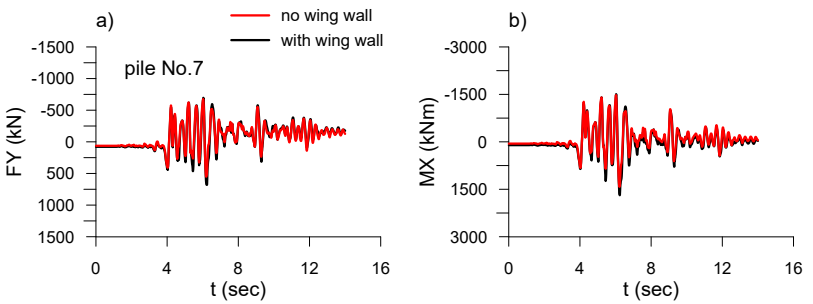

Fig. 7.9. Parkfield record: comparison between the models with and without the wing wall in the one-directional transverse analysis. Time histories of the internal forces FY (a) and MX (b) evaluated at the pile head No.7 in the left foundation.

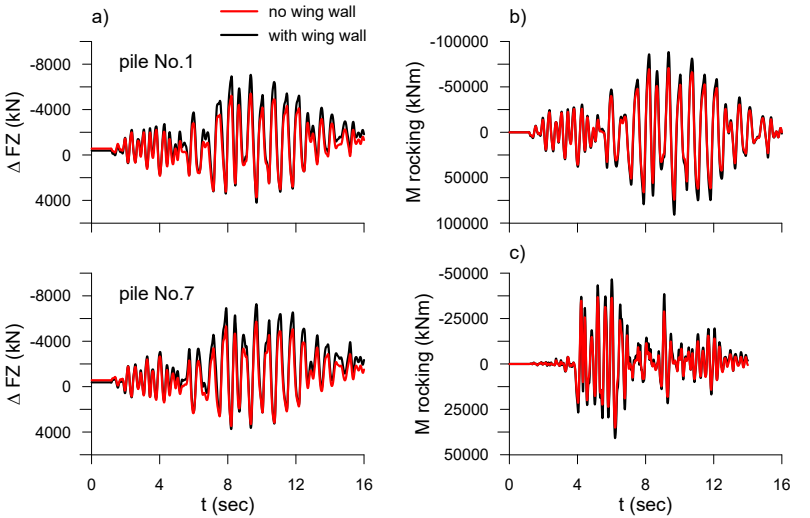

Fig. 7.10. One-directional transverse analyses: (a) increments of the axial forces in the pile No. 1 and 7 respect to the central pile of the foundation for both models, with and without the wing walls for Yamakoshi; rocking moment at the bottom of abutment for (b) Yamakoshi and (c) Parkfield.

Before commenting on the results, it is important to observe that, in Fig. 7.11, the ratios of the rocking moments obtained by the two-directional analysis of the two models are considered, even though the output of only tree piles for each foundation was included in the full 3D model. However, the comparison between the one-directional transverse analysis carried out with the full 3D model and with the half 3D model, where all seven piles are included in the output quantities, allows for the validation of this approximation. Specifically, although the absolute values computed with these two models differ, Table 7.1 indicates that the ratios are essentially the same.

By virtue of the decoupled behaviour, Fig. 7.11-a and Fig. 7.11-b, show that the variations referring to the two-directional analysis are essentially the same as those of the one-directional transverse analysis. In details, these variations bounded in the range 10-20 % for both ground motions.

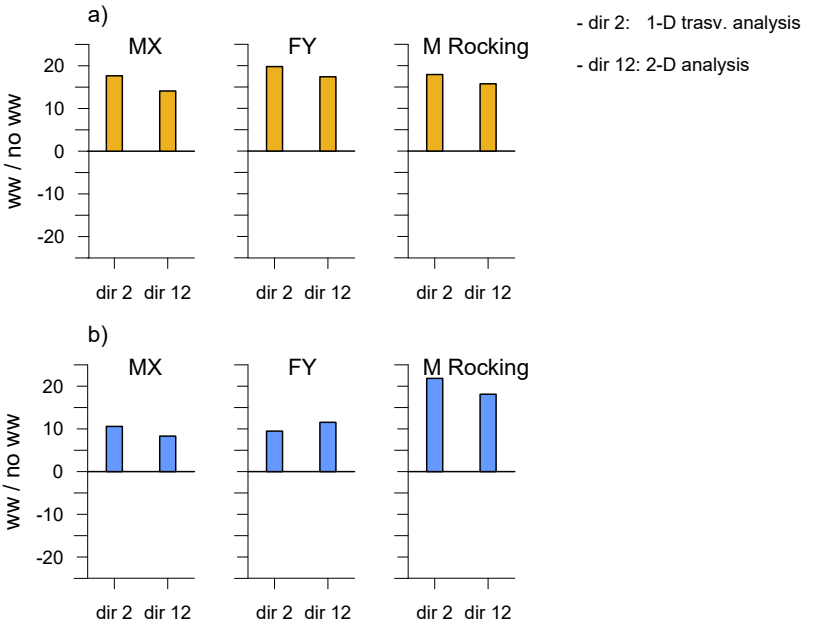

Fig. 7.11. Comparison (%) between the one-directional transverse analyses and the two-directional analyses carried out with models with and without the wing wall for (a) Yamakoshi and (b) Parkfield.

Tab. 7.1. One-directional transverse analysis: comparison between the evaluation of the rocking moment (in kNm) in the half 3D model (where all 7 piles are considered in the output) and in the full 3D model (where only 3 piles for each foundation are included in the output).

	$M_{rock,WW}$ *7 piles*	M_{rock} *7 piles*	*var* %	$M_{rock,WW}$ *3 piles*	M_{rock} *3 piles*	*var* %
Yamakoshi	90832	74325	18.2	61899	50807	17.9
Parkfield	46586	36816	21.0	33874	26480	21.8

7.3. Application of the simplified method

The simplified method proposed in section 6.2 is herein applied and validated against the results of several dynamic analyses carried out on the half 3D soil-bridge models, studying the effects produced by the presence of the wing walls. Fig. 7.12 and Fig. 7.13 present a systematic comparison of the increments of the internal stresses MX, FY and of the rocking moment for the ground motions listed in Table 6.1. Finally, the maximum value reached by the average of the time history increments, denoted by the label *max average*, and the rocking moment are used to provide a concise comparison of the two models, as summarised in Fig. 7.14.

As a general observation, it can be stated that the presence of the wing walls produces an increase of the internal forces in the pile foundation in the range of 15-20 %. Therefore, the wing walls should be appropriately considered for the seismic design in the transverse direction.

In the simplified calculation model, the presence of the wing wall can be taken into account by simply adjusting the dimension L of the embankment that participates in the transverse motion. The results of this validation are collected in Fig. 7.15, that shows, for each record and on average, the variations and the absolute values of the output quantities obtained with the simplified procedure (SP) and with the dynamic analyses (DYN). Fig. 7.15-a refers to the transverse force FY, Fig. 7.15-b to the bending moment MX and Fig. 7.15-c to the rocking moment.

Inspection of Fig. 7.15 indicates that the optimal embankment length to consider is bounded between 2 and 4 m; thus, it does not appear to be correlated with the actual length of the wing walls, which is approximately 10.5 m. As shown in the analysis without wing walls, the values of FY and MX can be overestimated by up to 60 %. However, these values align with the maximum values reached in the most loaded pile (Fig. 7.16). Table 7.2 presents in conclusion, the results of the adopted simplified procedure, reporting the same quantities described in Table 6.5.

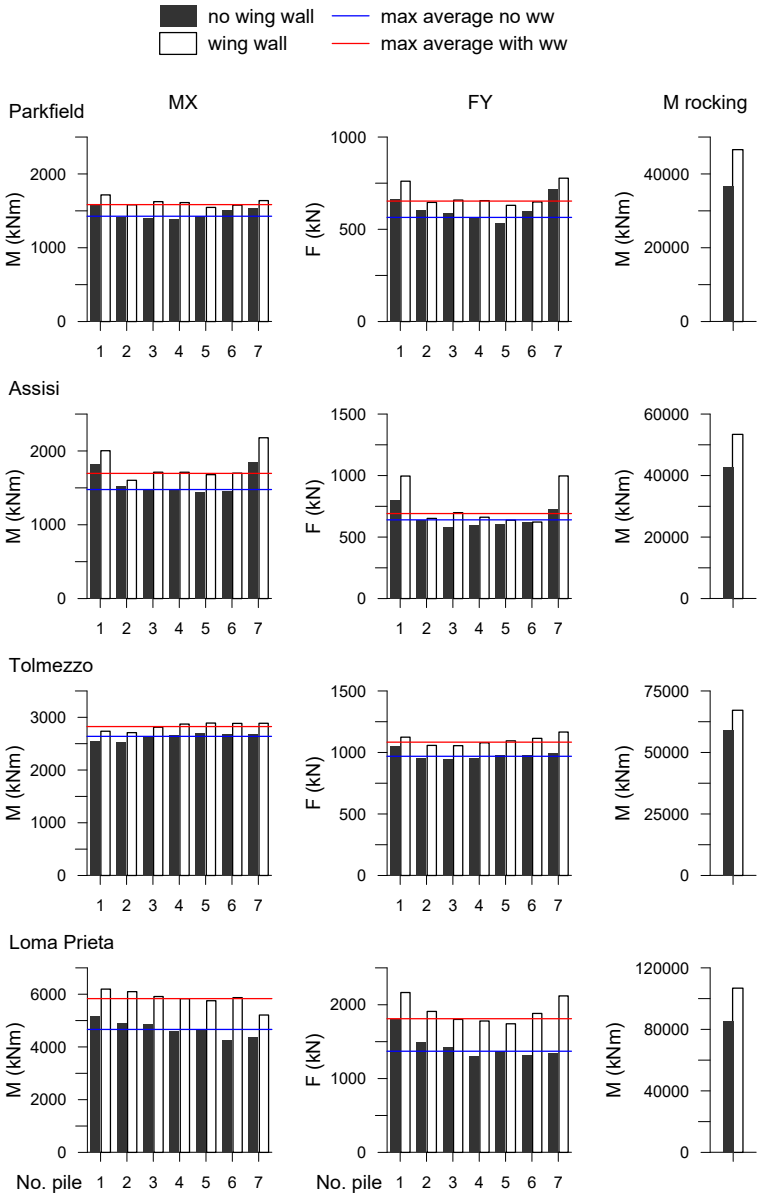

Fig. 7.12. Half 3D model and one-directional transverse analysis: comparison of the maximum increments of the internal stresses MX, FY and of the rocking moment in all seven piles; first four ground motions of Table 6.1.

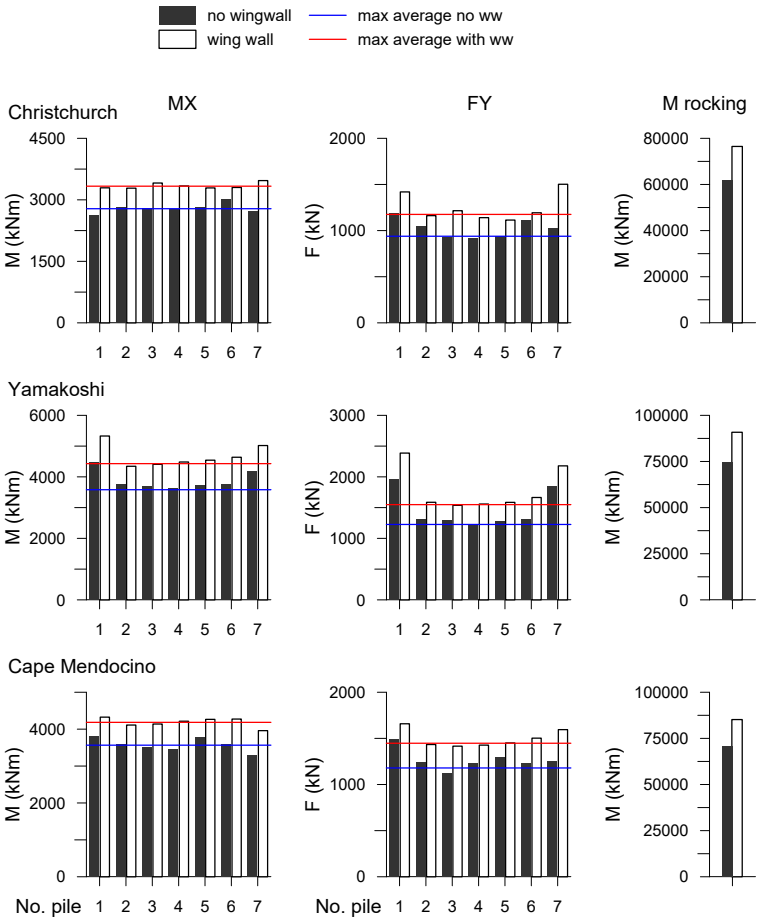

Fig. 7.13. Half 3D model and one-directional transverse analysis: comparison of the maximum increments of the internal stresses MX, FY and of the rocking moment in all seven piles; last three ground motions of Table 6.1.

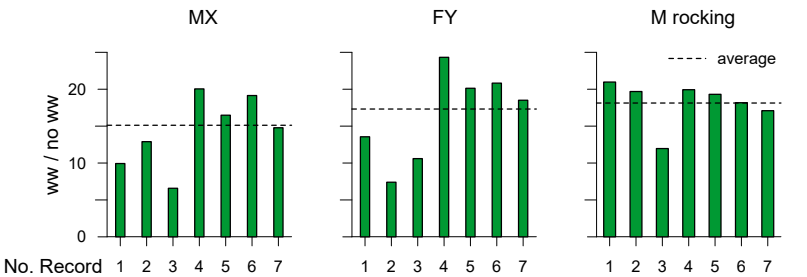

Fig. 7.14. Half 3D model and one-directional transverse analysis: average variations (%) of the internal forces in the pile foundation due to the presence of the wing walls.

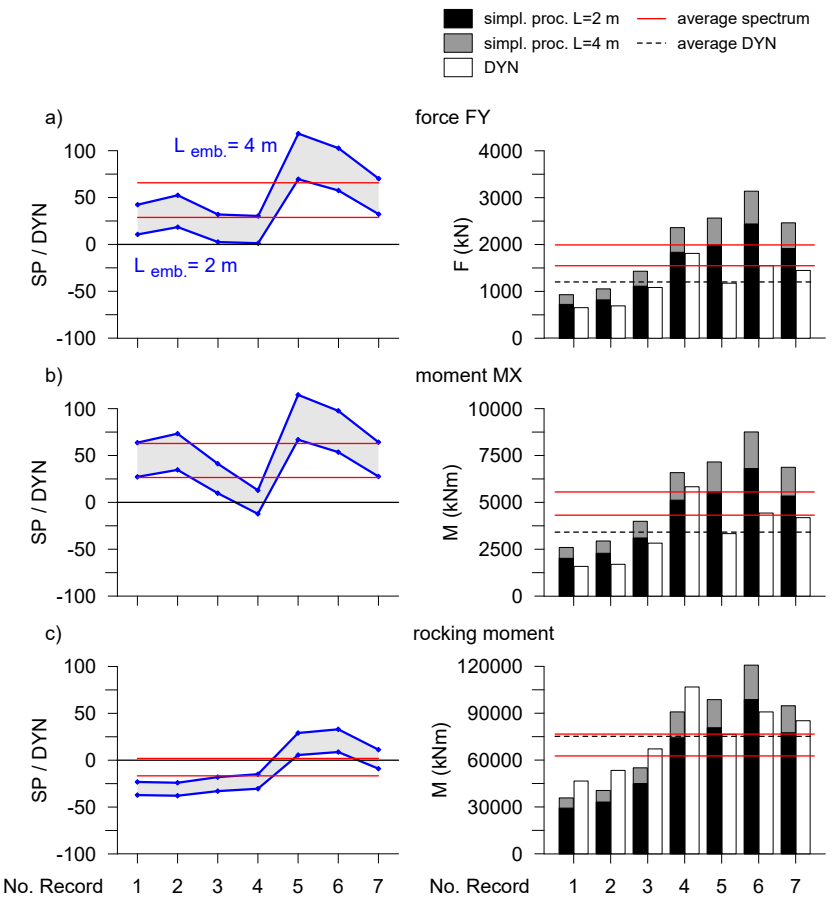

Fig. 7.15. Comparison (%) between the simplified procedure (SP) and the results of the dynamic analyses; (a) *FY*, (b) *MX* and (c) rocking moment.

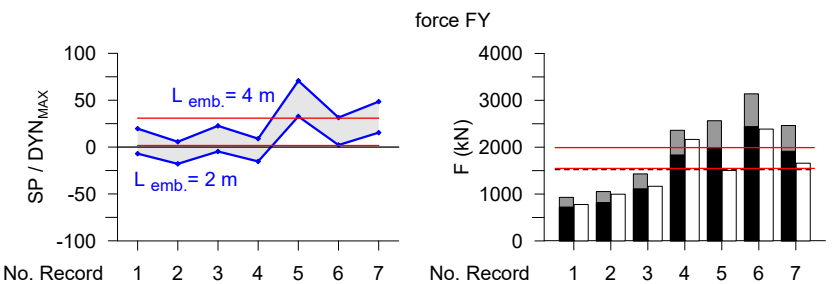

Fig. 7.16. Comparison (%) between the simplified procedure (SP) and the results of the dynamic analyses for *FY*. In this case, the maximum value recorded in the most loaded pile was considered, rather than the maximum value of the average time history increments.

Tab. 7.2. Internal forces provided by the simplified procedure and comparison with the dynamic values; FY (in kN), MX and rocking moment (in kNm). (M_{rot}) indicates the rocking moment obtained from the kinematic interaction only.

	DYN	$SP_{L=2}$ (M_{rot})	$SP_{L=4}$ (M_{rot})	$var_{L=2}$ %	$var_{L=4}$ %	DYN_{MAX}
FY	1201	1547	1991	28.8	65.8	1522
MX	3412	4317	5556	26.5	62.8	3729
rock. M	75207	62660 (5527)	76636 (7072)	−16.7	1.9	

7.4. Final remarks

This chapter addresses the influence of the cantilevered U-wing wall, illustrated in section 1.3.2, on the seismic behaviour of the single-span bridge with integral abutment herein examined. The detailed study shows that the behaviour of the system remains essentially decoupled. However, while no significant differences are observed in the longitudinal behavior between the models with and without the wing walls, the difference in the transverse direction can be paramount. In any case, this effect can still be easily incorporated in the simplified method developed for the transverse direction, considering an embankment length of approximately 50% of the abutment height. This length therefore does not appear to be related to length of the wing walls themselves, which is about 10.5 m.

In summary, the two simplified and complementary procedures illustrated for both the longitudinal and transverse directions can be used for the purpose of seismic design of these bridges even in the presence of wing walls. Nevertheless, appropriate considerations should be made if a different type of wing wall is chosen, or in case of irregular geometry.

Conclusions

Integral abutment bridges, and particularly the specific typology analysed in this work, are affected by an important mechanical interaction with the surrounding soil and with the approach embankments. The behaviour of the elements in contact with the soil, namely the abutment and its foundation, is fully coupled with the response of the superstructure. This is a classical example where soil-structure interaction cannot be neglected starting from the static design. Specifically, precisely because the construction sequence has a strong influence on the static and seismic response, it was accurately reproduced in a plausible way. Only subsequently, dynamic analyses were performed. Nonetheless, these full-dynamic analyses can rarely be used in practice since they require a large computational effort and a complex control of the response of the numerical models.

With the aim of providing simplified procedures that can be easily used for the ordinary design of such systems, this work has tried to concretise all the modeling efforts in the drafting of a novel approach for the seismic design of integral abutment bridges. This approach combines well-known design procedures, such as the decoupled approach and the non-linear static analysis, with methods deduced directly from the physical interpretation of the phenomena. A great contribution in this sense was offered by the original application of the modal analysis. Clearly, given the non-linearity involved mainly in the soil, the modal analysis does not constitute a design tool; however, in this case it has allowed to obtain a broader understanding of the problem under consideration. In this light, the results carry out on a fully 3D coupled soil-bridge system, implemented in the analysis framework OpenSees, were used as a benchmark to demonstrate the validity of the proposed

simplified procedures. These results however have not been achieved without cost. Numerous in-house codes have been necessary for the pre and post processing operations, as well as a large amount of time was dedicated to the single modelling details and the corresponding checks. Furthermore, the assessment of the results from the numerical models has been a tedious and slow process that could not proceed until all the encountered anomalies were thoroughly examined and explained.

Focusing on the longitudinal component of the seismic motion that typically dominates the design of this type of bridge and, taking advantage of the regular geometry of the case study examined, further numerical models were considered. In particular, a 2D and a half 3D longitudinal model have been developed. Then, considering on the one hand that the computation times of the dynamic simulations on the 2D model were reduced to a couple of hours of execution using OpenSeesSP and, on the other hand that a very similar response between the two models was observed, the 2D model proved to be an efficient modelling technique for extensive studies on the longitudinal seismic performance. In turn, the development of a static 2D numerical model was believed essential because the design under gravity loads should consider the effects of the construction sequence which is strongly affected by soil-structure interaction. In this regard, we have proposed to extend the use of this same 2D model to the seismic design of the bridge. This extension is obtained by performing on the same model a push-over analysis, according to two different distributions of equivalent seismic forces reproducing the deformation patterns associated with the dominant vibration modes and finally, using the resulting capacity curves in the context of the *well-known* capacity spectrum method, generalising the nonlinear static approach for geotechnical systems.

The two-directional analyses carried out on the full 3D model have showed that the transverse effects, given by the other component of the seismic motion, are basically independent from those computed for the longitudinal seismic action. Therefore, they can be evaluated separately and then superimposed. However, unlike the analysis in the longitudinal direction for which a 2D numerical model had to be developed to take into account the static conditions, the need for an ad hoc numerical model for the analysis in the transverse direction was not believed justifiable. Hence, an intuitive and simple method, based on the decoupled approach, was conceived in the transverse direction. In fact, this approach effectively accounted for the main sources of inter-

nal forces in the foundation piles and the deck-abutment-embankment system, incorporating them into a straightforward yet robust framework. Contrary to what might be thought, the volume of embankment involved does not seem to be relevant even in the presence of the wing walls. In closing, the two-directional dynamic analyses showed that the combination of this method with the one proposed in the longitudinal direction provides a complete tool for the design of these bridges under bidirectional seismic actions without any substantial underestimations.

Actually, a close inspection of two-directional analyses showed that the presence of the wing walls can accentuate the torsional effects increasing the stresses induced by the longitudinal component of the seismic motion. This effect, although not substantial, occurs when the two components of the seismic motion in the longitudinal and transverse direction are similar and, at the same time, in the longitudinal analysis no significant mobilisation of the pressure behind the abutment is achieved. On the other hand, these torsional effects could play an important role in cases of irregular geometry and different typology of the wing walls. Therefore, in the design of a single-span integral abutment bridge based on simplified procedures such as those provided in this work, it is recommended to maintain a geometry that is as regular as possible. Otherwise, given the three-dimensional nature of the problem, appropriate numerical 3D models must be devised.

The two complementary procedures developed in this work represent a starting point for the seismic design of integral abutment bridges in the near future, not only for the practical usefulness but also for the physical comprehension of the phenomena called into play. In particular, the nonlinear static analysis methodology is as a robust framework that, if properly validated, generalised and systematised, may be also extended for the seismic design of similar soil-structure systems. Finally, since both procedures use a decoupled approach for the definition of the seismic demand, the adoption of an appropriate spectrum prescribed by technical provisions makes this tool promptly applicable for the routine seismic design.

List of Figures

List of Tables

Bibliography

PD 6694-1. *Recommendations for the design of structures subject to traffic loading to BS EN 1997-1*. BSi: British Standard International. London, UK, 2011.

AASHTO. *LFRD bridge design specifications*. American Association of State Highway and Trasportation Officials, Washington, DC, 2012.

API. *Reccomanded practice for planning, designing, and constructing fixed offshore platforms.* American Petroleum Institute. Section 6.8 Soil Reaction for Laterally Load Piles, 2007.

A. Arias. Measure of earthquake intensity. In *Seismic Design for Nuclear Power Plants, edited by Hansen, R. J.*, pages 438–483. Cambridge, MIT Press, 1970.

A. Arias. Local directivity of strong ground motion. In *11th World Conference on Eartquake Engineering*, 1996. ISBN 0080428223.

ATC-40. *Seismic evaluation and retrofit of concrete buildings.* Applied Technology Council (ATC-40). Redwood City, California, 1996.

BA 42/96. *Design manual for roads and bridges*. Highway structures: approval procedures and general design, sect.3. general design, Part 12, the design of integral bridges, vol. 1. Highways Agency, 1996.

BA 42/96 amendment No.1. *Design manual for roads and bridges*. Highway structures: approval procedures and general design, sect.3. general design, Part 12, amendment No.1, the design of integral bridges, vol. 1. Highways Agency, 2003.

K. Been and M. Jefferies. A state parameter for sands. *Geotechnique*, 35: 99–112, 12 1985. doi: 10.1680/geot.1985.35.2.99.

J. J. Bommer and A. Martinez-Pereira. The effective duration of the eartquake strong motion. *Journal of Earthquake Engineering*, 03(02): 127–172, 1999. doi: 10.1142/S1363246999000077.

M. P. Jr. Burke. Integral bridges. In *Transportation Research Record No. 1275*, pages 53–61, Washington, D.C., 1990. TRB, National Research Council.

M. P. Jr. Burke. *Integral and semi-integral bridges*. Wiley-Blackwell, 2009. ISBN 1-282-68671-2.

L. Callisto. Capacity design of embedded retaining structures. *Géotechnique*, 64(3):204–214, 2014. doi: 10.1680/geot.13.P.091.

L. Callisto. On the seismic design of displacing earth retaining systems. In *Earthquake geotechnical engineering for protection and development of environment and constructions*, Proceedings of the 7th international conference on earthquake geotechnical engineering, pages 239–255, Rome, Italy, 2019. Associazione Geotecnica Italiana.

Caltrans. *Memo to Designers 5-1*. California Department of Transportation, Division of Structures, Sacramento, CA, 1988.

Caltrans. *Seismic design criteria, v.1.7*. California Department of Transportation, Division of Structures, Sacramento, CA, 2013.

A. Caristo, J. Barnes, and S. A. Mitoulis. Numerical modelling of integral abutment bridges under seasonal thermal cycles. *Proceedings of the Institution of Civil Engineers - Bridge Engineering*, 171(3):179–190, 2018. doi: 10.1680/jbren.17.00025.

I. F. Collins and G. T. Houlsby. Application of thermomechanical principles to the modelling of geotechnical materials. *Proceedings of the Royal Society of London. Series A: Mathematical, Physical and Engineering Sciences*, 453(1964):1975–2001, 1997. doi: 10.1098/rspa.1997.0107.

J. Connal. Integral abutment bridges: Australian and us practice. In *Fifth Austroads Bridge Conference*, Hobart, Tasmania, 2004.

C. B. Crouse, B. Hushmand, and G. Martin. Dynamic soil–structure interaction of a single-span bridge. *Earthquake Engineering & Structural Dynamics*, 15:711–729, 1987.

S.M. Day. Seismic response of embedded foundations. In *Proc. ASCE Convention*, Chicago, IL, October, Preprint No. 3450, 1978.

M. Dicleli and S. M. Albhaisi. Maximum length of integral bridges supported on steel H-piles driven in sand. *Engineering Structures*, 25 (12):1491–1504, 2003. ISSN 0141-0296. doi: 10.1016/S0141-0296(03) 00116-0.

M. Dicleli and S. M. Albhaisi. Estimation of length limits for integral bridges built on clay. *Journal of Bridge Engineering*, 9(6):572–581, 2004. doi: 10.1061/(ASCE)1084-0702(2004)9:6(572).

J. M. Duncan and C. Y. Chang. Nonlinear analysis of stress and strain in soils. *Journal of the Soil Mechanics and Foundations Division*, 96:1629–1653, 1970.

A. Elgamal, L. Yan, Z. Yang, and J. P. Conte. Three-dimensional seismic response of Humboldt Bay bridge-foundation-ground system. *Journal of Structural Engineering*, 134(7):1165–1176, 2008. doi: 10.1061/(ASCE) 0733-9445(2008)134:7(1165).

F. Elsabee and J.P. Morray. Dynamic behavior of embedded foundations. In *Rpt. No. R77-33*, Dept. of Civil Engrg., MIT, Cambridge, Mass., 1977.

G. L. England, N. C. M. Tsang, and D. I. Bush. *Integral bridges: a fundamental approach to the time–temperature loading problem*. Thomas Telford, 2000. doi: 10.1680/ibafattttlp.35416.

S. Erhan and M. Dicleli. Parametric study on the effect of structural and geotechnical properties on the seismic performance of integral bridges. *Bulletin of Earthquake Engineering*, 15:4163–4191, 10 2017. doi: 10.1007/s10518-017-0123-9.

FEMA 440. *Improvement of nonlinear static seismic analysis procedures*. Applied Technology Council (ATC-55 Project). Redwood City, California, 2005.

European Committee for Standardization. *EN 1998: Design of structures for earthquake resistance*. Brussels, Belgium, 2003.

P. Franchin and P. E. Pinto. Performance-based seismic design of integral abutment bridges. *Bulletin of Earthquake Engineering*, 12(2):939–960, 2014. ISSN 1573-1456. doi: 10.1007/s10518-013-9552-2.

S. A. Freeman. Review of the development of the capacity spectrum method. In *ISET Journal of Earthquake Technology*, volume 41, pages 1–13, 2004.

S. A. Freeman, J.P. Nicoletti, and J. V. Tyrell. Evaluation of existing buildings for seismic risk — A case study of Puget Sound Naval Shipyard, Bremerton, Washington. In *Proceedings of U.S. National Conference on Earthquake Engineering*, pages 113–122, Berkeley, 1975.

S. A. Freeman, J.P. Nicoletti, and J. V. Tyrell. Development and use of capacity spectrum method. In *Proceedings of the 6th U.S. National Conference on Earthquake Engineering*, Seattle, WA, 1998.

G. Gazetas. Seismic response of earth dams: some recent developments. *Soil Dynamics and Earthquake Engineering*, 6(1):2–47, 1987. ISSN 0267-7261. doi: https://doi.org/10.1016/0267-7261(87)90008-X. Special Issue - State-of-the-art.

GEOSPECTRA. *Design manual, foundation stiffnessess under seismic loading*. GEOSPECTRA, a division of Kleinfelder, Inc. Washington State Department of Transportation, 1997.

A. Ghofrani. *Development of Numerical Tools For the Evaluation of Pile Response to Laterally Spreading Soil*. PhD thesis, University of Washington, Seattle WA, 2018. URL https://digital.lib.washington.edu/researchworks/handle/1773/43004.

R. K. Goel. Earthquake characteristics of bridges with integral abutments. *Journal of Structural Engineering*, 123(11):1435–1443, 1997. doi: 10.1061/(ASCE)0733-9445(1997)123:11(1435).

R. K. Goel and A. K. Chopra. Evaluation of bridge abutment capacity and stiffness during earthquakes. *Earthquake Spectra*, 13(1):1–23, 1997. doi: 10.1193/1.1585929.

D. N. Gorini. *Soil-structure interaction for bridge abutments: two complementary macro-elements*. PhD thesis, Sapienza University of Rome, 2019. URL http://hdl.handle.net/11573/1260972.

D. N. Gorini and L. Callisto. A macro-element approach to analyse bridge abutments accounting for the dynamic behaviour of the superstructure. *Géotechnique*, 70(8):711–719, 2019. doi: 10.1680/jgeot.19.TI.012.

D. N. Gorini and L. Callisto. A coupled study of soil-abutment-superstructure interaction. In Francesco Calvetti, Federica Cotecchia, Andrea Galli, and Cristina Jommi, editors, *Geotechnical Research for Land Protection and Development*, pages 565–574. Springer International Publishing, 2020. doi: 10.1007/978-3-030-21359-6_60.

D. N. Gorini, L. Callisto, and A. Whitttle. An inertial macroelement for bridge abutments. *Géotechnique*, 10 2020a. doi: 10.1680/jgeot.19.P.397.

D. N. Gorini, A. J. Whittle, and L. Callisto. Ultimate limit states of bridge abutments. *Journal of Geotechnical and Geoenvironmental Engineering*, 146(7):04020054, 2020b. doi: 10.1061/(ASCE)GT.1943-5606.0002283.

D. N. Gorini, L. Callisto, and A. Whittle. Dominant responses of bridge abutments. *Soil Dynamics and Earthquake Engineering*, 148:106723, 09 2021. doi: 10.1016/j.soildyn.2021.106723.

E. C. Hambly. Integral bridges. *Proceedings of the Institution of Civil Engineers - Transport*, 123(1):30–38, 1997. doi: 10.1680/itran.1997.29177.

K. Ishihara, F. Tatsuoka, and S. Yasuda. Undrained deformation and liquefaction of sand under cyclic stresses. *Soils and Foundations*, 15: 29–44, 1975.

Italian Building Code. *Norme Tecniche per le Costruzioni. D.M. 14.01.2008*. Italian Ministry of Infrastructures and Transportation, Rome (in Italian), 2018.

W. D. Iwan. On a Class of Models for the Yielding Behavior of Continuous and Composite Systems. *Journal of Applied Mechanics*, 34(3): 612–617, 09 1967. ISSN 0021-8936. doi: 10.1115/1.3607751.

B. Jeremić, G. Jie, M. Preisig, and N. Tafazzoli. Time domain simulation of soil–foundation–structure interaction in non-uniform soils. *Earthquake Engineering & Structural Dynamics*, 38(5):699–718, 2009. doi: 10.1002/eqe.896.

J. Jiang, C. Xu, H. M. El Naggar, X. Du, Z. Xu, and J. Assaf. Improved pushover method for seismic analysis of shallow buried underground rectangular frame structure. *Soil Dynamics and Earthquake Engineering*, 140:106363, 2021. ISSN 0267-7261. doi: 10.1016/j.soildyn.2020.106363.

W. B. Joyner and A. T. F. Chen. Calculation of nonlinear ground response in earthquakes. *Bulletin of the Seismological Society of America*, 65(5): 1315–1336, 10 1975. ISSN 0037-1106.

A. Kotsoglou and S. Pantazopoulou. Modeling of embankment flexibility and soil-structure interaction in integral bridges. First European Conference on Earthquake Engineering and Seismology, Geneva, Switzerlan, 2006.

A. N. Kotsoglou and S. J. Pantazopoulou. Bridge–embankment interaction under transverse ground excitation. *Earthquake Engineering & Structural Dynamics*, 36(12):1719–1740, 2007a. doi: 10.1002/eqe.715.

A. N. Kotsoglou and S. J. Pantazopoulou. Soil-structure interaction: Capacity curve evaluation and seismic assessment of highway overcrossings. Proceedings of the 4th international conference on earthquake geotechnical engineering, Thessaloniki, Greece, 2007b.

S. L. Kramer. *Geotechnical Earthquake Engineering*. Prentice Hall, 1996.

O. S. Kwon and A. S. Elnashai. Seismic analysis of Meloland Road Overcrossing using multiplatform simulation software including SSI. *Journal of Structural Engineering*, 134(4):651–660, 2008. doi: 10.1061/(ASCE)0733-9445(2008)134:4(651).

S. Lacy. *Numerical procedures for nonlinear transient analysis of two-phase soil system*. PhD thesis, Princeton University, N.J., 1986.

C. C. Ladd, R. Foott, K. Ishihara, F. Schlosser, and H. G. Poulos. Stress deformation and strength characteristics. In *9th International Conference on Soil Mechanics and Foundation Engineering*, Tokyo, Japan, 1977.

R. Laguardia, D. Gallese, R. Gigliotti, and L. Callisto. A non-linear static approach for the prediction of earthquake-induced deformation of geotechnical systems. *Bulletin of Earthquake Engineering*, 18(15): 6607–6627, 2020. ISSN 1573-1456. doi: 10.1007/s10518-020-00949-2.

I.P. Lam and G.R. Martin. *FHWA/RD-86/102: Seismic design of highway bridge foundations. Volume II - Design procedures and duidelines.* Federal Highway Administration, 1986.

S. Lee, M. Feng, S. Kwon, and S. Hong. Equivalent modal damping of short-span bridges subjected to strong motion. *Journal of Bridge Engineering*, 16:316–323, 03 2011. doi: 10.1061/(ASCE)BE.1943-5592.0000149.

B. M. Lehane. Lateral soil stiffness adjacent to deep integral bridge abutments. *Géotechnique*, 61(7):593–603, 2011. doi: 10.1680/geot.9.P.135.

X. S. Li and Y. Wang. Linear representation of steady-state line for sand. *Journal of Geotechnical and Geoenvironmental Engineering*, 124(12):1215–1217, 1998. doi: 10.1061/(ASCE)1090-0241(1998)124:12(1215).

W.D. Liam Finn. A study of piles during earthquakes: Issues of design and analysis. *Bulletin of Earthquake Engineering*, 3:141–234, 01 2005. doi: 10.1007/s10518-005-1241-3.

J. Lysmer and R. L. Kuhlemeyer. Finite dynamic model for infinite media. *Journal of the Engineering Mechanics Division*, 95(4):859–877, 1969. doi: 10.1061/JMCEA3.0001144.

G. Masing. Eigenspannungen und Verfestingung beim Messing. *In: Proceedings Second International Congress of Applied Mechanics*, pages 332–335, 1926.

MATLAB. *Version R2020b*. The MathWorks Inc., Natick, Massachusetts, 2020. URL https://www.mathworks.com.

D. B. McCallen and K. M. Romstad. Dynamic analyses of a skewed short-span, box-girder overpass. *Earthquake Spectra*, 10(4):729–755, 1994. doi: 10.1193/1.1585795.

C. R. McGann. *Numerical Evaluation of Forces on Piled Bridge Foundations in Laterally Spreading Soil*. PhD thesis, University of Washington, Seattle WA, 2013. URL https://digital.lib.washington.edu/researchworks/bitstream/1773/23579/1/.

C. R. McGann, P. Arduino, and P. Mackenzie-Helnwein. A stabilized single-point finite element formulation for three-dimensional dynamic

analysis of saturated soils. *Computers and Geotechnics*, 66:126–141, 2015. ISSN 0266-352X. doi: 10.1016/j.compgeo.2015.01.002.

C. R. McGann, P. Arduino, and A. Ghofrani. *Numerical Evaluation of Forces on Piled Bridge Foundations in Laterally Spreading Soil*. Washington State Transportation Center (TRAC-UW), 2017. URL https://www.wsdot.wa.gov/research/reports/fullreports/874-1.pdf.

F. McKenna. *OpenSees. Object oriented finite element analysis: Frameworks for analysis algorithms and parallel computing*. PhD thesis, University of California, Berkeley, 1997.

F. McKenna and G.L. Fenves. Using the OpenSees interpreter on parallel computers. 2007. URL https://opensees.berkeley.edu/ParallelProcessing.pdf.

F. McKenna, M. H. Scott, and G. L. Fenves. OpenSees. Nonlinear finite-element analysis software architecture using object composition. *Journal of Computing in Civil Engineering*, 24(1):95–107, 2010. doi: 10.1061/(ASCE)CP.1943-5487.0000002.

A. Mita and J.E. Luco. Dynamic response of a square foundation embedded in an elastic half-space. *Soil Dynamics and Earthquake Engineering*, 8(2):54–67, 1989. ISSN 0267-7261. doi: https://doi.org/10.1016/S0267-7261(89)80013-2.

N. Mononobe, A. Takata, and M. Matamura. Seismic stability of the earth dam. In *Proceedings, 2nd Congress on Large Dams, Vol. IV.*, Washington, D.C, 1936.

Z. Mróz. On the description of anisotropic workhardening. *Journal of the Mechanics and Physics of Solids*, 15(3):163–175, 1967. ISSN 0022-5096. doi: https://doi.org/10.1016/0022-5096(67)90030-0.

D. Muir Wood. *Geotechnical Modelling*. Spon Press, 2004. doi: 10.1201/9781315273556.

D. Muir Wood and D. Nash. Earth pressures on an integral bridge abutment: A numerical case study. *Soils and Foundations*, 40(6):23–38, 2000. ISSN 0038-0806. doi: https://doi.org/10.3208/sandf.40.6_23.

S. Nakamura, Y. Momiyama, T. Hosaka, and K. Homma. New technologies of steel/concrete composite bridges. *Journal of Constructional Steel Research*, 58(1):99–130, 2002. ISSN 0143-974X. doi: https://doi.org/10.1016/S0143-974X(01)00030-X.

S. Nemat-Nasser and Y. Tobita. Influence of fabric on liquefaction and densification potential of cohesionless sand. *Mechanics of Materials*, 1(1):43–62, 1982. ISSN 0167-6636. doi: https://doi.org/10.1016/0167-6636(82)90023-0.

A. G. Papadimitriou, G. D. Bouckovalas, and Y. F. Dafalias. Plasticity model for sand under small and large cyclic strains. *Journal of Geotechnical and Geoenvironmental Engineering*, 127(11):973–983, 2001. doi: 10.1061/(ASCE)1090-0241(2001)127:11(973).

E. Parra. *Numerical modeling of liquefaction and lateral ground deformation including cyclic mobility and dilation response in soil systems*. PhD thesis, Rensselaer Polytechnic Institute, Troy, N.Y, 1996.

J. Prévost. A simple plasticity theory for frictional cohesionless soils. *International Journal of Soil Dynamics and Earthquake Engineering*, 4:9–17, 1985.

A. Rahmani, M. Taiebat, and W. D. Liam Finn. Nonlinear dynamic analysis of Meloland Road Overpass using three-dimensional continuum modeling approach. *Soil Dynamics and Earthquake Engineering*, 57: 121–132, 2014. ISSN 0267-7261. doi: 10.1016/j.soildyn.2013.11.004.

A. Rahmani, M. Taiebat, W. D. Liam Finn, and C. E. Ventura. Evaluation of substructuring method for seismic soil-structure interaction analysis of bridges. *Soil Dynamics and Earthquake Engineering*, 90:112–127, 2016. ISSN 0267-7261. doi: 10.1016/j.soildyn.2016.08.013.

E. M. Rathje, N. A. Abrahamson, and J. D. Bray. Simplified frequency content estimates of earthquake ground motions. *Journal of Geotechnical and Geoenvironmental Engineering*, 124(2):150–159, 1998. doi: 10.1061/(ASCE)1090-0241(1998)124:2(150).

E. M. Rathje, C. Dawson, J.E. Padgett, J.-P. Pinelli, D. Stanzione, A. Adair, P. Arduino, S.J. Brandenberg, T. Cockerill, C. Dey, M. Esteva, Jr. F.L. Haan, M. Hanlon, A. Kareem, L. Lowes, S. Mock, and G. Mosqueda. Designsafe: A new cyberinfrastructure for natural hazards engineering. 2017. doi: 10.1061/(ASCE)NH.1527-6996.0000246.

R. Ribó, M. Pasenau, E. Escolano, J.Suit. Perez, A. Coll, A. Melendo, and S. Gonzáles. *GiD v.9 User Manual*. Barcelona, Spain, 2008. URL https://www.gidhome.com/news-and-events/gid-versions/73/the-version-9-its-public/.

F. Sabetta and A. Pugliese. Attenuation of peak horizontal acceleration and velocity from italian strong-motion records. *Bulletin of the Seismological Society of America*, 77(5):1491–1513, 10 1987. ISSN 0037-1106. doi: 10.1785/BSSA0770051491.

SAP2000. *Integrated Software for Structural Analysis and Design*. CSI. Computers and Structures, Inc., Berkeley, California.

H.B. Seed, R.T. Wong, I.M. Idriss, and K. Tokimatsu. *Moduli and damping factors for dynamic analysis of cohesionless soil*. Earthquake Engineering Research Center Report UCB/EERC-84/14, 1984.

S. M. Springman, A. R. M. Norrish, and C. W. W. Ng. *Cyclic loading of sand behind integral bridge abutments*. TRL Project Report 146. Crowthorne, U.K.: Transport Research Laboratory, 1996.

M. Stucchi, C. Meletti, V. Montaldo, H. Crowley, G. M. Calvi, and E. Boschi. Seismic Hazard Assessment (2003–2009) for the Italian Building Code. *Bulletin of the Seismological Society of America*, 101(4): 1885–1911, 08 2011. ISSN 0037-1106. doi: 10.1785/0120100130.

M. Vucetic and R. Dobry. Effect of soil plasticity on cyclic response. *Journal of Geotechnical Engineering*, 117(1):89–107, 1991. doi: 10.1061/(ASCE)0733-9410(1991)117:1(89).

J. Waldin, J. Jennings, and P. Routledge. Critically damaged bridges and concepts for earthquake recovery. 2012 NZSEE Conference, 2012.

E.P. Wasserman and J.H. Walker. Integral abutments for steel bridges. In *Highway Structures Design Handbook*, volume 2. Structural Division: Tennessee Department of Transportation for the American Iron and Steel Institute, 1996.

S. D. Werner, J. L. Beck, and M. B. Levine. Seismic response evaluation of Meloland Road Overpass using 1979 Imperial Valley earthquake records. *Earthquake Engineering & Structural Dynamics*, 15(2):249–274, 1987. doi: 10.1002/eqe.4290150207.

H. White. Integral abutment bridges: Comparison of current practice between European countries and the United States of America. In *Special report 152*. Transportation research and development bureau. New York State Department of Transportation, 2007.

H. White. Wingwall type selection for integral abutment bridges: Survey of current practice the United States of America. In *Special report 154*. Transportation research and development bureau. New York State Department of Transportation, 2008.

H. White, H. Pétursson, and P. Collin. Integral abutment bridges: The european way. *Practice Periodical on Structural Design and Construction*, 15(3):201–208, 2010. doi: 10.1061/(ASCE)SC.1943-5576.0000053.

J. C. Wilson and B. S. Tan. Bridge abutments: Formulation of simple model for earthquake response analysis. *Journal of Engineering Mechanics*, 116(8):1828–1837, 1990a. doi: 10.1061/(ASCE)0733-9399(1990)116:8(1828).

J. C. Wilson and B. S. Tan. Bridge abutments: Assessing their influence on earthquake response of Meloland Road Overpass. *Journal of Engineering Mechanics*, 116(8):1838–1856, 1990b. doi: 10.1061/(ASCE)0733-9399(1990)116:8(1838).

J. H. Wood. Earthquake design of bridges with integral abutments. Proceedings of the 6th international conference on earthquake geotechnical engineering, Christchurck, New Zealand, 2015.

Z. Yang, A. Elgamal, and E. Parra. Computational model for cyclic mobility and associated shear deformation. *Journal of Geotechnical and Geoenvironmental Engineering*, 129(12):1119–1127, 2003. doi: 10.1061/(ASCE)1090-0241(2003)129:12(1119).

J. Zhang and N. Makris. Kinematic response functions and dynamic stiffnesses of bridge embankments. *Earthquake Engineering & Structural Dynamics*, 31(11):1933–1966, 2002a. doi: 10.1002/eqe.196.

J. Zhang and N. Makris. Seismic response analysis of highway overcrossings including soil–structure interaction. *Earthquake Engineering & Structural Dynamics*, 31(11):1967–1991, 2002b. doi: 10.1002/eqe.197.

O. C. Zienkiewicz and T. Shiomi. Dynamic behaviour of saturated porous media; the generalized biot formulation and its numerical

solution. *International Journal for Numerical and Analytical Methods in Geomechanics*, 8(1):71–96, 1984. doi: https://doi.org/10.1002/nag.1610080106.

Opera sottoposta a peer review. Il Consiglio scientifico-editoriale, anche attraverso i comitati scientifici di serie, assicura una valutazione trasparente e indipendente delle opere sottoponendole in forma anonima a due valutatori ignoti agli autori e ai curatori. Per ulteriori dettagli si rinvia al sito: www.editricesapienza.it

This work has been subjected to a peer review. The Scientific-editorial Board, also through the scientific committees of series, ensures a transparent and independent evaluation of the works by subjecting them anonymously to two reviewers, unknown to the authors and editors. For further details please visit the website: www.editricesapienza.it

Collana Studi e Ricerche

Per informazioni sui volumi precedenti della collana, consultare il sito: www.editricesapienza.it | *For information on the previous volumes included in the series, please visit the following website: www.editricesapienza.it*

155. Toward a Cultural History of the Cold War in Turkey
Ideological dynamics, cultural production, media
edited by Fulvio Bertuccelli

156. Leggenda, realtà e finzione nell'opera di Aleksej Remizov
Un'analisi di Podstrižennymi glazami
Maria Teresa Badolati

157. Estetiche della geolocalizzazione
Pratiche artistiche e media locativi
Paolo Berti

158. La codificazione di Haiti
Dal *Code Henry* al Codice civile del 1825
Iterio di Camillo

159. Soil-structure interaction for the seismic design of integral abutment bridges
Domenico Gallese

160. Probing the horizon of black holes with gravitational waves
Elisa Maggio

161. «Rhetorica eloquentia armat»
Evidentia e *amplificatio* nella prosa narrativa di Boccaccio
Serena Mauriello

162. Touch and the body
First-hand and others' tactile experiences reveal the embodied nature of pleasant social touch
Manuel Mello

163. Spectral theory of non-self-adjoint Dirac operators and other dispersive models
Nico Michele Schiavone

164. One protein many functions: the non-canonical interactions of SHMT1
The structural and functional characterization of SHMT1 interactions with RNA and in the *de novo* thymidylate synthesis complex
Sharon Spizzichino

Studi e Ricerche

Integral abutment bridges are bridges characterised by a monolithic connection between the deck and the abutments. Therefore, their behaviour during a seismic event is controlled by the interaction of the entire structure with the surrounding soil, and markedly with the approach embankment. Despite becoming a popular design due to low maintenance requirements, seismic design procedures still face uncertainties due to limited understanding of the dynamic soil-structure response.

Domenico Gallese is an engineer specialised in the assessment of major civil structures with a particular focus on seismic loading and soil-structure interaction. He earned his PhD with honours in 2022 from Sapienza University of Rome following a visiting research experience in the US. His passion for numerical modeling drives him to apply advanced mathematical concepts to solve complex engineering problems. Currently, as a professional designer, he is involved in important projects worldwide as well as in many R&D initiatives. He has published several papers in peer-reviewed journals and regularly presents at international conferences.

Winner of the Competition
"Prize for PhD Thesis 2023"
arranged by Sapienza
University Press.

ISBN 978-88-9377-362-1

www.editricesapienza.it